A VARIATIONAL FRAMEWORK FOR MULTI-SCALE DEFECT MODELING IN STRAINED ELECTRONICS AND PROCESSING OF COMPOSITE MATERIALS

BY

AHMAD AL-NASEEM

DISSERTATION

Submitted in partial fulfillment of the requirements
for the degree of Doctor of Philosophy in Civil Engineering
in the Graduate College of the
University of Illinois at Urbana-Champaign, 2018

Urbana, Illinois

Doctoral Committee:

Professor Arif Masud, Chair and Director of Research
Professor C. Armando Duarte
Associate Professor Oscar Lopez-Pamies
Professor Marcelo Garcia

Abstract

With the recent advances in material processing technologies and the introduction of the material genome initiative, material processing has gained an increased level of attention in the research community. Primary challenges in most material processing technologies and specifically in composite materials are the uncertainties concerning the material's performance under loading whether it be static, dynamic or cyclic. That is due to the variabilities in these technologies that may lead to the formation of defects within the material parts at critical location during processing. This dissertation presents a deterministic defect modeling framework based on a system of variationally consistent formulations that allow for the modeling of the material processing stage and incorporate multi-physics coupling for multi-constituent materials. A stabilized and novel discontinuity capturing formulation is developed to model multi-phase flow of the materials and their defect while sharply capturing the jumps in material properties, material compressibility and kinetic reaction across the multi-phase interfaces.

The method is based on employing structured non-moving meshes to solve the Navier-Stokes equations employing a finite element method (FEM) stabilized via the Variational Multiscale Method (VMS). Within VMS framework a discontinuity capturing method is derived that allows for sharp discontinuity capturing of the physical discontinuities of across phases within a single numerical element allowing for highly accurate and discrete representation of the interfacial physical phenomena. In addition, surface tension is incorporated into the formulation to discretely model jumps in the pressure field. The multi-phase interface is evolved employing a stabilized level-set method allowing for intricate motion of the two phases and the discontinuities within the Eulerian mesh. The formulation is then expanded to incorporate discontinuities in the governing system of equations allowing for modeling adjacent compressible-incompressible fluids within a unified formulation. Coupled with the

thermal evolution within the constituents of the material and accounting for phase change and mass leading to mass transfer across the interface the materials, kinetic evolution of the material viscosities is modeled at the material points accounting for variability in the flow behavior as a function of kinetic curing. Finally, a previously developed isogeometric FEM method is expanded to model quantum defect evolution of strained electronics and the effect of straining on the electronic properties of these materials.

Representative numerical tests involving complex multi-phase flows of physical instabilities, hydrodynamic collapse of bubbles and convective mass transfer along with electronic band-gap structures with strain effects are presented as validations and applications for the framework's robustness. Finally, the chemo-thermo-mechanical coupling and real-life application is presented via a fully coupled problem involving processing of a composite bracket during the early curing stages.

Acknowledgments

First and foremost, I thank and praise God for his endless blessing on me and my family and his guidance that allowed me to keep pushing through up till to today. I would like to express my sincere gratitude to my mentor and advisor Professor Arif Masud for his continued guidance, inspiration and devotion to his work and students that transformed me throughout my Ph.D. study and research. Holding me to his high standards in research elevated my character, work ethics and understanding of computational mechanics alike.

I want to also take the opportunity to thank the members of my doctoral committee Professor Armando Duarte, Professor Marcelo Garcia and Professor Oscar Lopez-Pamies for accepting to serve on the committee and for their technical and insightful comments to improve my work. I have had the honor to take multiple classes with both Professor Lopez-Pamies and Professor Duarte and learn from them both in class and outside of it. Although, I did not have the chance to take a course with Professor Garcia, I have benefited from his comments and guidance in developing this thesis.

I would also like to acknowledge the financial support and the openness into new research areas provided by Kuwait University through their scholarship that made it possible to attain this degree with minimal financial stress. This generous scholarship has also made it possible for me to be accompanied by my wife and daughters throughout the time of my study without compromising their growth and development. This is gratefully acknowledged.

During these five years at UIUC I have been blessed to be surrounded by very bright and helpful colleagues both inside and outside my research group. However, I would like to specifically mention in my gratitude Dr. Timothy Truster, Dr. Jaehyuk Kwack, Dr. Harishanker

Gajendran, Dr. Pinlei Chen, Lixing Zhu, Marcelino Anguiano, Soonpil Kang, Ian Tuttle, Shoaib Goraya and Ignasius Anugraha, for the supportive and rich environment that provided to me during my Ph.D. years.

Finally, I would like to thank the cornerstones of my life, my mother and father and siblings for their encouragement and support despite the far distances between us and to thank my soulmate and loving wife Asmaa Almunayes for her support and the burdens she carried with me all these years. I would also not forget to mention my lovely daughters Muna and Maryam. Despite their young age they have always been there for me to pick me up with a smile and a hug and allowed me to work putting me before their needs as children. Thank you all.

To my dear parents, siblings, wife and daughters, thank you all

Table of Contents

CHAPTER 1
INTRODUCTION

This dissertation is aimed to develop a stabilized finite element method capable of modeling defects' transport, growth, shrinkage, coalescence and splitting during a material's processing stage. The defects are modeled as voids or bubbles in a two-phase flow containing liquid and gaseous phases separated by an interface. The flow is modeled using Stokes flow equations for cases of viscous flow and incompressible Navier-Stokes equations for less viscous flows, whilst the interface is evolved through a Level-Set advection equation. In the complex process of defect evolution, and especially under laminar flow conditions, the dominant physical phenomena that govern the stability and accuracy of the simulations are the interfacial physical processes. Under immiscible fluid flow conditions where the defect void is allowed only to migrate and change shape, the main interfacial conditions are the a) discontinuous density, b) discontinuous viscosity and c) surface tension. These material parameter discontinuities lead to discontinuities in the velocity gradient of the momentum equations and the surface tension results in discontinuities in the pressure field as well. To model these discontinuities without resorting to any averaging scheme, we develop a unique technique using the Variational Multiscale Method to split the velocity into coarse and fine scales and then enriching the fine-scale shape functions with weakly discontinuous shape functions. This enrichment idea is inspired by the generalized finite element

method but differs in the sense that the enrichment is local to the element ad does not increase the size of the linear system.

Additionally, the enrichment function is easily formed using the underlying implicit interface field. This also allows for an automated enrichment that is only active in elements intersected by the interface and therefore adapts to the moving interface automatically without increasing the size of the global problem and slightly modifies the size of the local fine-scale problems of intersected element. The Level-Set method is used to track the interface and avoid the use of a Lagrangian mesh which requires high computational cost and is limited to simple noninvertible defamation of the elements. While the Level-Set interface is capable of modeling the interface with higher accuracy, the surface tension term requires the calculation of the curvature of the interface which requires higher-order derivatives (second order for CSF implementation and third order for our discontinuous formulation) of the Level-Set function and thus the use of higher order elements. Thus, to bypass this difficulty and continue to use low-order elements we adopt a curvature augmented Leve-Set method with a constrained formulation to ensure the satisfaction of the Eikonal equation as a property of the implicit interface function. This allows us to implement a sharply discontinuous surface tension term without resorting to a continuum surface forcing technique which misrepresents the shape of the void and the magnitude of the surface tension when solved by the momentum equations.

In the case where mixing or transport across the interface of the void is allowed, and while still assuming an incompressible flow condition, mass transfer of an underlying soluble contaminant material is modeled using a concentration advection diffusion equation. However, since the concentration of this contaminant is varying across the domains and exist in liquid phase within the liquid domain and in gaseous phase within the vapor domain an interfacial

condensation/evaporation reaction term is needed to model transfer of contaminant across the phases. This term is dependent on an activation concentration level, the vapor pressure inside the void and a coefficient of vaporization intrinsic to the two fluids. Finally, additional coupling with thermal evolution modeling interfacial phase-change is also examined. This complete coupled model is aimed to be a generic framework for such thermos-chemo-mechanical multi-flow problems when complete coupling is achieved across the different layers of physical phenomena on the same physical and numerical domains.

Chapter 2 presents a new stabilized method that is endowed with variationally derived Discontinuity Capturing (DC) features to model steep advection fronts and discontinuities that arise in multi-phase flows as well as in mixing flows of immiscible incompressible fluids. Steep fronts and discontinuities also arise in hypersonic compressible flows. The new method finds roots in the Variational Multiscale (VMS) framework that yields a coupled system of coarse and fine-scale variational problems. Augmenting the space of functions for the fine-scale fields with weak and/or strong discontinuities results in fine-scale models that naturally accommodate jumps in the fine fields. Variationally embedding the discontinuity enriched fine-scale models in the coarse-scale formulation leads to the Variational Multiscale Discontinuity Capturing (VMDC) method where stabilization tensors are naturally endowed with discontinuity capturing structure. In the regions with sharp gradients, these variationally projected fine-scale models augment the stability of the coarse-scale formulation to accurately capture sharply varying coarse solutions. Since the proposed method relies on local enrichment, it does not require either the complete or the dynamic enrichment algorithms that are invariably employed in methods that use global enrichment ideas. The scalar advection equation serves as a model problem to investigate the variational structure of the DC terms. The VMDC method is then applied to the Navier-Stokes equations and tested on

problems involving two-phase flows with and without surface tension. These test problems highlight that fine-scale models not only stabilize the weak form, variationally derived fine models that are endowed with sharp discontinuities also augment the coarse scale solutions with features that are otherwise not adequately resolved by variational formulations that act only at the coarse-scale levels.

In chapter 3 a unified method is presented to model the flow of adjacent compressible-incompressible multi-phase fluids with sharp jumps in the compressibility coefficients across the phase interface. The unified formulation incorporates state equations for each phase that allows for density variation as a function of pressure and temperature in time and space. The dependence is controlled via the isothermal compressibility coefficient that is allowed to vary sharply across the phase interface leading to a discontinuity in the underlying continuity equation. Employing the VMDC method to capture the discontinuities in the material properties and the compressibility coefficients adopted from the flow is modeled using a fixed Eularian mesh augmented with the level-set equation to capture the interface evolution. This method allows for flexibility in modeling gas bubble growth, shrinkage and collapse due to the nature of the gas being compressible. In addition, the method allows for modeling of transport of the deforming bubbles and is shown to accommodate merging and separation of bubbles across periodic boundary conditions which makes it possible to run long term channel flow simulations. The method is tested for cases where surface tension is active and plays a role in the shape evolution of the gas phase across the domain. These include problems in 2D and 3D, hence presenting the scalability of the method to higher dimensions.

Chapter 4 presents a variationally derived stabilized method that is endowed with Discontinuity Capturing (DC) features to model elliptic equations embedded with discontinuities in its coefficients and jumps in its solution field. Emanating from the Variational Multiscale (VMS) framework where the elliptic equation is decomposed into two sub-problems that variationally incorporates these discontinuities via a Lagrange multiplier formulation to enforce the interfacial discontinuity conditions. This formulation allows for a parameter free Nitsche like formulation to enforce the conditions without restoring to conforming meshes to the interface. Employing the fine-scale enriched shape functions to capture these discontinuities sharply, the previously developed Variational Multiscale Discontinuity Capturing (VMDC) is extended to elliptic equations. In addition, a variational surface tension formulation is embedded into the formulation allowing for the modeling of Marangoni effects at the interface with a modification the enrichment shape functions to allow for normal and tangential discontinuity of the pressure field across the interface. Additionally, the stabilized level-set method is employed to model interface evolution coupled with the advection diffusion equation to model the thermally induced phase change as well. The method is validated via a number of benchmark problems and numerical convergence studies are presented. Thereafter, the method is tested for industrial strength problems involving solute mass transfer of acid solute across the interface between two fluids.

Chapter 5 presents B-splines and NURBS based finite element method for self-consistent solution of the Schrödinger wave equation (SWE). The new equilibrium position of the atoms is determined as a function of evolving stretching of the underlying primitive lattice vectors and it gets reflected via the evolving effective potential that is employed in the SWE. The nonlinear SWE is solved in a self-consistent fashion wherein a Poisson problem that models the Hartree and local potentials is solved as a function of the electron charge density. The complex-valued generalized

eigenvalue problem arising from SWE yields evolving band gaps that result in changing electronic properties of the semiconductor materials. The method is applied to Indium, Silicon, and Germanium that are commonly used semiconductor materials. It is then applied to the material system comprised of Silicon layer on Silicon-Germanium buffer to show the range of application of the method.

Process modeling of polymeric materials involves reactive chemistry of multiple constituents that are invariably exothermic that gives rise to thermal gradients. The mechanical properties of the resulting material are a function of the spatial temporal distribution of the thermal field because of the dependence of cure on local temperature distribution. Degree of cure gets manifested via mechanical and thermal coefficients that are then embedded in the balance laws to carry out performance analysis of the produced part. Chapter 6 presents a summary of the models and methods covered in this work along with an introduction of a variationally consistent method, embedded with a phenomenological model for thermo-chemical curing of polymeric composites. Arrhenius model is employed to make curing a function of time and temperature. This model is embedded in the Stokes flow model for the spatial evolution of the bubbles in the viscous resin with evolving mechanical properties.

CHAPTER 2

VARIATIONALLY DERIVED DISCONTINUITY CAPTURING METHODS: FINE SCALE MODELS WITH EMBEDDED WEAK AND STRONG DISCONTINUITIES [a]

2.1 Motivation

Weak and strong discontinuities in the flow physics have been of prime significance in highly advective compressible flows [19, 41, 10, 35]. These issues also arise in the flow of immiscible fluids where sharp changes in the material properties across the fluid interfaces induce rapid changes in flow characteristics [9, 11, 13, 37, 1, 32, 22]. In multiphase flows involving gaseous bubbles in the surrounding liquid, surface tension effects induce sharp changes in the pressure field [4, 34, 22, 23]. In all these problem classes, steep gradients and discontinuities pose considerable challenge to the numerical methods to capture the fields without over-shoots and under-shoots across the interfaces of discontinuity.

The issue of steep gradients has largely been addressed in the domain of high-speed compressible flows and various Discontinuity Capturing (DC) techniques have been proposed [19, 41, 10, 37] that augment the stabilization facilitated by Streamline Upwind Petrov-Galerkin (SUPG) [19, 41, 10] and the Galerkin Least-Squares (GLS) [18, 26] methods to accurately capture the discontinuity. The DC term in SUPG and GLS methods is comprised of the residual of the

[a] This Chapter has been adapted from "Masud, A., & Al-Naseem, A. A. (2018). Variationally derived discontinuity capturing methods: Fine scale models with embedded weak and strong discontinuities. Computer Methods in Applied Mechanics and Engineering, In Press." The copyright owner has provided written permission to reprint the work.

Euler-Lagrange equations of the governing system, together with a DC operator that accounts for the location and orientation of the steep front [19, 41, 10]. On the other hand, in the context of incompressible multiphase flows several techniques have been proposed in the literature [14, 9, 11, 13, 37, 1, 32, 22, 23] to model flow features that arise due to sharp changes in the viscosity and/or density of the fluids across the immiscible interfaces. Commonly used methods are based on averaging techniques that smooth out the discontinuities and enforce a monotone transition of the material properties over a narrow band across the interface [4, 23]. These methods require a regularized Heaviside function that transitions from 0 to 1 across a strip of finite thickness at the interface. Although these approaches bypass the issues arising because of sharp discontinuity, they introduce parameter dependency that is based on the choice of the regularization function and the interface thickness over which this function is defined. Determining a regularized form of the Heaviside function and an appropriate thickness parameter that invariably depends on the element size has proved to be highly problem dependent [23].

From the perspective of immiscible fluids with different viscosities, it is important to examine the effects of discontinuity in the material properties on the velocity and pressure fields. In the momentum equation the viscous stress is represented by the gradient of the velocity field multiplied by the viscosity of the fluid. Any strong discontinuity in viscosity results in a weak discontinuity in the velocity field and a strong discontinuity in the velocity gradient. To make the discussion precise, by strong discontinuity we mean a steep jump in the field over an infinitesimal thickness, and a weak discontinuity corresponds to a discontinuity in the slope of the field at a given point. Thus, to accurately model the velocity field across the interface, weakly discontinuous interpolation functions are required.

A literature review reveals that attempts to modify the interpolation functions within the context of finite element methods are mainly divided in two groups: the XFEM/GFEM methods, and the Immersed Finite Element Methods (IFEM). In XFEM/GFEM the discontinuity in the solution and its gradients is accommodated via expansion of the underlying solution field through additional degrees of freedom [9, 39]. These newly added degrees of freedom are interpolated using modified (i.e., enriched) Lagrange shape functions that possess the same discontinuities as the solution and/or its gradients. The use of such interpolation functions directly in the coarse scale field requires modifying the functions in the neighboring elements as well that may not be intersected by the discontinuity. Consequently, a direct use of discontinuity enriched functions in the global problem results in considerable increase in the computational cost of the numerical method. Other methods have been proposed to bypass the need for additional degrees of freedom within the XFEM/GFEM methods and they are based on static condensation of the added enriched degrees of freedom [11, 1]. These methods still require stabilization techniques developed for the mixed-field FEM formulations. On the other hand the Immersed Finite Element Methods [40] are different in that the interpolation functions of the global degrees of freedom are directly modified while no addition degrees of freedom are added to any nodes. This eliminates the need for degree of freedom addition and subtraction algorithms as are used in XFEM, however as discussed in [25] IFEM still lacks optimal convergence due to potential discontinuity in the new interpolation functions across adjacent element edges. Another class of methods are based on penalty function formulation [25], and via Petrov-Galerkin method [44] they enforce the continuity of the fields to improve the convergence properties. However, these techniques rely on user defined parameters that are highly problem dependent. Other techniques that are based on discontinuous enrichment

method [12], weak Galerkin method [33, 43] and cut finite elements [6] have also been proposed for problems with embedded interfaces.

This chapter presents a new method for modeling weak and strong discontinuities in the solution and its gradients. The derivation is based on the Variational Multiscale (VMS) method that assumes a-priori direct sum decomposition of the space of functions into coarse and fine scale space. This results in an overlapping additive decomposition of the solution into coarse and fine scales, thereby yielding a system of coupled sub-problems. The fine-scale variational problem is employed to derive fine-scale models that are endowed with DC feature and they augment the global solution when embedded in the coarse-scale variational equation. Specifically, in the present VMDC method, the fine scales are interpolated by bubble functions that are modified via composition with discontinuity endowed interpolation functions. Accordingly, the product function is local to the element, but it is now also enriched with C^0 discontinuity that helps accurately represent the weak discontinuity at the embedded interface. In that sense the fine scales serve as an enrichment degree of freedom, an idea similar to the XFEM and GFEM methods. Nevertheless, due to the structure of the coarse-scale sub-problem we are able to variationally embed the fine-scale fields without the need to solve for the fine degrees of freedom explicitly at the global level.

An outline of this chapter is as follows: Section 2.2 presents the single field advection-diffusion equation and uses it to introduce the fine-scale enrichment method within the VMS framework. The structure of the DC term and the discontinuity embedded stabilization tensor τ is analyzed and compared with the widely used definition of the DC operator proposed in Hughes et al. [19]. Numerical integration with discontinuous functions over elements requires adaptive quadrature rules that are described in Section 2.2.4. Section 2.3 extends this formulation to the

Navier-Stokes equations. Surface tension effects are embedded in the governing system of equations in Section 2.3.1 to model multiphase fluids. The fine-scale models endowed with DC features are derived in Section 2.3.2. Section 2.4 briefly discusses the level-set method along with a reinitialization technique. Section 2.5 presents several numerical test cases to establish the validity of the proposed VMDC method and show its range of application.

2.2 A Model Scalar Field Problem: The Advection-Diffusion Equation

This section employs the advection-diffusion equation as a model problem to develop a new class of stabilized methods that are endowed with discontinuity capturing features. We present a novel treatment of the fine-scale variational problem that results in stabilization terms that naturally inherit a DC structure for modeling discontinuity.

Let $\Omega \subset \mathbb{R}^{n_{sd}}$ be an open bounded region with boundary Γ. The advection diffusion equation is

$$\boldsymbol{v} \cdot \nabla c - \kappa \Delta c = f \quad \text{in } \Omega \tag{2.1}$$

$$c = \hat{c} \quad \text{on } \Gamma \tag{2.2}$$

where c is the unknown field, κ is piecewise continuous diffusivity. $\boldsymbol{v}$ is the given flow velocity and is assumed solenoidal. The prescribed source function is given by $f(\boldsymbol{x})$, and $\hat{c}$ represents potentially discontinuous boundary conditions on Γ.

2.2.1 The VMS formulation

The standard weak form of the advection-diffusion equation is

$$(q, \boldsymbol{v} \cdot \nabla c) + (\nabla q, \kappa \nabla c) = (q, f) \tag{2.3}$$

where $(\cdot,\cdot) = \int_\Omega (\cdot)\, d\Omega$ is the $L_2(\Omega)$ inner product and q is the weighting function for the scalar field c. Employing VMS framework [15, 16, 28] we assume a multiscale decomposition of the trial solution and weighting function

$$c(\boldsymbol{x}) = \overline{c}(\boldsymbol{x}) + c'(\boldsymbol{x}) \tag{2.4}$$

$$q(\boldsymbol{x}) = \overline{q}(\boldsymbol{x}) + q'(\boldsymbol{x}) \tag{2.5}$$

with appropriate functional spaces for the two scales $\mathcal{C} = \overline{\mathcal{C}} \oplus \mathcal{C}'$. The coarse scale space is defined as $\overline{\mathcal{C}} = \left\{ \overline{c} : \overline{c} \in H_0^1(\Omega) \right\}$ and the fine scale space is defined as $\mathcal{C}' = \left\{ c' : c' = 0 \text{ on } \Gamma^e \right\}$, with the restriction that the two spaces are linearly independent. For the time-independent model problem considered here the weighting functions corresponding to each of the scales belong to the same functional space as that for the corresponding trial solution.

2.2.2 The variational multiscale problem

Following along [28], substituting (2.4) and (2.5) in (2.3) and employing linearity of the weighting function slot, we obtain coarse-scale and fine-scale sub-problems.

Coarse-scale sub-problem:

$$(\overline{q}, \boldsymbol{v} \cdot \nabla(\overline{c} + c')) + (\nabla \overline{q}, \kappa \nabla(\overline{c} + c')) = (\overline{q}, f) \tag{2.6}$$

Fine-scale sub-problem:

$$(q', \boldsymbol{v} \cdot \nabla(\overline{c} + c')) + (\nabla q', \kappa \nabla(\overline{c} + c')) = (q', f) \tag{2.7}$$

At this stage the fine-scale sub-problem is solved analytically in terms of the residual of the Euler Lagrange equation for the coarse scales. This yields a fine-scale model which is then substituted in (2.6) to arrive at the stabilized form as presented below.

2.2.2.1 The fine-scale sub-problem

We write the fine-scale sub-problem in a residual form

$$(q', \boldsymbol{v} \cdot \nabla c') + (\nabla q', \kappa \nabla c') = -(q', \overline{r}) \tag{2.8}$$

where the coarse-scale residual is

$$\overline{r} = \boldsymbol{v} \cdot \nabla \overline{c} - \kappa \Delta \overline{c} - f \tag{2.9}$$

It is important to note that the fine scale problem is driven by the residual of the Euler-Lagrange equation of the coarse scale problem, and this makes the method variationally consistent. Consequently the fine scale problem gets activated when the coarse residual is not zero. Another viewpoint is that when the residual is non-zero the fine-scale model represents the error or the missing physics.

2.2.2.1.1 Embedding discontinuity in the fine scale field

To solve the fine-scale sub-problem we make certain simplifying assumptions. One assumption is to consider that fine scales are non-zero within the elements but they vanish at the element boundaries Γ^e. This localizes the fine scales to element interiors such that

$$c' = q' = 0 \quad \text{on } \Gamma^e \tag{2.10}$$

To achieve this condition, we expand fine scale fields in terms of bubble functions $b_e(\boldsymbol{\xi})$ that are non-zero on element interior and zero at the element boundaries. We approach the problem of discontinuity by modifying the fine-scale shape functions via embedding the discontinuity capturing feature into the fine scales. This enrichment of the fine-scale shape functions is only carried out within elements that develop discontinuity in the solution. Consequently, the method

avoids any modification to the global system of equations, i.e., the coarse-scale formulation, since the shape function modification affects only the local fine-scale sub-problem. In this section we develop the bubble function enrichment method for the scalar field problem and in Section 2.5.1 it is tested on a problem with propagating discontinuity.

We expand the fine-scale field and the corresponding weighting function as follows

$$c' = b^e \psi \beta \tag{2.11}$$

$$q' = \hat{b}^e \psi \gamma \tag{2.12}$$

where $b^e\psi$ is the enriched bubble function, β is the trial solution coefficients and γ is the weighting function coefficient. As an example, the bubble function employed here is a triaxial function that is defined in N dimensions as

$$b^e(\xi_i) = \prod_{i=1}^{N} (1-\xi_i^2) \qquad \xi_i \in \{-1,1\} \tag{2.13}$$

Bubble function (2.13) is multiplied by an enrichment function ψ which augments the quadratic bubble function with a weak discontinuity across the embedded interface. These enrichment functions may be defined in terms of an implicit interface function (i.e., the signed distance function) in the case where material properties are discontinuous, and this option is examined in Section 2.3. In this section we focus on the case where the solution gradients are employed as discontinuity indicators, thus giving the following definition of the enrichment function

$$\psi = |\nabla c| \tag{2.14a}$$

$$\nabla \psi = \nabla |\nabla c| \tag{2.14b}$$

where $|\nabla c|$ is the norm gradient of the scalar field. Since discontinuity capturing methods invariably lead to nonlinear solution algorithms, the first iteration of the solution provides the spatial distribution of the scalar field c. We employ it to obtain a global maximum $c_{\max}$ and minimum $c_{\min}$ value and calculate the average of these values $c_{avg} = (c_{\max} + c_{\min})/2$. For any given element, $c^e_{\max}$ and $c^e_{\min}$ is the local max and min, respectively. An element that satisfies the condition $[(c^e_{\max} - c_{avg})/(c^e_{\min} - c_{avg})] < 0$ is the one that is traversed by discontinuity and therefore the enrichment technique is activated in these elements.

From the modeling perspective, this modification of the fine scale functions introduces extra terms in the fine-scale sub-problem. However, it does not increase the size of the coarse scale problem and therefore it does not affect the cost of solving the resulting method. Now we substitute the enriched representation of the fine scales into the fine-scale sub-problem (2.8) and invoking the mean value theorem for the coarse-scale residual that amounts to assuming a constant projection of the residual, we get the following algebraic problem

$$\left[\left(\nabla(b^e\psi), \kappa\nabla(b^e\psi)\right) + \left(\hat{b}^e\psi, \boldsymbol{v}\cdot\nabla(b^e\psi)\right)\right]\beta = -\left(b^e\psi, 1\right)\bar{r} \tag{2.15}$$

Note that additional terms appear when the gradient operator acts on the enriched bubble functions.

Remark: *The use of mean value theorem was studied in [28] and was found adequate to represent the fine-scal*e solution.

Remark: *In [28, 29] the bubble function employed in the weighting function was modified to incorporate the upwinding feature. In addition, it helped retain the advective term even under uniform velocity conditions. In these works a comparison with the SUPG formulation was carried out for the case of uniform advection (but without the enrichment modification) and identical*

results were achieved. Therefore, in our present developments we have used the same skewed-bubble function $\hat{b}^e$ *to expand the fine scale weighting function as was first presented in [28].*

Solving (2.15) for β we arrive at

$$\beta = -\hat{\tau}\left(b^e\psi, 1\right)\overline{r} \tag{2.16}$$

where

$$\hat{\tau} = \left[\left(\nabla(b^e\psi), \kappa\nabla(b^e\psi)\right) + \left(\hat{b}^e\psi, \boldsymbol{v}\cdot\nabla(b^e\psi)\right)\right]^{-1} \tag{2.17}$$

Substituting (2.16) in (2.11) leads to the fine-scale solution

$$c' = -\tau\overline{r} \tag{2.18}$$

where stabilization parameter that emanates via the variationally consistent derivation is given as

$$\tau = b^e\psi\hat{\tau}\left(b^e\psi, 1\right) \tag{2.19}$$

Remark: *The form of the fine scales in* (2.18) *possesses discontinuities across the interface only within the elements that develop discontinuous solutions as shown in Fig. 2.2. This necessitates appropriate numerical integration rules in these elements to accurately evaluate discontinuous integrals. Additionally,* τ *is part of the integrand in the coarse-scale sub-problem, therefore appropriate integration rule is used in these elements for the coarse-scale sub-problem as well.*

Remark: *We show the derivation in its entire generality while keeping all the terms that emanate via the variationally consistent derivation of* τ *. However, in the interest of the reader we simplify* (2.17) *to show its comparison with* τ^{DC} *in [19] and present numerical results in section 2.5 with a simplified* τ *.*

Remark: *The gradient of ψ drops out unless the coarse scale field is represented via quadratic shape functions or higher.*

2.2.2.2 Coarse-scale formulation with variationally embedded discontinuity

The last step in the development of the Variational Multiscale-Discontinuity Capturing (VMDC) method is to embed the fine model in the coarse scale equations. We consider the coarse-scale problem (2.6) and apply integration by parts to the terms that include the fine scale field c' to transfer the gradient operator from the fine scale field on to the weighting function. Employing the assumption of vanishing fine scales at the element edges we arrive at

$$\left(\overline{q}, \boldsymbol{v}\cdot\nabla\overline{c}\right) - \left(\boldsymbol{v}\cdot\nabla\overline{q}, c'\right) + \left(\nabla\overline{q}, \kappa\nabla\overline{c}\right) - \left(\Delta\overline{q}, \kappa c'\right) = \left(\overline{q}, f\right) \tag{2.20}$$

Substituting (2.18) in (2.20) we obtain the stabilized form for the advection diffusion equation

$$\left(\overline{q}, \boldsymbol{v}\cdot\nabla\overline{c}\right) + \left(\boldsymbol{v}\cdot\nabla\overline{q}, \tau\overline{r}\right) + \left(\nabla\overline{q}, \kappa\nabla\overline{c}\right) + \left(\Delta\overline{q}, \kappa\tau\overline{r}\right) = \left(\overline{q}, f\right) \tag{2.21}$$

This stabilized formulation inherits the attributes of the stabilized advection-diffusion equation presented in [28]. In addition, it is also endowed with discontinuity capturing features that accommodate discontinuous diffusivity κ and discontinuous solution field c. These attributes are numerically investigated via the discontinuous boundary condition in the skew-advection problem presented in Section 2.5.1.

2.2.3 Structure of τ

In order to understand the behavior of τ derived in (2.19), we first investigate the structure of τ for smooth regions where solution does not possess discontinuity or shock. As stated in the definition of the fine-scale enrichment, the fine-scale functions in elements belonging to the

smooth region are not augmented with the enrichment function ψ. Accordingly, for these elements $\psi = 1$. By substituting $\psi = 1$ in (2.15) the fine-scale sub-problem reduces to

$$\left[\left(\nabla \hat{b}^e, \kappa \nabla b^e\right) + \left(\hat{b}^e, \boldsymbol{v} \cdot \nabla b^e\right)\right]\beta = -\left(b^e, 1\right)\overline{r} \tag{2.22}$$

which is form identical to the stabilization derived in [28, 29].

Now we analyze the fine-scale model emanating from (2.15) for elements that are intersected by discontinuity. Accordingly, we consider the advection dominated case where $\kappa = 0$. The fine-scale model in (2.15) reduces to

$$\left[\left(\hat{b}^e\psi, \boldsymbol{v} \cdot \nabla(b^e\psi)\right)\right]\beta = -\left(b^e\psi, 1\right)\overline{r} \tag{2.23}$$

Following along the lines of the derivations in equations (2.16) to (2.19) we arrive at

$$\tau^{adv} = b^e\psi\left[\left(\hat{b}^e\psi, \boldsymbol{v} \cdot \nabla(b^e\psi)\right)\right]^{-1}\left(b^e\psi, 1\right) \tag{2.24}$$

τ^{adv} in (2.24) provides both stabilization for the advection equation in addition to facilitating the DC capturing feature in elements that have discontinuities in the solution. For comparison we recall the SUPG formulation and the corresponding DC parameter developed in Hughes *et al.* [19].

$$\tau_{SUPG} = \frac{h^e}{2|\boldsymbol{v}|} \tag{2.25}$$

Similarly, the DC stabilization parameter in [14] is

$$\tau_{SUPG}^{DC} = \frac{h^e}{2}\max\left(0, \left(\frac{1}{\left|\dfrac{\boldsymbol{v} \cdot \nabla c}{|\nabla c|^2}\nabla c\right|} - \frac{1}{|\boldsymbol{v}|}\right)\right) \tag{2.26}$$

The term $\frac{h^e}{2|\boldsymbol{v}|}$ in (2.26) is the SUPG stabilization parameter for the advection dominated case. The other term with a modified velocity that incorporates the direction of steep gradients of the unknown field c, is active only when the magnitude of the gradient is high as stipulated in (2.26). Consequently, in the spatial regions with steep gradients in the field c, SUPG stabilization parameter is replaced with a DC parameter that employs the component of velocity $\boldsymbol{v}$ in the direction of the gradient ∇c across the interface.

2.2.3.1 Analysis of the structure of stabilization parameter τ^{adv}

In order to understand the structure of the stabilization parameter τ^{adv} we first pull out the DC parameter from (2.26).

$$\tau^{DC} = \frac{h^e}{2} \frac{1}{\left| \frac{\boldsymbol{v} \cdot \nabla c}{|\nabla c|^2} \nabla c \right|} \tag{2.27}$$

We now consider (2.24) and the enrichment function to be defined as $\psi = \nabla c$, we obtain

$$\tau^{adv} = \frac{b^e \nabla c \left(b^e \nabla c, 1 \right)}{\left[\left(\hat{b}^e \nabla c, \boldsymbol{v} \cdot \nabla \left(b^e \nabla c \right) \right) \right]} \tag{2.28}$$

We expand the denominator employing $\nabla \left(b^e \nabla c \right) = \left(\nabla b^e \otimes \nabla c + b^e \nabla \otimes \nabla c \right)$, and ignoring the high order terms $(b^e \nabla \otimes \nabla c)$ leads to

$$\tau^{adv} = \frac{b^e \nabla c \left(b^e \nabla c, 1 \right)}{\left[\left(\hat{b}^e \nabla c, \boldsymbol{v} \left(\nabla b^e \otimes \nabla c \right) \right) \right]} \tag{2.29}$$

We make a simplifying choice of only considering the diagonal term of $(\nabla b^e \otimes \nabla c)$ that reduces (2.29) to

$$\tau^{adv} = \frac{b^e \nabla c \left(b^e \nabla c, 1 \right)}{\left[\left(\hat{b}^e \nabla c, (\boldsymbol{v} \cdot \nabla c) \nabla b^e \right) \right]} \tag{2.30}$$

For ease of discussion if we assume ∇c and $\boldsymbol{v}$ to be constant within the element, and considering that $(b^e, 1) = 1$, a simplified structure of τ^{adv} appears.

$$\tau^{adv} = \left(\frac{1}{\frac{[\boldsymbol{v} \cdot \nabla c]}{|\nabla c|^2} \nabla c} \right) \left(\frac{b^e}{\left(\hat{b}^e, \nabla b^e \right)} \right) \tag{2.31}$$

Let us now analyze (2.31) in one generic direction (i.e., 1D) and evaluate the second term on the RHS of (2.31). Using 1D quadratic shape function for b^e, and a linear shape functions with an embedded notion of upwinding for $\hat{b}^e$, we have

$$\left.\begin{aligned} b^e &= \left(1 - \xi^2\right) \\ b^e_{,x} &= b^e_{,\xi} \left(x_{,\xi} \right)^{-1} = -\frac{4\xi}{h^e} \\ \hat{b}^e &= -\frac{1}{2}(\xi - 1) \end{aligned}\right\} \tag{2.32}$$

Consequently, the denominator is

$$\left(\hat{b}^e, \nabla b^e \right) = \left[\frac{2}{h^e} \int_{-1}^{1} \left[\xi^2 - \xi \right] j d\xi \right] = j \frac{4}{3h^e} \tag{2.33}$$

Since the numerator in (2.31) is a part of τ^{adv} which appears inside the element integral we integrate the numerator to yield

$$\left(b^e,1\right)=\int_{-1}^{1} b^e\, j d\xi=\left[\int_{-1}^{1}\left(1-\xi^2\right) j d\xi\right]=j\frac{4}{3} \tag{2.34}$$

Substituting (2.33) and (2.34) in (2.31) yields

$$\tau^{adv}=\left(\frac{1}{\dfrac{[\boldsymbol{v}\cdot\nabla c]}{|\nabla c|^2}\nabla c}\right)\left(\frac{4j/3}{4j/(3h^e)}\right)=h^e\left(\frac{1}{\dfrac{[\boldsymbol{v}\cdot\nabla c]}{|\nabla c|^2}\nabla c}\right) \tag{2.35}$$

Comparing (2.27) and (2.35) we obtain the following relation between the two stabilizing parameters

$$\frac{1}{2}\left|\tau^{adv}\right|=\tau^{DC} \tag{2.36}$$

The variationally consistent derivation of τ^{adv} as presented above in (2.24) augmented with the enrichment function in (2.14a) accounts for both the magnitude as well as the direction of the steep gradients in the solution. This feature of embedded directionality is automatically manifested when τ^{adv} is integrated over the spatially distributed integration points inside the element in conjunction with the enrichment definition given in (2.14a). This is presented in the context of 2D bubble functions in Fig. 2.1. The spatially varying τ^{adv} when multiplied by the residual of the Euler-Lagrange equations triggers directionality in the residual over the element interiors. In our comparison with the classical definition of τ^{DC} presented in [19] we take the norm of (2.35) to compare the magnitude of τ^{adv} in the VMDC method with the magnitude of τ^{DC} in the SUPG-DC method. Note that SUPG and GLS methods invariably employ diagonal τ, thereby leading to triaxial stabilization.

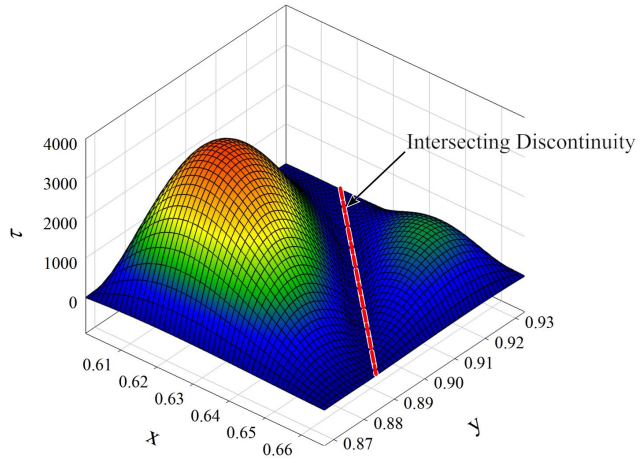

Fig. 2.1. Shape of τ^{adv} within an element intersected by a discontinuity in the field.

Remark: *The sub-grid scale bubble function in (2.11) when augmented via embedding the gradients of the field given in (2.14a) results in a method that automatically adapts itself to steep gradients in the solution field. In this case a priori information about the location of steep gradients is not required.*

Remark: *The derived* τ^{adv} *automatically becomes a discontinuity capturing parameter within the elements that are traversed by the discontinuity.*

Remark: *The difference between the simplified version of the derived stabilization parameter and* τ^{DC} *[19] is the appearance of bubble function and the integral of its gradient in the expression* (2.28), *thus making it a function that varies over the element domain. In our numerical calculations we investigate this feature of the variationally derived form of stabilization parameter via a 2D skew-advection problem.*

2.2.4 Adaptive quadrature construction

Integration of discontinuous functions has been a challenge for numerical methods. Although Gaussian quadrature exactly integrates continuous functions of different orders, it does not provide sufficient accuracy when discontinuous functions are present in the integrand. There are three main classes of numerical quadrature constructions for discontinuous functions. The first method that is most often used in XFEM/GFEM involves the splitting of intersected elements along the interface, thus producing two regions where the integrand is continuous. These sub-elements or sub-cells are further discretized into quadrilaterals or triangles in 2D [39]. Subsequently, the Gaussian quadrature rule of sufficiently high order is used to integrate over the sub-cells in the intersected elements. An adaptive quadrature construction algorithm is presented in [32] for numerical integration of discontinuous functions that are arbitrarily located within the element.

2.3 Two-Phase Navier-Stokes Equations with Surface Tension

This section considers a vector field problem wherein discontinuity appears due to jumps in the viscosity and density of the fluids across the interface Γ_s along which a surface tension force is also operational. Let $\Omega \subset \mathbb{R}^{n_{sd}}$ be a domain consisting of two sub-regions Ω_1 and Ω_2 that are separated by an interface Γ_s such that $\Omega = \Omega_1 \bigcup \Omega_2$ and $\Omega_1 \bigcap \Omega_2 = 0$. The two sub-domains are occupied by two incompressible and immiscible fluids as shown in Fig. 2.2. Subdomains Ω_1 and Ω_2 are bounded by piecewise smooth boundaries Γ_1 and Γ_2, where $\Gamma = (\Gamma_1 \bigcup \Gamma_2) \setminus \Gamma_s$ and $(\Gamma_1 \bigcap \Gamma_2) \setminus \Gamma_s = 0$. Let the velocity field be defined as $\boldsymbol{v}(\boldsymbol{x},t) : \Omega \times]0,T[\rightarrow \mathbb{R}^{n_{sd}}$ and the pressure

field $p(\boldsymbol{x},t):\Omega\times]0,T[\rightarrow\mathbb{R}$. Assuming incompressible two-phase fluid flow, the governing equations in each phase are written as follows

$$\rho_\beta\frac{\partial \boldsymbol{v}}{\partial t}-2\mu_\beta\nabla\cdot\boldsymbol{\varepsilon}(\boldsymbol{v})+\nabla p+\rho\boldsymbol{v}\cdot\nabla\boldsymbol{v}=\rho_\beta\boldsymbol{b}\ \text{ in }\Omega \tag{2.37}$$

These are augmented by the incompressibility constraint derived from the continuity equation for density.

$$\nabla\cdot\boldsymbol{v}=0\ \text{ in }\Omega \tag{2.38}$$

The Laplace-Young surface tension jump condition, and the boundary and initial conditions are given as follows

$$\left[\,p\boldsymbol{n}-2\mu\boldsymbol{\varepsilon}(\boldsymbol{v})\boldsymbol{n}\,\right]=\delta\kappa\boldsymbol{n}\quad\text{on }\Gamma_s \tag{2.39}$$

$$\boldsymbol{v}=\boldsymbol{g}\quad\text{on }\Gamma \tag{2.40}$$

$$\boldsymbol{v}\left(\boldsymbol{x},0\right)=\boldsymbol{v}_o\quad\text{in }\Omega \tag{2.41}$$

where $\beta=1,2$ corresponds to each phase in Fig. 2.2, $\boldsymbol{b}:\Omega\times]0,T[\rightarrow\mathbb{R}^{n_{sd}}$ is the body force, $\rho_\beta>0$ is the fluid density of each phase, $\mu_\beta>0$ is the kinematic viscosity of each phase, δ is the surface tension coefficient that depends on the two-phases (2.and is assumed constant in this presentation), $\kappa(\boldsymbol{x},t)$ and $\boldsymbol{n}(\boldsymbol{x},t)$ are the mean curvature and normal vector of the interface Γ_s, respectively. The normal vector associated with subdomain β is assumed to be directed outwards, as shown in Fig. 2.2. The initial condition $\boldsymbol{v}_o$ for the velocity field is subject to the incompressibility condition, and $\boldsymbol{g}$ represents the Dirichlet boundary conditions. The density ρ_β

and viscosity μ_β are assumed constant within each phase. The symmetric strain-rate tensor is defined as $\boldsymbol{\varepsilon}(\boldsymbol{v}) = \nabla^s \boldsymbol{v} = [\nabla \boldsymbol{v} + (\nabla \boldsymbol{v})^T]/2$.

Let $\boldsymbol{w}(\boldsymbol{x}) \in \boldsymbol{\mathcal{W}} \equiv \left\{ \left[H_0^1(\Omega) \right]^{n_{sd}} \right\}$ and $q(\boldsymbol{x}) \in \mathcal{Q} \equiv L^2(\Omega)$ represent the weighting functions for the velocity and pressure fields, respectively. The trial solutions for the velocity and pressure fields are $\boldsymbol{v}(\boldsymbol{x},t) \in \boldsymbol{\mathcal{V}} \equiv \left\{ \left[H_0^1(\Omega) \right]^{n_{sd}} \times \left[0,T\right] \right\}$ and $p(\boldsymbol{x},t) \in \mathcal{P} \equiv \left\{ L^2(\Omega / \Gamma_s) \times \left[0,T\right] \right\}$ respectively, and they satisfy the initial and boundary conditions. The weak form of (2.38) is as follows

$$\left(\rho_\beta \boldsymbol{w}, \frac{\partial \boldsymbol{v}}{\partial t} \right) - \left(2\mu_\beta \boldsymbol{w}, \nabla \cdot \boldsymbol{\varepsilon}(\boldsymbol{v}) \right) + \left(\boldsymbol{w}, \nabla p \right) + \left(\boldsymbol{w}, \rho \boldsymbol{v} \cdot \nabla \boldsymbol{v} \right) = \left(\rho_\beta \boldsymbol{w}, \boldsymbol{b} \right) \tag{2.42}$$

Integrating by parts the second and third terms in (2.42) and rearranging leads to

$$\left(\rho_\beta \boldsymbol{w}, \frac{\partial \boldsymbol{v}}{\partial t} \right) + \left(2\mu_\beta \nabla^s \boldsymbol{w}, \boldsymbol{\varepsilon}(\boldsymbol{v}) \right) - \left(\nabla \cdot \boldsymbol{w}, p \right) + \left(\boldsymbol{w}, \rho \boldsymbol{v} \cdot \nabla \boldsymbol{v} \right) + \left(\boldsymbol{w}, p\boldsymbol{n} - 2\mu_\beta \boldsymbol{\varepsilon}(\boldsymbol{v}) \boldsymbol{n} \right)_{\Gamma_s} = \left(\rho_\beta \boldsymbol{w}, \boldsymbol{b} \right)$$

(2.43)

Substituting the Laplace-Young surface tension condition leads to the weak form of the problem containing the surface tension conditions for equations (2.37)-(2.41).

$$\left(\rho \boldsymbol{w}, \frac{\partial \boldsymbol{v}}{\partial t} \right) + \left(2\mu \nabla^s \boldsymbol{w}, \boldsymbol{\varepsilon}(\boldsymbol{v}) \right) - \left(\nabla \cdot \boldsymbol{w}, p \right) + \left(\boldsymbol{w}, \rho \boldsymbol{v} \cdot \nabla \boldsymbol{v} \right) = \left(\rho \boldsymbol{w}, \boldsymbol{b} \right) - \left(\boldsymbol{w}, \delta \kappa \boldsymbol{n} \right)_{\Gamma_s} \tag{2.44}$$

$$\left(q, \nabla \cdot \boldsymbol{v} \right) = 0 \tag{2.45}$$

Where the density and viscosity are now defined via Heaviside function:

$$\rho = \left(1 - \mathrm{H}\left(\phi\right)\right)\rho_1 + \mathrm{H}\left(\phi\right)\rho_2 \tag{2.46}$$

$$\mu = \left(1 - \mathrm{H}\left(\phi\right)\right)\mu_1 + \mathrm{H}\left(\phi\right)\mu_2 \tag{2.47}$$

The Heaviside function is in turn a function of the signed distance field $\phi(\boldsymbol{x},t)$ that is used to implicitly track the interface which is defined as $\phi(\boldsymbol{x},t)=0$ for all $\boldsymbol{x}\in\Gamma_s$. The Heaviside function is a discrete step function defined as:

$$\mathrm{H}\left(\phi\right) = \begin{cases} 1 & \phi < 0 \\ 0 & \phi \geq 0 \end{cases} \tag{2.48}$$

Remark: *The surface tension condition is satisfied weakly via the Laplace-Young jump condition satisfying the interface integral in* $\mathbb{R}^{(n_{sd}-1)}$ *that emanates from the integration by parts form of the variational equation (2.44).*

Remark: *It is important to note that* (2.45) *and* (2.46) *accommodate solutions with a continuous velocity field, while the pressure field may change sharply across the interface* Γ_s *[13]. This results in the jump being manifested only in the pressure field across the interface and with a value equal to* $\delta\kappa$ *as in the Laplace-Young problem presented in Section 2.5.3.*

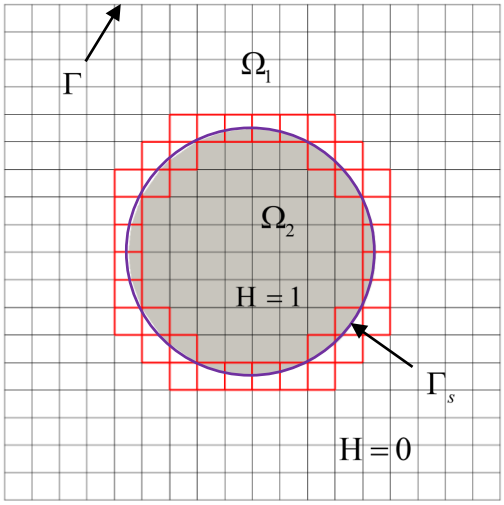

Fig. 2.2. Schematics of the two-phase flow domain on an Eulerian mesh with interface Γ_s for the two-phase problem; highlighted elements are intersected by the interface where enriched fine scales are used.

2.3.1 Discontinuous surface force

The surface tension term in (2.44) is usually transformed into a regularized volumetric integral over a finite width $\varepsilon = O(h)$ where h is the characteristic mesh element size, as is done in the continuum surface force technique [4]. In this section we employ the divergence theorem to derive a form of surface tension as a discontinuous force. Starting with the surface tension term given in (2.44) and employ (i) integration by parts, (ii) the definition of the Heaviside function whereby the surface integral vanishes and (iii) considering the surface tension coefficient to be constant, we have

$$\left(\boldsymbol{w}, \delta\kappa\boldsymbol{n}\right)_{\Gamma_s} = \left(\nabla\cdot\left(\boldsymbol{w}\right), \delta\kappa\right)_{\Omega_2} + \left(\boldsymbol{w}\delta, \nabla\kappa\right)_{\Omega_2} \tag{2.49}$$

This leads to a discontinuous surface force with surface tension applied only in Ω_2. Substituting the right hand side of (2.49) in place of the surface tension term in (2.44) leads to a weak form

where all integrals are volume integrals: Find $\boldsymbol{v}(\boldsymbol{x},t) \in \boldsymbol{\mathcal{V}}$ and $p(\boldsymbol{x},t) \in \mathcal{P}$ such that for all $\boldsymbol{w}(\boldsymbol{x}) \in \boldsymbol{\mathcal{W}}$ and $q(\boldsymbol{x}) \in \mathcal{Q}$,

$$\begin{aligned} &\left(\rho\boldsymbol{w}, \frac{\partial \boldsymbol{v}}{\partial t}\right) + \left(2\mu\nabla^s \boldsymbol{w}, \boldsymbol{\varepsilon}(\boldsymbol{v})\right) - \left(\nabla\cdot\boldsymbol{w}, p\right) + \left(\boldsymbol{w}, \rho\boldsymbol{v}\cdot\nabla\boldsymbol{v}\right) \\ &= \left(\rho\boldsymbol{w}, \boldsymbol{b}\right) - \left(\nabla\cdot\left(\boldsymbol{w}\right), \delta\kappa\right)_{\Omega_2} - \left(\boldsymbol{w}\delta, \nabla\kappa\right)_{\Omega_2} \end{aligned} \tag{2.50}$$

$$\left(q, \nabla\cdot\boldsymbol{v}\right) = 0 \tag{2.51}$$

Remark: *In the continuum surface force technique developed in [4] the continuum surface force is shown to approach the interfacial surface tension force as the* $\varepsilon \to 0$.

2.3.2 The variational multiscale method

As noted earlier, in this chapter the fine-scale variational problem is employed to exploit *a priori* known features of the solution, i.e., weak and strong discontinuities in the velocity and the pressure fields, respectively. For the problem under consideration these discontinuities are induced because of the discontinuous density and viscosity, as well as due to the discontinuous surface force that arises due to surface tension. In the context of multiphase flows, equation (2.37) reveals that the jump in the viscosity induces a jump in the velocity gradient, thereby leading to a weakly discontinuous velocity. The pressure is strongly discontinuous due to the jump in viscosity and in the surface tension force at the interface.

Following along the lines of our earlier works [7, 30] and the general framework presented in Section 2.2.1 we assume an overlapping additive decomposition of the velocity field $\boldsymbol{v}$ into coarse scale $\bar{\boldsymbol{v}}$ and fine scale $\boldsymbol{v}'$

$$\boldsymbol{v}\left(\boldsymbol{x},t\right) = \bar{\boldsymbol{v}}\left(\boldsymbol{x},t\right) + \boldsymbol{v}'\left(\boldsymbol{x},t\right) \tag{2.52}$$

Similarly, the weighting function is decomposed into coarse and fine scales

$$\boldsymbol{w}(\boldsymbol{x}) = \overline{\boldsymbol{w}}(\boldsymbol{x}) + \boldsymbol{w}'(\boldsymbol{x}) \tag{2.53}$$

Substituting (2.52) and (2.53) into (2.50) and (2.51) and utilizing the linearity of the weighting function we arrive at two sub-problems

Coarse-scale sub-problem:

$$\begin{aligned}&\left(\rho\overline{\boldsymbol{w}}, \frac{\partial\overline{\boldsymbol{v}}}{\partial t}\right) + \left(\rho\overline{\boldsymbol{w}}, \frac{\partial\boldsymbol{v}'}{\partial t}\right) + \left(2\mu\nabla^s\overline{\boldsymbol{w}}, \boldsymbol{\varepsilon}(\overline{\boldsymbol{v}} + \boldsymbol{v}')\right) - \left(\nabla\cdot\overline{\boldsymbol{w}}, p\right) + \left(\overline{\boldsymbol{w}}, \rho\left(\overline{\boldsymbol{v}} + \boldsymbol{v}'\right)\cdot\nabla\left(\overline{\boldsymbol{v}} + \boldsymbol{v}'\right)\right) \\ &= \left(\rho\overline{\boldsymbol{w}}, \boldsymbol{b}\right) - \left(\nabla\cdot\left(\overline{\boldsymbol{w}}\right), \delta\kappa\right)_{\Omega_2} - \left(\overline{\boldsymbol{w}}\delta, \nabla\kappa\right)_{\Omega_2}\end{aligned} \tag{2.54}$$

$$\left(q, \nabla\cdot\left(\overline{\boldsymbol{v}} + \boldsymbol{v}'\right)\right) = 0 \tag{2.55}$$

Fine-scale sub-problem:

$$\begin{aligned}&\left(\rho\boldsymbol{w}', \frac{\partial\overline{\boldsymbol{v}}}{\partial t}\right) + \left(\rho\boldsymbol{w}', \frac{\partial\boldsymbol{v}'}{\partial t}\right) + \left(2\mu\nabla^s\boldsymbol{w}', \boldsymbol{\varepsilon}(\overline{\boldsymbol{v}} + \boldsymbol{v}')\right) - \left(\nabla\cdot\boldsymbol{w}', p\right) + \left(\boldsymbol{w}', \rho\left(\overline{\boldsymbol{v}} + \boldsymbol{v}'\right)\cdot\nabla\left(\overline{\boldsymbol{v}} + \boldsymbol{v}'\right)\right) \\ &= \left(\rho\boldsymbol{w}', \boldsymbol{b}\right) - \left(\nabla\cdot\left(\boldsymbol{w}'\right), \delta\kappa\right)_{\Omega_2} - \left(\boldsymbol{w}'\delta, \nabla\kappa\right)_{\Omega_2}\end{aligned} \tag{2.56}$$

We now focus on the solution of the fine-scale sub-problem with the objective of deriving an analytical expression for the fine-scale velocity field in terms of the residual of the Euler-Lagrange equations of the coarse-scale governing equations.

Remark: *In linearizing the fine-scale convective term, we drop the higher-order fine-scale terms* $(\overline{\boldsymbol{w}}, \rho\boldsymbol{v}'\cdot\nabla\boldsymbol{v}')$ *and* $(\boldsymbol{w}', \rho\boldsymbol{v}'\cdot\nabla\boldsymbol{v}')$*. This is equivalent to adopting a first order approximation to the non-linear fine-scale problem whereby only a single iteration is needed to update the fine scales in each Newton Raphson iteration for the global nonlinear problem.*

2.3.2.1 The enriched fine-scale sub-problem: Modeling the fine-scale fields

Let us consider the fine-scale sub-problem given in (2.56). We use the linearity of the symmetric gradients and apply integration by parts to the coarse-scale velocity gradient in the third term and to the coarse scale pressure in the fourth term on the left-hand side of (2.56). Making a modeling assumption that surface tension is a global feature and therefore not present at the fine-scale level, we drop these terms.

$$\begin{aligned}&\left(\rho\boldsymbol{w}',\frac{\partial\boldsymbol{v}'}{\partial t}\right)+\left(2\mu\nabla^{s}\boldsymbol{w}',\boldsymbol{\varepsilon}(\boldsymbol{v}')\right)+\left(\boldsymbol{w}',\rho\boldsymbol{v}'\cdot\nabla\overline{\boldsymbol{v}}\right)+\left(\boldsymbol{w}',\rho\overline{\boldsymbol{v}}\cdot\nabla\boldsymbol{v}'\right)=\\&-\left(\rho\boldsymbol{w}',\frac{\partial\overline{\boldsymbol{v}}}{\partial t}\right)+\left(\boldsymbol{w}',2\mu\nabla\cdot\boldsymbol{\varepsilon}(\overline{\boldsymbol{v}})\right)-\left(\boldsymbol{w}',\nabla p\right)-\left(\boldsymbol{w}',\rho\overline{\boldsymbol{v}}\cdot\nabla\overline{\boldsymbol{v}}\right)+\left(\rho\boldsymbol{w}',\boldsymbol{b}\right)\end{aligned}\tag{2.57}$$

This simplification however does not deteriorate the modeling capability of the formulation because the discontinuous surface force is fully represented in the coarse-scale problem. Consequently, the strong and weak discontinuities are present in the fine-scale sub-problem, while the surface tension induced steep gradients are present in the coarse scale sub-problem. We thus write (2.57) as follows

$$\left(\rho\boldsymbol{w}',\frac{\partial\boldsymbol{v}'}{\partial t}\right)+\left(2\mu\nabla^{s}\boldsymbol{w}',\boldsymbol{\varepsilon}(\boldsymbol{v}')\right)+\left(\boldsymbol{w}',\rho\boldsymbol{v}'\cdot\nabla\overline{\boldsymbol{v}}\right)+\left(\boldsymbol{w}',\rho\overline{\boldsymbol{v}}\cdot\nabla\boldsymbol{v}'\right)=-\left(\boldsymbol{w}',\overline{\boldsymbol{r}}\right)\tag{2.58}$$

where

$$\overline{\boldsymbol{r}}\equiv\frac{\partial\overline{\boldsymbol{v}}}{\partial t}-2\mu\nabla\cdot\boldsymbol{\varepsilon}(\overline{\boldsymbol{v}})+\nabla p+\rho\overline{\boldsymbol{v}}\cdot\nabla\overline{\boldsymbol{v}}-\rho\boldsymbol{b}\tag{2.59}$$

is the residual of the Euler-Lagrange equations of the coarse scales, thereby resulting in residual driven fine-scale sub-problem. We discretize (2.58) in time using the generalized alpha method [21], although any other appropriate time integration technique can also be used. The semi-discrete form is

$$\begin{aligned}&\left(\rho\boldsymbol{w}',\left.\frac{\partial\boldsymbol{v}'}{\partial t}\right|_{n+\alpha_m}\right)+\left(2\mu\nabla^s\boldsymbol{w}',\boldsymbol{\varepsilon}\left(\boldsymbol{v}'_{n+\alpha_f}\right)\right)+\left(\boldsymbol{w}',\rho\boldsymbol{v}'_{n+\alpha_f}\cdot\nabla\overline{\boldsymbol{v}}_n\right)\\&+\left(\boldsymbol{w}',\rho\overline{\boldsymbol{v}}_n\cdot\nabla\boldsymbol{v}'_{n+\alpha_f}\right)=-\left(\boldsymbol{w}',\overline{\boldsymbol{r}}_{n+\alpha_f}\right)\end{aligned}\tag{2.60}$$

The update expression for $\partial_t\boldsymbol{v}'$ and $\boldsymbol{v}'$ are

$$\left.\frac{\partial\boldsymbol{v}'}{\partial t}\right|_{n+\alpha_m}=\left(1-\frac{\alpha_m}{\gamma}\right)\left.\frac{\partial\boldsymbol{v}'}{\partial t}\right|_n+\frac{\alpha_m}{\gamma\Delta t}\left(\boldsymbol{v}'_{n+1}-\boldsymbol{v}'_n\right)\tag{2.61}$$

$$\boldsymbol{v}'_{n+a_f}=\left(1-\alpha_f\right)\boldsymbol{v}'_n+\alpha_f\boldsymbol{v}'_{n+1}\tag{2.62}$$

where α_f, α_m and γ are the parameters from the generalized alpha method and Δt is the time step increment. Substituting (2.61) and (2.62) into (2.60) we get the fine-scale variational problem

$$\boxed{\begin{aligned}&\frac{\alpha_m}{\gamma\Delta t}\left(\rho\boldsymbol{w}',\boldsymbol{v}'_{n+1}\right)+\alpha_f\left[\left(2\mu\nabla^s\boldsymbol{w}',\boldsymbol{\varepsilon}\left(\boldsymbol{v}'_{n+1}\right)\right)+\left(\boldsymbol{w}',\rho\boldsymbol{v}'_{n+1}\cdot\nabla\overline{\boldsymbol{v}}_n\right)+\left(\boldsymbol{w}',\rho\overline{\boldsymbol{v}}_n\cdot\nabla\boldsymbol{v}'_{n+1}\right)\right]\\&=\frac{\alpha_m}{\gamma\Delta t}\left(\rho\boldsymbol{w}',\boldsymbol{v}'_n\right)-\left(1-\frac{\alpha_m}{\gamma}\right)\left(\rho\boldsymbol{w}',\left.\frac{\partial\boldsymbol{v}'}{\partial t}\right|_n\right)-\left(\boldsymbol{w}',\overline{\boldsymbol{r}}_{n+\alpha_f}\right)\\&-\left(1-\alpha_f\right)\left[\left(2\mu\nabla^s\boldsymbol{w}',\boldsymbol{\varepsilon}\left(\boldsymbol{v}'_n\right)\right)+\left(\boldsymbol{w}',\rho\boldsymbol{v}'_n\cdot\nabla\overline{\boldsymbol{v}}_n\right)+\left(\boldsymbol{w}',\rho\overline{\boldsymbol{v}}_n\cdot\nabla\boldsymbol{v}'_n\right)\right]\end{aligned}}\tag{2.63}$$

Remark: *It is evident from* (2.63) *that the fine-scale problem is dependent on the history of the fine-scale velocity and its time derivative. However, tracking fine-scale history terms significantly increases the computational cost. Based on the analysis presented in [7] we assume that fine-*

scales are quasi-static. This simplification has negligible effect on the accuracy of the time integration or the fine-scale solution. For more details interested reader is referred to [7].

Remark: *In our implementation we have used the BDF2 time integration scheme which can be considered a special case of the generalized alpha method with* $\alpha_f = 1$, $\alpha_m = 1.5$ *and* $\gamma = (\alpha_m - \alpha_f + 0.5)$.

2.3.2.2 Evaluating fine-scales via enriched bubble functions method

For the analytical derivation of the fine-scale models, and later on for computational expediency and parallelization, we assume the fine-scale trial and weighting functions to be non-zero within the element and vanish at the element edges:

$$\boldsymbol{v}' = \boldsymbol{w}' = 0 \quad \text{on } \Gamma^e \tag{2.64}$$

In our earlier works on Navier Stokes equations for flow problems without sharp discontinuities [7, 30], we expanded the fine-scale problem at the current time step $n+1$ in terms of bubble functions $b^e(\boldsymbol{\xi})$ that were defined on the interior of the elements. While this choice resulted in stabilized form for the mixed field problem [5], it did not account for discontinuities in the velocity and pressure fields, either at the fine-scale or at the coarse-scale levels.

This section presents a further generalization of the fine-scale problem within the VMS framework and it is carried out only in the elements that are intersected by the discontinuity interface. The knowledge of the presence of the interface Γ_s that is facilitated via level-set method provides an opportunity to embed discontinuities in the interpolation functions for the fine scales. Specifically, the bubble functions employed are modified by embedding the feature of

discontinuity via composition with a discontinuous function as shown in Fig. 2.3. This enhancement of the bubble functions helps in modeling discontinuities in the solution without introducing additional degrees of freedom to the global system. We employ these enriched bubbles to expand the fine-scale variable $\boldsymbol{v}'_{n+1}$.

Though the notion of enrichment of the degrees of freedom is also used in the XFEM/GFEM methods [8] there is a subtle difference in these methods and the proposed VMDC method. In GFEM enrichment is applied directly to the global problem and it requires enrichment degrees of freedom to be added to the global system. Specifically, nodes in the mesh are enriched if the support cloud of their numerical interpolation is intersected by the interface. Such enrichments lead to an increase in the size of the system of equations [8], resulting in a significant increase in the computational cost and a need for an algorithmic scheme to track the addition and removal of degrees of freedom as the interface moves across inter-element edges for the evolving interface problems.

On the contrary, in the fine-scale enrichment method proposed here, the enrichment is directly applied to the already existing fine-scale interpolation function. As a virtue of the local nature of the fine scale sub-problem no additional degrees of freedom are added to the global nodes and therefore the size of the coarse-scale problem is not altered. We wish to note that, like the XFEM/GFEM methods, the VMDC method also allows for the modeling of problems with evolving interfaces that do not conform to element edges.

In this section we show the embedding of strong discontinuity by multiplying the local bubble functions by a piecewise continuous function $\psi(\phi)$ that is defined in terms of the signed distance field as

$$\psi(\phi) = \left(|\phi| + \frac{\phi}{|\phi|} \right) \tag{2.65}$$

Accordingly, the fine scale trial solution and weighting functions are defined as

$$\boldsymbol{v}' = \boldsymbol{\beta} b^e(\boldsymbol{\xi}) \psi(\phi) \tag{2.66}$$

$$\boldsymbol{w}' = \boldsymbol{\gamma} b^e(\boldsymbol{\xi}) \psi(\phi) \tag{2.67}$$

where $\boldsymbol{\beta}$ and $\boldsymbol{\gamma}$ are the coefficients for the fine-scale trial solution and weighting function, respectively. Due to the multiplication of the enrichment function with the bubble function the fine-scale sub-problem is defined over sum of element interiors. Additionally, due to the local nature of the fine-scale sub-problem the enriched bubble functions are only used within elements that are intersected by the phase interface (see Fig. 2.2) without introducing the issues of blended nodes as is the case in XFEM/GFEM. Another salient feature of the proposed VMDC framework is that the enrichment is sensitive to any movement of the interface within the element. Furthermore, the fine-scale interpolation function enrichment can be automatically activated and deactivated within an element based on the definition of ϕ within that element.

Substituting (2.66) and (2.77) in (2.63), and ignoring the history dependence of the fine-scale terms we can solve for the trial solution coefficient $\boldsymbol{\beta}_{n+1}$ as follows

$$\boldsymbol{v}'_{n+1}(\boldsymbol{x}) = b^e \psi \boldsymbol{\beta}_{n+1} = -b^e \psi \left\{ \frac{\alpha_m}{\gamma \Delta t} \left(b^e \psi, b^e \psi \right) + \alpha_f \hat{\boldsymbol{\tau}} \right\}^{-1} \left(b^e \psi, \overline{\boldsymbol{r}}_{n+\alpha_f} \right) \tag{2.68}$$

where $\hat{\boldsymbol{\tau}}$ is defined as

$$\hat{\boldsymbol{\tau}} = \mu\int\left|\nabla\left(b^e\psi\right)\right|^2 d\Omega^e\boldsymbol{I} + \mu\int\nabla\left(b^e\psi\right)\otimes\nabla\left(b^e\psi\right)d\Omega^e + \int\left(b^e\psi\right)^2\nabla^T\overline{\boldsymbol{v}}d\Omega^e$$
$$+\int\left(b^e\psi\right)\overline{\boldsymbol{v}}\cdot\psi\nabla b^e d\Omega^e + \int\left(b^e\psi\right)\overline{\boldsymbol{v}}\cdot b^e\nabla\psi d\Omega^e \tag{2.69}$$

Employing the mean-value theorem for the coarse-scale residual $\overline{\boldsymbol{r}}_{n+\alpha_f}$ which amounts to an element-wise constant projection, (2.68) becomes

$$\boldsymbol{v}'_{n+1}\left(\boldsymbol{x}\right) = b^e\psi\boldsymbol{\beta}_{n+1} = -b^e\psi\left\{\frac{\alpha_m}{\gamma\Delta t}\left(b^e\psi, b^e\psi\right) + \alpha_f\hat{\boldsymbol{\tau}}\right\}^{-1}\left(b^e\psi, 1\right)\overline{\boldsymbol{r}}_{n+\alpha_f} \tag{2.70}$$

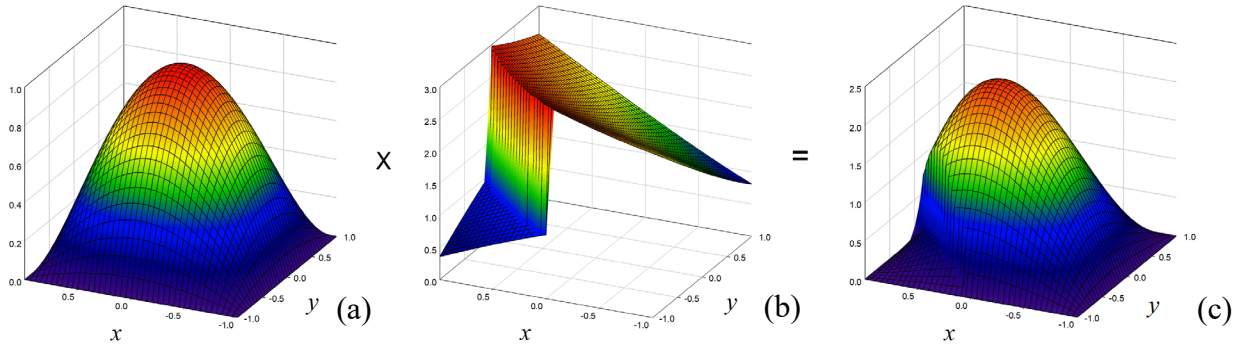

Fig. 2.3. Plot of (a) bubble function, (b) strong discontinuity enrichment function and (c) enriched bubble function in 2D for strong discontinuity.

Remark: *Although we have dropped history dependence of the fine scale, the stabilization tensor is still a function of* Δt *as shown in* (2.70)*. Furthermore,* (2.70) *leads to a system of ODE's that need a time integration method to convert it into an algebraic system.*

2.3.3 The Stabilized Weak Form of N.S. Equations with Embedded Discontinuity

We embed the fine-scale model into the coarse-scale variational problem by substituting (2.70) into (2.54) and (2.55). The formal statement for the modified stabilized form with embedded DC features is: Find $\boldsymbol{v}(\boldsymbol{x},t)\in\boldsymbol{\mathcal{V}}$ and $p(\boldsymbol{x},t)\in\mathcal{P}$ such that for all $\boldsymbol{w}(\boldsymbol{x})\in\boldsymbol{\mathcal{W}}$ and $q(\boldsymbol{x})\in\mathcal{Q}$:

$$\boxed{B_{Gal}\left(\left(\bar{\boldsymbol{w}},q\right),\left(\bar{\boldsymbol{v}},p\right)\right)+B_{VMS}^{Enr}\left(\left(\bar{\boldsymbol{w}},q\right),\left(\bar{\boldsymbol{v}},p\right)\right)+B_{div}\left(\bar{\boldsymbol{w}},\bar{\boldsymbol{v}}\right)=F_{Gal}\left(\bar{\boldsymbol{w}}\right)+F_{ST}\left(\bar{\boldsymbol{w}}\right)} \tag{2.71}$$

where the Galerkin terms are

$$B_{Gal}\left(\left(\bar{\boldsymbol{w}},q\right),\left(\bar{\boldsymbol{v}},p\right)\right)=\left(\rho\bar{\boldsymbol{w}},\frac{\partial\bar{\boldsymbol{v}}}{\partial t}\right)+\left(\bar{\boldsymbol{w}},\rho\bar{\boldsymbol{v}}\cdot\nabla\bar{\boldsymbol{v}}\right)+\left(2\mu\nabla^{s}\bar{\boldsymbol{w}},\boldsymbol{\varepsilon}\left(\bar{\boldsymbol{v}}\right)\right)-\left(\nabla\cdot\bar{\boldsymbol{w}},p\right)+\left(q,\nabla\cdot\bar{\boldsymbol{v}}\right) \tag{2.72}$$

$$F_{Gal}\left(\bar{\boldsymbol{w}}\right)=\left(\bar{\boldsymbol{w}},\rho\boldsymbol{b}\right) \tag{2.73}$$

and the enriched VMS terms are

$$B_{VMS}^{Enr}\left(\left(\bar{\boldsymbol{w}},q\right),\left(\bar{\boldsymbol{v}},p\right)\right)=\begin{pmatrix}-\dfrac{\alpha_m}{\gamma\Delta t}\rho\bar{\boldsymbol{w}}+2\mu\nabla\cdot\boldsymbol{\varepsilon}\left(\bar{\boldsymbol{w}}\right)+\bar{\boldsymbol{v}}\cdot\nabla\bar{\boldsymbol{w}}+\bar{\boldsymbol{v}}\cdot\nabla^{T}\bar{\boldsymbol{w}}+\nabla q,\\ \boldsymbol{\tau}\left(\dfrac{\partial\bar{\boldsymbol{v}}}{\partial t}-2\mu\nabla\cdot\boldsymbol{\varepsilon}\left(\bar{\boldsymbol{v}}\right)+\nabla p+\rho\bar{\boldsymbol{v}}\cdot\nabla\bar{\boldsymbol{v}}-\rho\boldsymbol{b}\right)\end{pmatrix} \tag{2.74}$$

The stabilization tensor that emanates from (2.70) is

$$\boldsymbol{\tau}\equiv b^{e}\psi\left\{\frac{\alpha_m}{\gamma\Delta t}\left(b^{e}\psi,b^{e}\psi\right)+\alpha_f\hat{\boldsymbol{\tau}}\right\}^{-1}\left(b^{e}\psi,1\right) \tag{2.75}$$

The discontinuous surface force due to surface tension is

$$F_{ST}\left(\bar{\boldsymbol{w}}\right)=\left(\nabla\cdot\left(\bar{\boldsymbol{w}}\right),\delta\kappa\right)_{\Omega_2}+\left(\bar{\boldsymbol{w}}\delta,\nabla\kappa\right)_{\Omega_2} \tag{2.76}$$

In our earlier work in [30] we added a *div*-stabilization term for global mass conservation. This additional term acts as a fine-scale pressure field stabilization term and helps improve mass conservation [30] and satisfaction of the incompressibility condition

$$B_{div}\left(\bar{\boldsymbol{w}},\bar{\boldsymbol{v}}\right)=\left(\nabla\cdot\bar{\boldsymbol{w}},\tau_c\nabla\cdot\bar{\boldsymbol{v}}\right) \tag{2.77}$$

and the stabilization parameter τ_c is adopted from [25].

$$\tau_c = \left(\tau_M \boldsymbol{G} \cdot \boldsymbol{G}\right)^{-1} \tag{2.78}$$

where $\boldsymbol{G}$ is a second order tensor given as a function of the isoparametric mapping $\boldsymbol{\xi}$ between the physical and reference coordinates defined as $\boldsymbol{G} = \partial_x \boldsymbol{\xi}^T \partial_x \boldsymbol{\xi}$. For our implementation we have employed

$$\tau_M = \frac{1}{3}\text{trace}\left(\boldsymbol{\tau}\right) \tag{2.79}$$

where $\boldsymbol{\tau}$ is given in (2.75).

This system of equations for the coarse-scale sub-problem is applied to all the elements in the mesh. The only difference is the use of the enriched fine scale bubble functions in the elements that are intersected by the interface.

Remark: *The activation/deactivation of fine-scale enrichment for the case of an evolving interface can be carried out through a simple check on the nodal values of the signed distance field in the element to see if it is traversed by the interface.*

Remark: *The div-stabilization term presented above can also be derived via the mixed VMS method presented in* [7].

Remark: *Numerical tests reveal that for the case of discontinuous viscosity and density, this div-stabilization term adds stability to the pressure field in the proximity of the interface. Without this additional stabilization, significant oscillations are observed in the pressure around the elements that have interface traversing through them.*

Remark: *The discontinuous surface force formulation augmented with the fine-scale enrichment leads to a sharper jump that is curtailed only within a single element. This results in a method that*

variationally converges with mesh refinement to the exact location of the interface and an accurate prediction of pressure field across the interface.

2.4 Level-Set Evolution Equation

The interface in two-phase flow problems is tracked via an implicit scalar function that evolves via a hyperbolic equation. This equation, commonly termed as the level-set equation is driven by the velocity field that is facilitated by the solution of the momentum equation. However the level-set equation being hyperbolic needs a stabilization schemes to yield stable solutions. Following along the lines of Sections 2 and 3 we employ the time dependent VMS method to stabilize the level-set equation. Since we have already presented the stabilized method for the advection diffusion equation in Section 2.2, we only present the final stabilized form of the hyperbolic equation for the level-set as follows

$$\begin{aligned}&\frac{\alpha_m}{\gamma\Delta t}\left(\overline{\eta},\overline{\phi}_{n+1}\right)-\frac{\alpha_m}{\gamma\Delta t}\left(\overline{\eta},\tau\overline{r}_{n+\alpha_f}\right)+\alpha_f\left(\overline{\eta},\boldsymbol{v}\cdot\nabla\overline{\phi}_{n+1}\right)+\alpha_f\left(\boldsymbol{v}\cdot\nabla\overline{\eta},\tau\overline{r}_{n+\alpha_f}\right)\\&=\frac{\alpha_m}{\gamma\Delta t}\left(\overline{\eta},\overline{\phi}_n\right)-\left(1-\frac{\alpha_m}{\gamma}\right)\left(\overline{\eta},\left.\frac{\partial\overline{\phi}}{\partial t}\right|_n\right)-\left(1-\alpha_f\right)\left(\overline{\eta},\boldsymbol{v}\cdot\nabla\overline{\phi}_n\right)\end{aligned} \tag{2.80}$$

where $\overline{\phi}$ is the coarse scale trial solution for the signed distance function defined as

$$\phi=\begin{cases}+d\left(\boldsymbol{x}-\Gamma_s\right) & \text{in } \Omega_1\\ -d\left(\boldsymbol{x}-\Gamma_s\right) & \text{in } \Omega_2\end{cases} \tag{2.81}$$

and $d\left(\boldsymbol{x}-\Gamma_s\right)$ is the normal distance function from the interface Γ_s to a point $\boldsymbol{x}$, and $\overline{\eta}$ is the coarse-scale weighting function. Due to the higher order derivatives needed to model the interface curvature and its gradient in the surface tension term, higher order basis functions are needed. One method of bypassing this requirement while still using linear basis functions for the level-set

equation is to construct a smoother projection of the gradient and curvature using an L_2-projection techniques for the gradient, thus yielding smooth gradients as the interface evolves in space and time. Nevertheless, accumulation of numerical noise after multiple time steps still leads to deviation of the signed distance function ϕ and it starts violating the Eikonal condition $|\nabla\phi| = 1$. To preserve this condition while still maintaining the value of the signed distance field at the interface, a post-processing procedure called reinitialization is required subsequent to the solution of the level-set equation.

2.4.1 Reinitialization

In order to assure the accuracy of the interface between phases, the signed distance property needs to be preserved. This is achieved by a reinitialization process which aims to satisfy the Eikonal equation $|\nabla\phi| = 1$, while maintaining the location of the zero level-set $\phi = 0$ at Γ_s. A commonly used method for reinitialization is to solve the nonlinear hyperbolic PDE [2]. This method preserves the location of the interface and is generally solved using pseudo-time steps where number of steps needed to obtain converged solution depends on the complexity of the interface, thereby resulting in increased computational cost. This technique however suffers from mass loss during repeated reinitialization and requires additional mass conserving techniques [2].

In [2] a new elliptic reinitialization method is proposed that bypasses the need to solve for multiple pseudo-time steps via solving an elliptic minimization problem. In [3] This approach is modified by restricting the minimization of the Eikonal equation to elements not intersected by the interface and it assure the interface to be held in place via a penalty term applied in the intersected elements.

2.5 Numerical Results

2.5.1 Skew-advection problem

The skew-advection problem shown in Fig. 2.4 is a classical benchmark problem for advecting a discontinuous field from the boundary into the domain. We use this problem as a test case for our embedded discontinuity method and consider the case with convected sharp discontinuities in the advected field. The problem is defined on a biunit domain $\Omega = [0,1] \times [0,1]$ with a constant advective velocity $v_x = v_y = 1$. The boundary conditions are shown in Fig. 2.4. Using the fine scale enrichment method along with the adaptive integration algorithm we obtain an accurate representation of the discontinuous field within the domain. As we refine the mesh we converge at optimal rates in the L^2 norm as shown in Fig. 2.7. Comparing our VMDC method (Fig. 2.5(b)) with the SUPG stabilization (Fig. 2.5(a)) that is augmented with DC terms [19] we observe an improvement in the sharpness of the represented discontinuity which is captured within a single element. Additionally, the VMDC method is able to advect the discontinuity induced at the boundary without any numerical diffusion as compared to the SUPG-DC case.

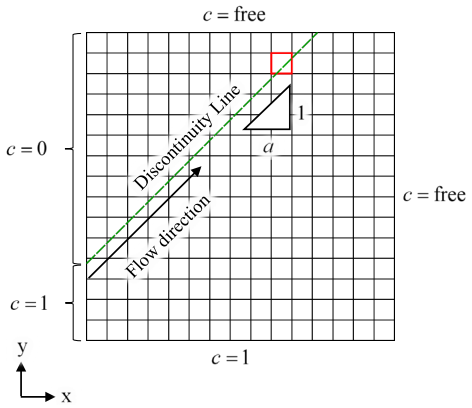

Fig. 2.4. Skew-advection problem, mesh, interface and boundary conditions, element outlined in red shows example of interface intersected element.

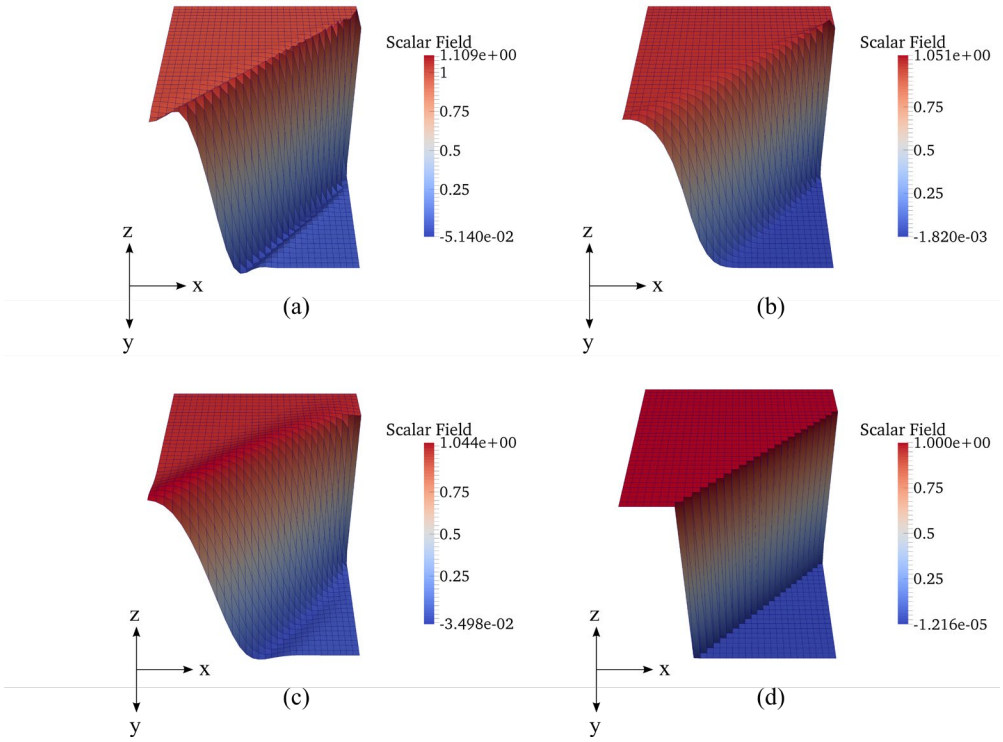

Fig. 2.5. Skew-advection solution profile for (a) SUPG, (b) SUPG-DC, (c) VMS and (b) VMDC.

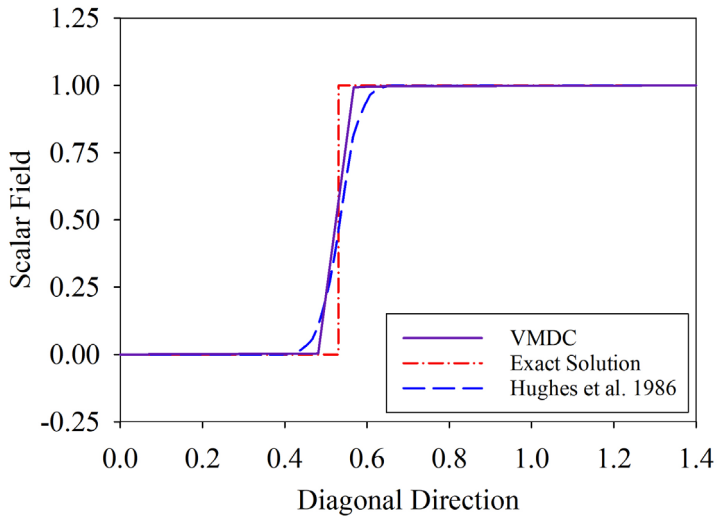

Fig. 2.6. Skew-advection field along diagonal ($0 < x < 1$; $1 < y < 0$), comparison between the VMDC, Exact solution, and SUPG-DC [19].

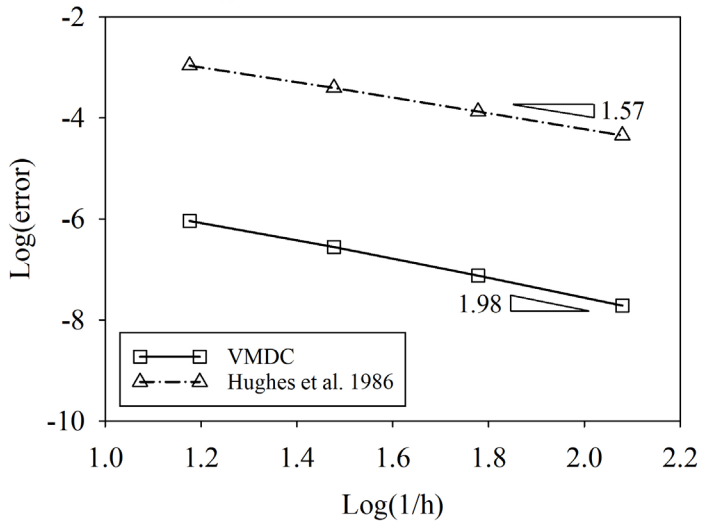

Fig. 2.7. L_2-convergence of the scalar field for the skew-advection problem ($h = 1/15,\ 1/30,\ 1/60,\ 1/120$).

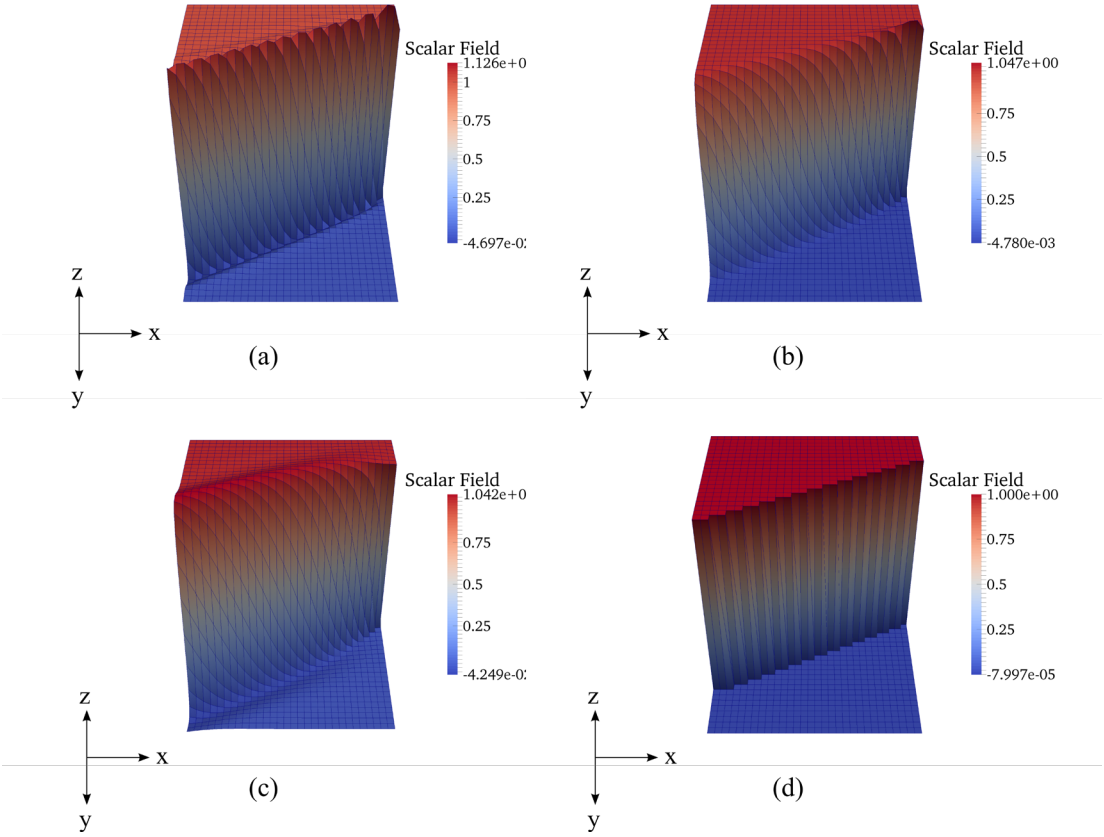

Fig. 2.8. Skew-advection solution profile for (a) SUPG, (b) SUPG-DC, (c) VMS and (d) VMDC.

Finally in Fig. 2.8 we show another skew-advection configuration where the interface is skewed in a 2:1 ratio. The VMDC method is able to capture the jump across a single element thus showing the versatility of the method in capturing different discontinuity orientations.

Remark: *The fine-scale bubble functions when augmented via the gradient of the field result in a non-linear scalar field. In this case the VMDC method introduces nonlinearity in the system because of the dependence of the stabilization parameter on the field itself. It is important to note that the variational consistency of the formulation and of the stabilization parameter results in quadratic convergence of the solution in the Euclidian norm.*

Remark: *For the case of discontinuous material properties where the interface is prescribed via the level-set field, convergence is attained in 1 iteration, as is expected of linear problems. This feature can result in substantial cost savings for large scale 3D problems.*

2.5.2 Extensional flow problem

This numerical problem involves two layered immiscible fluids that are subjected to a linearly varying skew flow, where the flow physics is dominated by the viscosity of the fluid. The jump in viscosity across the interface separating the two fluids induces a jump in the pressure field across the fluid interface. Since, the interface does not conform to the mesh lines, it introduces a discontinuity that requires a discontinuity capturing method to produce solution without oscillations. We compare the VMDC method to a pressure enrichment technique presented in [1]. The schematics of the problem setup is shown in given in Fig. 2.9. The problem domain is $\Omega = [0,1]\times[0,1]$, where the density for both the fluids is $\rho = 10$ and the viscosity varies sharply from $\mu_1 = 5$ for fluid-1 to $\mu_2 = 1$ for fluid-2.

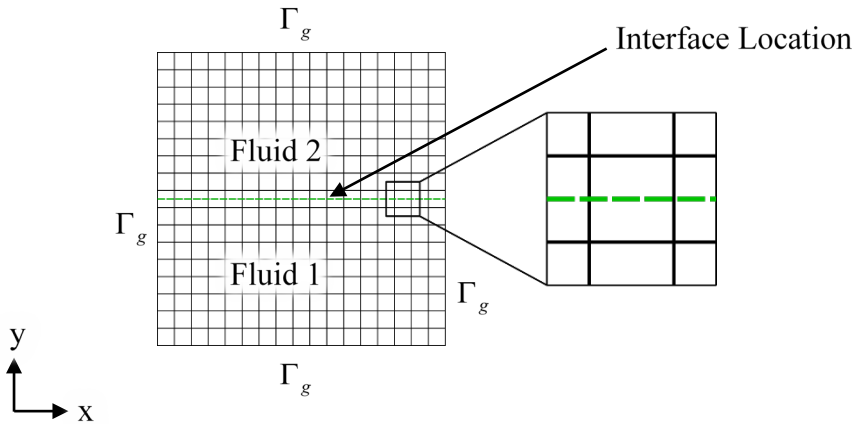

Fig. 2.9. Extensional flow problem setup.

The boundary conditions for velocity are $v_x = 1 - x$ and $v_y = y$ at Γ_g. These boundary conditions are applied along all the boundaries of the domain and considering zero gravity forces, the exact solution for this problem is given as

$$p(x,y) = \rho\left(x - \tfrac{1}{2}\left(x^2 + y^2\right)\right) + 2\left(\mu_1 - \mu_2\right)\mathrm{H}(a - y) \tag{2.82}$$

where the Heaviside function $\mathrm{H}(a-y)$ is defined as follows

$$\mathrm{H}(a-y) \equiv \begin{cases} 1 & \text{if } y < a \\ 0 & \text{if } y > a \end{cases} \tag{2.83}$$

For the present problem $a = 0.5$ in (2.83). By inspecting the results in Fig. 2.11 one could see the agreement between the present VMDC method and the pressure enrichment approach introduced in [1]. We are thus able to represent the pressure jump across a single element as shown in Fig. 2.10. Furthermore, in order to use equal order interpolation while satisfying the *inf-sup* conditions, Ausas *et al.* [1] require additional stabilization which is separate from the pressure enrichment. In the VMDC method both the *inf-sup* condition and the discontinuity capturing are achieved via the

variationally derived fine scales. Fig. 2.11 presents the pressure profile which is compared to the method presented in [1] and with the exact solution. It is evident that the VMDC method approaches the exact solution with a sharper jump. Since we have an exact solution for this problem, we can use it to numerically establish variational convergence of the VMDC method. As shown in Fig. 2.12, the VMDC method is able to achieve optimal convergence with reduced error when compared to the method presented in [1].

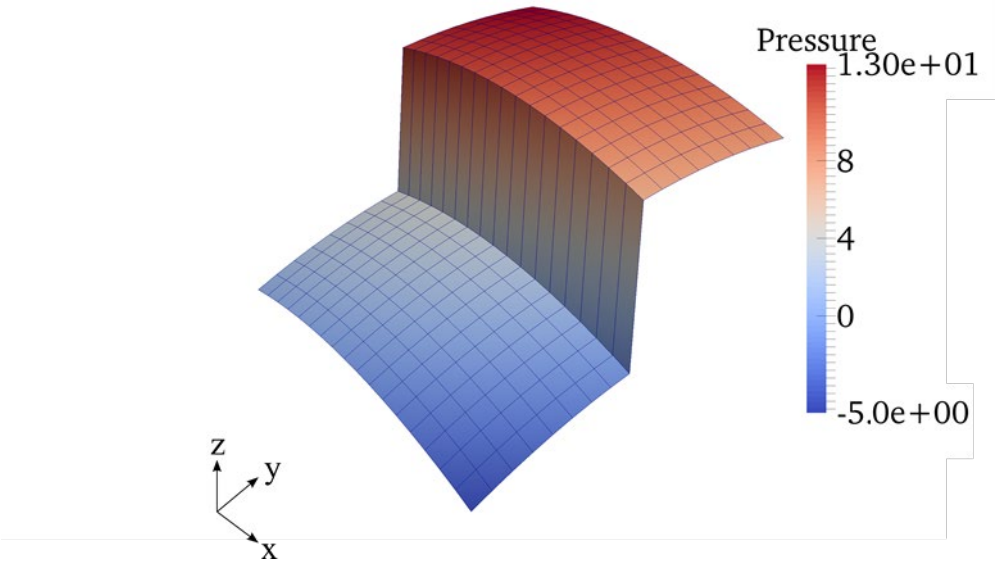

Fig. 2.10. Computed pressure profile.

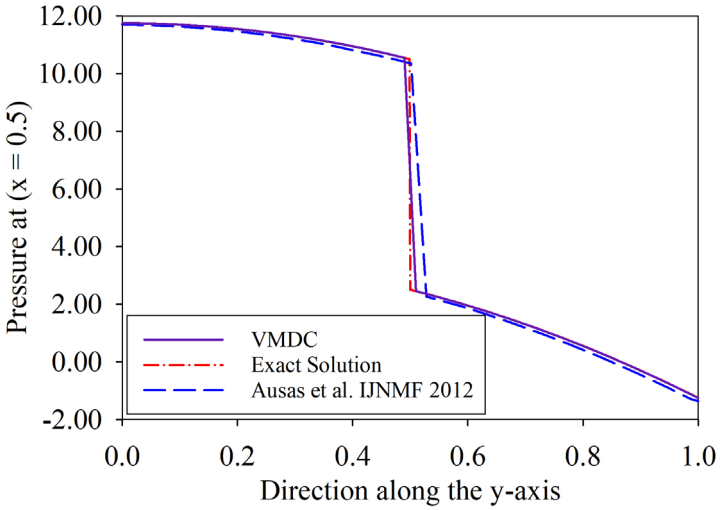

Fig. 2.11. Pressure profile across the interface for the 35×35 mesh.

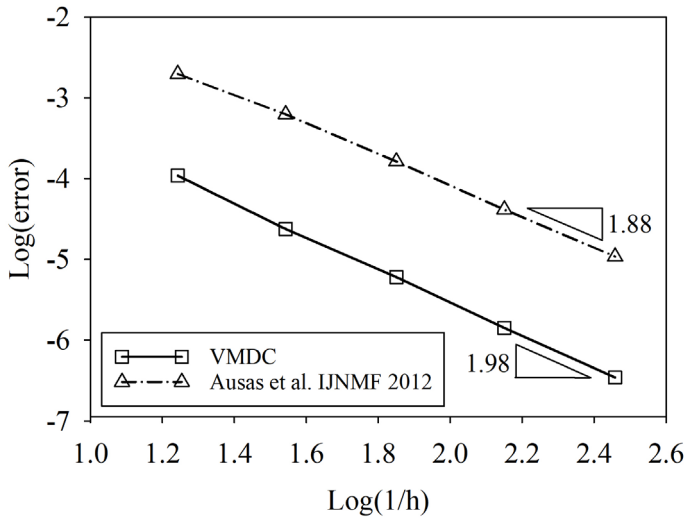

Fig. 2.12. L_2-convergence of the pressure field for extensional flow problem.

2.5.3 Laplace-Young problem

To compare the VMDC method with the classical continuum surface force method [4] in terms of accommodating the surface tension effects we employ the Laplace-Young problem (a.k.a. the static bubble problem). This test case verifies the accuracy of surface tension and the sharpness

of the jump in the pressure field. The problem is defined on a 2D domain $\Omega = [0,1]\times[0,1]$. A circular interface centered at $\boldsymbol{x} = (0.5, 0.5)$ with radius $R = 0.2$ is used to define the location of the interface between the liquid and gas phases for the application of the surface tension force. In order to highlight the jump induced in the pressure field due to surface tension alone and to avoid any contribution to the jump due to material parameter discontinuity, the density and viscosity of the fluids inside and outside the interface are both set equal to 1. All boundaries are set to zero pressure, and no-slip conditions are applied. The surface tension coefficient is set as $\delta = 1$ which results in a jump in the pressure field given by $\Delta p = \delta / R$. Using these parameters the exact solution is

$$p(\boldsymbol{x}) = \begin{cases} 0 & \phi > 0 \\ 5 & \phi < 0 \end{cases} \tag{2.84}$$

Where the signed distance function $\phi(\boldsymbol{x})$ is negative inside the circular interface. In Fig. 2.13 we compare the proposed discontinuous surface force method with the continuum surface force method [4] in terms of the surface tension representation. Using the regularized surface force via the continuum surface force formulation, the jump is spread over several elements and the effect is smeared, leading to reduced accuracy in the representation of the location of the interface. The discontinuous surface force formulation augmented with the fine-scale enrichment leads to a sharper jump that is contained only within a single element. This leads to a method that variationally converges with mesh refinement to the exact location of the interface and an accurate calculation of the pressure field inside the interface. Fig. 2.14 shows the pressure profile for a finer mesh using the VMDC method.

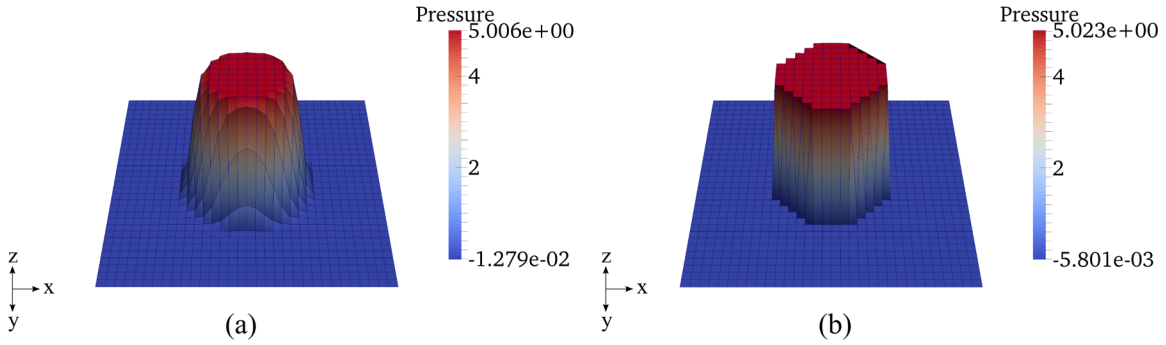

Fig. 2.13. Laplace-Young problem with surface tension: (a) regularized continuum surface force solution, and (b) sharp discontinous surface force solution. (coarse mesh)

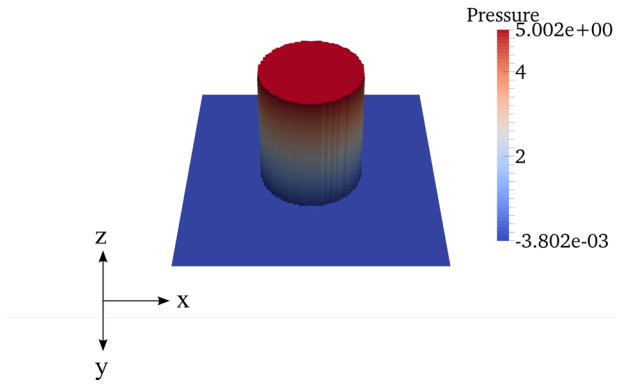

Fig. 2.14. Laplace-Young problem with surface tension for sharp discontinous surface force solution. (fine mesh)

The accurate and sharp representation of the discontinuity becomes increasingly important when several PDEs within a system, such as in the present case, depend on each other via the coupling terms that change sharply across the interface. In Fig. 2.15 we plot the pressure profile across $y = 0.5$ for the mesh comprised of 32×32 four node quadrilaterals. In Figures 2.16-2.17 we explore the case of two adjacent static bubbles of $R = 0.125$ which results in an exact pressure jump of $\Delta p = 8$. The VMDC method is shown to precisely model the jumps in the pressure field in very close proximity as shown in Fig. 2.16(a) where the two bubbles are separated by only two

elements. Fig. 2.16(b) shows pressure profile for a finer mesh. This shows the robustness of the method for application to problem classes where bubble migration and interaction may become important. Fig. 2.17 shows pressure profile for 128×128 mesh and the jump is captured within one element without overshoots or undershoots. Fig. 2.18 shows the optimal convergence of VMDC in comparison to [34]. The meshes used for this study are 16^2, 32^2, 64^2 and 128^2. Since we have an exact solution for this problem it can be used for checking variational convergence of the method. Specifically, the 16^2 mesh with VMDC yields approximately the same engineering accuracy as the 64^2 mesh using the method proposed in [34].

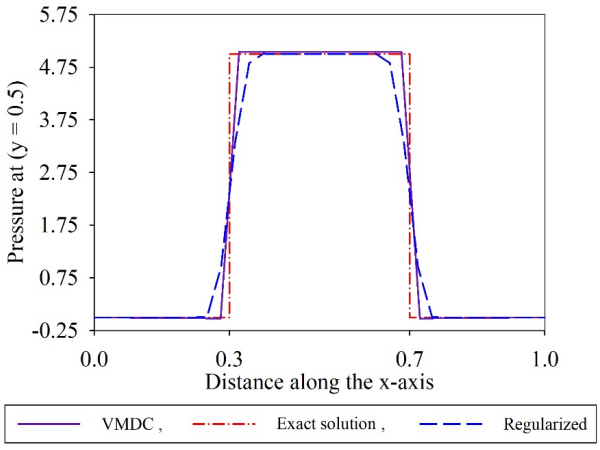

Fig. 2.15. Comparison of pressure profile, sharpness of gradient and proximity to exact interface location between the continuum surface force and the sharp discontinuous surface force methods.

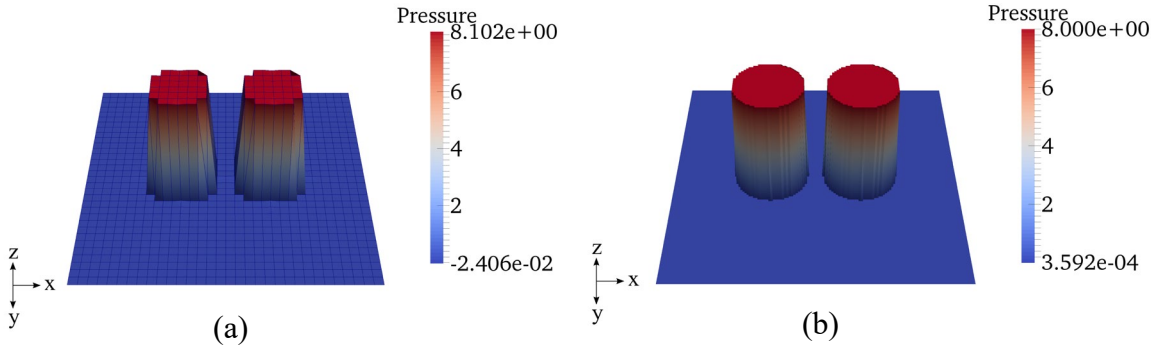

Fig. 2.16. Pressure profile for the two-bubble case (a) coarse mesh (32^2) and (b) fine mesh (128^2).

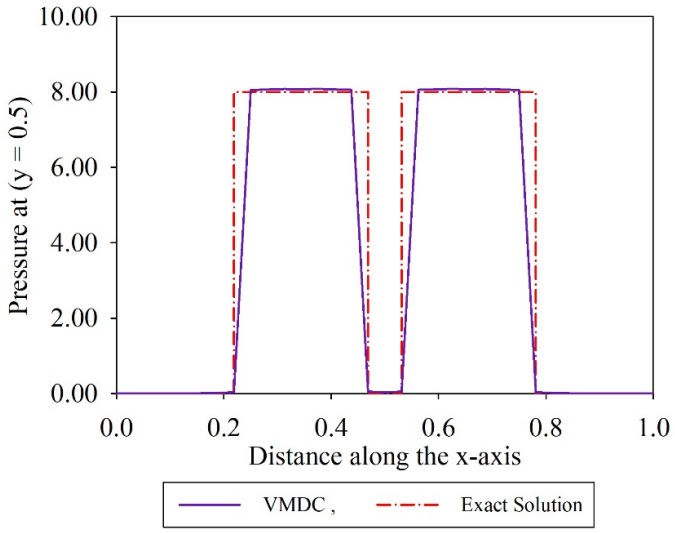

Fig. 2.17. Line plot for the pressure field through the centerline along x-axis.

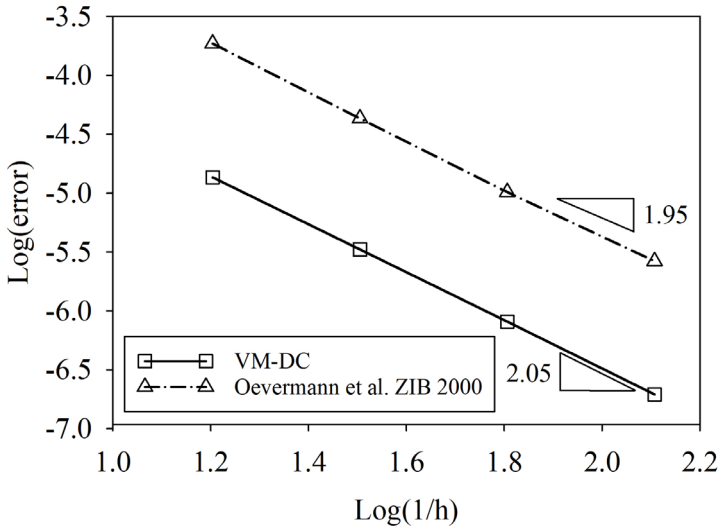

Fig. 2.18. L_2-convergence of the velocity field for single static bubble.

2.5.4 Rising Bubble with Surface Tension

The motion of a rising bubble is a moving interface problem. The material properties of the two immiscible fluids are taken from [20] and are presented in Table 2.1. The density and viscosity of the bubble is chosen to be less than that of the surrounding medium. The dimensions,

initial two-phase configuration, and the boundary conditions are shown in Fig. 2.19. The two fluids are initially at rest and the problem is driven by the buoyancy forces induced by the discontinuous material properties in addition to the surface tension that is applied along the interface.

Table 2.1: Material properties for the Rising Bubble problem.

Material properties of the two fluids	
Viscosity μ_l (surrounding medium)	1
Viscosity μ_b (bubble)	10
Density ρ_l (surrounding medium)	1000
Density ρ_b (bubble)	100
Gravity	0.98
Surface Tension	24.5

The problem is modeled using the Navier-Stokes equations augmented with VMDC and surface tension formulation as presented in Section 2.3, and the level-set method is employed to track the evolution of the interface. In addition to the material discontinuity, the evolution of this problem depends on the surface tension which dictates the jump in the pressure field and the shape of the bubble as it rises. While higher values of surface tension help in reducing the interface distortion during the rise of the bubble, the high surface tension coefficient leads to larger jumps in the pressure field. As the location and shape of the interface evolve, the VMDC method maintains a sharp representation of the pressure discontinuity within a single element that the interface traverses.

As the level-set field evolves the pressure discontinuity moves from one element to the next, which requires the local fine-scale enrichment to move along with the interface. The VMDC method naturally allows for this enrichment motion to occur due to the direct coupling between the enrichment functions used in the VMDC method and the level-set field itself. Therefore, enrichment is activated in the intersected elements and subsequently deactivated as the interface leaves these elements.

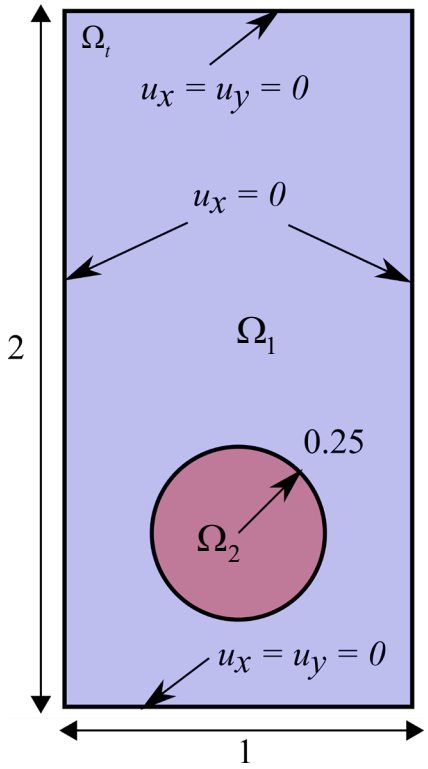

Fig. 2.19. Rising bubble problem: Domain dimensions and boundary conditions.

The simulation is run for 3 sec. with a fixed time step of $\Delta t = 1/50$ which is a coarse step size as compared to the step size used in [20]. The shape of the interface at time points $t = 0.6\ s$, $t = 1.2\ s$, $t = 1.8\ s$ and $t = 3\ s$ are shown in Fig. 2.20. In this simulation a 40×80 mesh was used that corresponds to the coarsest mesh size used in the methods presented in [20].

Remark: *The rising bubble problem has been run in [23] employing the anisotropic adaptive remeshing method and using a time step of* $\Delta t = 1/500$ *and for the coarsest mesh size in [20] the time step used was* $\Delta t = 1/640$. *These two time steps are approximately 10 times smaller than that used in the present VMDC method. This numerical example shows that the enhanced stability afforded by the VMDC formulation results in significant cost effectiveness of the method.*

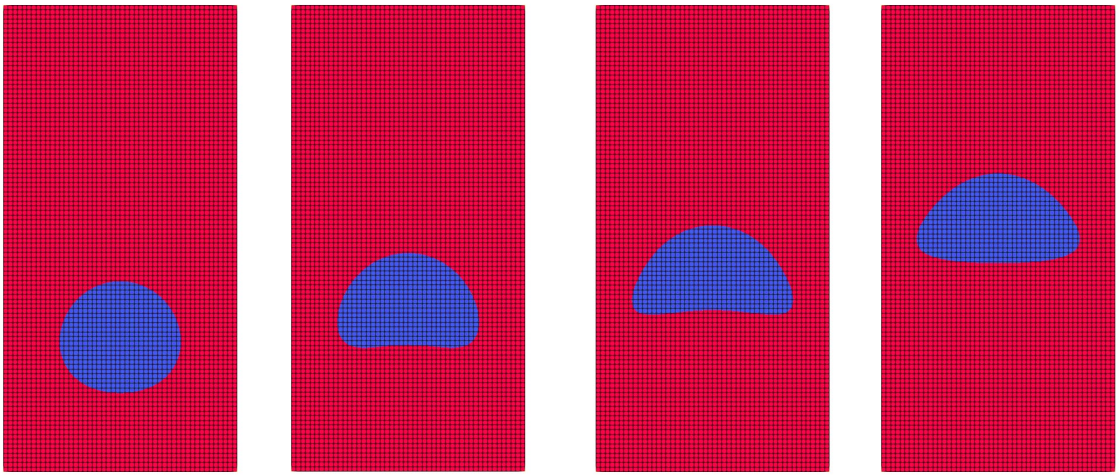

Fig. 2.20. Shape of the interface at 0.6, 1.2, 1.8 and 3 sec.

Fig. 2.21 presents the vorticity magnitude as the bubble rises. To provide a quantitative comparison with the results presented in [20] we use time evolution of the center of mass $\boldsymbol{X}_c = \int_{\Omega_2} \boldsymbol{x}\, d\Omega \big/ \int_{\Omega_2} 1\, d\Omega$ of the bubble and the rising velocity of the center of mass $\boldsymbol{V}_c = \int_{\Omega_2} \boldsymbol{v}\, d\Omega / \int_{\Omega_2} 1\, d\Omega$. We compare the VMDC method with the two methods in [20] that produce approximately identical results (TP2D and MoonMD) and therefore we use the plots of the later method in Fig. 2.22. The MoonMD method is an arbitrary Eulerian-Lagrangian method with grid motion and the VMDC coarse mesh shows close agreement with it for evolution of the center of mass in Fig. 2.22(a). Fig. 2.22(b) shows the comparison of the rising velocity of the

center of mass between the VMDC method and the MoonMD method. To illustrate the discontinuity capturing feature of the VMDC method for transient advective discontinuities, we present in Fig. 2.23 and Fig. 2.24 the warped pressure profile at different time steps. These figures highlight the sharp discontinuity in the pressure field and show the precise location of the interface Γ_s inside the elements intersected by the interface. The jump in pressure is not only captured in a single element, this feature of the method is maintained as the interface evolves the through layers of elements.

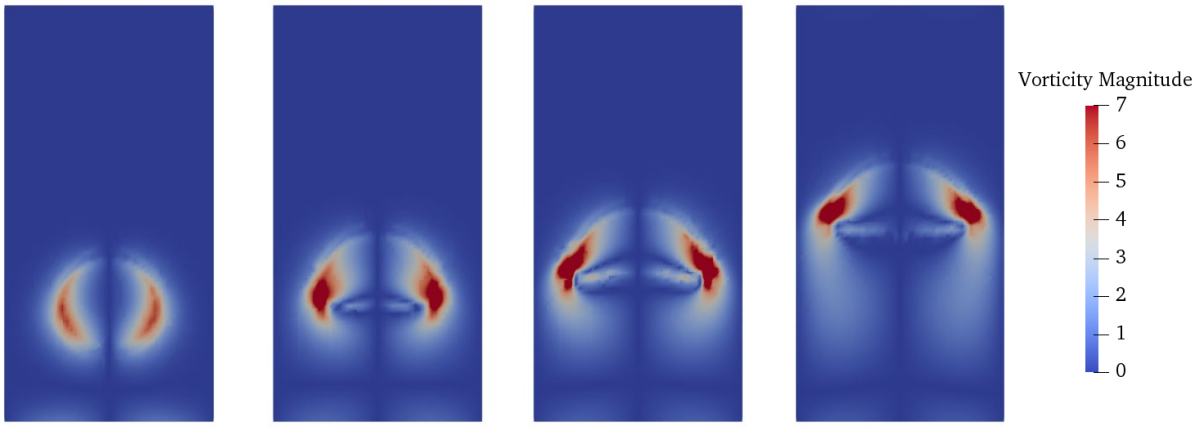

Fig. 2.21. Magnitude of vorticity at 0.6, 1.2, 1.8 and 3 sec.

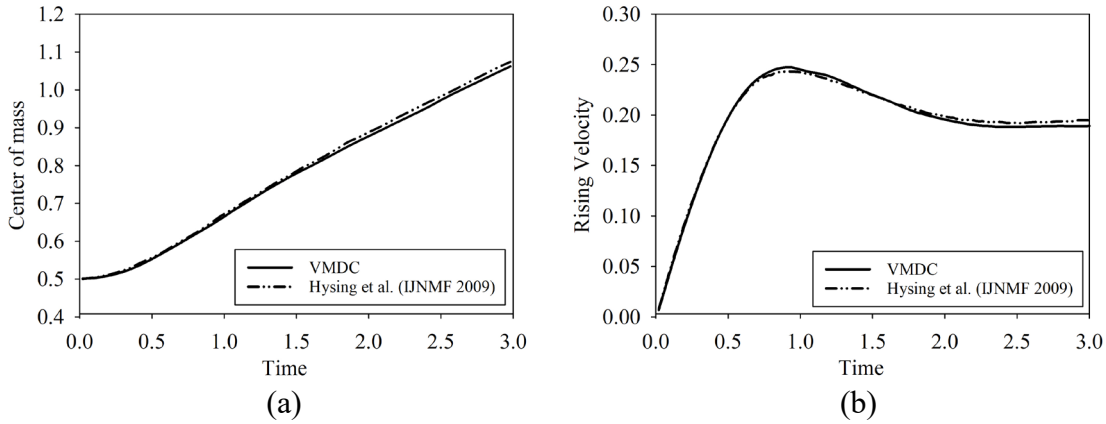

Fig. 2.22. Evolution of center of mass of the bubble: (a) position and (b) rising velocity.

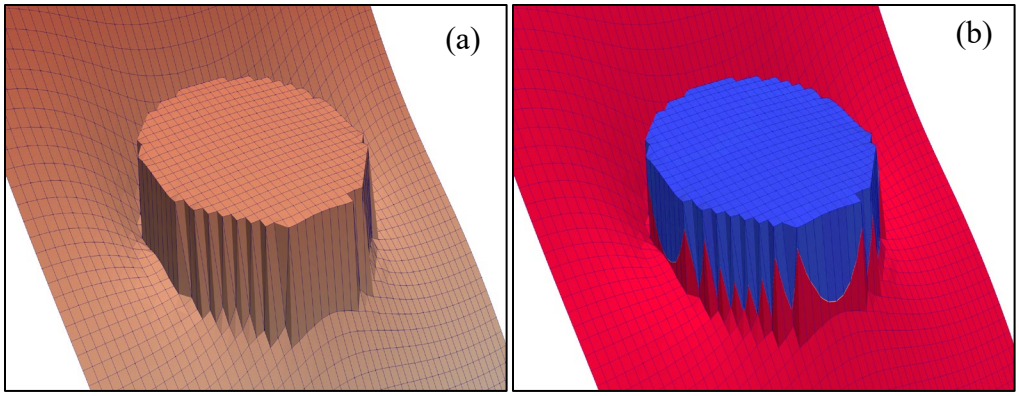

Fig. 2.23. Spatial distribution of (a) close up of pressure profile at 0.6 sec and (b) close up of the location of the interface Γ_s in the element.

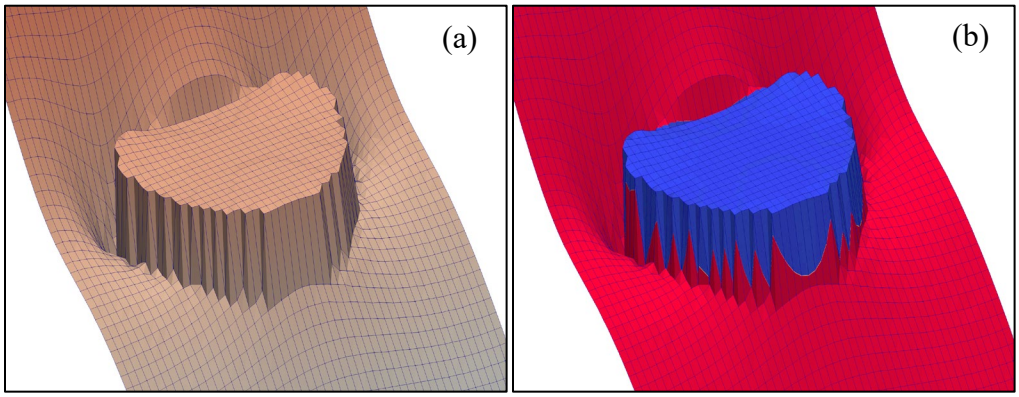

Fig. 2.24. Spatial distribution of (a) close up of pressure profile at 1.2 sec and (b) close up of the location of the interface Γ_s in the element.

We want to emphasize that as compared to the methods presented in [20], no mass correction step has been employed in the present method. Still the total mass loss is within 3 %. This mass loss can be significantly reduced with time step refinement and an addition of a mass correction algorithm. However, such an algorithm is not implemented in the present chapter.

2.5.5 Rayleigh-Taylor instability

This section presents transient mixing of two immiscible fluids with different densities also known as the Rayleigh-Taylor instability problem. The two fluids are initially at rest with the denser fluid on top of the lighter fluid. Fig. 2.25 shows the schematics of the problem where the

dimensions are $a = 1$ and $b = 4$. The initial interface is given by $y = 0.05\cos(2\pi x)$ dividing the domain into two sub-domains and slip boundary conditions are prescribed on all the boundaries. The material properties associated with each subdomain are given in Table 2.2.

Table 2.2: Material properties for the Rayleigh-Taylor instability problem.

Viscosity (top fluid) μ_t	0.0135 g/(cm s)
Viscosity (bottom fluid) μ_b	0.0045 g/(cm s)
Density (top fluid) ρ_l	3 kg/m3
Density (bottom fluid) ρ_g	1 kg/m3
Gravity	10 m/s2

The flow is modeled using incompressible Navier-Stokes equations, and the interface is evolved via the level-set advection equation. In this problem the dominant physical phenomena that govern the stability and accuracy of the simulation are the pressure and velocity field variations at the interface that are a function of (a) discontinuous density, and (b) discontinuous viscosity. These material parameter discontinuities lead to discontinuities in the velocity gradient and pressure field across the interface. To model these discontinuities without resorting to averaging schemes, we employ the stabilized two phase Navier-Stokes equations presented in Section 2.3. However, in this test case we do not consider the surface tension effects.

The level-set method presented in Section 2.4 is used to track the interface and it helps avoid the use of a Lagrangian mesh which can break down under excessive element distortions and therefore would require continuous re-meshing to yield a viable computational grid. The

enrichment idea in this method is local to the elements and does not increase the size of the linear system. Additionally, the enrichment function is easily formed using the underlying implicit interface field facilitated by the level-set evolution equation. This also allows for local enrichment that is only active in elements intersected by the interface and therefore adapts to the moving interface automatically. This method only slightly increases the computations in the local fine-scale sub-problems over the intersected element, but without increasing the size of the global problem.

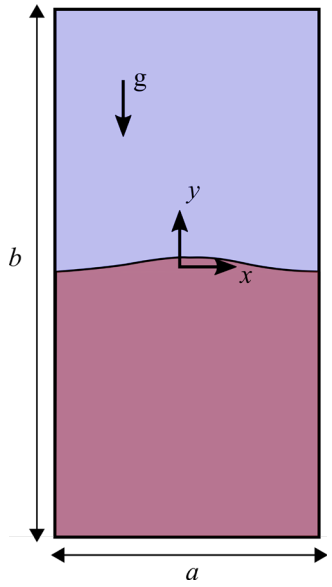

Fig. 2.25. Rayleigh-Taylor Instability interface and domain dimensions.

The simulation is run for 1.25 sec. with a fixed time step of $\Delta t = 0.01$ and the instantaneous interfacial profiles at time points $t = 0.5\ s$, $t = 0.7\ s$, $t = 1.0\ s$ and $t = 1.25\ s$ are shown in Fig. 2.26. The shape of the interface is compared with the data presented in [23] and a qualitatively good agreement is achieved using the VMDC method. In these simulations two meshes comprising 32×128 elements for the coarser mesh and 64×256 elements for the finer mesh are employed. The grid size of the finer mesh is similar to the finer mesh in [23]. However, unlike the evolving anisotropic element representation with adaptive re-meshing used in reference [23] our

calculations are all performed on the first formed mesh. It can be appreciated that as the problem evolves, the interface topology becomes quite intricate, thereby making the first formed mesh fairly coarse for the simulation. The provision of the fine scale variational problem with enhanced enrichment is not only able to stabilize the method, it is automatically able to account for the physics which would otherwise be lost because of the spatial grid becoming relatively coarser to capture the physical features that are much refined as compared to those at the start of the problem.

Table 2.3 presents the mass conservation property of the method for various time points for the two meshes, calculated in terms of the fluid area, during the evolution of the problem. The maximum mass loss after 1.25 sec. is 1.84% for the fine mesh and approximately 3% for the coarse mesh.

Table 2.3: Normalized mass loss for the Rayleigh-Taylor instability problem.

Time (sec)	Normalized Mass Loss	
	Coarse Mesh (32 X 128)	Fine Mesh (64 X 256)
0.70	0.0015	0.0011
1.00	0.0086	0.0048
1.25	0.0184	0.0328

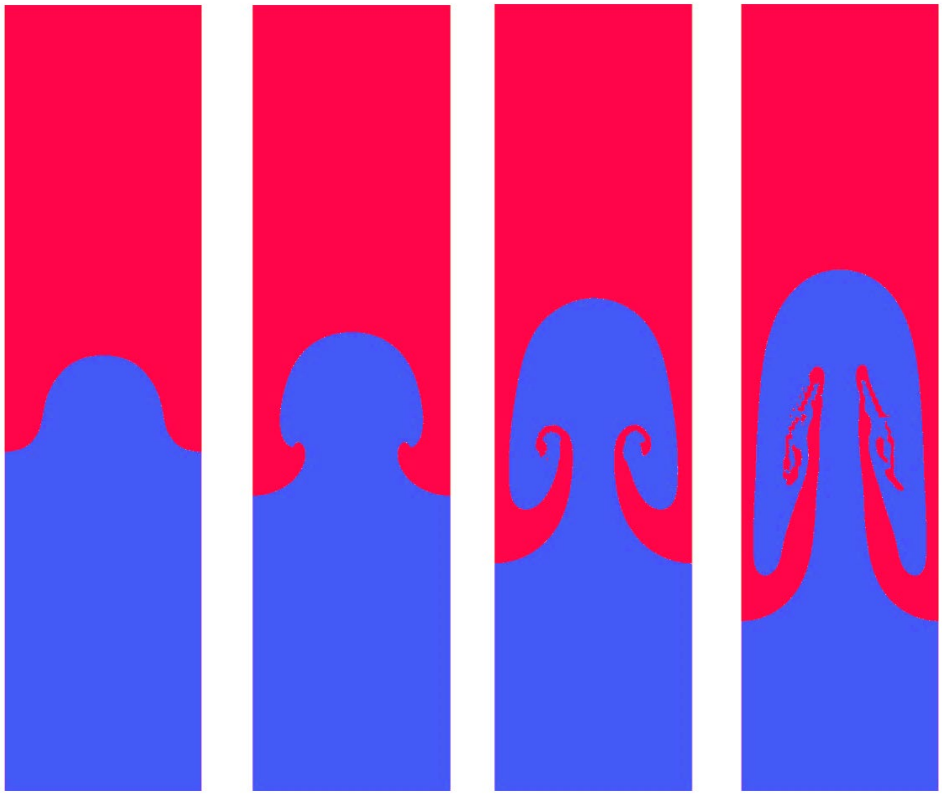

Fig. 2.26. Shape of the interface at 0.5, 0.7, 1.0 and 1.25 sec.

Fig. 2.27 presents the magnitude of the vorticity for the selected time points and highlights the evolving physical complexity of the flow. The velocity profile data for the coarse and fine mesh at $t = 1.00$ sec. and $t = 1.25$ sec. are shown in Figs. 2.28 and 2.29.

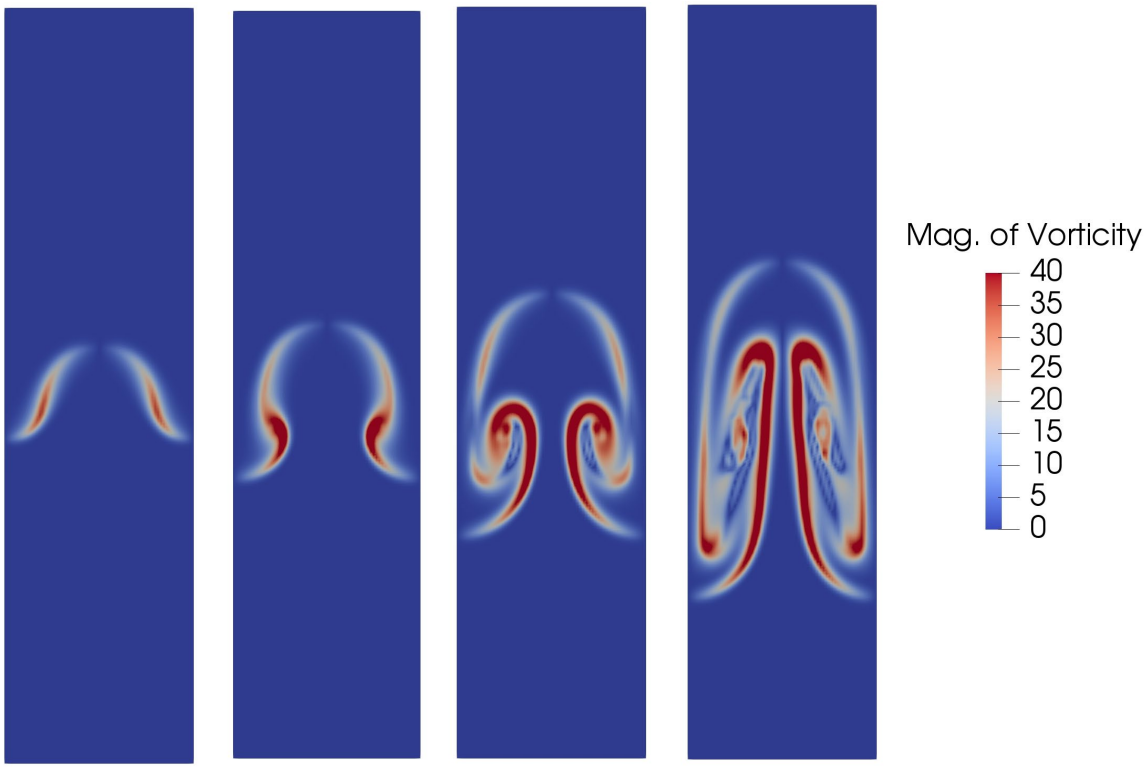

Fig. 2.27. Magnitude of vorticity for at 0.5, 0.7, 1.0 and 1.25 sec.

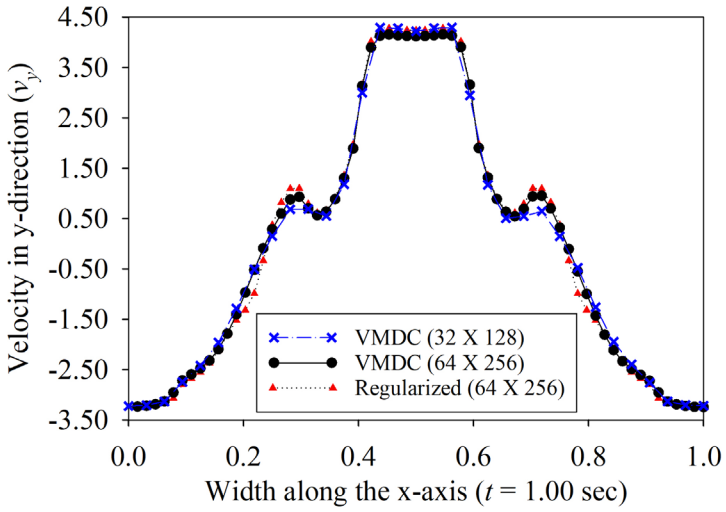

Fig. 2.28. Velocity component v_y across the width at $y = -0.375$ and $t = 1.00\,\text{sec}$.

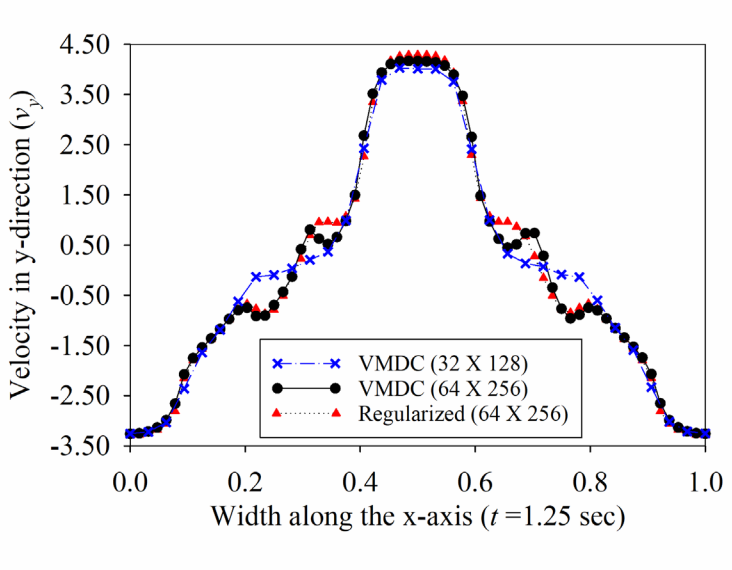

Fig. 2.29. Velocity component v_y across the width at $y=-0.375$ and $t=1.25\,\text{sec}$.

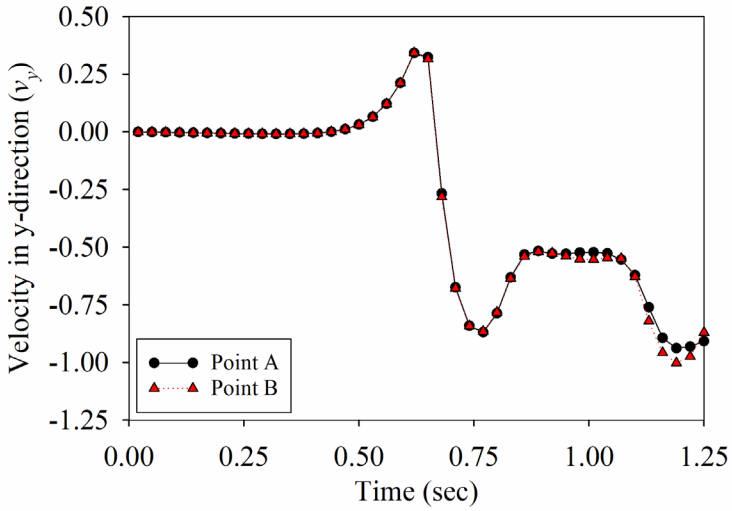

Fig. 2.30. Temporal evolution of velocity component v_y at spatial points A $(x=-0.28125, y=-0.375)$ and B $(x=0.28125, y=-0.375)$ for the fine mesh (64×256).

Fig. 2.30 presents time evolution of the vertical velocity for two symmetric points in the 64×256 mesh. The close agreement between the two symmetric points is used as a measure of robustness and accuracy in time of the VMDC method. To provide insight into the evolving complexity of

the physics in this problem we have plotted the nodal values of the Reynolds number in Fig. 2.31. As time progresses, not only the Reynolds number increases rapidly, there is a steep spatial variation in the Reynolds number. These high gradients in the Reynolds number can initiate weak instabilities in the solution. This is compounded by the intricate interface topology that makes the level-set field deviate from the strict definition of the singed distance field, which can trigger another weak instability in the solution that can eventually make it hard for the method to converge. This issue is also there in the Lagrangian mesh methods [36, 42] that require repeated remeshing and the first order projection errors between successive meshes eventually catch up with the stability of the method thereby leading to non-convergence of the numerical method.

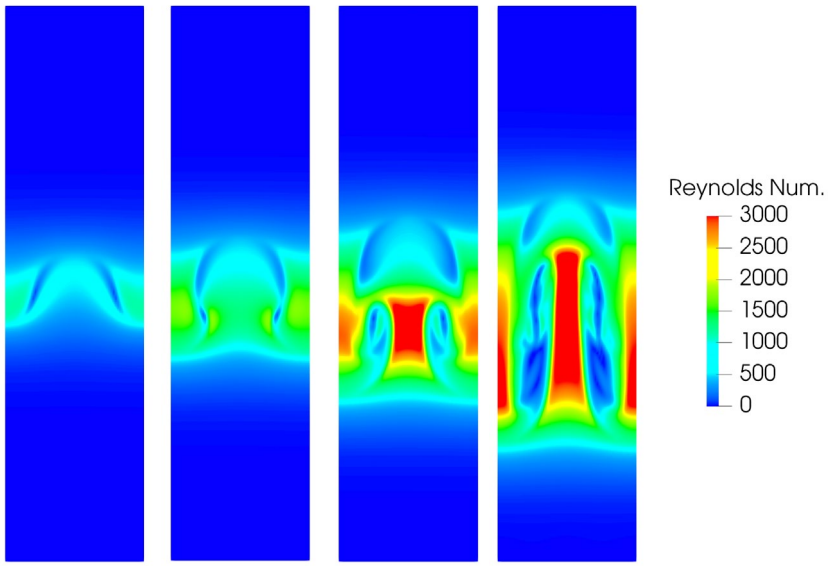

Fig. 2.31. Spatial distribution of instantaneous local Reynolds number for the Rayleigh-Taylor instability problem at 0.5, 0.7, 1.0 and 1.25 sec.

Additionally, in Fig. 2.32 we compare the interface shape on a given mesh of 64×256 elements using the regularized or the averaging method versus the proposed VMDC method with sharp fine-scale enrichment features at $t=1.0$ sec. We can see that the regularized method gives rise to artificial and erroneous interfaces within the lighter fluid.

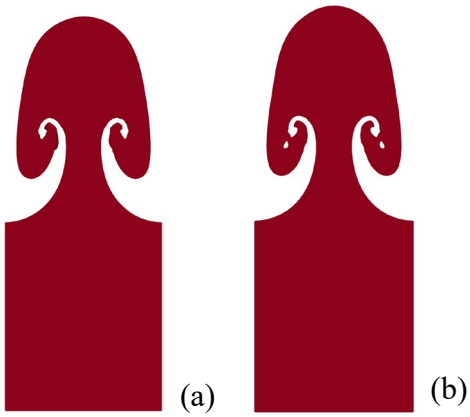

Fig. 2.32. Interface profile at t = 1.0 sec. for (a) the VMDC method and (b) the interface regularized method.

2.6 References

1. R.F. Ausas, C.B. Gustavo, R.I. Sergio, A new enrichment space for the treatment of discontinuous pressures in multi-fluid flows, International Journal for Numerical Methods in Fluids. 70 (2012) 829-850.

2. C. Basting, K. Dmitri, A minimization-based finite element formulation for interface-preserving level set reinitialization, Computing. 95 (2013) 13-25.

3. C. Basting, K. Dmitri, J.N. Shadid. Optimal control for reinitialization in finite element level set methods, International Journal for Numerical Methods in Fluids. 84 (2017) 292-305.

4. J.U. Brackbill, D.B. Kothe, C. Zemach, A continuum method for modeling surface tension, Journal of computational physics. 100 (1992) 335-354.

5. F. Brezzi, L.P. Franca, A. Russo, Further considerations on residual-free bubbles for advective-diffusive equations, Computer Methods in Applied Mechanics and Engineering. 166 (1998) 25-33.

6. E. Burman, D. Elfverson, P. Hansbo, M.G. Larson, and K. Larsson, Shape optimization using the cut finite element method. Computer Methods in Applied Mechanics and Engineering, 328 (2018) 242-261.

7. R. Calderer, A. Masud, Residual-based variational multiscale turbulence models for unstructured tetrahedral meshes, Computer Methods in Applied Mechanics and Engineering. 254 (2013) 238-253.

8. Y.C. Chang, T.Y. Hou, B. Merriman, S. Osher, A level set formulation of Eulerian interface capturing methods for incompressible fluid flows, Journal of computational Physics. 124 (1996) 449-464.

9. J, Chessa, T. Belytschko, An enriched finite element method and level sets for axisymmetric two-phase flow with surface tension, International Journal for Numerical Methods in Engineering. 58 (2003) 2041-2064.

10. R. Codina, A discontinuity-capturing crosswind-dissipation for the finite element solution of the convection-diffusion equation, Computer Methods in Applied Mechanics and Engineering. 110 (1993) 325-342.

11. A.H. Coppola-Owen, R. Codina, Improving Eulerian two-phase flow finite element approximation with discontinuous gradient pressure shape functions, International Journal for Numerical Methods in Fluids. 49 (2005) 1287-1304.

12. C. Farhat, I. Harari, L.P. Franca, The discontinuous enrichment method, Computer Methods in Applied Mechanics and Engineering. 190 (2001) 6455-6479.

13. S. Groß, A. Reusken, An extended pressure finite element space for two-phase incompressible flows with surface tension, Journal of Computational Physics. 224 (2007) 40-58.

14. N.G. Hadjiconstantinou, A.T. Patera. A variationally consistent finite element approach to the two-fluid internal contact-line problem, International Journal for Numerical Methods in Fluids. 34 (2000) 711-727.

15. T.J. Hughes, Multiscale phenomena: Green's functions, the Dirichlet-to-Neumann formulation, subgrid scale models, bubbles and the origins of stabilized methods. Computer Methods in Applied Mechanics and Engineering. 127 (1995) 387-401.

16. T.J. Hughes, G.R. Feijóo, L. Mazzei, and J.-B. Quincy. The variational multiscale method—a paradigm for computational mechanics. Computer Methods in Applied Mechanics and Engineering. 166 (1998) 3-24.

17. T.J. Hughes, L.P. Franca, A new finite element formulation for computational fluid dynamics: VII. The Stokes problem with various well-posed boundary conditions: symmetric formulations that converge for all velocity/pressure spaces. Computer Methods in Applied Mechanics and Engineering. 65 (1987) 85-96.

18. T.J. Hughes, L.P. Franca, G.M. Hulbert, A new finite element formulation for computational fluid dynamics: VIII. The Galerkin/least-squares method for advective-diffusive equations, Computer Methods in Applied Mechanics and Engineering. 73 (1989) 173-189.

19. T.J. Hughes, M. Mallet, A. Mizukami, A new finite element formulation for computational fluid dynamics: II. Beyond SUPG, Computer Methods in Applied Mechanics and Engineering. 54 (1986) 341-355.

20. S.R. Hysing, S. Turek, D. Kuzmin, N. Parolini, E. Burman, S. Ganesan, L. Tobiska, Quantitative benchmark computations of two-dimensional bubble dynamics, International Journal for Numerical Methods in Fluids. 60 (2009) 1259-1288.

21. K.E. Jansen, C.H. Whiting, G.M. Hulbert, A generalized-α method for integrating the filtered Navier–Stokes equations with a stabilized finite element method, Computer Methods in Applied Mechanics and Engineering. 190 (2000) 305-319.

22. H. Ji, Q. Zhang, A simple finite element method for Stokes flows with surface tension using unfitted meshes, International Journal for Numerical Methods in Fluids. 81 (2016) 87-103.

23. M. Khalloufi, Y. Mesri, R. Valette, E. Massoni, E. Hachem, High fidelity anisotropic adaptive variational multiscale method for multiphase flows with surface tension, Computer Methods in Applied Mechanics and Engineering. 307 (2016) 44-67.

24. R.J. Leveque, Z. Li, The immersed interface method for elliptic equations with discontinuous coefficients and singular sources, SIAM Journal on Numerical Analysis. 31 (1994) 1019-1044.

25. T. Lin, Y. Lin, X. Zhang, Partially penalized immersed finite element methods for elliptic interface problems, SIAM Journal on Numerical Analysis. 53 (2015) 1121-1144.

26. A. Masud, Preface, Computer Methods in Applied Mechanics and Engineering. 193 (2004), iii-iv.

27. A. Masud, L.P. Franca, A hierarchical multiscale framework for problems with multiscale source terms, Computer Methods in Applied Mechanics and Engineering. 197 (2008) 2692-2700.

28. A. Masud, R.A. Khurram, A multiscale/stabilized finite element method for the advection–diffusion equation, Computer Methods in Applied Mechanics and Engineering. 193 (2004) 1997-2018.

29. A. Masud, J. Kwack, A stabilized mixed finite element method for the first-order form of advection–diffusion equation, International Journal for Numerical Methods in Fluids 57 (2008) 1321-1348.

30. A. Masud, R. Calderer, A variational multiscale method for incompressible turbulent flows: Bubble functions and fine scale fields, Computer Methods in Applied Mechanics and Engineering. 200 (2011) 2577-2593.

31. A. Masud, Effects of mesh motion on the stability and convergence of ALE based formulations for moving boundary flows, Computational Mechanics. 38 (2006) 430-439.

32. S.E. Mousavi, J.E. Pask, N. Sukumar, Efficient adaptive integration of functions with sharp gradients and cusps in n-dimensional parallelepipeds, International Journal for Numerical Methods in Engineering. 91 (2012) 343-357.

33. L. Mu, J. Wang, G. Wei, X. Ye, S. Zhao, Weak Galerkin methods for second order elliptic interface problems, J. Comput. Phys. 250 (2013) 106–125.

34. M. Oevermann, R. Klein, M. Berger, J. Goodman, A projection method for two-phase incompressible flow with surface tension and sharp interface resolution, Konrad-Zuse-Zentrum für Informationstechnik, Berlin, ZIB-Report 00-17 (2000).

35. P.O. Persson, and J. Peraire, Sub-cell shock capturing for discontinuous Galerkin methods. 44th AIAA Aerospace Sciences Meeting and Exhibit, (2006) 112.

36. S. Quan, D.P. Schmidt, A moving mesh interface tracking method for 3D incompressible two-phase flows, Journal of Computational Physics. 221 (2007) 761-780.

37. F. Rispoli, A. Corsini, T.E. Tezduyar, Finite element computation of turbulent flows with the discontinuity-capturing directional dissipation (DCDD), Computers & Fluids. 36 (2007) 121-126.

38. H. Sauerland, T.P. Fries, The stable XFEM for two-phase flows, Computers & Fluids 87 (2013) 41-49.

39. S. Soghrati, A.M. Aragón, C.A. Duarte, P.H. Geubelle, An interface-enriched generalized FEM for problems with discontinuous gradient fields, International Journal for Numerical Methods in Engineering. 89 (2012) 991-1008.

40. Z. Tan, D.V. Le, K.M. Lim, B.C. Khoo, An immersed interface method for the incompressible Navier–Stokes equations with discontinuous viscosity across the interface, SIAM Journal on Scientific Computing. 31 (2009) 1798-1819.

41. T.E. Tezduyar, Y.J. Park, Discontinuity-capturing finite element formulations for nonlinear convection-diffusion-reaction equations, Computer Methods in Applied Mechanics and Engineering. 59 (1986) 307-325.

42. Z. Tuković, H. Jasak, A moving mesh finite volume interface tracking method for surface tension dominated interfacial fluid flow, Computers & Fluids. 55 (2012) 70-84.

43. J. Wang, X. Ye, A weak Galerkin finite element method for second-order elliptic problems, J. Comput. Appl. Math. 241 (2013) 103–115.

44. L. Zhang, A. Gerstenberger, X. W.K. Liu, Immersed finite element method, Computer Methods in Applied Mechanics and Engineering. 193 (2004) 2051-2067.

CHAPTER 3

A UNIFIED FORMULATION FOR COMPRESSIBLE INCOMPRESSIBLE MULTIPHASE FLOWS WITH CONVECTING INTERPHASE DISCONTINUITIES [b]

3.1 Motivation

Multiphase flows involving multiple fluid constituents that are governed by constituent specific balance laws and constitutive relations are invariably encountered in advanced engineering applications. Such problems are of great significance in micro-fluidics [11, 29, 31] as well as in biological fluid flows. In the design, processing, and manufacturing of modern engineered materials, multi-phase flows play a crucial role in evolving the material properties of the constituents as well as that of the final product. In injection molding of polymeric materials and in additive manufacturing with polymeric ink, chemical reactions that accompany these processes give rise to gaseous phase that results in the formation of bubbles. These bubbles evolve in shape and size till the time the liquid resin cures and jells into a solid phase. For these processes to be investigated in detail, robust numerical methods are required that can model the flow patterns and flow behaviors during the various manufacturing stages. These numerical methods also constitute the building blocks for simulation-based design of materials that can help in understanding the nonlinear instabilities [19, 40] that arise in complex flows.

[b] This Chapter has been adapted from "Al-Naseem, A. A., Masud, A. (2018). A Unified Formulation for Compressible Incompressible Multiphase Flows with Convecting Interphase Discontinuities." In Review.

A literature review reveals that most of the published work on multiphase flows has been limited to either incompressible two-phase flows or compressible two-phase flows. Among the methods that assume both the fluids to be incompressible include (i) Lagrangian methods [4, 16, 35, 18] that require mesh moving techniques to account for interface evolution, or (ii) meshfree methods such as the Smooth-Particle Hydrodynamics (SPH) methods [4, 16, 18] that allow for particle motion to accommodate the evolution of moving interfaces. The SPH methods have also been used to model the discontinuities in the Kelvin-Helmholtz instability by adding artificial viscosity terms [4, 18]. It has however been reported in the literature that artificial viscosity does alter the evolution of instability at the interface. Although both methods allow for sharp discontinuities in the material properties across the interfaces, they have invariably been presented in the context of either (i) two-phase compressible fluids or (ii) two-phase incompressible fluids. In these works the word multiphase refers to the use of different constitutive equations for the discretely represented constituents. A drawback in employing such schemes is that modeling gas and liquid phases as incompressible does not allow for volume change in the gaseous phase which is nonphysical and restricts hydrodynamic compression of gas bubbles. On the other hand modeling both phases as compressible requires an equation of state to impose the incompressibility condition in the liquid phase, else mass conservation would not be satisfied in the liquid subdomain. Relatively recently, the SPH methods have been extended to model combined compressible-incompressible flows in a unified way (ICSPH) [18] with weakly compressible SPH in the compressible phase while enforcing incompressibility in the liquid subdomain via a projection-based formulation. Although SPH method allows for complex motions of the interface due to the meshfree nature of the numerical scheme, the projection-based formulations for incompressible regions have been reported to suffer from inaccuracies and inconsistencies that are

not fully understood. Within the Finite Volume framework, various methods have been proposed [7] to address inter-constituent coupling in multiphase fluids that utilize the ghost fluid method (GFM). In GFM, each phase domain is extended across the interface into a ghost subdomain of the same fluid, and subsequently the solution of the subdomain is cut at the interface, thereby achieving a sharply discontinuous solution. Other methods employing discontinuous Galerkin formulations [30, 32] and multi-integrated moments [37, 38] have also been proposed in the literature.

A finite element method for unified compressible-incompressible system was introduced in [13, 14] and employed in [5, 12] for the modeling of two-phase flow of compressible gaseous phase interacting with an incompressible liquid phase. To account for the discontinuities in the viscosity and density across the phase boundaries and considering that density is no longer constant in the gaseous phase, we have developed the Variational Multiscale Discontinuity Capturing (VMDC) method [22]. In the current work we extend VMDC to multiphase flows and augment the formulation with a *div*-stabilization scheme that enforces element-wise incompressibility within the liquid phase while allowing for the compressibility effects in the gaseous phase as given by the corresponding equation of state. The VMDC method allows for sharp discontinuities in the pressure, velocity and density fields to be curtailed within the elements that are traversed by the interface, and without appearance of Gibbs phenomena or non-physical oscillations in the fields. This sharp DC capturing feature in our formulation [22] is in contrasts with other finite element methods that employ the unified compressible-incompressible formulation and assume a regularized variation of material properties and compressibility coefficients across the interface [5, 12]. The proposed method is then employed to study isothermal Kelvin-Helmholtz instability

to show the robustness of the new formulation and its applicability to outstanding fundamental problems of engineering interest.

The structure of this chapter is as follows: Section 3.2 presents the strong form of the unified compressible-incompressible formulation. It then presents the VMDC formulation to stabilize the mixed field problem and to account for the discontinuities in material properties and compressibility coefficients. Section 3.3 briefly discusses the level-set method and the reinitialization process employed to model interface evolution along with a global mass conservation algorithm for problems involving incompressible fluids alone. In Section 3.4 we present several numerical test cases involving shrinkage and compression of bubbles and model the isothermal Kelvin-Helmholtz instability. In addition, a 3D simulation of bubble migration and merging under buoyancy and surface tension effects is presented to show the applicability of the method to problems of engineering interest.

3.2 Compressible-Incompressible Navier-Stokes Equations

This section presents the Navier-Stokes equations with discontinuous material properties across the phase boundaries. Let $\Omega \subset \mathbb{R}^{n_{sd}}$ be an open bounded region consisting of two sub-regions Ω_1 and Ω_2 separated by an interface Γ_s such that $\Omega = \Omega_1 \bigcup \Omega_2$ and $\Omega_1 \bigcap \Omega_2 = 0$, with piecewise smooth boundaries $\partial\Omega_1$ and $\partial\Omega_2$ where $\partial\Omega = \left(\partial\Omega_1 \bigcup \partial\Omega_2\right) \setminus \Gamma$ that do not overlap $\left(\partial\Omega_1 \bigcap \partial\Omega_2\right) \setminus \Gamma = 0$. The phase interface is defined such that it does not necessarily conform to the element boundaries in the computational domain. The compressible Navier-Stokes equations for the conservation of mass and momentum including surface tension are:

$$\frac{\partial \rho_\chi}{\partial t} + \nabla \cdot (\rho_\chi \boldsymbol{v}) = 0 \qquad \text{in } \Omega \qquad (3.1)$$

$$\rho_\chi \frac{\partial \boldsymbol{v}}{\partial t} + \rho_\chi \nabla \cdot (\boldsymbol{v} \otimes \boldsymbol{v}) - \mu_\chi \Delta \boldsymbol{v} + \nabla p = \boldsymbol{f} \qquad \text{in } \Omega \qquad (3.2)$$

$$\left[p\boldsymbol{n} - 2\mu \boldsymbol{\varepsilon}(\boldsymbol{v})\boldsymbol{n} \right] = \delta \kappa \boldsymbol{n} \qquad \text{on } \Gamma_s \qquad (3.3)$$

where $\boldsymbol{v}$ is the velocity field, p is the pressure field and ρ_χ is the density which is piecewise continuous within each sub-region and discontinuous across the interface. μ_χ is the piecewise constant viscosity which varies sharply across the interface Γ_s, and the subscript $\chi = 1, 2$ corresponds to the two sub-regions, respectively. $\boldsymbol{f} = \rho \boldsymbol{b}$ is the body force is and the parameter δ is the surface tension coefficient. κ is the curvature of the interface between the phases at a point and $\boldsymbol{n}$ is the outward unit normal to the interface at that point. It is important to note that the surface tension term in (3.3) induces a jump in the pressure field that will need careful attention to develop a stable and convergent numerical method.

3.2.1 Unified Compressible-Incompressible Formulation

To develop a unified formulation, it is necessary to append to (3.1)-(3.3) an equation of state that defines the evolution of density as a function of pressure in the compressible sub-region of the domain Ω. We adopt the formulation in [13, 14] where the state equation is given as

$$\frac{d\rho_\chi}{dt} = \left. \frac{\partial \rho_\chi}{\partial p} \right|_T \frac{dp}{dt} \qquad (3.4)$$

Substituting (3.4) in (3.1) yields

$$\frac{1}{\rho_\chi} \left. \frac{\partial \rho_\chi}{\partial p} \right|_T \left(\frac{\partial p}{\partial t} + \boldsymbol{v} \cdot \nabla p \right) + \nabla \cdot \boldsymbol{v} = 0 \qquad (3.5)$$

which is an equation expressed in terms of the pressure field since density varies through dependence on pressure as given by the state equation. Equation (3.5) therefore constitutes the modified continuity equation where $\beta_p^\chi \equiv \frac{1}{\rho_\chi}\frac{\partial \rho_\chi}{\partial p}$ is defined as the isothermal compressibility coefficient. This leads to a unified continuity equation:

$$\beta_p^\chi \left(\frac{\partial p}{\partial t} + \boldsymbol{v} \cdot \nabla p \right) + \nabla \cdot \boldsymbol{v} = 0 \tag{3.7}$$

The value of the coefficients β_p^χ determines if the fluid is compressible $(\beta_p^\chi \neq 0)$ or incompressible $(\beta_p^\chi = 0)$. The sharp discontinuity in this coefficient across the phase boundaries can lead to instabilities in the pressure field that requires a stabilized discontinuity capturing method. In this work we employ the VMDC [22] method which is modified for the unified continuity equation.

The standard weak form that accommodates the jump induced by the surface tension given in (3.3) is written as:

$$(\boldsymbol{w}, \rho_\chi \boldsymbol{v}_t) + (\boldsymbol{w}, \rho_\chi \boldsymbol{v} \cdot \nabla \boldsymbol{v}) + (\nabla \boldsymbol{w}, \mu_\chi \nabla \boldsymbol{v}) - (\nabla \cdot \boldsymbol{w}, p) = (\boldsymbol{w}, \boldsymbol{f}) - (\boldsymbol{w}, \delta \kappa \boldsymbol{n})_\Gamma \tag{3.9}$$

$$(q, \beta_p^\chi p_t) + (q, \beta_p^\chi \boldsymbol{v} \cdot \nabla p) + (q, \nabla \cdot \boldsymbol{v}) = 0 \tag{3.10}$$

where $(\cdot,\cdot) = \int_\Omega (\cdot)\, d\Omega$ is the $L_2(\Omega)$ inner product where $\boldsymbol{w}$ is the weighting function for the velocity field, $\boldsymbol{v}_t = \partial \boldsymbol{v}/\partial t$ is the time derivative of the velocity field, q is the weighting function for the pressure field and $p_t = \partial p/\partial t$ is the time derivative of the pressure field. The last term on the right-hand side of (9) is an interfacial term that is defined along the interphase boundary and will be evaluated along the discretized interfaces in the elements that are traversed by the

interphase boundary. Linear approximation is adopted to model discrete interfaces within the element, namely, a line in 2D and a surface in 3D. Subsequently, a triangulation of the traversed element is performed to obtain the integration sub-cells that are then used to evaluate the discontinuous functions. This triangulation scheme is briefly presented in Section 3.2.4.

Remark: *The density is neither constant nor uniform within the compressible sub-domain and varies as a function of the pressure field. In this chapter the state equation used is the ideal gas law which is enforced locally. Accordingly, density is calculated point wise at each integration point using the relation* $\rho_{comp} = p/RT$, *where the universal gas constant is* $R = 287$, *and the reference temperature for the isothermal cases presented in the numerical section is* $T = 300$ *(i.e.* 27^o *C).*

3.2.2 The refined variational multiscale problem

In this section we employ the Variational Multiscale framework (VMS) [8, 23, 25, 26] to develop a stabilized formulation for the class of compressible-incompressible multiphase flows. These problems are amenable to Kelvin-Helmholtz instability induced because of velocity shear in a single fluid or due to velocity difference across the phase boundary Γ_s. Kelvin-Helmholtz instability is a global phenomenon and numerical methods proposed to model this physical instability tackle it at the global mesh level. These methods however introduce mesh dependent parameters [19, 40]. This chapter takes a fundamental departure from this line of thought and attempts to address the Kelvin-Helmholtz instability directly at the element level. Using the variationally consistent fine-scale modeling method that is facilitated by the VMS framework [24, 17], we extended [22] to stabilized methods with the provision for sharp internal layers across phase boundaries. Following along the developments in [22] we highlight the additional terms that

appear in the governing equations that permeate all through the variational framework, and subsequently appear in the fine-scale models. Accounting for these effects in the fine-scale fields and employing the notion of residual based stabilization directly over the sum of element interiors we derive a method that is stable and convergent. The VMDC stabilization also provides a means for the enforcement of interface conditions between the phase boundaries. Pressure is computed as a field variable in the incompressible domain where the density field remains constant. In the compressible region the evolving pressure dictates the evolution of density via the modified equation of state, as schematically shown in Fig. 3.1. The two equations of state that are operational across the phase boundary even within an element are triggered by the isothermal compressibility coefficient at the time of evaluation of element quantities via the sub-cell integration as discussed in section 3.2.4. In the SPH method on the other hand these conditions are imposed discretely along interphase boundaries [4, 18].

The VMDC method extended to the unified compressible-incompressible formulation provides a variational basis for interfacial coupling as well as interfacial stabilization. Consequently, sharp shifts in the governing system of PDEs [36, 15] from incompressible NSEs to compressible NSEs across the phase boundary along with sharp changes in the material coefficients of viscosity and density are addressed directly at the element level and without resorting to ad-hoc diffusive approximations of the interface.

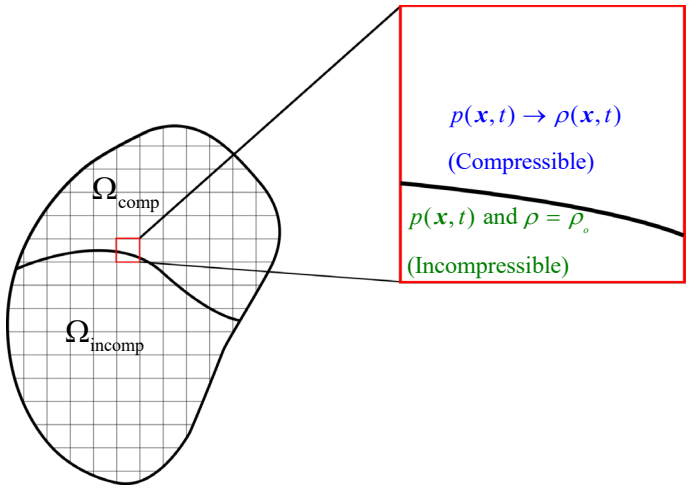

Fig. 3.1. Interphase boundary and density evolution in the compressible phase.

The velocity field and its corresponding weighting function is split into a coarse-scale and fine-scale as follows:

$$\boldsymbol{v}(\boldsymbol{x},t) = \bar{\boldsymbol{v}}(\boldsymbol{x},t) + \boldsymbol{v}'(\boldsymbol{x},t) \tag{3.11}$$

$$\boldsymbol{w}(\boldsymbol{x}) = \bar{\boldsymbol{w}}(\boldsymbol{x}) + \boldsymbol{w}'(\boldsymbol{x}) \tag{3.12}$$

In the nonlinear case this scale separation is to be viewed in the context of projections where $\bar{\boldsymbol{v}}(\boldsymbol{x},t) = \mathbb{P}\boldsymbol{v}(\boldsymbol{x},t)$ is the projection of the total solution on to the space of resolvable or computable scales $\bar{\mathcal{V}}$. The fine scales $\boldsymbol{v}'(\boldsymbol{x},t) \in \mathcal{V}' = \mathcal{V} \setminus \bar{\mathcal{V}}$ such that $\mathcal{V} = \bar{\mathcal{V}} \oplus \mathcal{V}'$ where $\bar{\mathcal{V}}$ and $\mathcal{V}'$ are L_2 orthogonal, and $\oplus$ is a direct sum decomposition on the admissible spaces of functions. We substitute (3.11) and (3.12) into (3.9) and (3.10) to yield two sub-problems for the unified multiphase formulation.

Coarse-scale sub-problem:

$$\begin{aligned}&\left(\rho\bar{\boldsymbol{w}},\bar{\boldsymbol{v}}_t\right) + \left(\rho\bar{\boldsymbol{w}},\boldsymbol{v}'_t\right) + \left(2\mu\nabla^s\bar{\boldsymbol{w}},\boldsymbol{\varepsilon}(\bar{\boldsymbol{v}}+\boldsymbol{v}')\right) - \left(\nabla\cdot\bar{\boldsymbol{w}},p\right) + \left(\bar{\boldsymbol{w}},\rho\left(\bar{\boldsymbol{v}}+\boldsymbol{v}'\right)\cdot\nabla\left(\bar{\boldsymbol{v}}+\boldsymbol{v}'\right)\right) \\ &= \left(\rho\bar{\boldsymbol{w}},\boldsymbol{b}\right) - \left(\bar{\boldsymbol{w}},\delta\kappa\boldsymbol{n}\right)_\Gamma\end{aligned} \tag{3.13}$$

$$(q,\beta_p p_t)+(q,\beta_p(\overline{\boldsymbol{v}}+\boldsymbol{v}')\cdot\nabla p)+(q,\nabla\cdot(\overline{\boldsymbol{v}}+\boldsymbol{v}'))=0 \tag{3.14}$$

Fine-scale sub-problem:

$$\begin{aligned}&\left(\rho\boldsymbol{w}',\overline{\boldsymbol{v}}_t\right)+\left(\rho\boldsymbol{w}',\boldsymbol{v}_t'\right)+\left(2\mu\nabla^s\boldsymbol{w}',\boldsymbol{\varepsilon}(\overline{\boldsymbol{v}}+\boldsymbol{v}')\right)-\left(\nabla\cdot\boldsymbol{w}',p\right)+\left(\boldsymbol{w}',\rho\left(\overline{\boldsymbol{v}}+\boldsymbol{v}'\right)\cdot\nabla\left(\overline{\boldsymbol{v}}+\boldsymbol{v}'\right)\right)\\&=\left(\rho\boldsymbol{w}',\boldsymbol{b}\right)-(\boldsymbol{w}',\delta\kappa\boldsymbol{n})_\Gamma\end{aligned} \tag{3.15}$$

where the density, viscosity and compressibility coefficient vary sharply as a function of the level-set field $\phi(\boldsymbol{x},t)$ which is defined as a singed-distance function.

$$\left.\begin{aligned}\rho&=\rho_1(1-\mathcal{H})+\rho_2\mathcal{H}\\\mu&=\mu_1(1-\mathcal{H})+\mu_2\mathcal{H}\\\beta_p&=\beta_p^1(1-\mathcal{H})+\beta_p^2\mathcal{H}\end{aligned}\right\} \tag{3.16}$$

and $\mathcal{H}(\phi)$ is the Heaviside function defined in terms of the level-set field $\phi(\boldsymbol{x},t)$ which is positive inside domain $\chi=1$ and negative in the second domain $\chi=2$.

$$\mathcal{H}(\phi)=\begin{cases}1 & \text{if } \phi\le 0\\0 & \text{if } \phi>0\end{cases}\qquad\qquad \phi(\boldsymbol{x})=\begin{cases}-d(\boldsymbol{x}) & \text{in } \chi=2\\d(\boldsymbol{x}) & \text{in } \chi=1\\0 & \text{on } \Gamma_s\end{cases} \tag{3.17}$$

We now turn to obtaining an analytical solution for the fine-scales by expanding the fine-scales via bubble functions that are non-zero within the element and zero on the element boundaries (i.e. $\boldsymbol{v}'=\boldsymbol{w}'=0$ on $\partial\Omega^e$). This choice localizes the discrete problem to a set of local problems over the sum of element interiors. Without loss of generality in this work we have used quadratic bubble functions though other admissible options can also be employed. Moreover, we employ the VMDC method [22] for enriching the bubble functions to capture the discontinuities in the velocity and pressure fields across the interphase boundaries. In the context of the unified compressible-incompressible formulation this allows the modeling of two fluids with significantly different state

equations that are activated via the discontinuous compressibility coefficients. The fine-scale velocity and corresponding weighting function are given as:

$$\boldsymbol{v}' = \boldsymbol{\beta} b^e \psi \tag{3.18}$$

$$\boldsymbol{w}' = \boldsymbol{\gamma} b^e \psi \tag{3.19}$$

where b^e is the element bubble function, while the enrichment function ψ is defined with the help of the signed distance field ϕ that is used to track the location of the interface. Therefore, the enrichment is given as $\psi(\phi) = |\phi|$ which allows for weak discontinuity in the velocity field and sharp discontinuity in the pressure field. Since the fine-scale problem (3.15) is time-dependent, its linearization yields a system of ordinary differential equations (ODEs) that requires an ODE integrator or time stepping method. Although one can use any appropriate time integrator for ODEs, we employ the generalized alpha method and substitute (3.18) and (3.19) into (3.15) to derive the fine-scale model.

$$\boldsymbol{v}'_{n+1}(\boldsymbol{x}) = b^e \psi \boldsymbol{\beta}_{n+1} = -b^e \psi \left\{ \frac{\alpha_m}{\gamma \Delta t} \left(b^e \psi, b^e \psi \right) + \alpha_f \hat{\boldsymbol{\tau}} \right\}^{-1} \left[\left(b^e \psi, \overline{\boldsymbol{r}}_{n+\alpha_f} \right) - \left(b^e \psi, \boldsymbol{r}_{ST} \right)_\Gamma \right] \tag{3.20}$$

where the residual vectors and stabilization tensor $\hat{\boldsymbol{\tau}}$ are defined as:

$$\begin{aligned}
&\overline{\boldsymbol{r}} \equiv \overline{\boldsymbol{v}}_t - 2\mu \nabla \cdot \boldsymbol{\varepsilon}(\overline{\boldsymbol{v}}) + \nabla p + \rho \overline{\boldsymbol{v}} \cdot \nabla \overline{\boldsymbol{v}} - \rho \boldsymbol{b} \\
&\boldsymbol{r}_{ST} \equiv \delta \kappa \boldsymbol{n} \\
&\hat{\boldsymbol{\tau}} \equiv \mu \int \left| \nabla \left(b^e \psi \right) \right|^2 d\Omega^e \boldsymbol{I} + \mu \int \nabla \left(b^e \psi \right) \otimes \nabla \left(b^e \psi \right) d\Omega^e + \int \left(b^e \psi \right)^2 \nabla^T \overline{\boldsymbol{v}} d\Omega^e \\
&\quad + \int \left(b^e \psi \right) \overline{\boldsymbol{v}} \cdot \psi \nabla b^e d\Omega^e + \int \left(b^e \psi \right) \overline{\boldsymbol{v}} \cdot b^e \nabla \psi d\Omega^e
\end{aligned} \tag{3.21}$$

In this work we have chosen to circumvent the fine-scale solution procedure and suffice with the presentation of the final form for the fine scales. Interested readers are referred to [22] for full derivation of the method.

Remark: *In [22] the surface tension force was transformed into a discontinuous volume force. In the present work surface tension is applied at the discretized interface which preserves this term in the fine-scale sub-problem. This introduces an interfacial stabilizing term in the representation of fine scales in the elements that are traversed by the interface.*

3.2.3 Embedding the Fine-Scale model into the Coarse-Scale formulation

Now we embed the fine scale solution (3.20) into (3.13) and (3.14) to obtain the stabilized coarse-scale formulation. The formal statement for the unified formulation of the Navier-Stokes equations with discontinuity capturing features is: Find $\boldsymbol{v}(\boldsymbol{x},t)$ and $p(\boldsymbol{x},t)$ such that for all $\boldsymbol{w}(\boldsymbol{x})$ and $q(\boldsymbol{x})$:

$$B_{Gal}^{Uni}\left(\left(\overline{\boldsymbol{w}},q\right),\left(\overline{\boldsymbol{v}},p\right)\right)+B_{VMDC}^{Uni}\left(\left(\overline{\boldsymbol{w}},q\right),\left(\overline{\boldsymbol{v}},p\right)\right)+B_{div}^{Uni}\left(\overline{\boldsymbol{w}},\overline{\boldsymbol{v}}\right)=F_{Gal}\left(\overline{\boldsymbol{w}}\right)+F_{ST}\left(\overline{\boldsymbol{w}}\right) \tag{3.22}$$

The Galerkin terms and body force are given as

$$\begin{aligned} B_{Gal}^{Uni}\left(\left(\overline{\boldsymbol{w}},q\right),\left(\overline{\boldsymbol{v}},p\right)\right)=&\left(\rho\overline{\boldsymbol{w}},\overline{\boldsymbol{v}}_t\right)+\left(\overline{\boldsymbol{w}},\rho\overline{\boldsymbol{v}}\cdot\nabla\overline{\boldsymbol{v}}\right)+\left(2\mu\nabla^s\overline{\boldsymbol{w}},\boldsymbol{\varepsilon}\left(\overline{\boldsymbol{v}}\right)\right)\\ &-\left(\nabla\cdot\overline{\boldsymbol{w}},p\right)+\left(q,\nabla\cdot\overline{\boldsymbol{v}}\right)+\left(q,\beta_p p_t\right)+\left(q,\beta_p\overline{\boldsymbol{v}}\cdot\nabla p\right)\end{aligned} \tag{3.23}$$

$$F_{Gal}\left(\overline{\boldsymbol{w}}\right)=\left(\overline{\boldsymbol{w}},\rho\boldsymbol{b}\right) \tag{3.24}$$

and the VMDC stabilization for the compressible-incompressible formulation is

$$B_{VMDC}^{Uni}\left(\left(\overline{\boldsymbol{w}},q\right),\left(\overline{\boldsymbol{v}},p\right)\right)=\begin{pmatrix}-\frac{\alpha_m}{\gamma\Delta t}\rho\overline{\boldsymbol{w}}+2\mu\nabla\cdot\boldsymbol{\varepsilon}\left(\overline{\boldsymbol{w}}\right)+\overline{\boldsymbol{v}}\cdot\nabla\overline{\boldsymbol{w}}+\overline{\boldsymbol{v}}\cdot\nabla^T\overline{\boldsymbol{w}}+\nabla q+\beta_p q\nabla p,\\ \boldsymbol{\tau}\left(\overline{\boldsymbol{v}}_t-2\mu\nabla\cdot\boldsymbol{\varepsilon}\left(\overline{\boldsymbol{v}}\right)+\nabla p+\rho\overline{\boldsymbol{v}}\cdot\nabla\overline{\boldsymbol{v}}-\rho\boldsymbol{b}\right)+\boldsymbol{\tau}_{ST}\left(b^e\psi,\delta\kappa\boldsymbol{n}\right)_\Gamma\end{pmatrix} \tag{3.25}$$

The stabilization tensors that are extracted from (3.20) are

$$\begin{aligned}\boldsymbol{\tau}&\equiv b^e\psi\left\{\frac{\alpha_m}{\gamma\Delta t}\left(b^e\psi,b^e\psi\right)+\alpha_f\hat{\boldsymbol{\tau}}\right\}^{-1}\left(b^e\psi,1\right)\\ \boldsymbol{\tau}_{ST}&\equiv b^e\psi\left\{\frac{\alpha_m}{\gamma\Delta t}\left(b^e\psi,b^e\psi\right)+\alpha_f\hat{\boldsymbol{\tau}}\right\}^{-1}\end{aligned} \tag{3.26}$$

The interface surface tension force is given as

$$F_{ST}\left(\overline{\boldsymbol{w}}\right)=-\left(\overline{\boldsymbol{w}},\delta\kappa\boldsymbol{n}\right)_\Gamma \tag{3.27}$$

In our previous work involving incompressible flows [22] we had added a *div*-stabilization term for the conservation of global mass in the incompressible fluid in order to help enforce element-wise incompressibility condition. However, with the unified compressible-incompressible formulation the residual of the continuity equation is no longer $\nabla\cdot\boldsymbol{v}$ and therefore we substitute the residual presented in (3.7) to enforce mass conservation in the locations that corresponds to the incompressible liquid phase and allow for volume change within the compressible gaseous region.

$$B_{div}^{Uni}\left(\overline{\boldsymbol{w}},\overline{\boldsymbol{v}}\right)=\left(\tau_c\nabla\cdot\overline{\boldsymbol{w}},\beta_p\left(p_t+\overline{\boldsymbol{v}}\cdot\nabla p\right)+\nabla\cdot\overline{\boldsymbol{v}}\right) \tag{3.28}$$

As in [22] the *div*-stabilization parameter τ_c is

$$\tau_c=\left(\tau_M\boldsymbol{G}\cdot\boldsymbol{G}\right)^{-1} \tag{3.29}$$

where $\boldsymbol{G}$ is defined in terms of the gradient of the mapping $\boldsymbol{G}=\partial_x\boldsymbol{\xi}^T\partial_x\boldsymbol{\xi}$ and τ_M is given as

$$\tau_M = \frac{1}{3}\,\mathrm{trace}(\boldsymbol{\tau}) \tag{3.30}$$

and $\boldsymbol{\tau}$ is given in (3.26a).

The system presented in (3.22) provides the variational formulation for the unified compressible-incompressible multi-phase fluids incorporating VMDC stabilization. This formulation accommodates equal order interpolation and is endowed with discontinuity capturing features.

3.2.4 Numerical Integration via Sub-cell Method

While evaluating integrals of discontinuous functions via adaptive quadrature [27] is adequate for 2D problems [22], the computational cost for 3D problems becomes exceedingly high because of the large number of integration points involved. For the application of the method in 3D, we utilize the integration sub-cell algorithm [20] in elements that are traversed by the interface along with discrete interface representation and tessellation of these elements. We present general ideas in the context of trilinear hexahedral element; however the method is not limited to this element type alone. This process is carried out in three steps. The first step is to utilize the nodal values of the level-set field $\phi(\boldsymbol{x},t)$ to identify the intersection points along each edge if the value of level-set at the two nodes sharing the edge differ in sign as given by the formula $x_{\text{int}} = x_1 - \frac{\phi_1(x_2 - x_1)}{(\phi_2 - \phi_1)}$. After all intersection points are identified a Delaunay tessellation is performed to generate sub-cells (triangles in 2D and tetrahedrons in 3D) where integration points are defined in terms of reference coordinates ξ, ζ and η. The weights of the integration points are then rescaled based on the volume ratio between the sub-cell and the hexahedron element. In addition, the intersection points are used to form a linear discrete representation of the interface (line in 2D and plane surface in

3D) which is also triangulated to generate corresponding integration points for surface integrations. This algorithm allows for the evaluation of the discontinuous integrals with significantly less integration points compared to the brute-force adaptive quadrature and does not require a tolerance criterion either. Hence, this algorithm is much more suited for larger simulations in 3D due to its cost effectiveness in terms of total number of integration points per tessellated element.

3.3 The Level-Set Method

To track the phase interface evolution, we employ the well-established level-set method [2, 3]. In the level-set method the interface is tracked via a signed distance field $\phi(\boldsymbol{x},t)$ that is transported through an advection equation.

$$\phi_t + \boldsymbol{v}\cdot\nabla\phi = 0 \tag{3.31}$$

where the velocity $\boldsymbol{v}$ is obtained from the solution of the Navier-Stokes equation presented in section 3.2. As a result of this choice, the transport velocity may be highly complex and thus a stabilization is required to obtain a non-oscillatory solution of the level-set equation. As presented in [22] we employ the VMS formulation along with the generalized alpha method for time discretization. The VMS stabilization induce time-dependent stabilization parameter τ that results in accurate non-diffusive stabilization. During the evolution of the interface, and due to the accumulation of numerical noise in the level-set field, this field may slowly deviate from its original signed distance definition. Therefore, a reinitialization process is periodically required during the simulation to retain the signed distance definition of the ϕ field which is achieved via an elliptic reinitialization step as presented in [2]. We refer readers who are interested in the VMS stabilization of the level-set equation to [22] and those interested in the elliptic reinitialization process to [2] for more information.

3.3.1 Mass Conservation Algorithm

The level-set equation given in (3.31) is a non-conservative advection equation that does not conserve the mass of the regions separated by the interface. Although the VMDC method was shown to have low mass loss error, even for complex interface flows [34], we employ a mass conservation algorithm to satisfy global mass for cases of incompressible flow in both regions**.** In these problems of the numerical section we employ the algorithm presented in [34] where a correction term $\phi_{corr}^{n+1} = (V_g^{int} - V_g^{n+1}) \big/ S^{n+1}$ is employed to shift the level-set field after the transport and reinitialization processes are performed for a time step. In this correction V_g^{int} is the initial volume of the gas phase at the beginning of the simulation, which is used as a reference for correction and V_g^{n+1} is the gas phase volume at the current step after the transport and reinitialization and S^{n+1} is the interface area of the current step. This correction is added to the level-set field before the time step is advanced $\phi_{New}^{n+1} = \phi_{uncorr}^{n+1} + \phi_{corr}^{n+1}$. This algorithm provides global mass conservation even under large interface deformations and bubble merging problems as presented in the numerical section.

3.4 Numerical Section

In this section we present 2D and 3D problems utilizing the unified compressible-incompressible formulation with and without surface tension. Three types of test cases are explored to analyze the mathematical attributes of stability and accuracy of the method: (i) mixed compressible-incompressible flows, (ii) incompressible flows of two immiscible fluids, and (iii) flow of compressible fluids. Another feature investigated in the numerical section is the cell-cutting method for sub-cell integration inside the elements that are traversed by the interface. This

method provides accurate integration of discontinuous functions in the variational formulation without resorting to an extensively high number of integration points nor to adaptive integration schemes that result in increased computational time.

An important technical issue that arises in the coupled modeling and analysis of compressible and incompressible fluids across a common interface is related to the difference in densities and density evolution of the two mediums as it affects the speed of sound in each medium. In addition, a second pronounced feature is that of compressibility across the interface. These features give rise to the well-known Kelvin-Helmholtz instability [19, 40]. Typical methods to solve this class of problems involve simplifying assumptions by considering either a compressible or an incompressible flow of the bilayer fluids that are undergoing shearing velocity at phase boundary.

The method developed in this chapter addresses this issue right at the element level via a variationally consistent fine-scale enrichment that couples two different PDEs across the interphase boundary even at the element level. It therefore provides a unique method to couple both compressible and incompressible fluids that exist in the traversed elements. We embed discontinuity in the fine scale shape functions and it gives rise to stabilization terms in (3.25). The bubble translation case presented in section 3.4.1 is employed to analyze the cut elements and to plot $\mathrm{tr}(\boldsymbol{\tau})$ for a generic element during the translation process. In problems 4.2 and 4.3 where air and water are modeled the corresponding isothermal compressibility coefficient used is $\beta_p^a = 9.8692327\times10^{-6}$ Pa^{-1} (in air) and $\beta_p^w = 0.444\times10^{-9}$ Pa^{-1} (in water). The VMDC method is extended to model 3D incompressible flows involving complex interface motion including translation and merging of bubbles. Finally, the Kelvin-Helmholtz instability problem which is significant in several applications and tracks physical instability in the fluid system is analyzed.

3.4.1 Bubble translation with periodic BCs

This section presents a numerical test case of a single bubble translating across a section of a pipe under a parabolic mean flow. Objective of this test case is to evaluate the proposed method with and without surface tension along the interface as it passes across the periodic boundaries. This would allow for the simulation of long term flow behavior and hydrodynamic and mass transfer characteristics of slug flow in pipes. These flows contain dispersed small bubbles that give rise to gas-liquid interfaces of different length scales [39, 21]. In these flows the unique aspects of the problem are primarily observed around the moving and deforming bubbles. Simulating such problems without the need for discretizing the entire length of the pipe significantly reduces the computational cost. The problem description shown in Fig. 3.2 is a biunit domain with periodic boundary conditions in the x-axis direction. A bubble of radius $R = 0.2$ is placed in the center of the domain at time t_o. The density inside the bubble is $\rho_b = 1$ and density in the surrounding liquid is $\rho_l = 1000$. The viscosity inside the bubble is $\mu_b = 0.1$ while in the surrounding medium is given as $\mu_l = 10$.

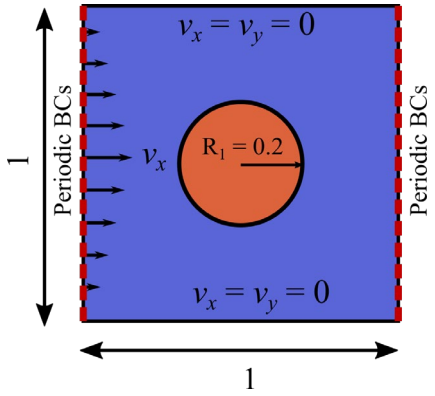

Fig. 3.2. Translating bubble: problem domain and boundary conditions.

The problem is modeled using three different mesh sizes 20^2, 40^2, and 80^2 where we track the migration of the bubble under a parabolic horizontal velocity profile applied at the inflow boundary with a maximum value of $v_x = 0.25$ at $y = 0.5$. The time step employed is $\Delta t = 0.05$ for all mesh sizes and the model is simulated until the bubble is approximately back to its initial position. This test is considered both with and without surface tension effects.

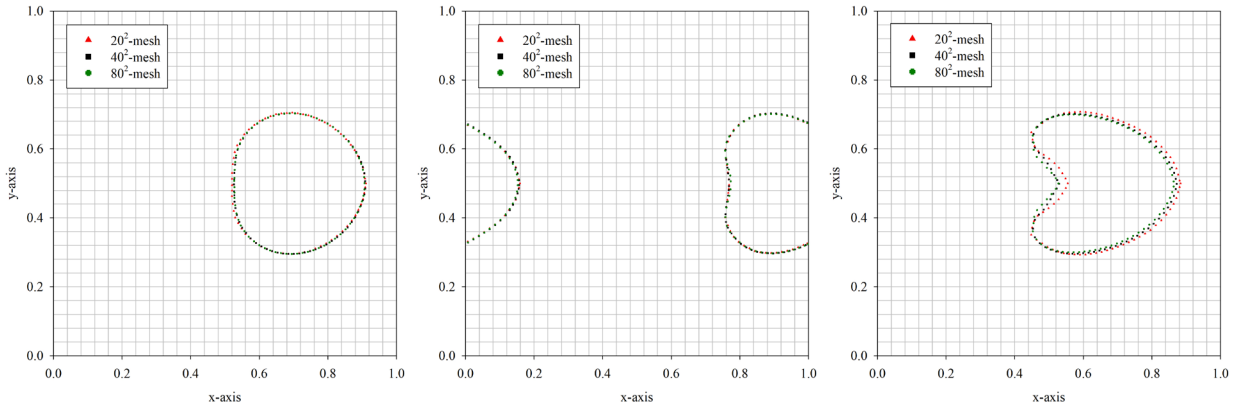

Fig. 3.3. Interface evolution without surface tension: (a) $t = 1.2$ (b) $t = 1.8$ and (c) $t = 3.0$

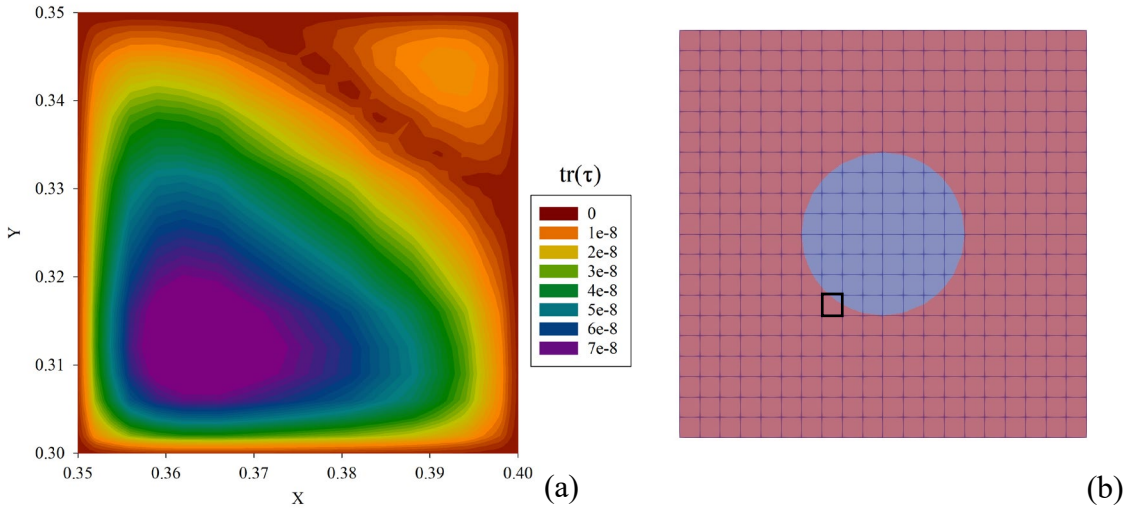

Fig. 3.4. The contour of (a) trace of stabilization tensor $\boldsymbol{\tau}$ within a single traversed element, and (b) the location of the plotted element that is highlighted with dashed line in the 20^2 mesh.

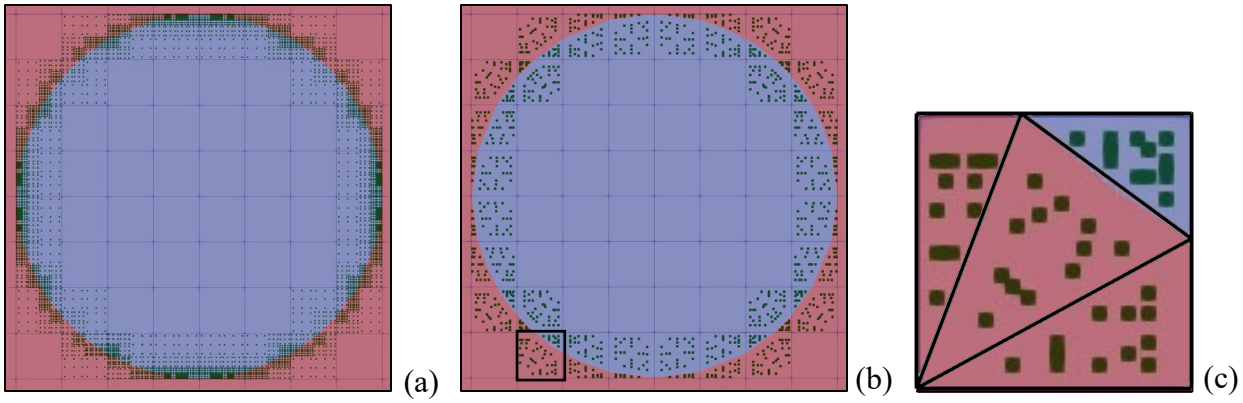

Fig. 3.5. Comparison of (a) adaptive integration and (b) sub-cell integration and (c) the triangulation of an element.

Fig. 3.3 shows the profiles of each mesh at different time steps where Fig. 3.3(b) presents a step during which the bubble is crossing the periodic boundary. Mass conservation in section 3.3.1 was not activated in this problem so as to assess the intrinsic mass conservation capability of the method as bubbles pass through the periodic boundary. After a cycle of translational flow, the bubble is deformed into the parabolic shape as that of the inflow velocity profile. The mass loss for each mesh is 4.26%, 2.02% and 0.81% for the meshes 20^2, 40^2, and 80^2 respectively. The convergence of the mass conservation to the original mass as the mesh is refined shows that the proposed method has a variational structure that helps achieve better conservation properties with refinement. In addition, in Fig. 3.4 we show a contour of the values of the trace of the stabilizing tensor and how it varies within a single element traversed by the interface. In Fig. 3.4(a) the effect of the enrichment is apparent through the skewed value of $\mathrm{tr}(\boldsymbol{\tau})$ such that each section of the intersected element accounts for the stability of a different fluid. A comparison is drawn in Fig. 3.5 showing the difference in density of integration points and hence computational cost between the adaptive integration algorithm [27] and the sub-cell integration technique [20] employed in the proposed method. As the former algorithm leads to an extensive number of integration points when

high accuracy is needed, the sub-cell technique produces approximately 99 % less integration points with comparable accuracy as shown in Table 3.1.

Table 3.1. Comparison of computational cost via integration points for two quadrature generation algorithms

Quadrature Method	Adaptive integration (ref. [27])	Dense Gaussian integration	Sub-cell integration (ref. [20])
Generation Algorithm	Compare 3-point Gauss rule with 8-point Gauss rule with octree subdivision	20-point Gauss rule for brick element	Triangulation of intersected elements
Tolerance of integration accuracy	1×10^{-6}	NA	NA
Resulting number of integration points	137589	8000	1560

In Fig. 3.6 we show the weak discontinuity in the pressure field for the case without surface tension while in Fig. 3.7 the pressure jump across the interface is shown due to surface tension effects with a coefficient of $\delta = 10$ captured sharply across a single element on both sides of the periodic boundary.

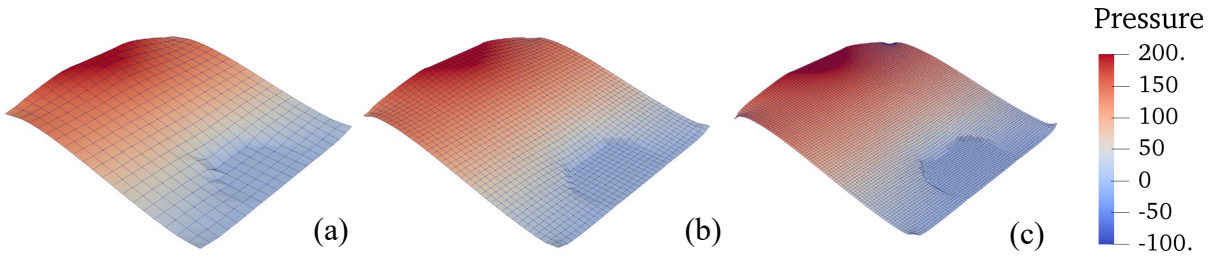

Fig. 3.6. Pressure profile at $t = 1.8$ for the meshes (a) 20^2, (b) 40^2 and (c) 80^2 (without surface tension).

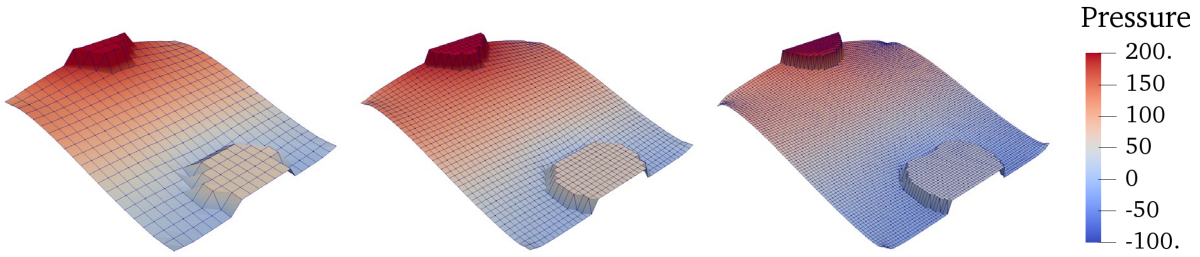

Fig. 3.7. Pressure profile at $t = 1.8$ for the meshes (a) 20^2, (b) 40^2 and (c) 80^2 (with surface tension).

3.4.2 Bubble shrinkage under applied pressure.

This problem presents the case of a uniformly shrinking air bubble because of the compressibility of the gaseous phases under high applied pressure. The problem is defined on a square domain of side length 0.1 m with an initial circular air bubble of radius $R = 0.03$ m with non-homogeneous inflow boundary conditions as shown in Fig. 3.8.

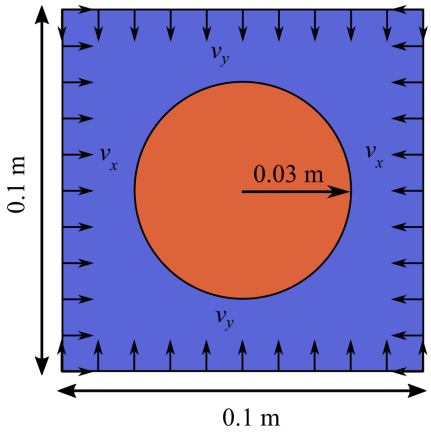

Fig. 3.8. Configuration and inflow conditions for the shrinkage problem.

The gaseous bubble is surrounded by water (considered incompressible) and is compressed uniformly form all directions with an inflow velocity of 0.0025 ms^{-1} prescribed along all the boundaries. The pressure is initially set equal to zero all through both domains and the density of water is held at a constant value of $\rho_w = 1000$ kgm^{-3}, while the initial density of the bubble is $\rho_a^0 = 1.1768$ kgm^{-3}. The density of the air bubble evolves following the ideal gas law $\rho_a^{n+1} = \rho_a^0 + p/rT$ where $r = 287$ is ideal gas constant, $T = 300$ is the ambient temperature, and p is the kinematic pressure. The problem is run using two mesh sizes 32^2 and 64^2 with a time step of $\Delta t = 0.01$ used for both the meshes. In Fig. 3.9 we show the evolution of the shape and volume of the bubble as it shrinks at different time levels on an underlying fixed mesh of 64^2 elements.

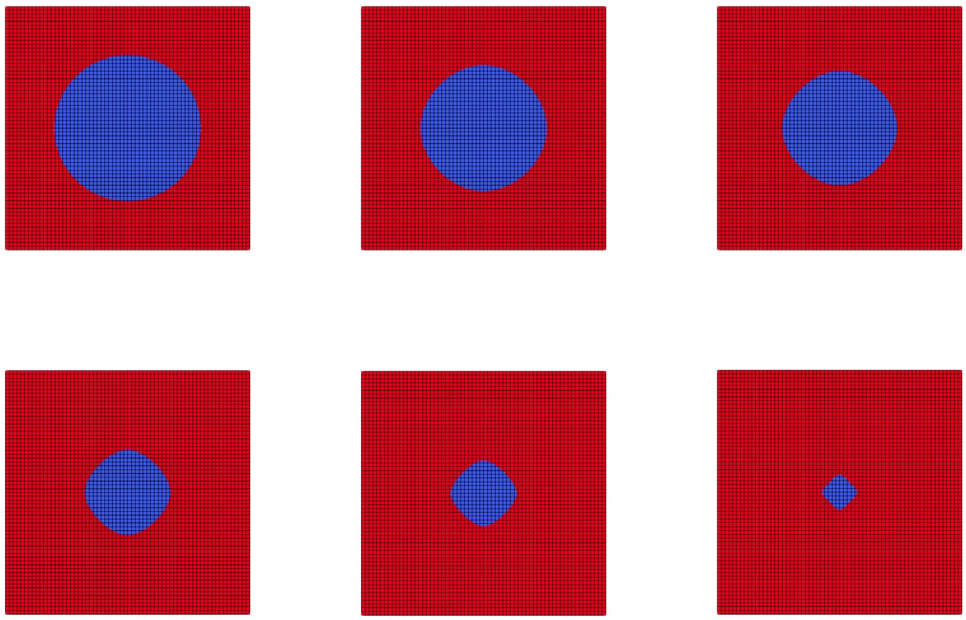

Fig. 3.9. Bubble shrinkage under external pressure field.

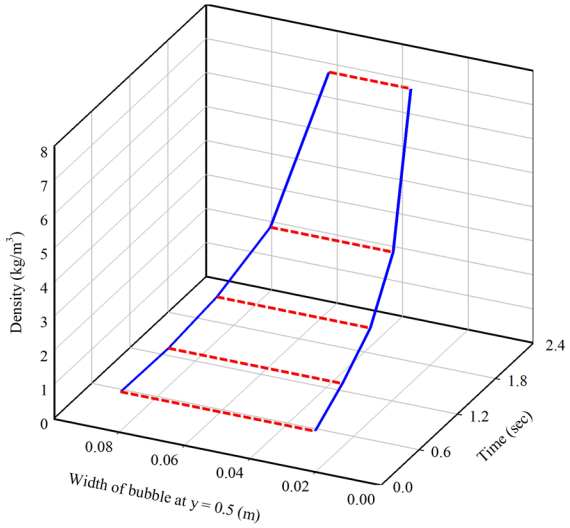

Fig. 3.10. Density and bubble width evolution at $y = 0.5$ over 5 different time steps as the bubble shrinks.

Due to the incompressibility of the water surrounding the bubble the water density does not evolve in time, however in Fig. 3.10 we track the density evolution within the bubble as evaluated via the ideal gas law at different time step. Fig. 3.10 shows the decrease of the bubble width as it shrinks over time represented by the dashed line, while the density increases as the volume of the bubble decreases as expected. This shows the incorporation of volume and density evolution at the same time due to the unified compressibility formulation. As the bubble shrinks, the pressure inside the cavity increases nonlinearly as shown in Fig. 3.11. The bubble density asymptotes to a very high value up to the collapses of the bubble at 2.82 sec. This value is determined via the analytical expression of the density given as $\rho_a^{exact}(t) = \rho_a^0 / (1 - \frac{0.001t}{\pi R^2})$. The corresponding exact pressure is calculated via the ideal gas law and hence we present a comparison of the present numerical method with the analytical pressure along with the numerical solutions of other methods in the literature in Fig. 3.11. The pressure evolution with two mesh sizes using the proposed method is shown to better capture the pressure evolution in comparison with [9, 12] where a finite volume framework is employed coupled with a conservative volume of fluid method to track the interface. The present method is also shown to converge to the analytical solution with mesh refinement as opposed to the remeshing technique presented in [12] which overestimates the pressure using an evolving mesh with 10,000 elements. Fig. 3.12 shows the optimal convergence of the error in the pressure field as the numerical domain is refined at a specific time step. Hence the method is shown to retain the variational convergence features even for such a nonlinearly evolving problem.

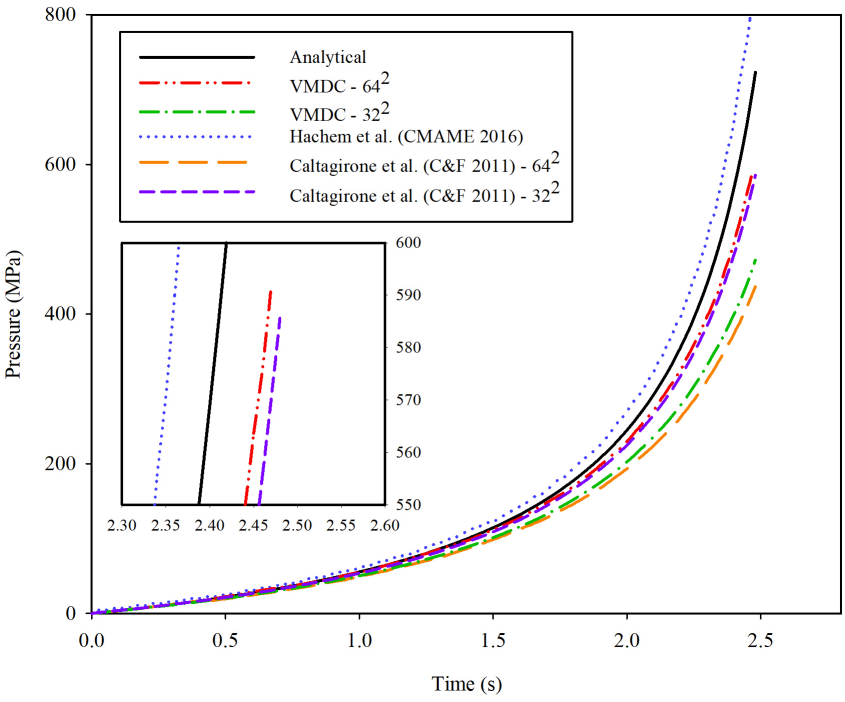

Fig. 3.11. Pressure evolution inside the bubble.

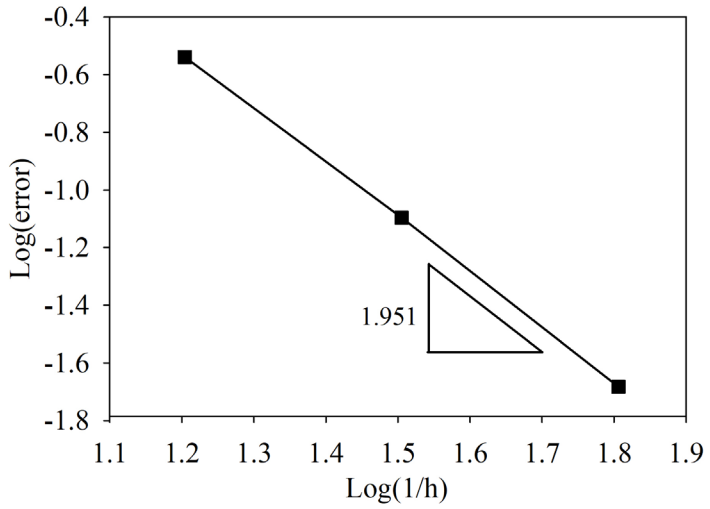

Fig. 3.12. L_2-norm of the pressure error at time step $t = 0.65$.

Remark: *It is important to not that the time step used in the present method is approximately 10 times coarser than that used in [9, 12] which indicates the cost effectiveness of the proposed numerical method.*

3.4.3 One-sided compression of bubble

This section models one-sided compression of an air bubble in a water cavity. The gaseous bubble has a radius of $r = 0.25$ and is contained within a closed square cavity with side length of 1m that is filled with water. The dotted boundaries in Fig. 3.13 represent the walls enclosing the cavity with slip boundary conditions, and the inlet is shown to be on the left side at $0.25 \le y \le 0.75$. The inflow velocity along this open region is given as $v_x(x=0,t) = -(y^2 - y + \frac{3}{16})\ 100t$ which leads to an analytical volume reduction of the bubble given by $V_a(t) = \frac{\pi}{16} - \frac{100t^2}{96}$. The time step used is $\Delta t = 0.01$ sec. for two mesh sizes of 50^2 and 100^2. The pressure in the domain is set to an initial value of $p(t=0) = 10^5$. The effect of gravity is ignored, so the pressure grows uniformly in the surrounding liquid.

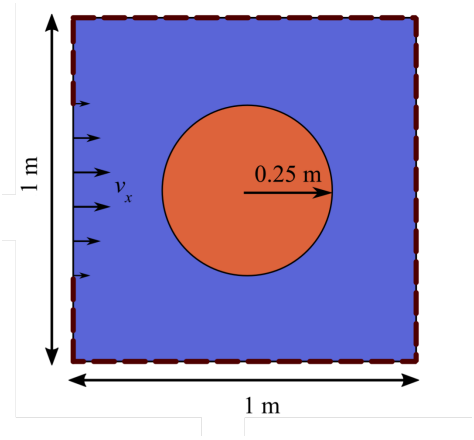

Fig. 3.13. Configuration and inflow conditions for one-sided compression problem.

In Fig. 3.14(a) and Fig. 3.15(a) we show the level-set field corresponding to the shape of the bubble at different two different time steps on top of the velocity magnitude profile. Fig. 3.14(b) and Fig. 3.15(b), show the velocity contour on the profile. As a virtue of the discontinuity capturing feature of the formulation, the velocity is shown to have a weak discontinuity across the single layer of elements that are traversed by the interface. A volume evolution obtained via the present method is compared in Fig. 3.16 with the analytical solution and other numerical method [5, 12]. In both 50^2 and 100^2 meshes the present method is shown to better capture the volume evolution in comparison to where the present method employs a sharp discontinuity of the compressibility coefficients and material properties instead of the regularization technique employed in [5, 12]. In Fig. 3.17 we present the shape evolution of the bubble as it is compressed at successive time steps. Fig. 3.18 shows the spatial and temporal evolution of the divergence of the velocity field, which is an indicator for the compressibility of the fluid. As the bubble is compressed, the divergence of velocity within the bubble increases while the $\nabla \cdot \boldsymbol{v} \approx 0$ is consistently maintained within the surrounding incompressible medium. In addition, this sharp difference is shown to be independent of the mesh as it is not evolved to capture such discontinuity in the flow.

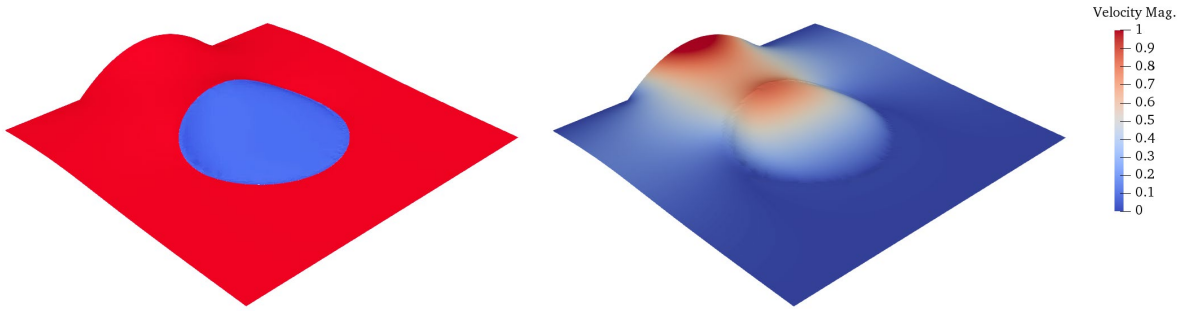

(a) (b)

Fig. 3.14. Warped magnitude of the velocity field at $t = 0.16$ sec: (a) Shape of the level-set, and (b) Contour of velocity magnitude.

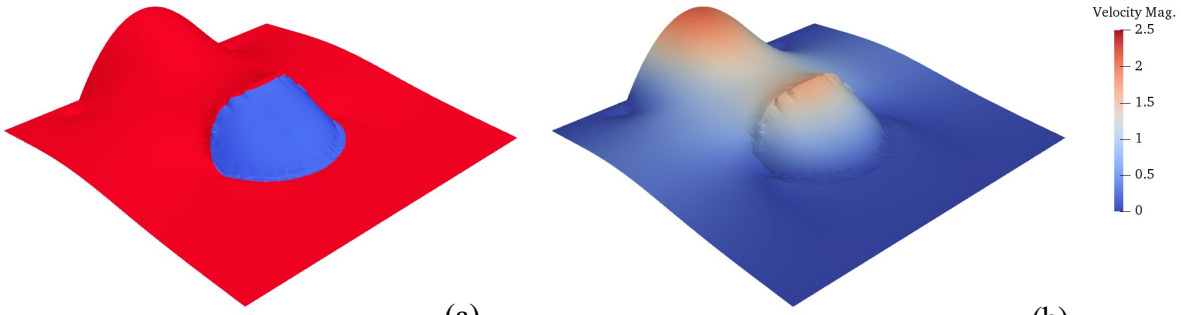

Fig. 3.15. Warped magnitude of the velocity field at $t = 0.33$ sec: (a) Shape of the level-set, and (b) Contour of velocity magnitude.

Remark: *The mesh used in this problem is a fixed mesh. The enhanced accuracy in the calculation of the volume as a function of time is primarily due to the capability of the variational discontinuity capturing method to accurately model the jumps within one element. Moreover, the adaptive mesh evolving technique used in [12] employs two meshes, a coarse mesh with 3579 elements and a fine mesh with 12,548 elements.*

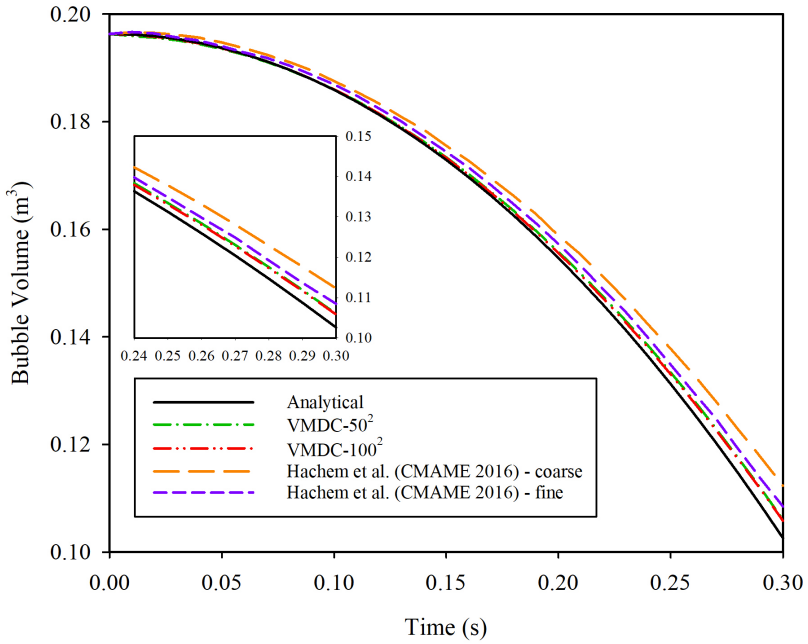

Fig. 3.16. Comparison of the volume reduction with the analytical solution and other numerical methods.

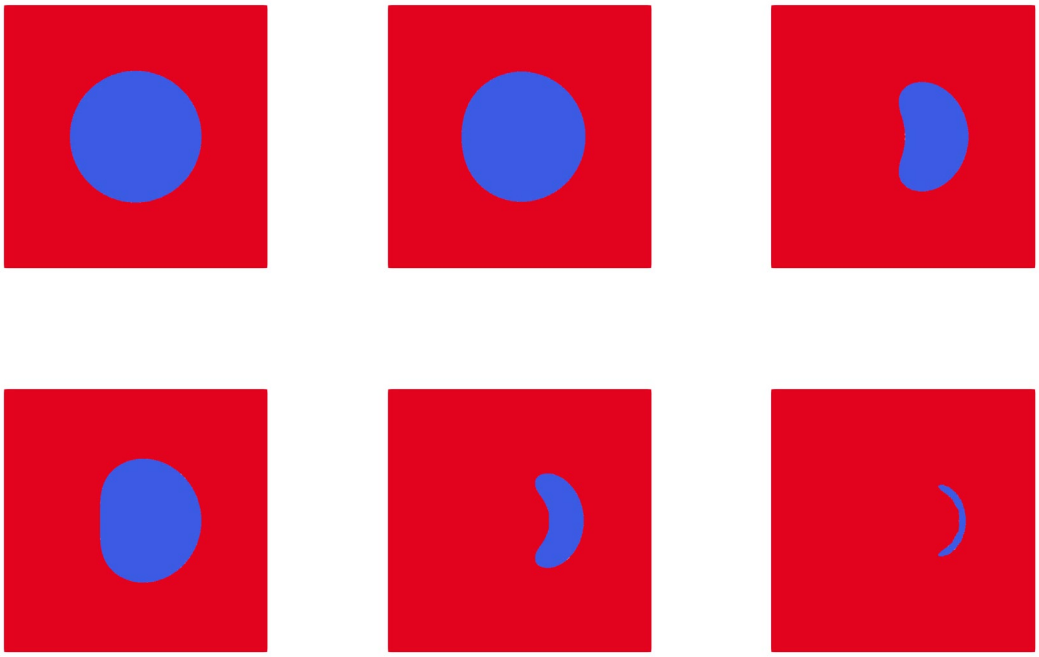

Fig. 3.17. Evolution of the interface at different times.

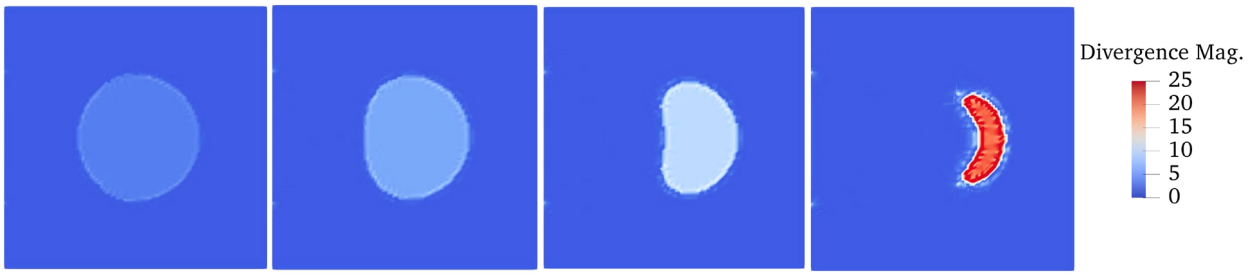

Fig. 3.18. Magnitude of the divergence of velocity field.

3.4.4 Merging of 3D bubbles with surface tension

Merging of convecting bubbles poses a challenge for numerical methods due to the intricacy of the interface evolution during the merging process [1, 10]. In this section we present a case of merging of two misaligned air bubbles with surface tension effects that are being convected due to buoyancy effects. The problem is modeled employing the unified formulation with a value of zero for the isothermal compressibility coefficient in both phases. This reduces the unified formulation to an incompressible two-constituent form so that we can compare our computed results with published data under same modeling assumptions as that in the literature. This problem is important in validating the robustness of the method for modeling complex motion of the interface. Two spherical bubbles of same volume ($R = 0.5$) are slightly misaligned where the lower bubble is centered at $(x = 1.5, y = 1.5, z = 1.0)$ and upper bubble at $(x = 1.5, y = 1.75, z = 2.25)$ in a domain of $\Omega = [0, L] \times [0, L] \times [0, \frac{4}{3} L]$ where $L = 3$. The top boundary is modeled as an outflow boundary while all other boundaries of the domain are defined as non-penetration boundaries. The two bubbles constitute one phase and have same density and viscosity which is given as ($\rho_b = 0.04$ kg/m^3 , $\mu_b = 0.005$ kg/ms). The surrounding medium is the second constituent that has different values of density and viscosity (

$\rho_m = 1.0$ kg/m^3, $\mu_m = 0.1$ kg/ms). Bubbles rise because of buoyancy effects and gravity driving this problem is chosen as $g = 10$ ms^{-1} which is applied in the z-direction. The surface tension coefficient is selected $\delta = 0.2$. The mesh employed for this problem is comprised of $30 \times 30 \times 40$ hexahedral elements with a constant time step of $\Delta t = 0.001$. A literature review reveals that qualitative comparison of interface shape evolution has been employed as a measure for validating the method [1, 10]. Figure 3.19 presents the interface for different time steps which is in close agreement with the shape of the interface reported in [1].

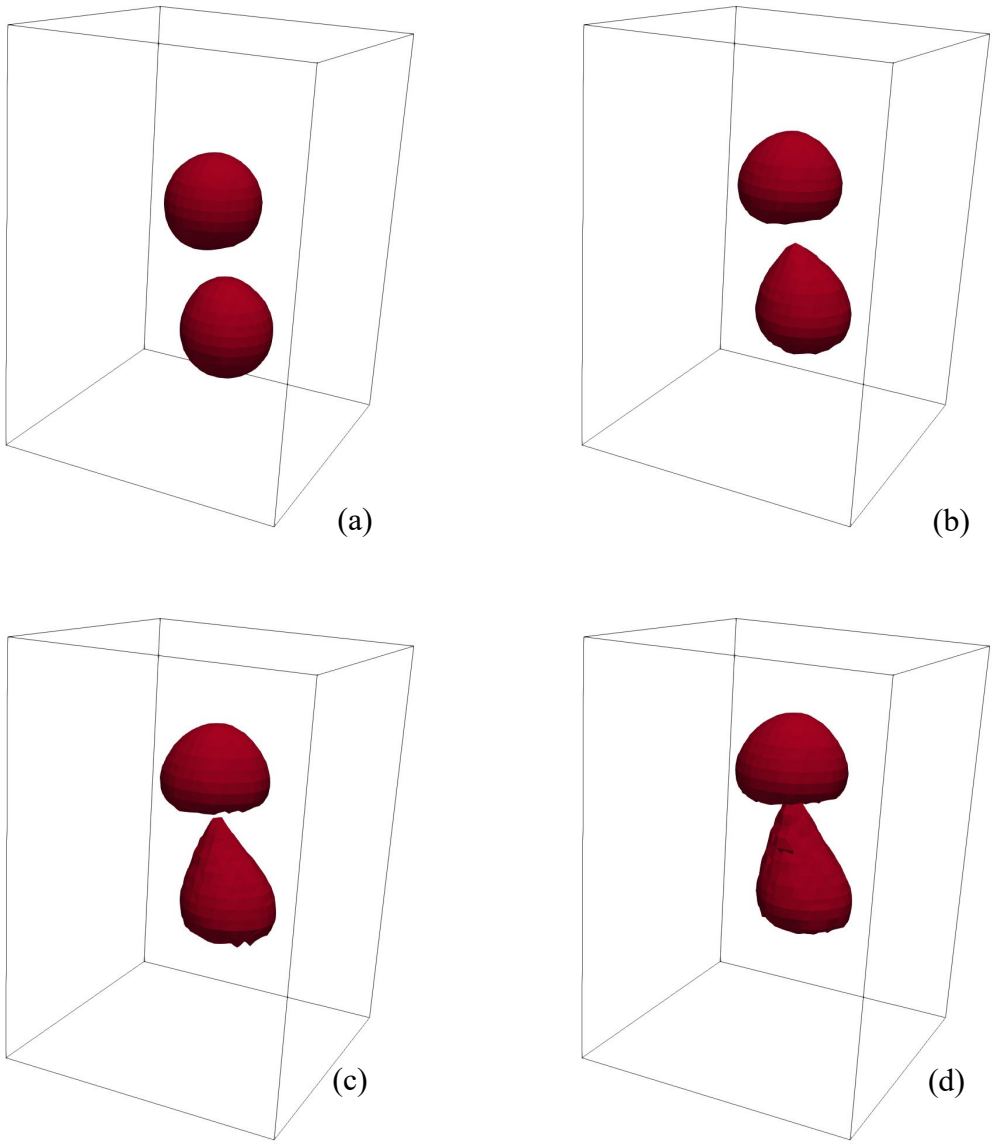

Fig. 3.19. Shape of the interface at different time levels: (a) $t = 0.125s$, (b) $t = 0.25s$, (c) $t = 0.35s$, and (d) $t = 0.4s$.

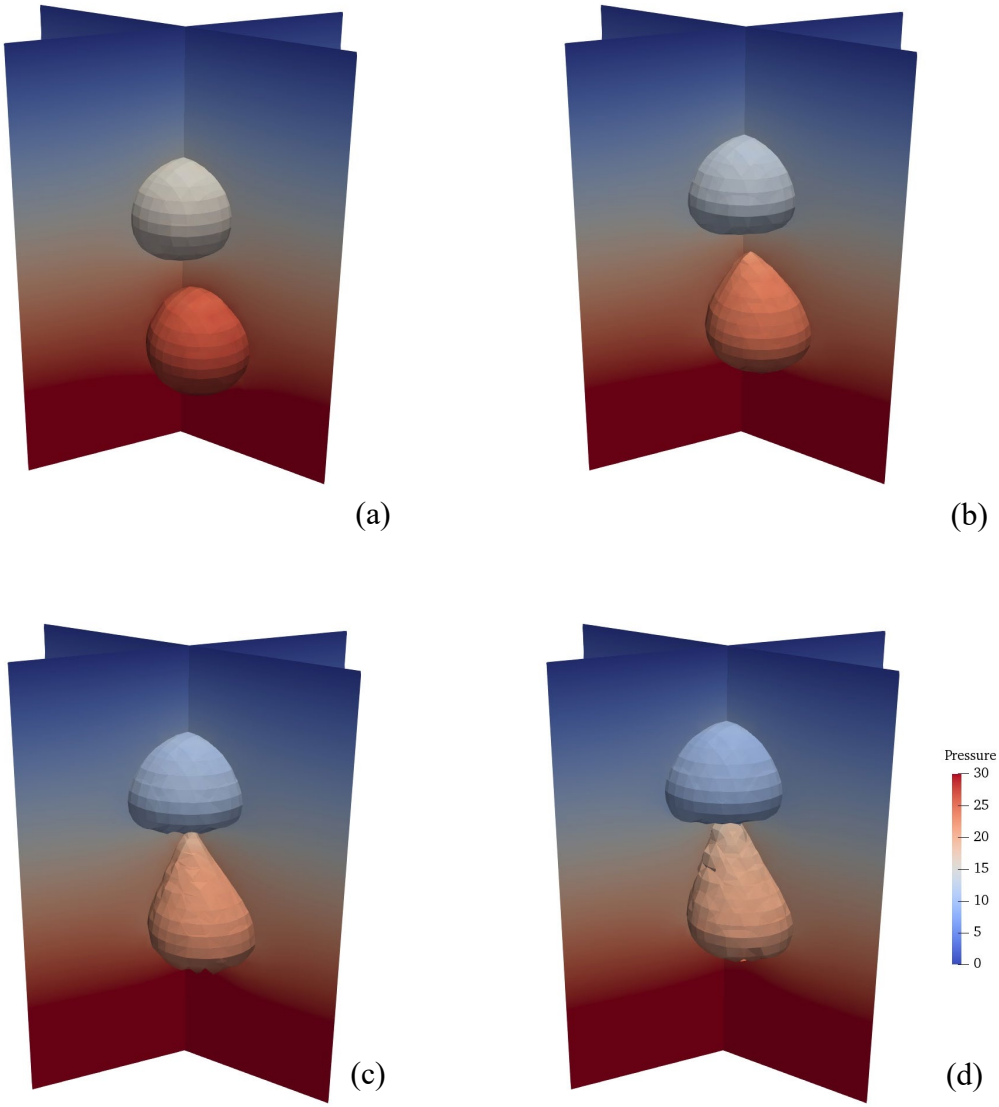

Fig. 3.20. Pressure profile at different time levels: (a) $t = 0.125s$, (b) $t = 0.25s$, (c) $t = 0.35s$, and (d) $t = 0.4s$.

Figure 3.20 shows pressure profile at different time levels with pressure field projected on the surface of the bubbles along with cross sectional view of the pressure field in the surrounding fluid. Figure 3.21 provides internal view of the pressure profile at multiple cut planes along the three axes for two different time levels. The pressure discontinuity that arises due to surface tension effects is captured within a single layer of elements in all spatial directions and for the two time

points. These figures show the robustness of the method in accurately capturing the discontinuities within a single layer of elements in higher dimensions.

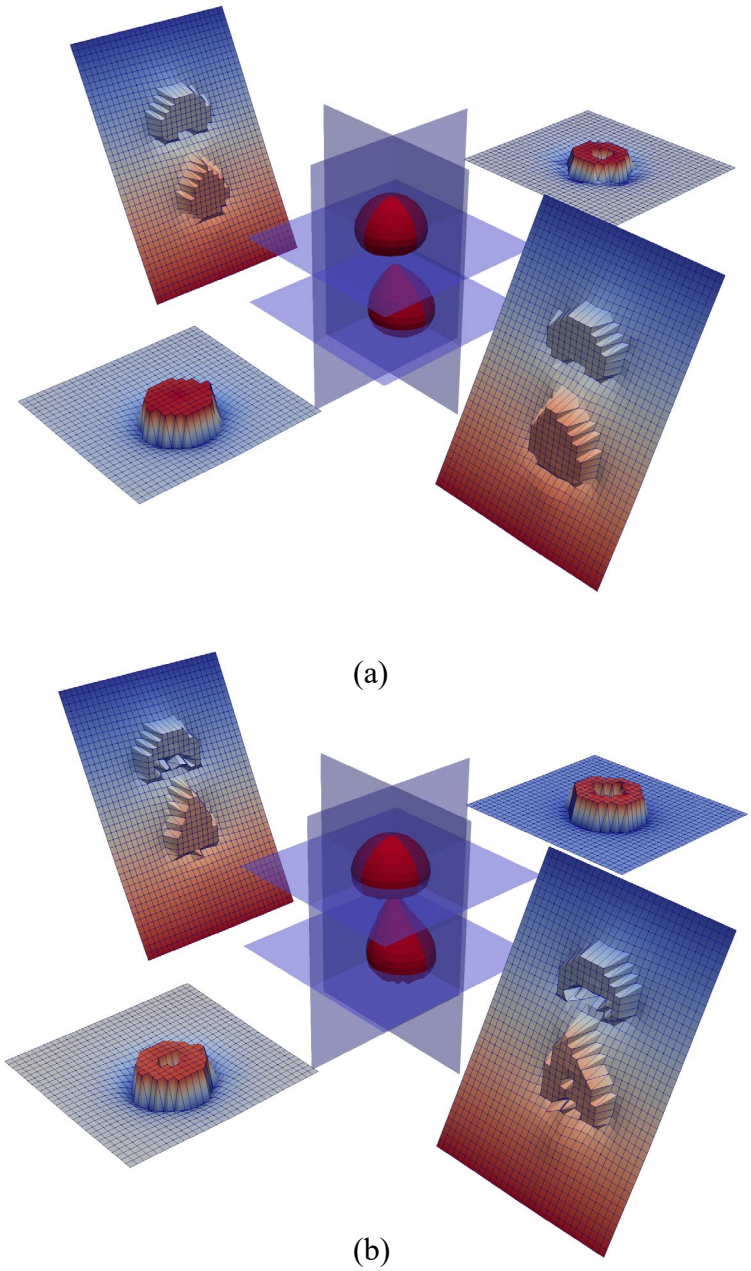

(a)

(b)

Fig. 3.21. Pressure profiles along multiple cut planes in the 3D domain at time levels: (a) $t = 0.25s$, (b) $t = 0.35s$.

Remark: *It is notable to specify that the current method allows for the reduction of the number of elements compare to previously presented methods in [1, 10]. This is apparent as we use a coarse mesh with nearly 5 % the number of elements used for the same problem in [1].*

3.4.5 Kelvin-Helmholtz Instability

In this section we present coupled compressible-incompressible flow that gives rise to the well-known Kelvin-Helmholtz instability. This instability arises due to shearing velocity across the interface between the two fluids that have discontinuous material properties and different governing equations for each constituent. The biunit domain $\Omega = [0,1]\times[0,1]$ is divided into a middle strip that lies between $0.25 < y < 0.75$ and is comprised of a denser incompressible fluid that is flowing with a uniform initial velocity in the *x*-direction of magnitude $v_x = -0.5$. On either side of this middle strip $(0 < y \le 0.25,\ 0.75 \le y < 1)$ lies the lighter compressible fluid which is initialized with a uniform velocity in the opposite direction, i.e., $v_x = 0.5$. The instability at the interface is initiated via a perturbation to the velocity in the *y*-direction given as:

$$v_y = \delta v \sin(2\pi x/\lambda) \times \begin{cases} e^{-|y-0.25|} & 0 \le y < 0.5 \\ e^{-|(1-y)-0.25|} & 0.5 \le y \le 1.0 \end{cases} \tag{32}$$

where the perturbation amplitude is $\delta v = 0.025$ and the wavelength is $\lambda = 1/6$. The density in the incompressible domain is set equal to $\rho_1 = 2$ and the density in the compressible domain is $\rho_2 = 1$. This 2:1 ratio in density has been chosen to allow for the instability to evolve into a vortex as high ratios have been shown to suppress such an evolution of the disturbance [33]. The viscosity for both fluids has been chosen to be $\mu = 0.0005$ to reduce the role of viscosity in the suppression of

instability. The Eulerian computational domains consists of 200^2 and 400^2 elements with a time step of $\Delta t = 0.0125$.

Fig. 3.22 shows interface evolution for various time points during the initial stage with an apparent evolution of the interface that grows into vortices along the interface. These figures show the evolution of the instability in the full nonlinear regime and the rolling vortices can clearly be seen. The proposed VMDC method embedded with stabilized terms for multiphase flows together with level-set based capturing of the interface successfully captures the evolving instabilities all through the nonlinear regime. The corresponding vorticity is shown in Fig. 3.23 where the magnitude and vortex formation are also shown to evolve with time. To examine the evolution of the instability during the initial stages a comparison with the linear stability theory is presented in Fig. 3.24. Within the range from $t = 0$ to $t = 0.15$ the evolution of interfacial disturbance follows the trend given by the linear stability theory. Furthermore, in the linear regime the error stays curtailed within the element characteristic length $h = 1/\Delta x$. However, as noted in reference [18] departure from the linear instability theory is expected as the instability evolves further into the nonlinear regime.

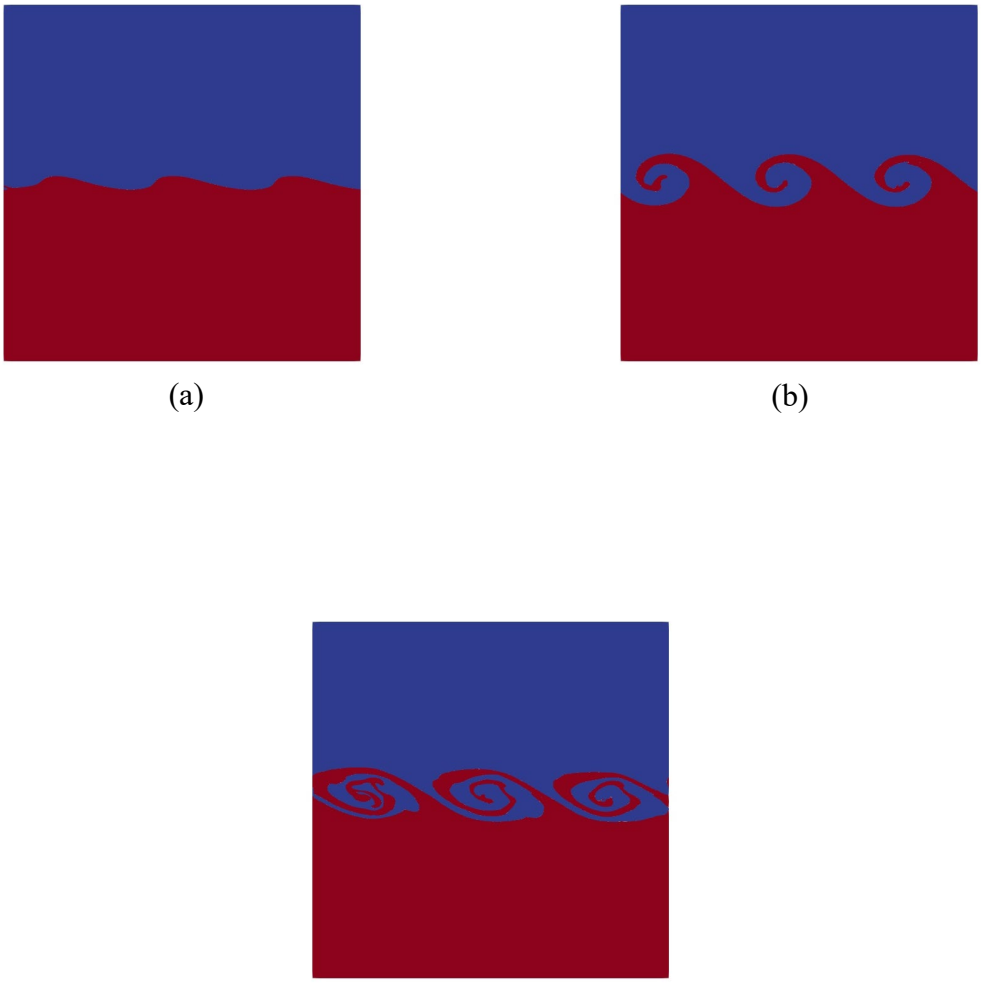

(a) (b)

(c)

Fig. 3.22. Interface evolution at different time steps: (a) $t = 0.5s$, (b) $t = 1.0s$, and (c) $t = 1.5s$.

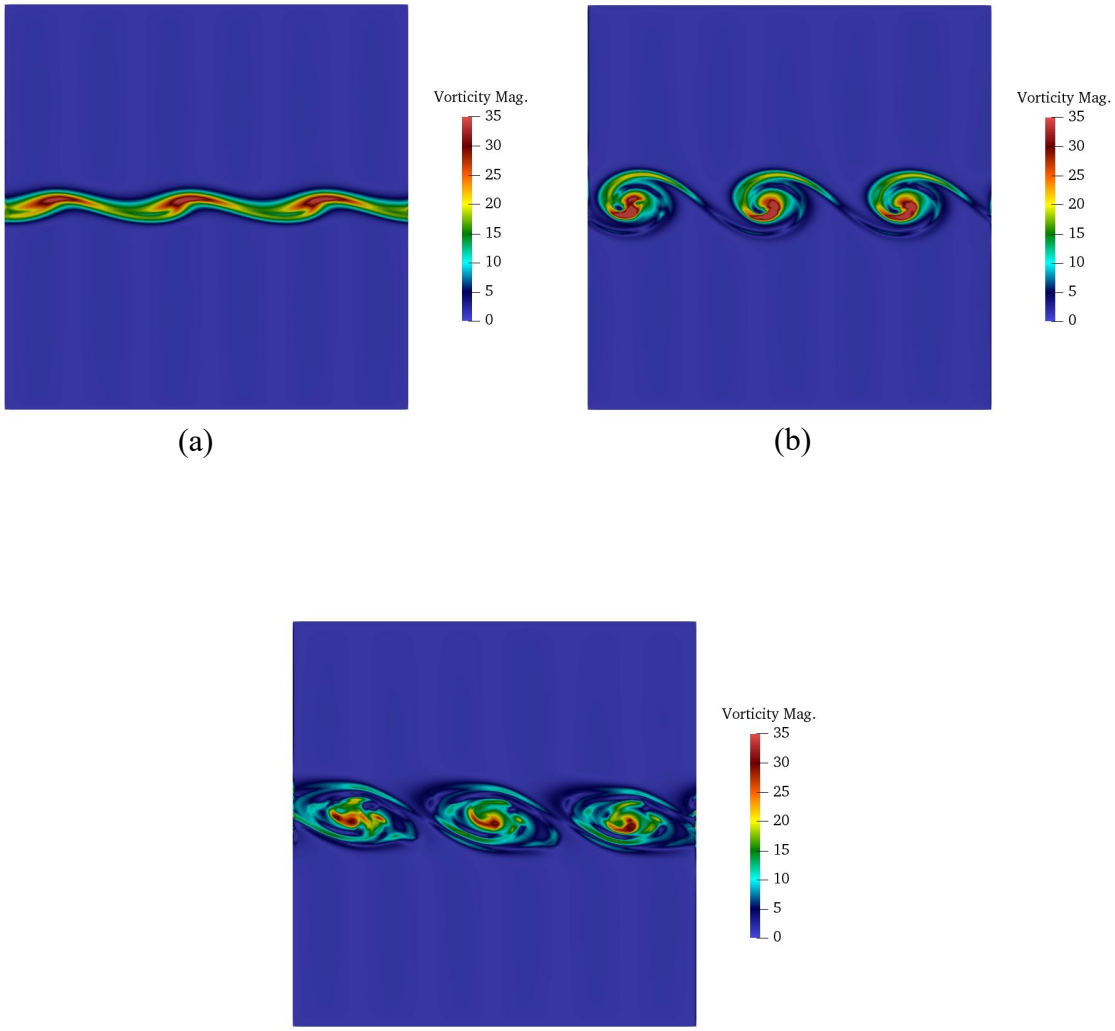

Fig. 3.23. Vorticity magnitude at different time steps: (a) $t = 0.5s$, (b) $t = 1.0s$, and (c) $t = 1.5s$.

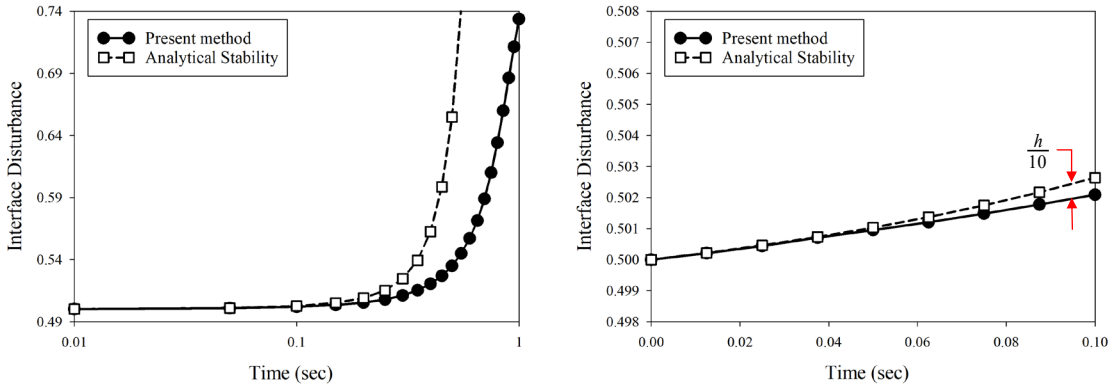

Fig. 3.24. Interface disturbance evolution comparison with analytical stability estimate.

In Fig. 3.25 at three different time steps we show local Reynolds number with pointwise variation and jumps across the interface. In Fig. 3.25(a)-(c) we see the evolution of the jump of the Reynolds number across the interface with sharp jumps captured with single elements via the proposed method. In Fig. 3.25(d) the profile jumps are shown at the interface despite the relatively high variation and complex interface structure.

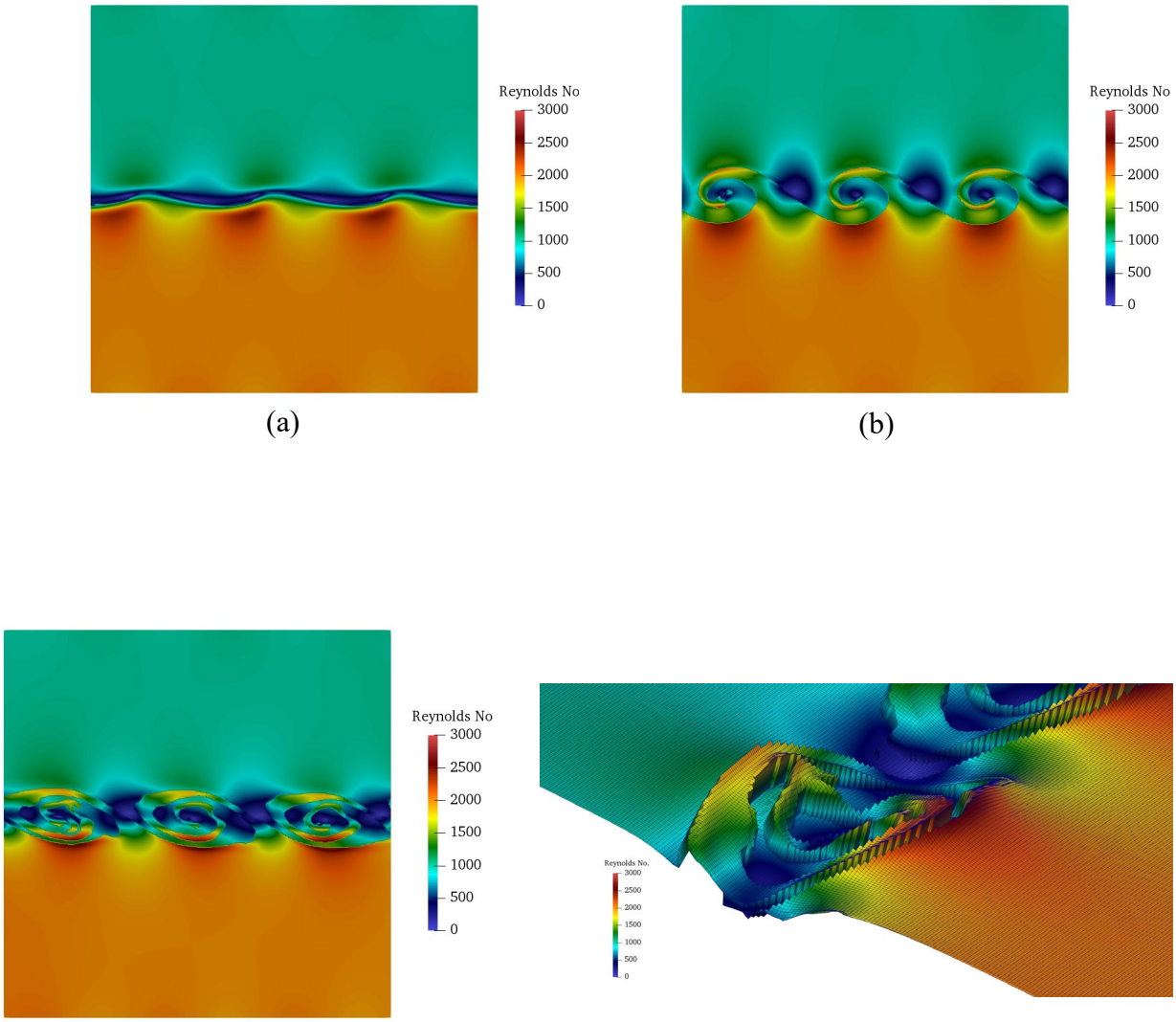

Fig. 3.25. Local Reynolds Number evolution across the domain at different time steps: (a) $t = 0.5s$, (b) $t = 1.0s$, and (c) $t = 1.5s$ and a close-up of the warped Reynolds number in (d) at $t = 1.5s$.

3.5 References

1. Ausas, R. F., Sousa, F. S., & Buscaglia, G. C. (2010). An improved finite element space for discontinuous pressures. Computer Methods in Applied Mechanics and Engineering, 199(17-20), 1019-1031.

2. Basting, C., & Kuzmin, D. (2013). A minimization-based finite element formulation for interface-preserving level set reinitialization. Computing, 95(1), 13-25.

3. Basting, C., Kuzmin, D., & Shadid, J. N. (2017). Optimal control for reinitialization in finite element level set methods. International Journal for Numerical Methods in Fluids, 84(5), 292-305.

4. Beck, A. M., Murante, G., Arth, A., Remus, R. S., Teklu, A. F., Donnert, J. M., Dolag, K., (2015). An improved SPH scheme for cosmological simulations. Monthly Notices of the Royal Astronomical Society, 455(2), 2110-2130.

5. Billaud, M., Gallice, G., & Nkonga, B. (2011). A simple stabilized finite element method for solving two phase compressible–incompressible interface flows. Computer Methods in Applied Mechanics and Engineering, 200(9-12), 1272-1290.

6. Burman, E., Claus, S., Hansbo, P., Larson, M. G., & Massing, A. (2015). CutFEM: discretizing geometry and partial differential equations. International Journal for Numerical Methods in Engineering, 104(7), 472-501.

7. Caiden, R., Fedkiw, R. P., & Anderson, C. (2001). A numerical method for two-phase flow consisting of separate compressible and incompressible regions. Journal of Computational Physics, 166(1), 1-27.

8. Calderer, R., & Masud, A. (2013). Residual-based variational multiscale turbulence models for unstructured tetrahedral meshes. Computer Methods in Applied Mechanics and Engineering, 254, 238-253.

9. Caltagirone, J. P., Vincent, S., & Caruyer, C. (2011). A multiphase compressible model for the simulation of multiphase flows. Computers & fluids, 50(1), 24-34.

10. De Sousa, F. S., Mangiavacchi, N., Nonato, L. G., Castelo, A., Tomé, M. F., Ferreira, V. G., et al. (2004). A front-tracking/front-capturing method for the simulation of 3D multi-fluid flows with free surfaces. Journal of Computational Physics, 198(2), 469-499.

11. Giordano, J., & Burtschell, Y. (2006). Richtmyer-Meshkov instability induced by shock-bubble interaction: Numerical and analytical studies with experimental validation. Physics of Fluids, 18(3), 036102.

12. Hachem, E., Khalloufi, M., Bruchon, J., Valette, R., & Mesri, Y. (2016). Unified adaptive Variational MultiScale method for two phase compressible–incompressible flows. Computer Methods in Applied Mechanics and Engineering, 308, 238-255.

13. Hauke, G., & Hughes, T. J. R. (1994). A unified approach to compressible and incompressible flows. Computer Methods in Applied Mechanics and Engineering, 113(3-4), 389-395.

14. Hauke, G., & Hughes, T. J. (1998). A comparative study of different sets of variables for solving compressible and incompressible flows. Computer Methods in Applied Mechanics and Engineering, 153(1-2), 1-44.

15. Hlepas, G., Truster, T., & Masud, A. (2014). A heterogeneous modeling method for porous media flows. International Journal for Numerical Methods in Fluids, 75(7), 487-518.

16. Hu, X. Y., & Adams, N. A. (2007). An incompressible multi-phase SPH method. Journal of Computational Physics, 227(1), 264-278.

17. Hughes, T. J., Feijóo, G. R., Mazzei, L., & Quincy, J. B. (1998). The variational multiscale method—a paradigm for computational mechanics. Computer Methods in Applied Mechanics and Engineering, 166(1-2), 3-24.

18. Lind, S. J., Stansby, P. K., & Rogers, B. D. (2016). Incompressible–compressible flows with a transient discontinuous interface using smoothed particle hydrodynamics (SPH). Journal of Computational Physics, 309, 129-147.

19. Lecoanet, D., McCourt, M., Quataert, E., Burns, K. J., Vasil, G. M., Oishi, J. S., O'Leary, R.M., (2015). A validated non-linear Kelvin–Helmholtz benchmark for numerical hydrodynamics. Monthly Notices of the Royal Astronomical Society, 455(4), 4274-4288.

20. Loehnert, S., Mueller-Hoeppe, D. S., & Wriggers, P. (2011). 3D corrected XFEM approach and extension to finite deformation theory. International Journal for Numerical Methods in Engineering, 86(4-5), 431-452.

21. Kjeldby, T. K., Henkes, R. A. W. M., & Nydal, O. J. (2013). Lagrangian slug flow modeling and sensitivity on hydrodynamic slug initiation methods in a severe slugging case. International Journal of Multiphase Flow, 53, 29-39.

22. Masud, A., Al-Naseem, A. (2018). Variationally Derived Discontinuity Capturing Methods: Fine Scale Models with Embedded Weak and Strong Discontinuities. Computer Methods in Applied Mechanics and Engineering, In Press 2018. 340, 0-32. DOI: https://doi.org/10.1016/j.cma.2018.05.029.

23. Masud, A., & Calderer, R. (2011). A variational multiscale method for incompressible turbulent flows: Bubble functions and fine scale fields. Computer Methods in Applied Mechanics and Engineering, 200(33-36), 2577-2593.

24. Masud, A., & Franca, L. P. (2008). A hierarchical multiscale framework for problems with multiscale source terms. Computer Methods in Applied Mechanics and Engineering, 197(33-40), 2692-2700.

25. Masud, A., & Khurram, R. A. (2004). A multiscale/stabilized finite element method for the advection–diffusion equation. Computer Methods in Applied Mechanics and Engineering, 193(21-22), 1997-2018.

26. Masud, A., & Kwack, J. (2008). A stabilized mixed finite element method for the first-order form of advection–diffusion equation. International journal for numerical methods in fluids, 57(9), 1321-1348.

27. Mousavi, S. E., Pask, J. E., & Sukumar, N. (2012). Efficient adaptive integration of functions with sharp gradients and cusps in n-dimensional parallelepipeds. International Journal for Numerical Methods in Engineering, 91(4), 343-357.

28. Nagrath, S., Jansen, K., Lahey Jr, R. T., & Akhatov, I. (2006). Hydrodynamic simulation of air bubble implosion using a level set approach. Journal of Computational Physics, 215(1), 98-132.

29. Osterman, A., Dular, M., & Sirok, B. (2009). Numerical simulation of a near-wall bubble collapse in an ultrasonic field. Journal of Fluid Science and Technology, 4(1), 210-221.

30. Pesch, L., & van der Vegt, J. J. (2008). A discontinuous Galerkin finite element discretization of the Euler equations for compressible and incompressible fluids. Journal of Computational Physics, 227(11), 5426-5446.

31. Popinet, S., & Zaleski, S. (2002). Bubble collapse near a solid boundary: a numerical study of the influence of viscosity. Journal of Fluid Mechanics, 464, 137-163.

32. Schaal, K., Bauer, A., Chandrashekar, P., Pakmor, R., Klingenberg, C., & Springel, V. (2015). Astrophysical hydrodynamics with a high-order discontinuous Galerkin scheme and adaptive mesh refinement. Monthly Notices of the Royal Astronomical Society, 453(4), 4278-4300.

33. Shadloo, M. S., & Yildiz, M. (2011). Numerical modeling of Kelvin–Helmholtz instability using smoothed particle hydrodynamics. International Journal for Numerical Methods in Engineering, 87(10), 988-1006.

34. Smolianski, A. (2001). Numerical modeling of two-fluid interfacial flows. University of Jyväskylä.

35. Springel, V. (2010). E pur si muove: Galilean-invariant cosmological hydrodynamical simulations on a moving mesh. Monthly Notices of the Royal Astronomical Society, 401(2), 791-851.

36. Truster, T. J., & Masud, A. (2014). Primal interface formulation for coupling multiple PDEs: a consistent derivation via the variational multiscale method. Computer Methods in Applied Mechanics and Engineering, 268, 194-224.

37. Xiao, F. (2004). Unified formulation for compressible and incompressible flows by using multi-integrated moments I: one-dimensional inviscid compressible flow. Journal of Computational Physics, 195(2), 629-654.

38. Xiao, F., Akoh, R., & Ii, S. (2006). Unified formulation for compressible and incompressible flows by using multi-integrated moments II: Multi-dimensional version for compressible and incompressible flows. Journal of Computational Physics, 213(1), 31-56.

39. Yan, K., & Che, D. (2011). Hydrodynamic and mass transfer characteristics of slug flow in a vertical pipe with and without dispersed small bubbles. International Journal of Multiphase Flow, 37(4), 299-325.

40. Yue, T., Pearce, F., Kruisbrink, A., & Morvan, H. (2015). Numerical simulation of two-dimensional Kelvin–Helmholtz instability using weakly compressible smoothed particle hydrodynamics. International Journal for Numerical Methods in Fluids, 78(5), 283-303.

CHAPTER 4

A STABILIZED DISCONTINUITY CAPTURING FORMULATION: COUPLED MULTIPHASE FLOW WITH SOLUTE MASS TRANSFER AND PHASE CHANGE EFFECTS

4.1 Motivation

In [11] we employed ADE to develop a stable method with provision for developing and capturing steep gradients over any given set of elements that are traversed by discontinuity which is motivated by the level-set field. The diffusivity of the ADE was assumed the same on either side of the interface. In the vector field equations of NSE, we embedded this feature via a novel fine-scale model. Surface tension effects were embedded but in an equivalent volumetric sense. In this paper we extend the ADE model to accommodate a-priori discontinuity in the field and its gradient across, to account for the provision of jump in the diffusivity coefficients n the equations. With these features, this ADE model corresponds to convective-diffusive heat transfer across two immiscible fluids with different thermal conductivities. Accordingly, we need to enforce jump conditions both on the fields and its gradients that become a part of the governing system of equations. This same advective-diffusive model can also be used for evolution of concentration over subdomains with well-defined boundaries and markedly different diffusivity coefficients exist. We will first present a stabilized form for this model equation, and it will then be coupled with the NSE in Section 4.3 to develop a coupled thermomechanical system. We will employ this framework for concentration evolution in multiphase flow with well-defined inter phase

boundaries. We start with the general framework presented in [25] for Laplace equations and employed in [26] for diffusive heat transfer.

In various areas of material processing such as additive manufacturing and injection molding of composite materials, material flow during these processes involves multiple aspects including the existence of dissolved solutes, thermal variation and phase change of the constituents of the material. This complex coupling of multiple physical phenomena controls the overall structural integrity, reliability and even the material porosity within manufactured parts. Modeling such processes in a coupled manner would mean the need of an accurate and consistent predictive numerical method that allows the investigation of the effects of each one of these variables on the final product.

This chapter is organized as follows. In Section 4.2 we present the concentration evolution equation with interfacial condition enforcement via the Lagrange multiplier method. Section 4.3 presents the coupled thermo-mechanical formulation showing the final form of the stabilized thermal equations, where the derivation is analogous to the concentration equations in the preceding section. In Section 4.4 we briefly discuss the employed interface tracking algorithm via the level-set method and in section 4.5 we present numerical problems that show the viability of the method for mass transfer and thermally induced phase change.

4.2 The concentration ADE with embedded discontinuities

This section considers the transient concentration advection diffusion problem with a discontinuous diffusion coefficient and strong discontinuity in the scalar field. The issue of sharp discontinuities has been studied in the literature and various DC techniques have been proposed. Interested reader is referred to [11, 16, 3, 4] and references therein. Our objective is to derive a

stabilized form that is based on a novel treatment of the fine-scale variational problem and we show that the stabilization terms thus derived naturally inherit a DC structure for modeling discontinuity while also enforcing jump conditions at the embedded interface.

Let $\Omega \subset \mathbb{R}^{n_{sd}}$ be an open bounded region consisting of two sub-regions Ω_1 and Ω_2 separated by an interface Γ_s such that $\Omega = \Omega_1 \bigcup \Omega_2$ and $\Omega_1 \bigcap \Omega_2 = 0$, with piecewise smooth boundaries $\partial\Omega_1$ and $\partial\Omega_2$ where $\partial\Omega = \left(\partial\Omega_1 \bigcup \partial\Omega_2\right) \setminus \Gamma_s$ that do not overlap $\left(\partial\Omega_1 \bigcap \partial\Omega_2\right) \setminus \Gamma_s = 0$. The advection diffusion equation over the composite domain is:

$$c_t + \boldsymbol{v} \cdot \nabla c - \kappa_\alpha \Delta c = f \qquad \text{in } \Omega \tag{4.1}$$

$$\left[\!\left[\kappa_\alpha \nabla c_\alpha \right]\!\right]_\Gamma \cdot \boldsymbol{n} = 0 \qquad \text{on } \Gamma_s \tag{4.2}$$

$$\left[\!\left[\mathcal{H}_\alpha c_\alpha \right]\!\right]_\Gamma = 0 \qquad \text{on } \Gamma_s \tag{4.3}$$

where c is the concentration field, κ and $\mathcal{H}$ are piecewise continuous diffusivity and jump coefficient, respectively, which sharply vary across the interface Γ, $\alpha = 1, 2$. The discontinuity in (4.3) is analogous to the Henry's law discontinuity which induces discontinuity in the scalar field for mass transfer problems. $\boldsymbol{v}$ is the given flow velocity, which may also be a solution of the momentum equation as shown in the numerical section and is assumed solenoidal. The term $f(\boldsymbol{x})$ is possibly a discontinuous forcing term across the interface.

4.2.1 The VMS formulation

Employing the Lagrange multiplier λ to enforce the discontinuity at the interface we hence arrive at the following weak form of the advection-diffusion equation is:

$$\left(q, c_t\right) + \left(q, \boldsymbol{v} \cdot \nabla c\right) + \left(\nabla q, \kappa_\alpha \nabla c\right) - \left(\lambda, \left[\!\left[\mathcal{H}_\alpha q \right]\!\right]_{\Gamma_s}\right)_{\Gamma_s} = \left(q, f\right) \tag{4.4}$$

$$(\eta, [\![\mathcal{H}_\alpha c]\!]_{\Gamma_s})_{\Gamma_s} = 0 \tag{4.5}$$

where $(\cdot,\cdot) = \int_\Omega (\cdot)\, d\Omega$ is the $L_2(\Omega)$ inner product, q is the weighting function corresponding to the scalar field c and η is the weighting function corresponding to the Lagrange multiplier λ. We note that the weak function is multiplied by the discontinuous coefficient $\mathcal{H}_\alpha$ to enforce (4.3) weakly in the Galerkin formulation. The fourth term in (4.4) emanates from the conservation of the flux field across the interface defined in (4.2). Employing the Variational Multiscale Method (VMS), we decompose both the trial solution and weighting function as follows:

$$c(\boldsymbol{x}) = \overline{c}(\boldsymbol{x}) + c'(\boldsymbol{x}) \tag{4.6}$$

$$q(\boldsymbol{x}) = \overline{q}(\boldsymbol{x}) + q'(\boldsymbol{x}) \tag{4.7}$$

defined as $\overline{c}, \overline{q} \in H_0^1(\Omega)$ where $H_0^1(\Omega) := \{a \in L^2(\Omega) : [\![a]\!] = 0\}$ and the fine scale is defined as $c', q' \in \mathcal{V}$ where $\mathcal{V} := \{a \in L^2(\Omega) : [\![\mathcal{H}_\alpha a]\!] = 0\}$. This leads to expanding the coarse scale trial and weighting functions using piecewise continuous linear shape functions and the fine scale trial and weighting functions using the enriched bubble shape function as done in [11]. The scalar decomposition of the functional spaces for the two scales is $\mathcal{C} = \overline{\mathcal{C}} \oplus \mathcal{C}'$. The coarse scale space is defined as $\overline{\mathcal{C}} = \left\{ \overline{c} : \overline{c} \in H_0^1(\Omega) \right\}$ and the fine scale space is defined as $\mathcal{C}' = \left\{ c' : c' \in \mathcal{V} \,|\, c' = 0 \text{ on } \Gamma^e \right\}$, with the restriction that the two spaces are linearly independent and that the fine-scale is quasi-static (i.e. $c'_t = 0$). The weighting function corresponding to each of the scales belong to the same functional space as that for the trial solution.

4.2.1.1 The variational multiscale problem

We follow along the lines of [12], substituting (4.6) and (4.7) in (4.4) and (4.5) and employing linearity of the weighting function slot, leads to coarse-scale and fine-scale sub-problems:

Coarse-scale sub-problem

$$\left(\overline{q},\overline{c}_t\right)+\left(\overline{q},\boldsymbol{v}\cdot\nabla\overline{c}\right)+\left(\nabla\overline{q},\kappa_\alpha\nabla\overline{c}\right)+\left(\overline{q},\boldsymbol{v}\cdot\nabla c'\right)+\left(\nabla\overline{q},\kappa_\alpha\nabla c'\right)-\left(\lambda,[\![\overline{q}]\!]_{\Gamma_s}\right)_{\Gamma_s}=\left(\overline{q},f\right) \tag{4.8}$$

$$(\eta,[\![\overline{c}]\!]_{\Gamma_s})_{\Gamma_s}+(\eta,[\![\mathcal{H}_\alpha c']\!]_{\Gamma_s})_{\Gamma_s}=0 \tag{4.9}$$

Fine-scale sub-problem

$$\begin{aligned}&\left(\mathcal{H}_\alpha q',\overline{c}_t\right)+\left(\mathcal{H}_\alpha q',\boldsymbol{v}\cdot\nabla(\overline{c}+c')\right)+\left(\mathcal{H}_\alpha\nabla q',\kappa_\alpha\nabla(\overline{c}+c')\right)\\&-\left(\lambda,[\![\mathcal{H}_\alpha q']\!]_{\Gamma_s}\right)_{\Gamma_s}=\left(\mathcal{H}_\alpha q',f\right)\end{aligned} \tag{4.10}$$

The fine-scale sub-problem is now solved analytically in terms of the residual of the Euler Lagrange equation for the coarse scales. The resulting fine-scale model will be then substituted in (4.8)-(4.9) to yield the final stabilized form.

4.2.1.2 The fine-scale sub-problem

In order to solve the fine-scale sub-problem we first state the fine-scale problem in a residual form:

$$\left(\mathcal{H}_\alpha q',\boldsymbol{v}\cdot\nabla c'\right)+\left(\mathcal{H}_\alpha\nabla q',\kappa_\alpha\nabla c'\right)=-\left(\mathcal{H}_\alpha q',\overline{r}\right)+\left([\![\mathcal{H}_\alpha q']\!],\lambda-\kappa_\alpha\nabla\overline{c}\cdot\boldsymbol{n}\right)_{\Gamma_s} \tag{4.11}$$

where the coarse-scale residual is:

$$\overline{r}=\overline{c}_t+\boldsymbol{v}\cdot\nabla\overline{c}-\kappa_\alpha\Delta\overline{c}-f \tag{4.12}$$

The coarse scale jump term is reduced via reverse integration by parts. In this case the residual of the Euler-Lagrange equation is the main drive for the derived fine-scale solution which lead to a variationally consistent method and therefore reduces the error in the coarse-scale. Therefore, the fine-scale residual accounts for the non-zero residual error along with the discontinuities and the discontinuities that are enforced along the evolving interface. Moreover, any physical implications are modeled via the fine-scale solution as a function of the residual error.

4.2.1.3 Embedding discontinuity in the fine scale while enforcing jump conditions

In order to solve, the fine-scale sub-problem we adopt certain assumptions in our formulation. The initial assumption is to consider a fine scale which is non-zero within the elements but vanishes at the element boundaries Γ^e. This localization of the fine scales keeping it within the element interior is achieved by:

$$c' = q' = 0 \quad \text{on } \Gamma^e \tag{4.13}$$

In order for these assumptions to be met we expand fine scale fields in terms of bubble functions $b_e(\xi)$ that are non-zero on element interior and zero on the element boundaries. Due to the discontinuity in the scalar field and its gradients induced because of (4.3) and the discontinuity in the coefficient κ_α across the interface Γ that cuts through the element the solution possesses either strong or weak discontinuity across the interface. In this case, the interface location, across which the parameters are discontinuous, is known a priori via the embedded level-set function, it can be incorporated in the solution. Literature review reveals that a common procedure by which such discontinuities are accounted for is regularization of the discontinuity over several elements usually spanning the region adjoining the interface. This smoothing procedure eliminates any

abrupt jumps that are difficult to be modeled monotone using piecewise continuous shape functions.

Using the VMDC method presented in [11] we approach the problem of discontinuity by modifying the fine-scale shape functions via embedding the discontinuity capturing capability into our fine scales. However, this enrichment of the fine-scale shape function is only carried out within elements that develop discontinuity in the solution. This method avoids any modification to the global system of equations, i.e., the coarse-scale sub-problem, since the shape function modification affects only the local fine-scale sub-problem. In this section we develop the bubble function enrichment method for the scalar field problem. In section 5.4 it is tested on a problem with discontinuity in the scalar field across the interface.

We expand the fine-scale solution and the corresponding weighting function as follows:

$$c' = b^e \psi \beta \tag{4.14}$$

$$q' = \hat{b}^e \psi \gamma \tag{4.15}$$

where $b^e\psi$ is the enriched bubble function, β is the trial solution coefficients and γ is the weighting function coefficient. The bubble function employed here is a triaxial function that is defined in N dimensions as:

$$b^e\left(\xi_i\right) = \prod_{i=1}^{N} \left(1-\xi_i^2\right) \qquad \xi_i \in \{-1,1\} \tag{4.16}$$

The bubble function (4.16) is composed with an enrichment function ψ which allows the fine-scale to model a strong discontinuity across the multi-phase interface in both the field and its gradients. This enrichment of shape functions adds to the mathematical modeling ability of the

fine-scale to represent the discontinuity feature that is otherwise missing from the coarse scales because of the C^1 continuity of the element shape functions that are typically used in the coarse scale variational-problem. This enrichment function may be defined in terms of an implicit interface function (i.e. the signed distance function) in the case where material properties are discontinuous.

$$\psi = \left[\left(1 + \frac{\phi}{|\phi|} \right) \mathcal{H}_1 + \left(1 - \frac{\phi}{|\phi|} \right) \mathcal{H}_2 \right] \frac{|\phi|}{2} \tag{4.17}$$

In the enrichment function ϕ is the gradient of the scalar solution field that detects the location of high gradients where the discontinuity of the scalar field exists. In all generality, this modification introduces extra terms in the fine-scale sub-problem but does not increase the size of the coarse scale problem and therefore it does not affect the cost of solving the coarse scale problem. Substituting the enriched bubble function expansion into the fine-scale sub-problem (4.10) and invoking the mean value theorem for the coarse-scale residual:

$$\begin{aligned} &\left[\left(\mathcal{H}_\alpha \psi b^e, \boldsymbol{v} \cdot \nabla (\psi b^e) \right) + \left(\mathcal{H}_\alpha \nabla (\psi b^e), \kappa_\alpha \nabla (\psi b^e) \right) \right] \beta \\ &= -\left(\mathcal{H}_\alpha \psi b^e, \overline{r} \right) + \left(\left[\!\left[\mathcal{H}_\alpha \psi b^e \right]\!\right], \lambda - \kappa_\alpha \nabla \overline{c} \cdot \boldsymbol{n} \right)_{\Gamma_s} \end{aligned} \tag{4.18}$$

This is equivalent to assuming a constant projection of the residual which. In additional the existence of the enrichment functions leads to multiple new terms that appear when we expand the gradient operator that acts on the enriched bubble functions.

Remark: *In our previous work we have investigated the effect of employing the mean value theorem* [19] *and was found adequate to represent the fine-scale solution.*

Remark: *As done in* [18, 19] *the upwinding bubble function is employed in the weighting function for the advection term to incorporate the upwinding feature. This allows the advection term to be retained for advection-dominated problems and for the advection term to not vanish during the integration process of the fin-scale terms. Therefore, the same skewed-bubble function* $\hat{b}^e$ *is used to expand the fine scale weighting function.*

We now solve for β to arrive at:

$$\beta = -\tau\left[\left(\mathcal{H}_\alpha \psi b^e, 1\right)\overline{r} - \left(\left[\!\left[\mathcal{H}_\alpha \psi b^e\right]\!\right], 1\right)_{\Gamma_s}(\lambda - \kappa_\alpha \nabla \overline{c}\cdot \boldsymbol{n})\right] \tag{4.19}$$

where

$$\tau = \left[\left(\mathcal{H}_\alpha \psi b^e, \boldsymbol{v}\cdot\nabla(\psi b^e)\right) + \left(\mathcal{H}_\alpha \nabla(\psi b^e), \kappa_\alpha \nabla(\psi b^e)\right)\right]^{-1} \tag{4.20}$$

Substituting (4.19) in (4.14) we arrive at the fine-scale solution:

$$c' = \beta b^e \psi \tag{4.21}$$

Remark: *The fine-scale solution given in* (4.21) *accounts for the discontinuities across the interface for elements that are intersected by the interface and is automatically inactivated for all other elements. This is also the case for the interfacial conditions that are existent only along the discrete interface within the intersected elements. The use of discontinuous enrichment functions requires appropriate numerical integration rules in these elements to accurately evaluate discontinuous integrals. This special integration, employed via sub-cell integration, is need in the evaluation of the coarse-scale integrand with these elements as well since* τ *is part of the integrand in the coarse-scale sub-problem.*

4.2.1.4 Coarse-scale formulation with variationally embedded discontinuity

The last step in the development of the Variational Multiscale-Discontinuity Capturing (VMDC) method with embedded interfacial conditions is to embed the fine model in the coarse scale equations. We consider the coarse-scale problem (4.8)-(4.9) and first start by embedding the fine-scale solution into (4.9) to arrive at a closed form expression for the Lagrange multiplier. This reduces the need for solving a mixed field problem with dedicated degrees of freedom for the Lagrange multiplier and bypasses the need to satisfy the *inf-sup* conditions for a mixed field problem. To simplify the solution of (4.9), the interior residual is ignored which is analogous to assuming orthogonality between the coarse and fine scales. In addition, we employed the mean-value theorem to extract the jump residual r_Γ outside the integral which makes the equation local. Now we can substitute the fine scale back into the CS problem, where we start by embedding it into the continuity equation (4.9)

$$\begin{aligned}&(\eta,[\![\overline{c}]\!]_{\Gamma_s})_{\Gamma_s}-(\eta,[\![\mathcal{H}_\alpha\psi b^e]\!]_{\Gamma_s})_{\Gamma_s}\tau(\mathcal{H}_\alpha\psi b^e,\overline{r})\\&+(\eta,[\![\mathcal{H}_\alpha\psi b^e]\!]_{\Gamma_s})_{\Gamma_s}\tau([\![\mathcal{H}_\alpha\psi b^e]\!],\lambda)_{\Gamma_s}\\&-(\eta,[\![\mathcal{H}_\alpha\psi b^e]\!]_{\Gamma_s})_{\Gamma_s}\tau([\![\mathcal{H}_\alpha\psi b^e]\!],\kappa_\alpha\nabla\overline{c}\cdot\boldsymbol{n})_{\Gamma_s}=0\end{aligned}\tag{4.22}$$

Now we assume the second term in (4.22) to be zero (i.e. the internal residual is ignored which is analogous to assuming orthogonality between coarse and fine-scale) in the elements that are intersected by the interface. In other elements the Lagrange multiplier is zero and therefore (4.9) is not active and the stabilization simply reduces to the VMS stabilization for ADE as in [12]. We also employ the mean value theorem for the Lagrange multiplier and the coarse-scale flux term at the interface which will yield

$$(\eta,[\![\overline{c}]\!]_{\Gamma_s})_{\Gamma_s}+(\eta,[\![\mathcal{H}_\alpha\psi b^e]\!])_{\Gamma_s}\tau([\![\mathcal{H}_\alpha\psi b^e]\!],1)_{\Gamma_s}(\lambda-\kappa_\alpha\nabla\overline{c}\cdot\boldsymbol{n})=0\tag{4.23}$$

Imposing the requirement that (4.23) holds for all values η results in the following expression which is solved analytically for λ at the interface.

$$\lambda = -\hat{\tau}^{-1}[\![\overline{c}]\!]_{\Gamma_s} + \kappa_\alpha \nabla \overline{c} \cdot \boldsymbol{n} \tag{4.24}$$

Where the stabilizing parameter is defined as:

$$\hat{\tau} = \tau\left([\![\mathcal{H}_\alpha \psi b^e]\!], 1\right)^2_{\Gamma_s} \tag{4.25}$$

Applying integration by parts to the terms that include the fine scale field c' to transfer the gradient operator from the fine scale field on to the weighting functions. Employing the assumption of vanishing fine scales at the element edges (4.8) becomes

$$\left(\overline{q}, \overline{c}_t\right) + \left(\overline{q}, \boldsymbol{v} \cdot \nabla \overline{c}\right) - \left(\boldsymbol{v} \cdot \nabla \overline{q}, c'\right) + \left(\nabla \overline{q}, \kappa_\alpha \nabla \overline{c}\right) - \left(\Delta \overline{q}, \kappa_\alpha c'\right) - \left(\lambda, [\![\overline{q}]\!]_\Gamma\right)_\Gamma = \left(\overline{q}, f\right) \tag{4.26}$$

Substituting (4.21) and (4.24) in (4.26) we obtain the stabilized form for the advection diffusion equation:

$$\begin{aligned} &\left(\overline{q}, \overline{c}_t\right) + \left(\overline{q}, \boldsymbol{v} \cdot \nabla \overline{c}\right) + \left(\nabla \overline{q}, \kappa_\alpha \nabla \overline{c}\right) + (\tilde{\tau} \overline{r}, \boldsymbol{v} \cdot \nabla \overline{q}) + (\tilde{\tau} \overline{r}, \kappa_\alpha \Delta \overline{q}) \\ &+ \left(\hat{\tau}^{-1}[\![\overline{c}]\!]_{\Gamma_s}, [\![\overline{q}]\!]_{\Gamma_s}\right)_{\Gamma_s} + \left(\{\kappa_\alpha \nabla \overline{c} \cdot \boldsymbol{n}\}, [\![\overline{q}]\!]_{\Gamma_s}\right)_{\Gamma_s} + \left(\{\kappa_\alpha \nabla \overline{q} \cdot \boldsymbol{n}\}, [\![\overline{c}]\!]_{\Gamma_s}\right)_{\Gamma_s} = \left(\overline{q}, f\right) \end{aligned} \tag{4.27}$$

Where the parameter $\tilde{\tau}$ and the average due to the contribution from both sides of the interface are given as

$$\begin{aligned} \tilde{\tau} &= \tau \psi b^e \left(\psi b^e, 1\right) \\ \{a_\alpha\} &= (a_1 + a_2)/2 \end{aligned} \tag{4.28}$$

The final stabilized formulation accounts for the stabilization of the advection-diffusion equation as done in previous work [18, 19]. However, it is also endowed with discontinuity capturing features that accommodate discontinuous diffusivity κ_α and discontinuous solution field c and

allows for the enforcement of the interfacial boundary conditions given in the strong form of the governing equation.

Remark: *This formulation allows for one-way coupling between the concentration advection-diffusion equation and the momentum equations where the momentum equation drives the advection of the concentration while still retaining the interface conditions. However, two-way coupling may be achieved by allowing the concentration at or near the interface to affect the surface tension coefficient and the fluid viscosity within the bulk of the phases. This is validated via variability in the surface tension coefficient that is discussed in the next section.*

4.3 Thermo-Mechanical Flow Governing Equations

In this section we revisit the stabilized Navier-Stokes equations presented in [11] with a modified surface tension term by bringing the variability of the surface tension coefficient along the interface. This variability leads to a spatial variation in the surface tension coefficient which activates the Marangoni effects that add a new term to the surface tension jump condition in the tangential direction to the interface. Therefore, the pressure jump across the interface will be a jump both in the normal and tangential directions to the interface. This added effect allows for the two-way coupling between the concentration evolution and the momentum equations which is essential for the cases of defect evolution in manufacturing processes. This will require a modification the enrichment function used in the VMDC method to capture the pressure discontinuities in both normal and tangential directions. We also present the thermal field evolution equations that allow for thermo-mechanical coupling and incorporating phase change at the interface. This phase change leads to mass transfer from one phase to the other in cases of vaporization and condensation.

4.3.1 Coupling of Governing Equations

Let $\Omega \subset \mathbb{R}^{n_{sd}}$ be a domain consisting of two regions Ω_1 and Ω_2 that are separated by an interface Γ_s such that $\Omega = \Omega_1 \bigcup \Omega_2$ and $\Omega_1 \bigcap \Omega_2 = 0$. The two regions are occupied by two different fluid phases. Regions Ω_1 and Ω_2 are bounded by piecewise smooth boundaries Γ_1 and Γ_2, where $\Gamma = (\Gamma_1 \bigcup \Gamma_2) \setminus \Gamma_s$ and $(\Gamma_1 \bigcap \Gamma_2) \setminus \Gamma_s = 0$. Let the velocity field be defined as $\boldsymbol{v}(\boldsymbol{x},t) : \Omega \times]0,T[\rightarrow \mathbb{R}^{n_{sd}}$ and the pressure field $p(\boldsymbol{x},t) : \Omega \times]0,T[\rightarrow \mathbb{R}$. Modeling the two-phase fluid flow via the Navier-Stokes equations

$$\rho_\beta \frac{\partial \boldsymbol{v}}{\partial t} - 2\mu_\beta \nabla \cdot \boldsymbol{\varepsilon}(\boldsymbol{v}) + \nabla p + \rho_\beta \boldsymbol{v} \cdot \nabla \boldsymbol{v} = \rho_\beta \boldsymbol{b} + f_{ST} \qquad \text{in } \Omega \qquad (4.29)$$

Augmented with the continuity equation for density evolution

$$\frac{\partial \rho_\beta}{\partial t} + \nabla \cdot (\rho_\beta \boldsymbol{v}) = 0 \qquad \text{in } \Omega \qquad (4.30)$$

and the thermal evolution equation

$$\rho_\beta c_{p_\beta} \frac{\partial \theta}{\partial t} + \rho_\beta c_{p_\beta} \boldsymbol{v} \cdot \nabla \theta - \kappa_\beta \Delta \theta = R \qquad \text{in } \Omega \qquad (4.31)$$

subject to the interface Dirichlet condition enforcing the temperature to equal the saturation temperature θ_{sat} at the interface

$$\begin{aligned} &[\![\theta]\!] = 0 && \text{on } \Gamma_s \\ &[\![\kappa_\alpha \nabla \theta \cdot \boldsymbol{n}]\!] = \theta_{sat} && \text{on } \Gamma_s \qquad (4.32) \\ &\theta = \theta_{sat} && \text{on } \Gamma_s \end{aligned}$$

which is enforced in a manner similar to that presented in section 2. In the previous equations $\boldsymbol{b}:\Omega\times]0,T[\rightarrow\mathbb{R}^{n_{sd}}$ is the body force, $\rho_\beta>0$ is the fluid density of each phase, $\mu_\beta>0$ is the kinematic viscosity of each phase. The symmetric strain-rate tensor is defined as $\boldsymbol{\varepsilon}(\boldsymbol{v})=\nabla^s\boldsymbol{v}=[\nabla\boldsymbol{v}+(\nabla\boldsymbol{v})^T]/2$ and f_{ST} is the surface force due to surface tension condition at the interface. θ is the thermal field, the discontinuous thermal capacity is $c_{p_\beta}>0$ and the heat flux is $\boldsymbol{q}=-\kappa_\beta\nabla\theta$ defined using Fourier's law with different thermal diffusivities across the interface and r is the heat source/sink. The boundary and initial conditions are given as follows

$$\boldsymbol{v}=\hat{\boldsymbol{v}}\quad \text{on } \Gamma \tag{4.33a}$$

$$\boldsymbol{v}(\boldsymbol{x},0)=\boldsymbol{v}_o\quad \text{in } \Omega \tag{4.33b}$$

$$\theta=\hat{\theta}\quad \text{on } \Gamma \tag{4.34a}$$

$$\theta(\boldsymbol{x},0)=\theta_o\quad \text{in } \Omega \tag{4.34b}$$

Here $\beta=1,2$ corresponds to each phase, The initial condition is given as $\boldsymbol{v}_o$ for the velocity field and $\hat{\boldsymbol{v}}$ represents the Dirichlet boundary conditions. The density and viscosity are defined discontinuous across the interface via the Heaviside function:

$$\rho=\left(1-\mathrm{H}(\phi)\right)\rho_1+\mathrm{H}(\phi)\rho_2 \tag{4.35a}$$

$$\mu=\left(1-\mathrm{H}(\phi)\right)\mu_1+\mathrm{H}(\phi)\mu_2 \tag{4.35b}$$

$$c_{p_\beta}=\left(1-\mathrm{H}(\phi)\right)c_{p_1}+\mathrm{H}(\phi)c_{p_2} \tag{4.36a}$$

$$\kappa_\beta=\left(1-\mathrm{H}(\phi)\right)\kappa_1+\mathrm{H}(\phi)\kappa_2 \tag{4.36b}$$

The Heaviside function is a function of the signed distance field $\phi(\boldsymbol{x},t)$ which is employed in the level-set method to track the interface where $\phi(\boldsymbol{x},t)=0$ for all $\boldsymbol{x}\in\Gamma_s$. The Heaviside function is given as:

$$\mathrm{H}(\phi)=\begin{cases}1 & \phi<0\\ 0 & \phi\geq 0\end{cases} \tag{4.37}$$

4.3.2 Mass transfer and thermal expansion

To account for mass transfer across the interface we introduce the definition of the discontinuous density into (4.30) as done in [21] and define a temperature dependent mass flux term $m(\theta)$ which introduces mass transfer and allows for the volume growth of either phases.

$$\frac{\partial}{\partial t}\Big(\big(1-\mathrm{H}(\phi)\big)\rho_1\Big)+\nabla\cdot\Big(\big(1-\mathrm{H}(\phi)\big)\rho_1\boldsymbol{v}\Big)=-m(\tfrac{\partial \mathrm{H}}{\partial\phi}) \tag{4.38}$$

$$\frac{\partial}{\partial t}\big(\mathrm{H}(\phi)\rho_2\big)+\nabla\cdot\big(\mathrm{H}(\phi)\rho_2\boldsymbol{v}\big)=m(\tfrac{\partial \mathrm{H}}{\partial\phi}) \tag{4.39}$$

Here $\frac{\partial \mathrm{H}}{\partial\phi}$ localizes the mass transfer term on the right to the interface and $\boldsymbol{n}=\frac{\nabla\phi}{|\nabla\phi|}$ is the normal vector pointing towards the region Ω_1. Therefore, the mass can transfer to the liquid phase via condensation or the gaseous phase via evaporation as a function of the thermal fluxes at the interface. Now if we divide (4.38) by ρ_1 and divide (4.39) by ρ_2 and then adding the two equations the continuity equation (4.30) reduces to the incompressible flow continuity equations with an interfacial mass transfer forcing term.

$$\nabla\cdot\boldsymbol{v}=m\left(\frac{1}{\rho_1}-\frac{1}{\rho_2}\right)(\tfrac{\partial \mathrm{H}}{\partial\phi}) \tag{4.40}$$

and the mass transfer flux is defined as

$$m = \frac{\left[\!\left[\kappa_\beta \nabla \theta \cdot \boldsymbol{n} \right]\!\right]}{h} \tag{4.41}$$

Thus m is controlled by the jump in thermal flux at the interface and h is the difference in latent heat during phase change at the interface. Accounting for phase change as done in (4.40) leads to a discontinuity in the velocity field $[\![\boldsymbol{v}]\!] = m\left[\!\left[\frac{1}{\rho_\beta}\right]\!\right]\boldsymbol{n}$ in contrast to the discontinuity in the pressure field modeled in [11] due to surface tension. Furthermore, phase change adds to the pressure discontinuity which is now given as $[\![p]\!] = f_{ST} + m^2\left[\!\left[\frac{1}{\rho_\beta}\right]\!\right]$ thus including an additional jump due to phase transition effects [22]. For full derivation of the mass flux m interested readers are referred to [21, 22]. As mass transfer is allowed to occur at the interface via the mass flux m, the coupling between the momentum equation and the temperature is still not achieved due to the lack of thermally induced flows. Adopting the temperature-driven flow approximation given by the Boussinesq force [22], the body force in (4.29) is defined as:

$$\boldsymbol{b} = \boldsymbol{g}(1 - \xi_\beta(\theta - \theta_{ref})) \tag{4.42}$$

where $\boldsymbol{g}$ is gravity, ξ_β is the thermal expansion coefficient within each phase and θ_{ref} is the reference temperature. This modification to the density in gravity driven flow term allows for expansion and contraction of the fluid based on ξ_β and thus completes the coupling across the three governing equations.

4.3.3 Stabilized Variational formulation

Here we develop the weak form of the governing equations and derive the stabilized form leading to the final stabilized formulation. Let $\boldsymbol{w}(\boldsymbol{x}) \in \mathcal{W} \equiv \left\{\left[H_0^1(\Omega)\right]^{n_{sd}}\right\}$ and $q(\boldsymbol{x}) \in \mathcal{Q} \equiv L^2(\Omega)$

represent the weighting functions for the velocity and pressure fields, respectively. The trial solutions for the velocity and pressure fields are $\boldsymbol{v}(\boldsymbol{x},t) \in \boldsymbol{\mathcal{V}} \equiv \left\{ \left[H_0^1(\Omega) \right]^{n_{sd}} \times \left[0,T \right] \right\}$ and $p(\boldsymbol{x},t) \in \mathcal{P} \equiv \left\{ L^2(\Omega / \Gamma_s) \times \left[0,T \right] \right\}$ respectively, and they satisfy the initial and boundary conditions. The weak form of (4.29-4.31) is as follows

$$\left(\rho \boldsymbol{w}, \frac{\partial \boldsymbol{v}}{\partial t} \right) + \left(2\mu \nabla^s \boldsymbol{w}, \boldsymbol{\varepsilon}(\boldsymbol{v}) \right) - \left(\nabla \cdot \boldsymbol{w}, p \right) + \left(\boldsymbol{w}, \rho \boldsymbol{v} \cdot \nabla \boldsymbol{v} \right) = \left(\rho \boldsymbol{w}, \boldsymbol{b} \right) + \left(\boldsymbol{w}, f_{ST} \right)_{\Gamma_s} \tag{4.43}$$

$$\left(q, \nabla \cdot \boldsymbol{v} \right) = \left(q, m \left(\frac{1}{\rho_1} - \frac{1}{\rho_2} \right) \right)_{\Gamma_s} \tag{4.44}$$

Remark: *The derivation of the thermal field equations leading to the stabilized formulation is form identical to that of the concentration equation presented in section* 4.2. *The only difference is that the there is no jump in temperature across the interface rather it is held at the saturation temperature via a penalty term. We state the final stabilized form in the end of section* 4.3.3.4.

4.3.3.1 Variational surface tension formulation

In order to derive the stabilized weak form, we first present the surface tension force f_{ST} in a variational form as derived in [2]. The Laplace-Young surface tension condition is a jump condition for the pressure field and is generally given as

$$f_{ST} = \delta k \boldsymbol{n} - \nabla_\Gamma \delta \tag{4.45}$$

The second term in (4.38) denoted as the Marangoni force, brings dependence of the surface tension force on the variation of the surface tension coefficient $\delta(\boldsymbol{x})$ on space via the tangential gradient ∇_Γ . This spatial variability could be defined through dependence on temperature, solute

concentration or other surface values that may vary in space and time as well. A well-known phenomenon that depends on the spatial variability of $\delta(\boldsymbol{x})$ is the Marangoni effect which is investigated in the numerical section. Therefore casting (4.45) in a variational formulation would yield

$$(\boldsymbol{w}, \delta k\boldsymbol{n} - \nabla_{\Gamma}\delta)_{\Gamma} \tag{4.46}$$

which would replace the last term in (4.43). At this stage two challenges arise with (4.46), the first being the calculation of the curvature $k(\boldsymbol{x})$ at the interface, which is difficult when employing lower order shape functions along with an implicit definition of the interface such as the signed distance field. Secondly, the surface tangential gradient would also require an accurate calculation of the local tangent vector at each point along the interface. In order to circumvent both issues, the Laplace-Beltrami operator is employed as proposed by Bansch [23] and the variational surface tension force is defined as

$$-\int_{\Gamma} \delta \boldsymbol{P} : \nabla \boldsymbol{w} \; d\Gamma \tag{4.47}$$

where $\boldsymbol{P} \equiv \boldsymbol{1} - \boldsymbol{n} \otimes \boldsymbol{n}$ is the tangential projection tensor where (4.47) would replace the last term in (4.43). This equivalent form incorporates both the normal and tangential jump introduced by surface tension and accounts for surface forces at the boundaries of the interface $\partial\Gamma_s$ in the case were the interface is not closed. This leads to a variational surface tension that not only incorporates Marangoni effects but also depends solely on the first gradient of the signed distance field via the normal vector $\boldsymbol{n} = \nabla\phi / |\nabla\phi|$.

4.3.3.2 Fine-scale and Coarse-scale problems

Employing the multiscale decomposition to stabilize the momentum equations and incorporate the discontinuity capturing feature [11] we decomposition of the velocity field $\boldsymbol{v}$ into coarse scale $\bar{\boldsymbol{v}}$ and fine scale $\boldsymbol{v}'$ along with the corresponding weighting function $\boldsymbol{w}$ into its respective coarse scale $\bar{\boldsymbol{w}}$ and fine scale $\boldsymbol{w}'$ as follows

$$\boldsymbol{v}(\boldsymbol{x},t)=\bar{\boldsymbol{v}}(\boldsymbol{x},t)+\boldsymbol{v}'(\boldsymbol{x},t) \tag{4.48}$$

$$\boldsymbol{w}(\boldsymbol{x})=\bar{\boldsymbol{w}}(\boldsymbol{x})+\boldsymbol{w}'(\boldsymbol{x}) \tag{4.49}$$

Substituting (4.48) and (4.49) into (4.43) and (4.44) and utilizing the linearity of the weighting function we arrive at two sub-problems

Coarse-scale sub-problem:

$$\begin{aligned}&\left(\rho\bar{\boldsymbol{w}},\frac{\partial\bar{\boldsymbol{v}}}{\partial t}\right)+\left(\rho\bar{\boldsymbol{w}},\frac{\partial\boldsymbol{v}'}{\partial t}\right)+\left(2\mu\nabla^{s}\bar{\boldsymbol{w}},\boldsymbol{\varepsilon}(\bar{\boldsymbol{v}}+\boldsymbol{v}')\right)-\left(\nabla\cdot\bar{\boldsymbol{w}},p\right)+\left(\bar{\boldsymbol{w}},\rho(\bar{\boldsymbol{v}}+\boldsymbol{v}')\cdot\nabla(\bar{\boldsymbol{v}}+\boldsymbol{v}')\right)\\&=\left(\rho\bar{\boldsymbol{w}},\boldsymbol{b}\right)-(\delta\boldsymbol{P},\nabla\bar{\boldsymbol{w}})_{\Gamma}\end{aligned} \tag{4.50}$$

$$\left(q,\nabla\cdot(\bar{\boldsymbol{v}}+\boldsymbol{v}')\right)=\left(q,m\left(\frac{1}{\rho_1}-\frac{1}{\rho_2}\right)\right)_{\Gamma_s} \tag{4.51}$$

Fine-scale sub-problem:

$$\begin{aligned}&\left(\rho\boldsymbol{w}',\frac{\partial\bar{\boldsymbol{v}}}{\partial t}\right)+\left(\rho\boldsymbol{w}',\frac{\partial\boldsymbol{v}'}{\partial t}\right)+\left(2\mu\nabla^{s}\boldsymbol{w}',\boldsymbol{\varepsilon}(\bar{\boldsymbol{v}}+\boldsymbol{v}')\right)-\left(\nabla\cdot\boldsymbol{w}',p\right)\\&+\left(\boldsymbol{w}',\rho(\bar{\boldsymbol{v}}+\boldsymbol{v}')\cdot\nabla(\bar{\boldsymbol{v}}+\boldsymbol{v}')\right)=\left(\rho\boldsymbol{w}',\boldsymbol{b}\right)-(\delta\boldsymbol{P},\nabla\boldsymbol{w}')_{\Gamma}\end{aligned} \tag{4.52}$$

At this stage the solution we focus on obtaining the solution of the fine-scale problem in terms of the coarse-scale residual and derive an analytical expression for the fine-scale velocity.

4.3.3.3 Evaluating fine-scales via enriched bubble functions method

For evaluating the fine-scale solution we first assume that the fine-scale velocity and corresponding weighting function both vanish at the edge of the element and are non-zero within the element.

$$\boldsymbol{v}' = \boldsymbol{w}' = 0 \quad \text{on } \Gamma^e \tag{4.53}$$

Following along the cases in [11] and in order to adopt the embed the discontinuity capturing feature of the VMDC method we define an enrichment function that is local within the intersected elements in the domain. This function is defined in terms of the signed distance field which is used to track the interface location via the level-set method. The enrichment function is defined as:

$$\psi(\phi) = \left(|\phi| + \frac{\phi}{|\phi|} \right) \tag{4.54}$$

Accordingly, the fine scale solutions would be expanded in terms of the composition of the quadratic bubble function $b^e(\boldsymbol{\xi})$ and the enrichment function $\psi(\phi)$ in order to localize the capture of the discontinuity within the element. As a departure from the enrichment presented in [11] is the fact that the gradient of the enrichment function is defined separately in this case where:

$$\frac{\partial \psi}{\partial x} = \frac{\partial \psi}{\partial y} = \frac{\partial \psi}{\partial z} = \left(|\phi| + \frac{\phi}{|\phi|} \right) \tag{4.55}$$

This modification to the natural gradient (4.55) is introduced to allow for tangential discontinuity capturing in the velocity and pressure alike. Such a modification is adopted due to the *a priori* knowledge of the existence of the tangential discontinuity due to the Marangoni forces

described in section 3.1.2.1. Although the underlying formulation remains the same this modification is important in order to accurately capture the tangential force discontinuities within the single element without oscillations. The velocity and weighting function are now expanded as follows:

$$\boldsymbol{v}' = \boldsymbol{\beta} b^e(\boldsymbol{\xi})\psi(\phi) \tag{4.56}$$

$$\boldsymbol{w}' = \boldsymbol{\gamma} b^e(\boldsymbol{\xi})\psi(\phi) \tag{4.57}$$

where $\boldsymbol{\beta}$ and $\boldsymbol{\gamma}$ are the coefficients for the fine-scale trial solution and weighting function, respectively. Employing the generalized alpha method to discretize in time and substituting (4.56) and (4.57) in (4.52), and ignoring the history dependence of the fine-scale terms we can solve for the trial solution coefficient $\boldsymbol{\beta}_{n+1}$ as follows

$$\boldsymbol{v}'_{n+1}(\boldsymbol{x}) = b^e\psi\boldsymbol{\beta}_{n+1} = -b^e\psi\left\{\frac{\alpha_m}{\gamma\Delta t}\left(b^e\psi, b^e\psi\right) + \alpha_f\hat{\boldsymbol{\tau}}\right\}^{-1}\left[\left(b^e\psi, \overline{\boldsymbol{r}}_{n+\alpha_f}\right) + \left(\boldsymbol{r}^{ST}{}_{n+\alpha_f}, \nabla(b^e\psi)\right)_{\Gamma_s}\right] \tag{4.58}$$

where $\hat{\boldsymbol{\tau}}$ is defined as

$$\begin{aligned}\hat{\boldsymbol{\tau}} = {} & \mu\int\left|\nabla\left(b^e\psi\right)\right|^2 d\Omega^e\boldsymbol{I} + \mu\int\nabla\left(b^e\psi\right)\otimes\nabla\left(b^e\psi\right)d\Omega^e + \int\left(b^e\psi\right)^2\nabla^T\overline{\boldsymbol{v}}d\Omega^e \\ & + \int\left(b^e\psi\right)\overline{\boldsymbol{v}}\cdot\psi\nabla b^e d\Omega^e + \int\left(b^e\psi\right)\overline{\boldsymbol{v}}\cdot b^e\nabla\psi d\Omega^e\end{aligned} \tag{4.59}$$

and the residuals are:

$$\begin{aligned}\overline{\boldsymbol{r}} &\equiv \frac{\partial\overline{\boldsymbol{v}}}{\partial t} - 2\mu\nabla\cdot\boldsymbol{\varepsilon}(\overline{\boldsymbol{v}}) + \nabla p + \rho\overline{\boldsymbol{v}}\cdot\nabla\overline{\boldsymbol{v}} - \rho\boldsymbol{b} \\ \boldsymbol{r}^{ST} &= \delta\boldsymbol{P}\end{aligned} \tag{4.60}$$

We note that the mean-value theorem is used to extract the residual $\bar{\boldsymbol{r}}$ from the integral but is not used on the surface tension force term $\boldsymbol{r}^{ST}$.

Remark: *It is important to note that as the terms with the gradient of the enrichment $\nabla\psi$ in (4.58) and (4.59) were ignored for simplicity in [11], they are required in this formulation where the Marangoni effects are active. Nevertheless, with the modified definition of $\nabla\psi$ and the inclusion of the gradient terms is backward compatible with cases where the tangential discontinuities are nonexistent and produces similar results to the formulation presented in [11].*

Remark: *Although we have dropped history dependence of the fine scale, the stabilization tensor is still a function of Δt as shown in (4.58). Furthermore, (4.58) leads to a system of ODE's that need a time integration method to convert it into an algebraic system.*

4.3.3.4 Stabilized weak form for NSE with phase change and Marangoni effects

We embed the fine-scale model into the coarse-scale variational problem by substituting (4.58) into (4.50) and (4.51). The formal statement for the modified stabilized form with embedded phase change and Marangoni forces is: Find $\boldsymbol{v}(\boldsymbol{x},t)\in\boldsymbol{\mathcal{V}}$ and $p(\boldsymbol{x},t)\in\mathcal{P}$ such that for all $\boldsymbol{w}(\boldsymbol{x})\in\boldsymbol{\mathcal{W}}$ and $q(\boldsymbol{x})\in\mathcal{Q}$:

$$B_{Gal}\left(\left(\bar{\boldsymbol{w}},q,\bar{\omega}\right),\left(\bar{\boldsymbol{v}},p,\bar{\theta}\right)\right)+B_{VMDC}\left(\left(\bar{\boldsymbol{w}},q,\bar{\omega}\right),\left(\bar{\boldsymbol{v}},p,\bar{\theta}\right)\right)=F_{PC}(\bar{\boldsymbol{w}})+F_{Gal}\left(\bar{\boldsymbol{w}},\bar{\omega}\right)+F_{ST}\left(\bar{\boldsymbol{w}}\right) \tag{4.61}$$

where the Galerkin terms are

$$\begin{aligned}B_{Gal}\left(\left(\bar{\boldsymbol{w}},q\right),\left(\bar{\boldsymbol{v}},p\right)\right)=&\left(\rho\bar{\boldsymbol{w}},\frac{\partial\bar{\boldsymbol{v}}}{\partial t}\right)+\left(\bar{\boldsymbol{w}},\rho\bar{\boldsymbol{v}}\cdot\nabla\bar{\boldsymbol{v}}\right)+\left(2\mu\nabla^{s}\bar{\boldsymbol{w}},\boldsymbol{\varepsilon}\left(\bar{\boldsymbol{v}}\right)\right)-\left(\nabla\cdot\bar{\boldsymbol{w}},p\right)\\&+\left(q,\nabla\cdot\bar{\boldsymbol{v}}\right)+(\bar{\omega},\rho c_{p}\bar{\theta}_{t})+(\bar{\omega},\rho c_{p}\boldsymbol{v}\cdot\nabla\bar{\theta})+(\nabla\bar{\omega},\kappa\nabla\bar{\theta})\\&+\left(\left[\!\left[\bar{\theta}\right]\!\right]_{\Gamma_{s}},\{\kappa\nabla\bar{\omega}\cdot\boldsymbol{n}\}\right)_{\Gamma_{s}}+\left(\{\kappa\nabla\bar{\theta}\cdot\boldsymbol{n}\},\left[\!\left[\bar{\omega}\right]\!\right]\right)_{\Gamma_{s}}\end{aligned} \tag{4.62}$$

$$F_{Gal}\left(\bar{\boldsymbol{w}},\bar{\omega}\right)=(\rho\boldsymbol{b},\bar{\boldsymbol{w}})+(R,\bar{\omega}) \tag{4.63}$$

where the body force includes the Boussinesq forces as well. The phase change forcing terms are:

$$F_{PC} = \left(q, m\left(\frac{1}{\rho_1} - \frac{1}{\rho_2} \right) \right)_{\Gamma_s} \tag{4.64}$$

and the VMDC terms with variational surface forces are

$$\begin{aligned} B_{VMDC}\left((\bar{\boldsymbol{w}}, q, \bar{\omega}), (\bar{\boldsymbol{v}}, p, \bar{\theta}) \right) = & \begin{pmatrix} -\dfrac{\alpha_m}{\gamma \Delta t}\rho \bar{\boldsymbol{w}} + 2\mu \nabla \cdot \boldsymbol{\varepsilon}(\bar{\boldsymbol{w}}) + \bar{\boldsymbol{v}} \cdot \nabla \bar{\boldsymbol{w}} + \bar{\boldsymbol{v}} \cdot \nabla^T \bar{\boldsymbol{w}} + \nabla q, \\ \boldsymbol{\tau}\left(\dfrac{\partial \bar{\boldsymbol{v}}}{\partial t} - 2\mu \nabla \cdot \boldsymbol{\varepsilon}(\bar{\boldsymbol{v}}) + \nabla p + \rho \bar{\boldsymbol{v}} \cdot \nabla \bar{\boldsymbol{v}} - \rho \boldsymbol{b} \right) + \boldsymbol{\tau}^{ST} \end{pmatrix} \\ & + (\tilde{\tau} \bar{r}_T, \rho c_p \boldsymbol{v} \cdot \nabla \bar{g}) + (\tilde{\tau} \bar{r}, k \Delta \bar{g}) + \left(\hat{\tau}^{-1} [\![\bar{\theta}]\!], [\![\bar{\omega}]\!] \right)_{\Gamma_s} \end{aligned} \tag{4.65}$$

The stabilization tensors and parameters that emanate from (4.52) and the thermal VMS solution

$$\begin{aligned} \boldsymbol{\tau} &\equiv b^e \psi \left\{ \frac{\alpha_m}{\gamma \Delta t}\left(b^e \psi, b^e \psi \right) + \alpha_f \hat{\boldsymbol{\tau}} \right\}^{-1} \left(b^e \psi, 1 \right) \\ \boldsymbol{\tau}^{ST} &\equiv b^e \psi \left\{ \frac{\alpha_m}{\gamma \Delta t}\left(b^e \psi, b^e \psi \right) + \alpha_f \hat{\boldsymbol{\tau}} \right\}^{-1} \left(\delta \boldsymbol{P}, \nabla (b^e \psi) \right)_{\Gamma_s} \\ \tau &= \left[\left(\psi b^e, \boldsymbol{v} \cdot \nabla (\psi b^e) \right) + \left(\nabla (\psi b^e), \kappa \nabla (\psi b^e) \right) \right]^{-1} \\ \hat{\tau} &= \tau \left([\![\psi b^e]\!], 1 \right)^2_{\Gamma_s} \\ \tilde{\tau} &= \tau \psi b^e \left(\psi b^e, 1 \right) \end{aligned} \tag{4.66}$$

The discontinuous surface force due to surface tension is

$$F_{ST}(\bar{\boldsymbol{w}}) = -(\delta \boldsymbol{P}, \nabla \bar{\boldsymbol{w}})_{\Gamma} \tag{4.67}$$

along with a *div*-stabilization term that is added as in [11]. The stabilized formulation in (4.61) is not only embedded with discontinuity capturing features in directions normal to the interface, but now accommodate tangential discontinuity in both the velocity and pressure fields. In addition, this formulation of the NSE accounts for two-way coupling with the temperature evolution

equation which leads to a multi-physically coupled system of equations capable of modeling phase change across the interphase boundary and thermal expansion. In order to circumvent any possible repetition and due to the large similarity between the stabilized formulation presented in section 4.2 and the stabilized thermal equations we suffice with the stabilized formulation presented therein.

4.4 Level-Set equations

In the context of interface translation, merging or separation the level-set equation is a primary instrument used to capture this evolution. As presented in [11] the stabilized level-set equations will be used with the velocity field induced by the momentum equation in addition to the interfacial mass transfer term. To derive the total advective velocity evolving the level-set equation as done in [21, 24], we start by expanding (4.38) and (4.39) as follows:

$$-\rho_1 \frac{\partial \mathrm{H}(\phi)}{\partial t} + \rho_1 \left(1-\mathrm{H}(\phi)\right)\nabla\cdot\boldsymbol{v} - \rho_1 \nabla \mathrm{H}(\phi)\cdot\boldsymbol{v} = -m(\tfrac{\partial \mathrm{H}}{\partial \phi}) \tag{4.68}$$

$$\rho_2 \frac{\partial \mathrm{H}(\phi)}{\partial t} + \rho_2 \mathrm{H}(\phi)\nabla\cdot\boldsymbol{v} + \rho_2 \nabla \mathrm{H}(\phi)\cdot\boldsymbol{v} = m(\tfrac{\partial \mathrm{H}}{\partial \phi}) \tag{4.69}$$

Dividing (4.68-4.69) by $(\rho_2 - \rho_1)$ and summing the two equations leads to:

$$\frac{\partial \mathrm{H}(\phi)}{\partial t} + \nabla \mathrm{H}(\phi)\cdot\boldsymbol{v} = \frac{\rho}{(\rho_2-\rho_1)}\nabla\cdot\boldsymbol{v} \tag{4.70}$$

Expanding the temporal and spatial derivatives as follows:

$$\frac{\partial \mathrm{H}(\phi)}{\partial t} = \frac{\partial \mathrm{H}}{\partial \phi}\frac{\partial \phi}{\partial t} = \left.\frac{\partial \phi}{\partial t}\right|_{\Gamma_s} \tag{4.71}$$

$$\nabla \mathrm{H}(\phi) = \left.\nabla \phi\right|_{\Gamma_s} \tag{4.72}$$

Substituting (4.71-4.72) and (4.40) into (4.70) and extending this definition of the level-set to the whole domain we arrive at a modified level-set equation:

$$\frac{\partial \phi}{\partial t} + \left(\boldsymbol{v} - \frac{\rho}{\rho_1 \rho_2} m \boldsymbol{n} \right) \cdot \nabla \phi = 0 \tag{4.73}$$

Therefore, the advective velocity now accounts for the phase change effects when evolving the interface boundary. Following along our previous work [11] the stabilized variational formulation of (4.73) is derived and a cost effective reinitialization technique is employed to assure the numerical stability of the signed distance field during the evolution of the interface. For further information interested readers are referred to section 4 of [11].

4.5 Numerical Section

4.5.1 Planar Interface with Interface Conditions

In this section we present a problem adopted from [15] to evaluate the accuracy in enforcing the interfacial Dirichlet conditions given via Henry's condition in (4.3). The enforcement of this condition corresponds to the mass transfer equilibrium condition for vaporization in solute convection and mass transfer problems as well as the cases of enforcing fixed saturation temperature at the interface for thermo-mechanical flows. This problem validates the enforcement of equal flux and the discontinuity of the solution field at the interface. The problem is defined on a 3D domain $\Omega = [0,1]^3$ where the interface is located at the plane $x = 0.25$ across the unit block. The diffusivity coefficients are given as $\kappa_1 = 1$ and $\kappa_2 = 5$ whereas the solution jump coefficients are $\mathcal{H}_1 = 2$ and $\mathcal{H}_2 = 1$. Homogeneous Dirichlet boundary conditions are enforced at the boundaries $z = 0$ and $z = 1$, where homogeneous Neuman boundary conditions are enforced on

the other boundaries of the domain. Given a prescribed constant velocity field $\boldsymbol{v} = \left(y(1-z), x, 0\right)^T$ a designed exact solution is proposed in [15] given as:

$$c(\boldsymbol{x},t) = \begin{cases} e^{-t}\cos(\pi x)\cos(2\pi y)az(z+b) & \text{in } \Omega_1 \\ e^{-t}\cos(\pi x)\cos(2\pi y)z(z-1) & \text{in } \Omega_2 \end{cases} \tag{4.74}$$

A corresponding forcing term $f(\boldsymbol{x},t)$ is chosen to satisfy this exact solution where the exact solution parameters are $a = -0.8972$ and $b = 0.0261$. The problem is modeled till time $T = 0.15$ with a time step $\Delta t = 0.01$ for four mesh sizes of 8^3, 16^3, 32^3 and 64^3. In Fig. 4.1 we show the interface location cutting through the element for the coarsest mesh without resorting to mesh refinement around or near the interface.

Remark: *Although the Nitsche-XFEM method is employed in [15] gradual refinement of the mesh is employed within the proximity of the interface. This is not adopted in this work.*

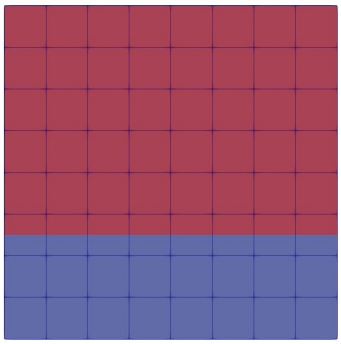

Fig. 4.1. Location of the interface at $x = 0.25$ in the y-z plane.

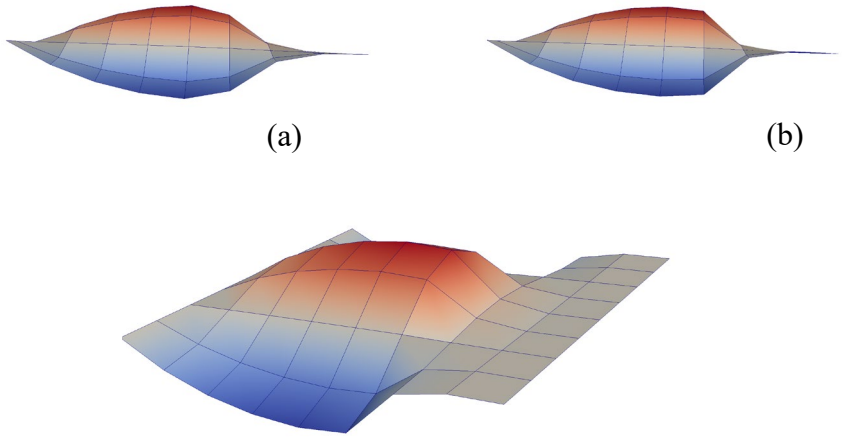

Fig. 4.2. Scalar profile modeled with (a) VMS and (b) VMDC and (c) profile of solution for 8^3 mesh at time $T = 0.15$ across the plane $x = 0.25$.

Fig. 4.2 shows the discontinuity capturing feature of the proposed method incorporating the variational Dirichlet condition enforcement method presented in section 2. However, without the use of the enriched fine-scales via the VMDC method, the jump is smeared as shown in Fig. 4.2(a) while the discontinuity is better contained within a single element in Fig. 4.2(b). An L_2 convergence is performed for the problem and compared to values presented in [15] (see Fig. 4.3). The mesh sizes employed in plotting the error norm from [15] correspond to the size of elements far from the interface, while the authors refine the elements closer to the interface twice. Hence, as the error is higher for the proposed method, it is important to note that this further mesh refinement in the proximity of the interface is not employed in this work. Therefore, when comparing the errors it would be better suited to compare the error corresponding to a 8^3 mesh from [15] to a mesh of size 32^3 for the proposed method, which would clearly show the superiority in error reduction of the proposed method with the XFEM-Nitsche method presented in [15]. Nevertheless, the proposed method which bypasses the prescription of predefined parameters used by the Nitsche method is shown to achieve optimal convergence with mesh refinement.

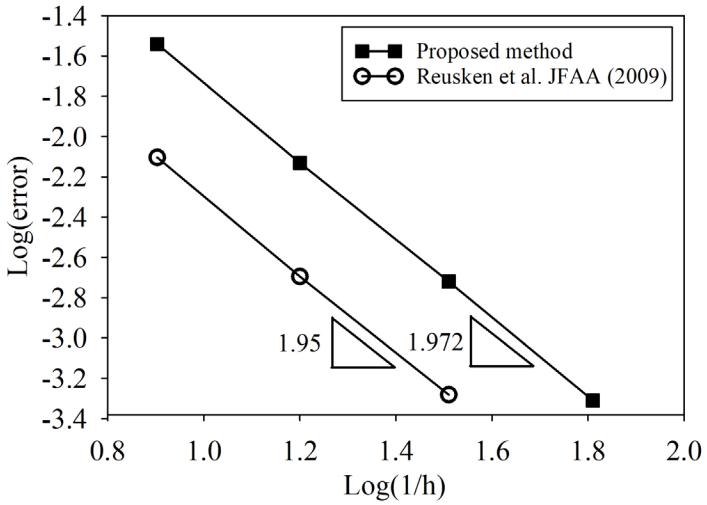

Fig. 4.3. L_2-error norm for scalar field.

4.5.2 Rotating flow field

This section presents an advection dominated flow that rotates an internal boundary AB around the computational domain. Although this problem involves convection of a smooth profile, it presents a good test case for the assessing the accuracy of the method in terms of any spurious crosswind diffusion that can induce amplitude error after the flow transports the scalar field back to the location of the internal boundary. The problem is defined on a bi-unit domain $\Omega = [-0.5, 0.5]\times[-0.5, 0.5]$ where the velocity is given as $\boldsymbol{v} = (-y, x)$ and the diffusivity is set equal to $\kappa = 1\times10^{-6}$. The Dirichlet boundary conditions at the boundaries of the domain are shown in Fig. 4.4(a) and the internal boundary is defined at $(x = 0, -0.5 \le y \le 0)$ along line AB where $c = \frac{1}{2}\left(\cos\left(4\pi y + \pi\right) + 1\right)$. The profile of the scalar field along the internal boundary is given in Fig. 4.4(b). We compare the VMS, VMDC and SUPG-DC [6] methods on this problem to assess the level of diffusion error induced by each method, and to assess if the discontinuity capturing terms in the VMDC and SUPG-DC methods perform identically. We employ the results from VMS [12] as the reference for comparison since they are nearly exact (see Fig. 4.5(a)). If we examine Fig.

4.5(c) we can see that the SUPG-DC method suffers from a loss in accuracy in amplitude due to accumulated error of approximately 10% reduction in amplitude by the end of the simulation, and this is in accordance with the remark presented in Hughes *et al.* [6]. On the other hand, the VMDC method shown in Fig. 4.5(b), using either enrichment functions (i.e., scalar field gradient or level-set based enrichment functions), is able to accurately maintain the amplitude of the scalar field with an amplitude reduction of only 1% as presented in Fig. 4.6.

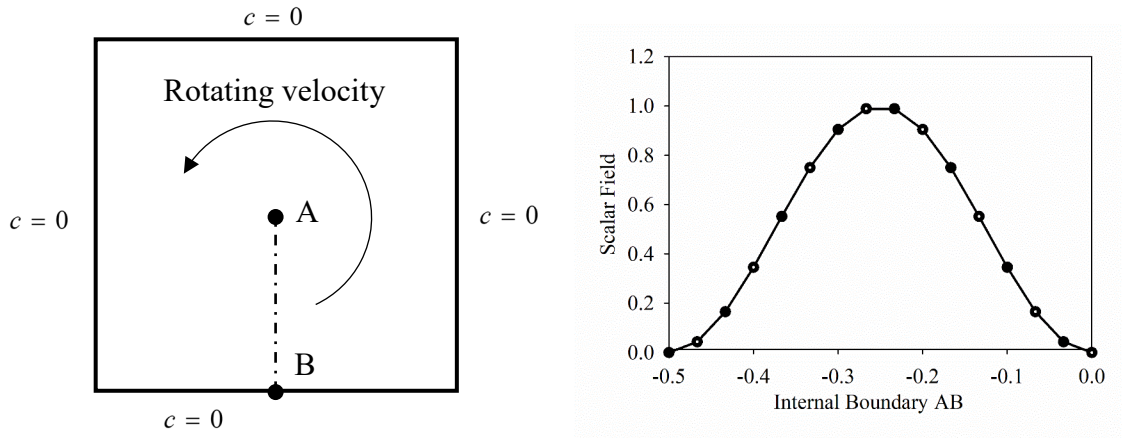

Fig. 4.4. Rotating flow problem: (a) Dirichlet boundary conditions and internal boundary AB, (b) Scalar field value along AB.

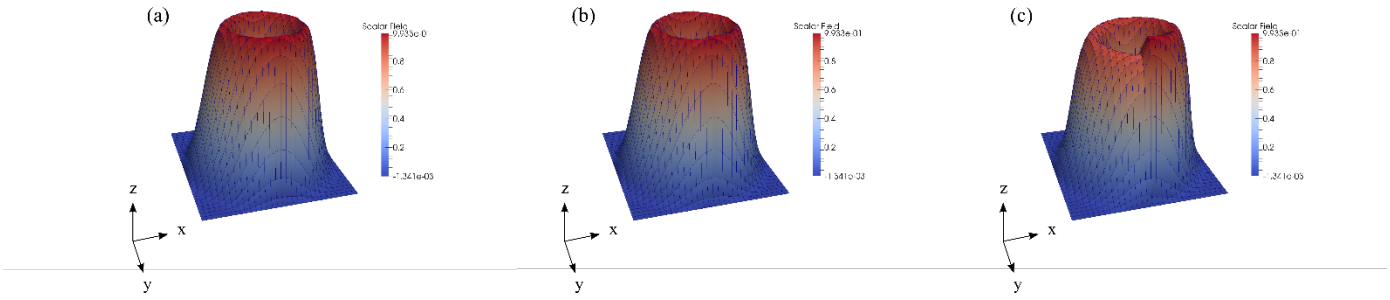

Fig. 4.5. Scalar field profile for (a) VMS, (b) VMDC and (c) SUPG-DC [6].

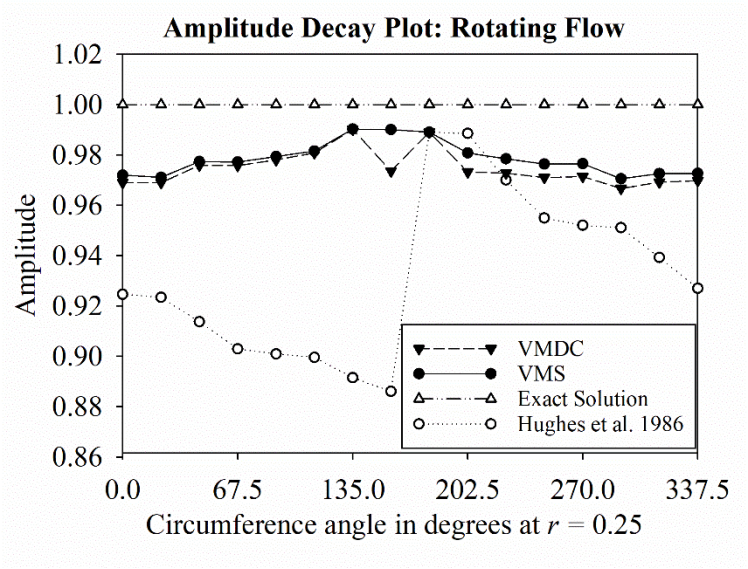

Fig. 4.6. Scalar field amplitude decay along the circumference at r = 0.25.

4.5.3 Couette flow problem with discontinuous force

In this section we use the couette flow problem to investigate the VMDC method to capture discontinuities that are introduced by a discontinuous forcing term. These discontinuities may not conform to the mesh lines, e.g., the surface tension force described in Section 3. The domain of the problem is a rectangle given by $\Omega = [0, L] \times [0, H]$ where $L = 3$ is the length and $H = 1$ is the height of the domain. An interface cuts the mesh through a single element as shown in Fig. 4.7 along a vertical line at $x = 2$. Although the discontinuous forcing term is defined as a line force in [1] via a discrete representation of the interface, in the present work we transform the interface force into a discontinuous body force that produces equivalent effects to test our discontinuous surface force technique. Although this problem is solved over a 2D mesh, the discontinuity is orthogonal to the x-axis and therefore discontinuity capturing capability is verified only in the x-direction. The material properties do not change across the interface, with a constant value of $\rho = 1$

for the density and $\mu = 1$ for the viscosity all over the domain. This allows for the test case to highlight the jump in the pressure field that is induced due to the discontinuous force.

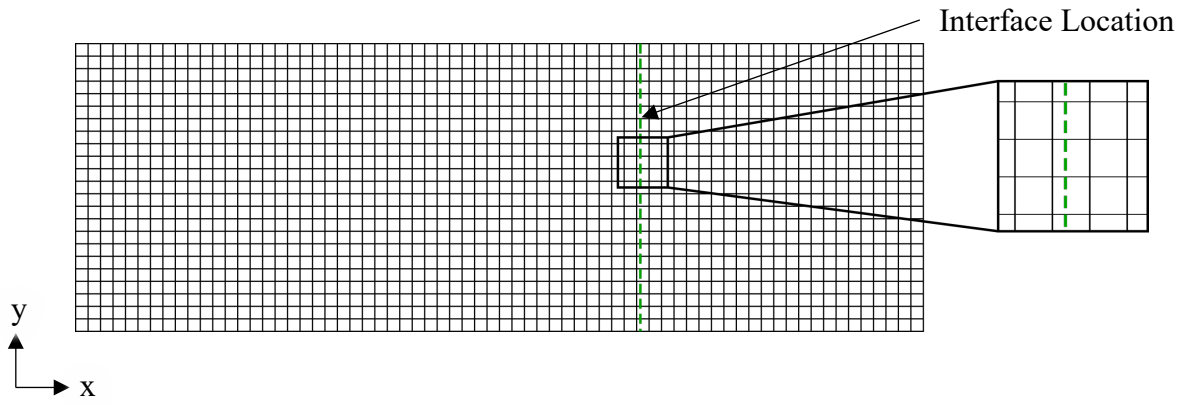

Fig. 4.7. Couette flow problem setup.

We prescribe no-slip boundary condition at the top and bottom, and periodic boundary conditions in the x-direction. Additionally, to simulate the line force which is prescribed in [1] as $f = 1$ at the interface $x = 2$, we apply a discontinuous body force that is defined as

$$f(x) = \begin{cases} -\dfrac{x}{3} & x \le 2 \\ 1 - \dfrac{x}{3} & x > 2 \end{cases} \tag{4.75}$$

This problem has the following exact solution

$$p(x, y) = -\frac{1}{L}x + \mathrm{H}(x - a) \tag{4.76}$$

The Heaviside function is defined as

$$\mathrm{H}(x - a) \equiv \begin{cases} 1 \text{ if } x \ge a \\ 0 \text{ if } x < a \end{cases} \tag{4.77}$$

For the present problem $a = 2$ in (4.77). Fig. 4.8 presents a comparison between the VMDC method and the pressure enrichment method presented in [1], showing enhanced performance of the present method. Additionally, the convergence study in Fig. 4.9 shows superior performance of the VMDC method with mesh refinement, both in terms of the rate convergence as well as the absolute value of the computed error.

Remark: *The characteristic size of the mesh was chosen to be the same as that in [1] for both test problems presented in Sections 5.2 and 5.3. It is important to note that the jump or discontinuity represented by VMDC is confined within a single element, namely, only the element that is intersected by the discontinuity. Since coarse scale shape functions are* C^1 *continuous over element interiors, therefore no kinks can be represented within the element. The variational feature that is yielded by the strong discontinuity at the fine scale level is that the coarse scale jump is confined to a single element only.*

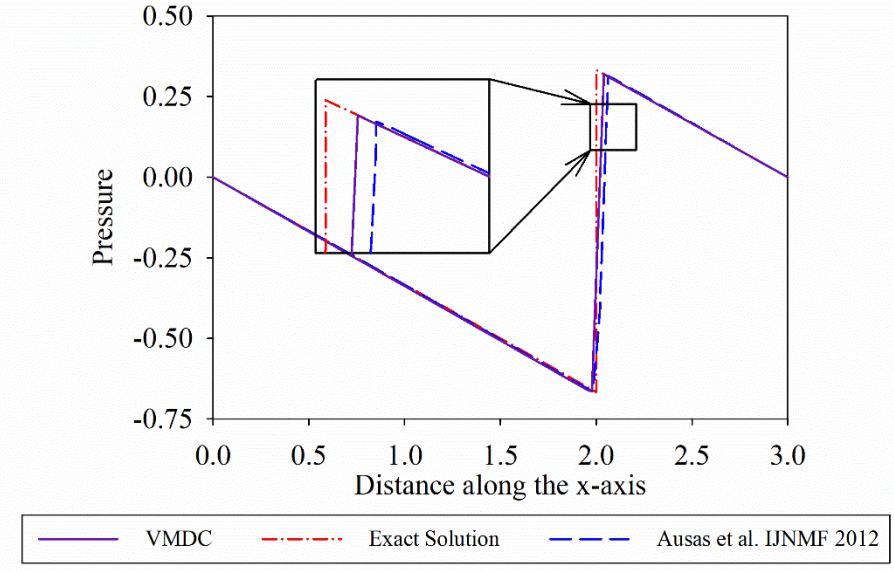

Fig. 4.8. Pressure field across the discontinuity.

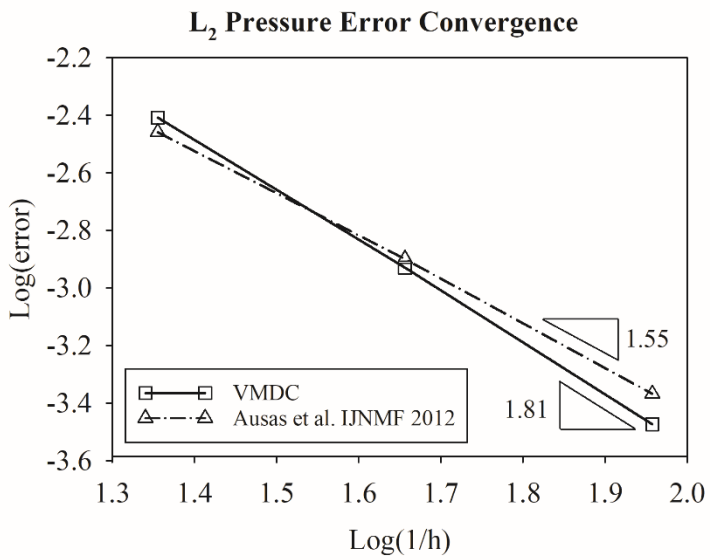

Fig. 4.9. L_2-convergence for Couette flow problem with discontinuous force.

4.5.4 Marangoni effect

In this problem adopted from [2] we examine the dependence of the surface tension force on different aspects of the flow such as temperature, solute concentration or surfactant on the interface between the two phases. This dependence induces variation in the surface tension coefficient along the interface resulting in the Marangoni effect. The Marangoni effect incorporate the variability of surface tension forces in the tangential direction to the interface. This problem is defined on a domain $\Omega = [0,12R]\times[0,4R]$ where the surface tension coefficient is allowed to vary as $\gamma(\boldsymbol{x}) = \gamma_o - \dot{\gamma}x$ with the coefficients being $\gamma_o = 3$ and $\dot{\gamma} = 1$. The interface is centered at $\boldsymbol{x} = (6R, 2R)$ where $R = 0.25$. Along with homogeneous Dirichlet boundary conditions around the domain and unit densities and viscosities in both domains, the exact solution of the problem is given as:

$$p = \begin{cases} p = p_b & r > R \\ p = p_b + \frac{2}{R}(\gamma_o - \dot{\gamma} r\cos\theta) & r < R \end{cases} \tag{4.78}$$

Employing the variational Laplace-Beltrami form of surface tension presented in section 3.1.3 along with the tangentially discontinuous fine-scale enrichment functions proposed therein, the problem is solved with four different meshes of 15×45, 30×90, 60×180 and 120×360 with the corresponding pressure field profiles shown in Fig. 4.10.

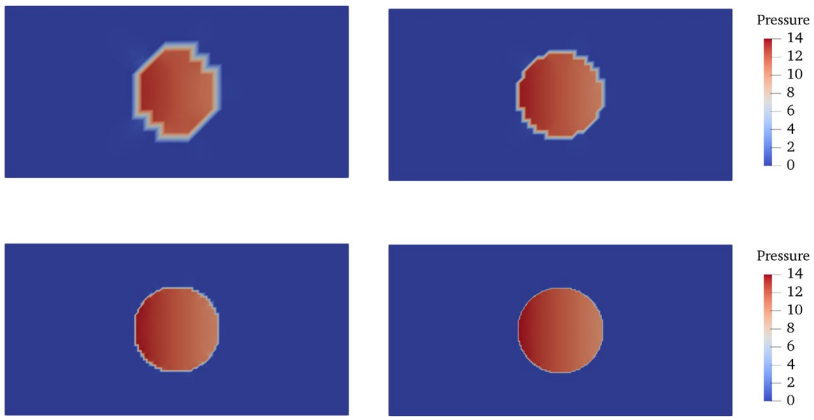

Fig. 4.10. Schematic of the problem.

The pressure field is shown to vary both normal to the interface as well as tangentially along the interface as the pressure jump is not uniform all through the inner domain. This solution is compared with the solution from [2] our VMDC implementation in Fig. 4.11 and superior agreement to the exact solution profile is observed

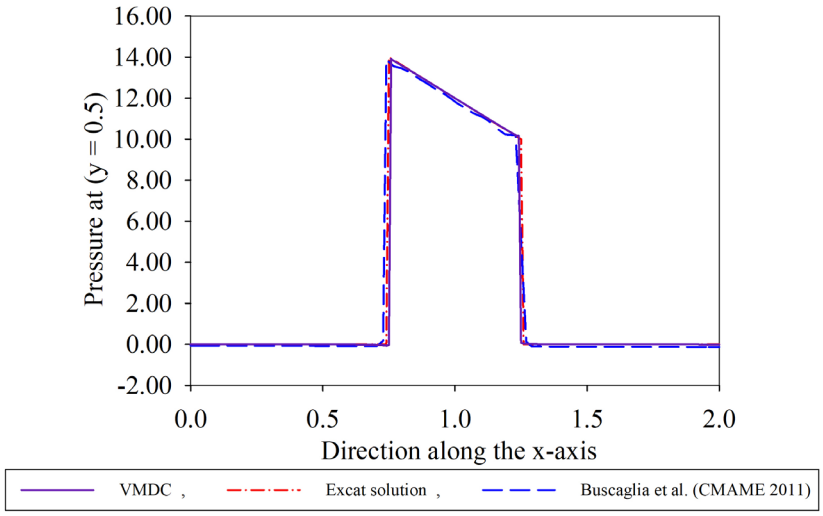

Fig. 4.11. Pressure profile comparison between [2], the VMDC method (60×180 mesh) and the exact solution.

In addition, a convergence study is performed to show optimal convergence achieved by the VMDC method in Fig. 4.12. This confirms the variational consistency of the proposed method and the role of the tangentially discontinuous enrichment functions in accommodating the tangential pressure discontinuity along the interface.

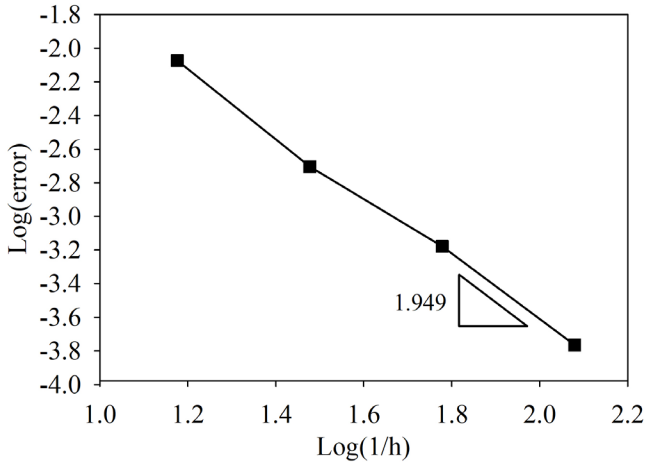

Fig. 4.12. L_2-norm convergence of the pressure field.

4.5.5 Falling Droplet with Solute Mass Transfer

In this section we present a problem involving mass transfer of a solute across an interface of a falling droplet in a lighter fluid. The droplet contains water and the surrounding medium is of Butanol which is saturated with Succinic acid. The problem adopted from [20] starts with a zero-initial concentration of the acid in the water droplet and as the denser droplet falls the acid difusses into the droplet. The properties of the two fluids is given in Table 4.1 including the solubility coefficient that dictates the jump across the interface that is enforced throughout the simulation.

Table 4.1: Material properties for the Falling Droplet Problem.

Material properties of the two fluids	
Viscosity (water droplet)	277 N.s/mm^2
Viscosity (Butanol)	100 N.s/mm^2
Density (water droplet)	996 kg/m^3
Density (Butanol)	866 kg/m^3
Mass Diffusivity (water droplet)	0.037 m^2/s
Mass Diffusivity (Butanol)	0.016 m^2/s
Solubility coefficient (water-droplet)	0.88
Solubility coefficient (Butanol)	1.0

The surface tension coefficient is $\delta = 1$ N/mm which reduceds the deformation of the droplet as it falls. Fig. 4.13-4.16 shows the shape and concentration of the bubble as at different time steps during the simulation which was run with a time step of $\Delta t = 0.01s$. The consecutive stages show

the increase increase in concentration inside the falling droplet despite the sustained jump in concentration at the interface due to Henry's law. This is achieved across a single element due to the discontinuity capturing features of the present method.

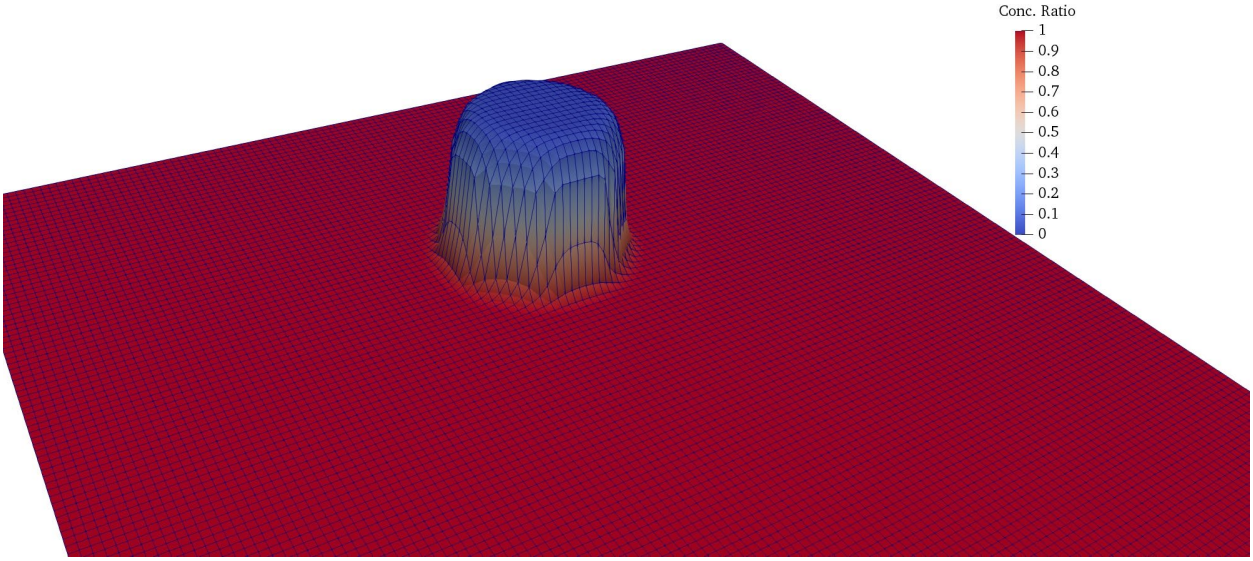

Fig. 4.13. Concentration field at $t = 0.5s$.

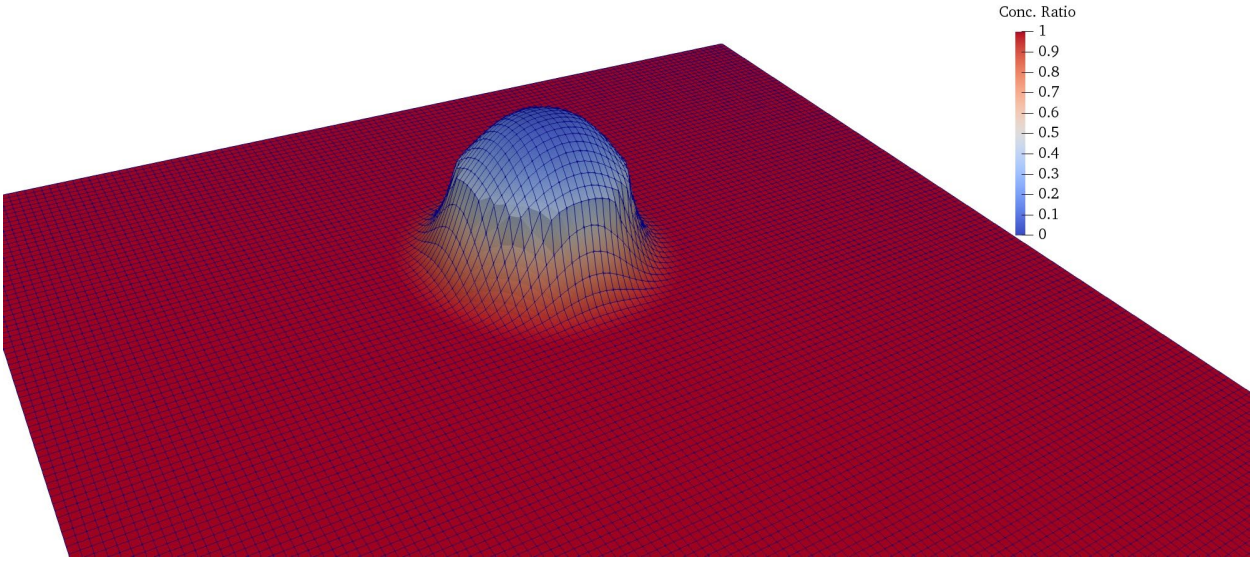

Fig. 4.14. Concentration field at $t = 1.0s$.

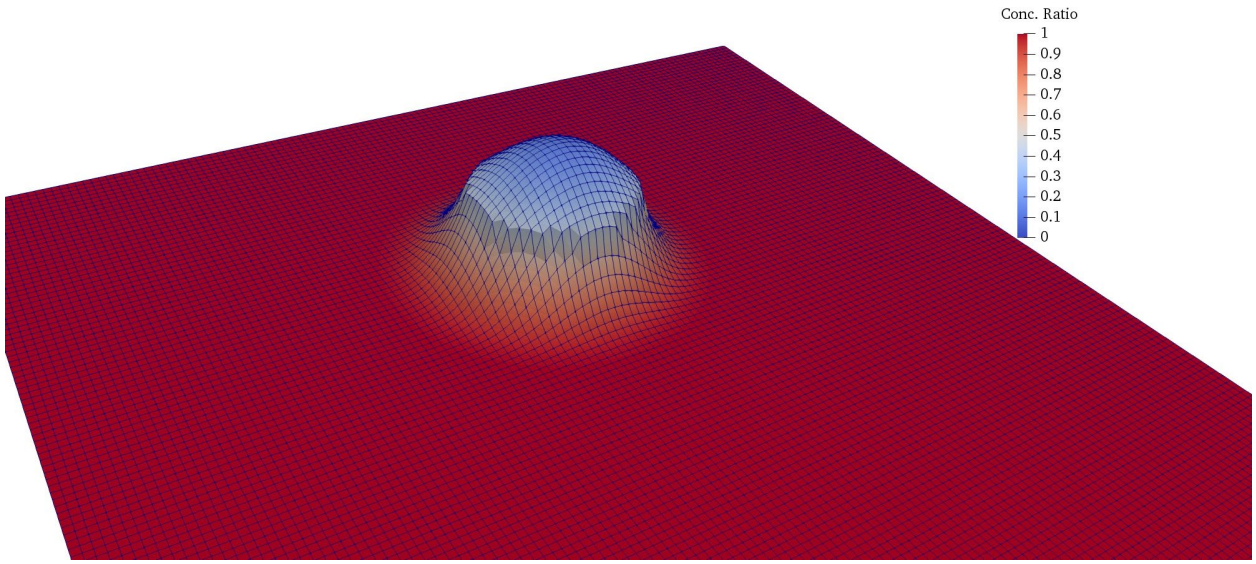

Fig. 4.15. Concentration field at $t = 1.5s$.

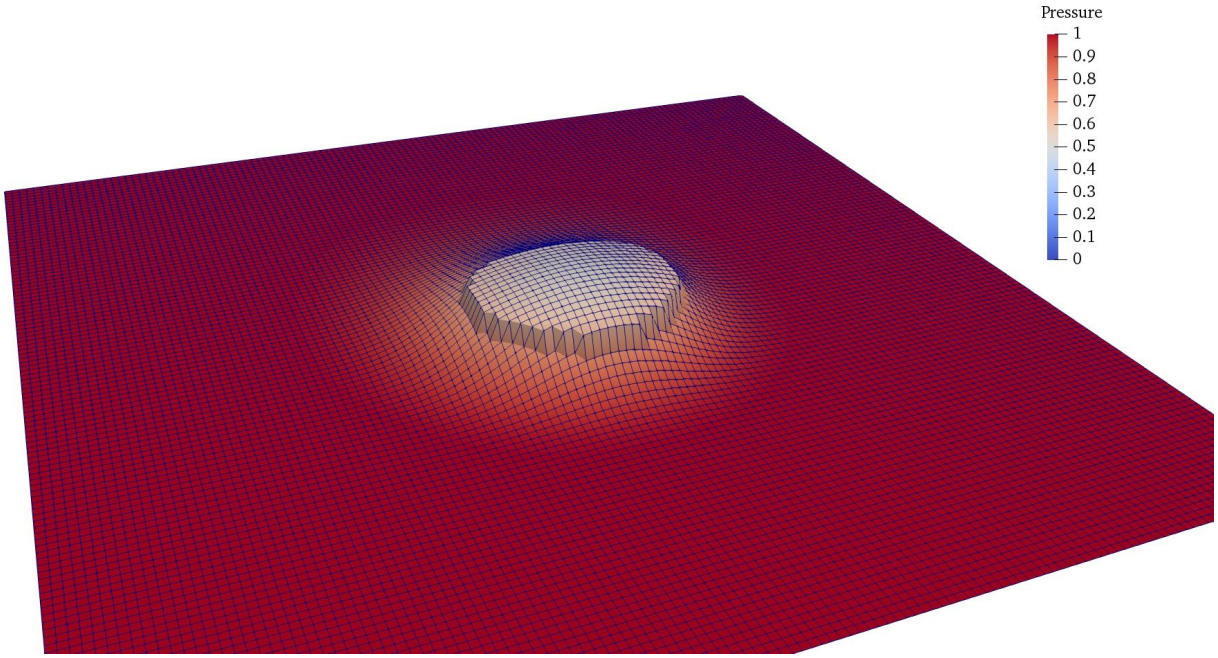

Fig. 4.16. Concentration field at $t = 2s$.

In addition, Fig. 4.17 shows the pressure field jump due to surface tension along with the shape evolution for two time steps. This problem shows the one way coupling between the mommntum equations that drive the concentration advection and also present an example of

oscillation free mass transfer of solute species between fluids while enforcing interface conditions.

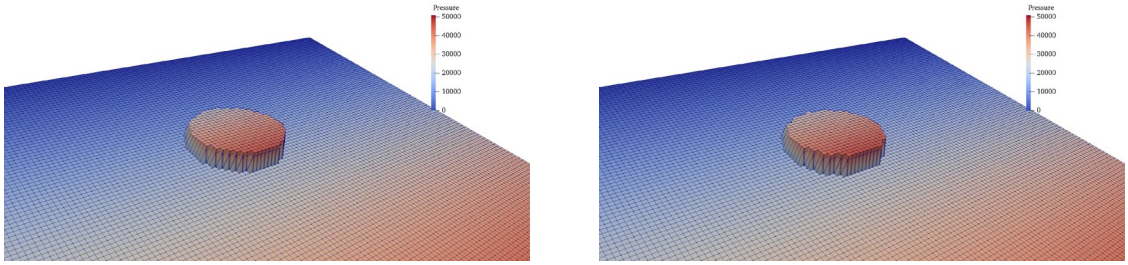

Fig. 4.17. Pressure field at $t = 0.5s$ and $t = 1.0s$.

4.6 References

1. R.F. Ausas, G.C. Buscaglia, R.I. Sergio, A new enrichment space for the treatment of discontinuous pressures in multi-fluid flows, International Journal for Numerical Methods in Fluids. 70 (2012) 829-850.

2. G.C. Buscaglia, R.F. Ausas, Variational formulations for surface tension, capillarity and wetting, Computer Methods in Applied Mechanics and Engineering. 200 (2011) 3011-3025.

3. R. Codina, A discontinuity-capturing crosswind-dissipation for the finite element solution of the convection-diffusion equation, Computer Methods in Applied Mechanics and Engineering. 110 (1993) 325-342.

4. S. Groß, A. Reusken, An extended pressure finite element space for two-phase incompressible flows with surface tension, Journal of Computational Physics. 224 (2007) 40-58.

5. S. Gross, A. Reusken. Numerical methods for two-phase incompressible flows, Springer Science & Business Media. Vol. 40 (2011).

6. T.J. Hughes, M. Mallet, A. Mizukami, A new finite element formulation for computational fluid dynamics: II. Beyond SUPG, Computer Methods in Applied Mechanics and Engineering. 54 (1986) 341-355.

7. S.C. Kwang, D.Y. Kwak, Discontinuous bubble scheme for elliptic problems with jumps in the solution, Computer Methods in Applied Mechanics and Engineering. 200 (2011) 494-508.

8. J. Lee, G. Son, A sharp-interface level-set method for compressible bubble growth with phase change, International Communications in Heat and Mass Transfer. 86 (2017) 1-11.

9. R.J. Leveque, Z. Li, The immersed interface method for elliptic equations with discontinuous coefficients and singular sources, SIAM Journal on Numerical Analysis. 31 (1994) 1019-1044.

10. T. Lin, Y. Lin, X. Zhang, Partially penalized immersed finite element methods for elliptic interface problems, SIAM Journal on Numerical Analysis. 53 (2015) 1121-1144.

11. A. Masud, A. Al-Naseem, Variationally Derived Discontinuity Capturing Methods: Fine Scale Models with Embedded Weak and Strong Discontinuities, Computer Methods in Applied Mechanics and Engineering. In Review.

12. A. Masud, R.A. Khurram, A multiscale/stabilized finite element method for the advection–diffusion equation, Computer Methods in Applied Mechanics and Engineering. 193 (2004) 1997-2018.

13. E. Marchandise, P. Geuzaine, N. Chevaugeon, J. Remacle, A stabilized finite element method using a discontinuous level set approach for the computation of bubble dynamics. Journal of Computational Physics. 225 (2007) 949-974.
14. A. Onea, M. Woerner, D. Cacuci, A qualitative computational study of mass transfer in upward bubble train flow through square and rectangular mini-channels. Chemical Engineering Science. 64 (2009) 1416-1435.

15. A. Reusken, T.H. Nguyen. Nitsche's method for a transport problem in two-phase incompressible flows, Journal of Fourier Analysis and Applications. 15 (2009) 663-683.

16. T.E. Tezduyar, Y.J. Park, Discontinuity-capturing finite element formulations for nonlinear convection-diffusion-reaction equations, Computer Methods in Applied Mechanics and Engineering. 59 (1986) 307-325.

17. B. Vaughan, B. Smith, D. Chopp, A comparison of the extended finite element method with the immersed interface method for elliptic equations with discontinuous coefficients and singular sources, Communications in Applied Mathematics and Computational Science. 1 (2007) 207-228.

18. A. Masud, J. Kwack, A stabilized mixed finite element method for the first-order form of advection–diffusion equation, International Journal for Numerical Methods in Fluids 57 (2008) 1321-1348.

19. A. Masud, R. Calderer, A variational multiscale method for incompressible turbulent flows: Bubble functions and fine scale fields, Computer Methods in Applied Mechanics and Engineering. 200 (2011) 2577-2593.

20. Wang, J., Lu, P., Wang, Z., Yang, C., & Mao, Z. S., Numerical simulation of unsteady mass transfer by the level set method. Chemical Engineering Science, 63(12)- (2008), 3141-3151.

21. Gibou, F., Chen, L., Nguyen, D., & Banerjee, S., A level set based sharp interface method for the multiphase incompressible Navier–Stokes equations with phase change. Journal of Computational Physics, 222(2)-(2007), 536-555.

22. Gjennestad, M. A., & Munkejord, S. T., Modelling of heat transport in two-phase flow and of mass transfer between phases using the level-set method. Energy Procedia, 64(2015) 53-62.

23. Bänsch, E., Finite element discretization of the Navier–Stokes equations with a free capillary surface. Numerische Mathematik, 88(2)-(2001), 203-235.

24. Denis. R., Modelisation and simulation of Leidenfrost effect in micro-droplets. Phd thesis, Université de Grenoble, November 2012.

25. Masud, A., Truster, T. J., A framework for residual-based stabilization of incompressible finite elasticity: Stabilized formulations and F methods for linear triangles and tetrahedra. Computer Methods in Applied Mechanics and Engineering. 267(2013), 359-399.

26. Chen, P., Truster, T. J., Masud, A., Interfacial stabilization at finite strains for weak and strong discontinuities in multi-constituent materials. Computer Methods in Applied Mechanics and Engineering. 328(2018) 717-751.

CHAPTER 5

B-SPLINES AND NURBS BASED FINITE ELEMENT METHODS FOR STRAINED ELECTRONIC STRUCTURE CALCULATIONS[c]

5.1 Motivation

Flexible and stretchable electronics is bringing fundamental changes in the way electronics is getting integrated in our daily lives. At the root of the flexible and stretchable electronics revolution lies the class of materials that retain and even enhances their electronic transport properties in high strain environments. Significant breakthroughs include foldable electronic displays and intelligent textiles comprised of wearable electronics, to name a few. Stretchable electronics is also being conceived for various medical devices. Flexible sheets of electrodes that can be draped over delicate tissues have been used to map abnormalities in the brain [2]. Stretchable high-performance silicon electronics is being used in prosthetic neural interfaces to brain implants for controlling Parkinson's disease [2]. A bio-integrable electronic device attached to the skin can provide irritation-free monitoring of heart and muscle activity [3], and noninvasive diagnosis of sleep apnea.

[c] This Chapter has been adapted from "Masud, A., Al-Naseem, A. A., Kannan, R., & Gajendran, H. (2018). B-Splines and NURBS Based Finite Element Methods for Strained Electronic Structure Calculations. Journal of Applied Mechanics, 85(9), 091009." The copyright owner has provided written permission to reprint the work.

Flexible electronics involves large mechanical deformations of the substrate in which electronic circuits are embedded. Understanding the coupled behavior involving the influence of mechanical strains on electronic properties is fundamental to the design of flexible electronics [4]. Strained silicon is a basic material in the microchip technology today. In strained silicon, electrons experience less resistance and flow up to 70 percent faster, which leads to chips that are up to 35 percent faster. Likewise, with a drive towards smaller and faster microprocessors, the new generation of transistors is being conceived with Carbon nanotubes (CNTs) and graphene as the building blocks. These materials possess remarkable mechanical and electronic properties [5, 6] that are needed in strained nanotechnology. Although availability of accurate interatomic potentials makes classical MD simulations a prominent tool for modeling nanotubes [7], however single scale methods such as “ab initio” quantum mechanical methods or molecular dynamics (MD) methods have difficulty in analyzing hybrid structures due to the limitations in terms of the time and the length scales that these methods are confined to [8, 9]. As such, multiscale theories and algorithms become the only viable option.

This chapter presents a mechano-electronic model for integrated analysis of strained Germanium and strained Silicon Germanium buffer (SiGe) due to a Silicon layer overlay. The electronic structure modeling is done via a self-consistent solution of the Schrödinger wave equation (SWE) that employs electronic potentials that are functions of inter atomic bond lengths and angles. Evolving mechanical strains result in new equilibrated atomic locations that get manifested in the evaluation of the electronic band gap via the evolving nonlinear electronic potentials. A significant feature of the method is a NURBS based finite element formulation for the solution of the Schrödinger wave equation [10] in a self-consistent fashion. In this method the electronic potentials that are based on the interatomic bond-lengths and bond-angles are

consistently updated via the new equilibrated atomic configurations and provide the updated electronic properties of the nanomaterial system. SWE is solved over the continuously deforming nanomaterial, and for each converged and updated state, the self-consistent solution of SWE at critical locations in the spatial domain provides an estimate of the evolving electronic structure of the deforming nanomaterial.

Structure of the chapter is as follows. In Section 5.2 the electronic structure DFT formulation is presented via complete variational formulations of the SWE and Poisson equation to solve the problem in a self-consistent fashion. In Section 5.3 we present a general coupling framework for the mechano-electronic problems and describe how the mechanical properties are evolved to drive the electronic properties used in the SWE. Section 5.4 presents a comparative study for solving the Poisson problem using Isogeometric basis functions with two novel optimal and reduced integration rules for NURBS. Moreover, a full self-consistent problem is solved in Section 5.4 along with two problems incorporating strained electronics.

5.2 Electronic Structures Modeling of Strained Nanomaterials

Strain dependence of the electronic properties has been well documented in the literature. Mechanical strains lead to changes in atomic structure in terms of changes in interatomic bond lengths and bond angles that in turn affect the nano-scale based material properties [11, 12, 13]. Employing the concepts from kinematics, we apply stretching effects to the unit cell lattice vectors of the crystal structure. Modification to the lattice vectors creates a relative shift in the band gap that results from the effect of stretching on the conductive properties of the underlying material. However, this shift is not easily seen in the band-gap diagram unless a similar shift is applied to

the k-points that are used to evaluate the band structure. This results in a shifted band-gap structure that shows the effect of the stretching on the conductivity of the bulk material.

The electronic structure is modeled via the density functional theory (DFT) that provides a framework for calculating electronic properties of materials [14]. In DFT, Schrodinger wave equation and Poisson equation are solved self-consistently until convergence is achieved. Traditional numerical techniques for electronic structure calculations employ plane-wave (PW) basis functions [15, 16], which are not local in the real space and therefore limit the size of the problem that can be solved. In addition, PW functions are limited to periodic boundary conditions which is disadvantageous with respect to cluster and surface calculations.

We have developed a higher-order formulation for the Schrodinger wave equation using B-spline and NURBS basis functions in a finite element setting. In the finite element framework, basis functions have local support that yields banded matrices and minimizes communication between processors in a parallel environment. Finite element framework also accommodates various types of boundary conditions [17], namely Dirichlet, Neumann, and mixed boundary conditions. In addition, FEM based methods accommodate periodic boundary conditions that are particularly useful for cluster and surface calculations. Although, in this chapter we have presented a FEM based method capable to run periodic problems, other FEM based methods have also been proposed in [17, 18, 19] that extend FEM to non-periodic solids. These papers employ FEM with the orbital-free density function theory (OF-DFT) which depends on approximating the exchange energy, correlation energy, and kinetic energy so as to bypass the self- consistent loop and thus help reduce the computational cost. Since the proposed NURBS method is FEM based, it can be used to run non-periodic problems as well. In our earlier work [10] we presented the cost effectiveness of the NURBS-FEM formulation as compared to the costlier planewave formulation.

The present work extends the method for computationally economic solutions via employing the optimal or reduced integration rules as shown in the numerical section. In addition, the advantage of B-spline and NURBS basis functions with respect to Lagrange basis functions is that B-splines and NURBS provide C^{p-1} continuity, where p is the order of B-spline or NURBS. Furthermore, the higher order basis functions can represent high gradient atomic potentials more accurately. Unlike Lagrange basis functions that display Gibbs phenomenon for higher order polynomials, B-spline and NURBS functions have variation diminishing property [20] that is useful in representing high gradients in the solution.

5.2.1 A Variational method for the Schrödinger Wave Equation (SWE):

Schrödinger wave equation (SWE) is a quantum mechanical equation which is used to determine the electronic structure of periodic solids. The eigen-solutions of SWE correspond to different quantum states of the system. SWE has a differential form that involves continuous functions of continuous variables and is therefore suitable for the application of variational methods. Various approaches [9, 15] have been adopted for the solution of SWE that include finite element [21, 22, 23] and finite difference methods [7, 24]. The advantages and utility of finite element method over ab-initio methods are discussed in [10]. In [10] we developed a NURBS based finite element method for SWE which is the basis of present developments.

The SWE for periodic solids can be written as:

$$-\frac{1}{2}\Delta v(\mathbf{x}) - i\mathbf{k}\cdot\nabla v(\mathbf{x}) + \frac{1}{2}k^2 v(\mathbf{x}) + V(\mathbf{x})v(\mathbf{x}) = \varepsilon(\mathbf{k})v(\mathbf{x}), \qquad \forall \mathbf{x} \in \Omega \tag{5.1}$$

$$v(\mathbf{x}) = v(\mathbf{x}+\mathbf{R}), \qquad \forall \mathbf{x} \in \Gamma \tag{5.2}$$

$$\mathbf{n}\cdot\nabla v(\mathbf{x}) = \mathbf{n}\cdot\nabla v(\mathbf{x}+\mathbf{R}) \qquad \forall \mathbf{x} \in \Gamma \tag{5.3}$$

where $\Omega \subset \mathbb{R}^{n_{sd}}$ is an open bounded region with piece wise smooth boundary Γ, $n_{sd} = 3$ is the number of space dimensions, $v(\mathbf{x})$ is the complex valued cell periodic function or the unknown complex scalar field, namely the wave function (eigenfunction), i is the imaginary unit, $\mathbf{x}$ represents the position vector, $\mathbf{n}$ represents outward unit normal vector to the boundary Γ of a unit cell, $V(\mathbf{x})$ is the electronic potential or the potential energy of an electron in a charge density $\rho_e(\mathbf{x})$ at the position $\mathbf{x}$ and is considered periodic over a unit cell. $\varepsilon(\mathbf{k})$ is the eigen-energy associated with the particle as a function of wavevector (position vector in reciprocal space) $\mathbf{k}$.

In the context of pseudopotential approximation [25] and Kohn-Sham framework, the all-electron potential $V(\mathbf{x})$ is replaced by V_{eff}

$$V_{eff} = V_a^L + V_a^{nL} + V_H + V_{XC} \tag{5.4}$$

V_a^L and V_a^{nL} are the local and non-local terms in the pseudopotential approximation [25] for an atom denoted by subscript a. V_{XC} is the exchange correlation potential, and V_H is the Hartree potential.

The Schrödinger wave equation (5.1) is solved in a periodic and finite domain. However, the non-local term V^{nL} involves integration over entire space and over all atoms. Pask *et al.* [20] have proposed a method to reduce the non-local term integrated over all space to an integral form defined over a unit cell. Therefore, we consider a fully separable pseudopotential for an atom denoted by subscript a that usually has the following form.

$$V_a^{nL}(\mathbf{x}, \mathbf{x}') = \sum_{l,m} \chi_{lm}^a(\mathbf{x})\, h_l^a\, \chi_{lm}^a(\mathbf{x}') \tag{5.5}$$

where $\chi^a_{lm}(\mathbf{x})$ is the product of a projector function and spherical harmonics and h^a_l is a constant. This reduces the non-local term to an integral over all space centered around an atom located at $\mathbf{t}_a$ in a unit cell with origin $\mathbf{R}_n$, where n runs over all lattice vectors $\mathbf{R}_n$, and a runs over all atoms in the unit cell. As presented in [10, 20] the integral centered at an atom a can be written as sum of integrals over unit cells surrounding the atom, which can be further reduced to integral over a unit cell.

$$\begin{aligned}&\int \chi^a_{lm}(\mathbf{x}'-\mathbf{t}_a-\mathbf{R}_n)\, v(\mathbf{x}')\, e^{i\mathbf{k}\cdot\mathbf{x}'}\, d\mathbf{x}' = \sum_{n'}\int_{\Omega_{n'}} \chi^a_{lm}(\mathbf{x}'-\mathbf{t}_a-\mathbf{R}_n)\, v(\mathbf{x}')\, e^{i\mathbf{k}\cdot\mathbf{x}'}\, d\mathbf{x}' \\ &= \sum_{n'}\int_{\Omega} \chi^a_{lm}(\mathbf{x}'-\mathbf{t}_a-\mathbf{R}_n-\mathbf{R}_{n'})\, v(\mathbf{x}'-\mathbf{R}_{n'})\, e^{i\mathbf{k}\cdot(\mathbf{x}'-\mathbf{R}_{n'})}\, d\mathbf{x}'\end{aligned} \tag{5.6}$$

Replacing $\mathbf{x}'-\mathbf{R}_n$ by $\mathbf{x}'$ and using $v(\mathbf{x}) = v(\mathbf{x}+\mathbf{R})$ we have

$$\int \chi^a_{lm}(\mathbf{x}'-\mathbf{t}_a-\mathbf{R}_n)\, v(\mathbf{x}')\, e^{i\mathbf{k}\cdot\mathbf{x}'} d\mathbf{x}' = \sum_{n'}\int_{\Omega} \chi^a_{lm}(\mathbf{x}'-\mathbf{t}_a-R_{n'})\, v(\mathbf{x}')\, e^{i\mathbf{k}\cdot\mathbf{x}'}\, e^{i\mathbf{k}\cdot\mathbf{R}_n}\, e^{-i\mathbf{k}\cdot\mathbf{R}_{n'}} d\mathbf{x}' \tag{5.7}$$

The non-local term $e^{-i\mathbf{k}\cdot\mathbf{x}}\, V^{nL}\, e^{i\mathbf{k}\cdot\mathbf{x}}\, v(\mathbf{x})$ then reduces to

$$\sum_{a,l,m}\left\{\begin{aligned}&e^{-i\mathbf{k}\cdot\mathbf{x}}\sum_n\left[e^{i\mathbf{k}\cdot\mathbf{R}_n}\ \chi^a_{lm}(\mathbf{x}-\mathbf{t}_a-\mathbf{R}_n)\right]\times h^a_l \times \\ &\int_\Omega\left(e^{i\mathbf{k}\cdot\mathbf{x}'}\sum_{n'}\left[e^{-i\mathbf{k}\cdot\mathbf{R}_{n'}}\ \chi^a_{lm}(\mathbf{x}'-\mathbf{t}_a-\mathbf{R}_{n'})\right] v(\mathbf{x}')\, d\mathbf{x}'\right)\end{aligned}\right\} \tag{5.8}$$

5.2.2 The standard weak form for SWE

The standard weak form for SWE is:

$$-\left(w, i\mathbf{k}\cdot\nabla v\right)+\frac{1}{2}\left(\nabla w,\nabla v\right)+\frac{1}{2}\left(w,k^2 v\right)+\left(w,V_{eff}\, v\right)=\left(w,\varepsilon\, v\right) \tag{5.9}$$

where w is the weighting function for v, and $(\cdot,\cdot)=\int_\Omega(\cdot)\,\mathrm{d}\Omega$ i.e., L_2 product of the indicated arguments over domain Ω. We denote as $\mathcal{V}\subset H^1(\Omega^{n_{sd}})\cap C^0(\Omega^{n_{sd}})$ the space of trial solutions and weighting functions for the unknown scalar field.

$$\mathcal{V}=\left\{v\,|\,v\in H^1(\Omega^{n_{sd}}),v(\mathbf{x})=v(\mathbf{x}+\mathbf{R})\quad\forall\mathbf{x}\in\Gamma\right\} \tag{5.10}$$

Let $\mathcal{V}^h\subset\mathcal{V}$ denote the finite-dimensional approximation of space of trial solutions and weighting functions for the unknown scalar field. The Galerkin form of the problem is

$$-\left(w^h,i\mathbf{k}\cdot\nabla v^h\right)+\frac{1}{2}\left(\nabla w^h,\nabla v^h\right)+\frac{1}{2}\left(w^h,k^2v^h\right)+\left(w^h,V_{eff}v^h\right)=\left(w^h,\varepsilon\,v^h\right) \tag{5.11}$$

Let $v^h=\sum_{i=1}^n c_iN_i$ and $w^h=\sum_{i=1}^n d_iN_i$, where c_i,d_i are complex coefficients associated with corresponding shape functions for the trial solution and weighting functions, respectively. Since the shape functions have local support, the discrete equation takes the following form.

$$\sum_j K_{ij}c_j=\varepsilon\sum_j M_{ij}c_j \tag{5.12}$$

where

$$K_{ij}=\mathop{\mathbb{A}}_{e=1}^{numel}K_{ij}^e;\quad M_{ij}=\mathop{\mathbb{A}}_{e=1}^{numel}M_{ij}^e \tag{5.13}$$

$$K_{ij}^e=\int_{\Omega^e}\left(\frac{1}{2}\nabla N_i\cdot\nabla N_j-i\mathbf{k}\cdot N_i\nabla N_j+\frac{1}{2}\mathbf{k}^2N_iN_j+V_{eff}N_iN_j\right)d\mathbf{x} \tag{5.14}$$

$$M_{ij}^e=\int_{\Omega^e}N_iN_j\,d\mathbf{x} \tag{5.15}$$

where $\mathbb{A}$ stands for the assembly operation, $\int_{\Omega^e}$ represents integration over an element domain Ω^e in the finite element mesh, and *numel* is the total number of elements in the finite element mesh.

The effective potential, V_{eff}, is non-linear because of the presence of V_H and V_{XC} that are in turn functions of the electronic charge density. The electronic density (ρ_e) is calculated from eigenfunctions [10].

5.2.3 Evaluation of Hartree and Local pseudopotential approximations

The Hartree potential V_H and the local terms in the pseudopotential approximation V_a^L are obtained via the solution of the Poisson problem for the total Coulomb potential together with periodic Dirichlet and Neumann boundary conditions.

$$\nabla^2 V_C = f(\mathbf{x}), \qquad \forall \mathbf{x} \in \Omega \tag{5.16}$$

$$V_C(\mathbf{x}) = V_C(\mathbf{x}+\mathbf{R}), \qquad \forall \mathbf{x} \in \Gamma \tag{5.17}$$

$$\mathbf{n} \cdot \nabla V_C(\mathbf{x}) = \mathbf{n} \cdot \nabla V_C(\mathbf{x}+\mathbf{R}), \qquad \forall \mathbf{x} \in \Gamma \tag{5.18}$$

where $V_C = V_H + V_a^L$, and $f(\mathbf{x}) = -4\pi\rho_e(\mathbf{x}) + \sum_a 4\pi\rho_a^L(\mathbf{x})$, and $\mathbf{n}$ represents outward unit normal vector to the boundary Γ of the unit cell Ω. The charge densities that are consistent with a derivative periodic smoothly varying function are required to be net neutral in the unit cell.

$$\begin{aligned} \int_\Omega f(\mathbf{x})\, d\Omega &= \int_\Omega \Delta V_C(\mathbf{x})\, d\Omega = \int_\Gamma \mathbf{n} \cdot \nabla V_C(\mathbf{x})\, d\Gamma \\ &= \int_\Gamma \left(\mathbf{n} \cdot \nabla V_C(\mathbf{x}) - \mathbf{n} \cdot \nabla V_C(\mathbf{x}+\mathbf{R}) \right) d\Gamma = 0 \end{aligned} \tag{5.19}$$

The local pseudopotential term is converted into equivalent density term. These density terms for each nuclei position are then superimposed at a location $\mathbf{x}$ in order to obtain the total density. (See section 4 of Pask *et al*. [22] for details.) In addition, the density term $f(\mathbf{x})$ also includes the

electron charge density. Thus, the solution of Poisson equation includes the effects of local pseudopotential term as well as the Hartree potential.

The standard weak form for the Poisson problem can be written as

$$-\left(\nabla w, \nabla V_C\right) = \left(w,\, f\left(\mathbf{x}\right)\right) \tag{5.20}$$

where w is the weighting function for V_C. The space of trial solutions and weighting functions for the unknown scalar field is defined as

$$\mathcal{S} = \left\{ V_C \,|\, V_C \in H^1(\Omega^{n_{sd}}), V_C\left(\mathbf{x}\right) = V_C\left(\mathbf{x}+\mathbf{R}\right) \quad \forall \mathbf{x} \in \Gamma \right\} \tag{5.21}$$

Let $\mathcal{S}^h \subset \mathcal{S}$ denote the finite-dimensional approximation of space of trial solutions. The discretized weak form is:

$$-\left(\nabla w^h, \nabla V_C^h\right) = \left(w^h,\, f\left(\mathbf{x}\right)\right) \tag{5.22}$$

In [10] we developed a solution method for the Schrodinger wave equation that employs a higher-order formulation using B-spline and NURBS basis functions in a finite element setting. B-splines and NURBS (Non-uniform rational B-splines) are parametric functions of rational polynomials. A rational B-spline curve in $\mathbb{R}^{n_{sd}}$ is defined as follows.

$$C\left(\xi\right) = \sum_{i=1}^{n} B_i R_{i,p}\left(\xi\right) \tag{5.23}$$

where

$$R_{i,p}\left(\xi\right) = \frac{N_{i,p}\left(\xi\right) w_i}{\sum_{j=1}^{n} N_{j,p}\left(\xi\right) w_j} \tag{5.24}$$

is the i^{th} rational B-spline basis function of degree p corresponding to control point $B_i \in \mathbb{R}^{n_{sd}}$

and weight w_i for a knot vector $\Xi = \{\xi_i\}_{i=1}^{n+p+1}$. When rational B-splines are defined in a knot vector that is non-uniform and open, they are called non-uniform rational B-splines (NURBS). Higher dimensional NURBS are defined by taking tensor product of one-dimensional NURBS. For a detailed description on how to obtain control points and control net for different geometric configurations, interested reader is referred to Hughes *et al*. [20] and Piegl and Tiller [26].

The advantage of B-spline and NURBS basis functions with respect to Lagrange basis functions are that B-splines and NURBS provide C^{p-1} or C^{p-1-k} continuity, where p is the order of B-spline or NURBS, and k refers to multiplicity of knot values in knot vector. In addition, the higher order basis functions can represent high gradient atomic potentials more accurately. In addition, unlike Lagrange basis functions that display Gibbs phenomenon for higher order polynomials, B-spline and NURBS functions have variation diminishing property [20] This property is extremely useful in representing high gradients in the solution. Another significant attribute of the use of NURBS functions in our method is that it can lead to an exact representation of the geometric description of the domain under consideration. Specifically, for electronic structure calculations, NURBS functions can represent geometries with conic sections, like cylinders or spheres, accurately with minimum parameters. Unlike the wave-function based technology that is primarily applicable to periodic solids, the finite element-based method will be applicable to CNTs and nanoribbons that have non-periodic geometric configurations.

5.3 Coupled Mechano-Electronic Modeling

For the mechano-electronic interaction problems, each of the two coupled components has different mathematical and numerical properties, as well as well-established but distinct numerical solvers. Advancing the mechanical and electronic systems simultaneously and in a loosely coupled

manner is appealing because it has the potential of reducing the total simulation time and therefore be computationally economical. A coupling strategy between quasi-continuum methods and Kohn-Sham DFT formulations has been a topic of discussion for non-periodic problems [18, 19]. One option is to solve the nonlinear multiscale mechanical problem for elastically deforming substrate [27, 28] or employ the general multiscale framework facilitated by [29, 30, 31]. Quasi continuum methods for elastically deforming nanomaterials have also been employed to evaluate mechanical properties of these nanomaterials [13, 32, 33]. This would provide information on the distribution of strain fields that in turn would provide the new equilibrated bond lengths and bond angles as shown in Fig. 5.1. Once the updated mechanical configuration is obtained, a self-consistent solution of the Schrödinger wave equation [10, 34] is obtained on the updated mechanically deformed nanomaterial to extract the effects of mechanical deformations on the changes in electronic structure and properties. This leads to a procedure that can be described as a loosely coupled solution algorithm, shown in Fig. 5.2. Here W and U are the vectors of state variables for the mechanical and electronic problem, respectively. The spatial coordinates of the nanomaterial are updated via the evolving nanoscale based displacement field represented as d_n, and this algorithm facilitates one-way coupling between the interacting fields. In the numerical section we model the effects of the mechanical part via an applied strain field as described in section 5.3.2.

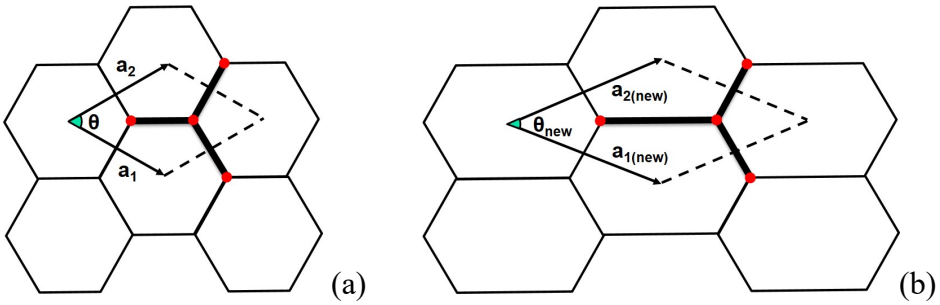

Fig. 5.1: Schematic plot of (a) unstrained lattice and (b) strained lattice vectors.

5.3.1 The prescribed strain tensor for Unit Cell problem

Our objective in this work is to focus on the electronic structure calculations of stretchable semiconducting materials. Consequently, we apply mechanical deformation as an applied strain field, which in the nonlinear elastic framework is incrementally applied, thereby giving rise to evolving effective potential that drives the SWE. Due to the planar configuration of semiconductors, this stretching is applied biaxially in the plane parallel to the layout of the semiconductor, and it results in a reduction in thickness in the direction perpendicular to the stretched layer. This is analogous to the Poisson effect in continuum, but in the present context it is at the quantum scale. The applied strains that lead to the stretching of the unit cell can be specified in multiple ways. In this work we have employed two loading conditions. In the first case we directly prescribe the biaxial strain in the planar directions and calculate the strain in the third direction using empirically determined moduli [35, 36]. In the second case we utilize empirical formulas for strain that is induced by overlaying of a Silicon layer on Germanium to create a SiGe buffer. Nevertheless, the modification of the lattice vectors and *k*-point location is the same in both the cases as shown by the band-structures in sections 5.4.2.4 and 5.4.2.5, respectively.

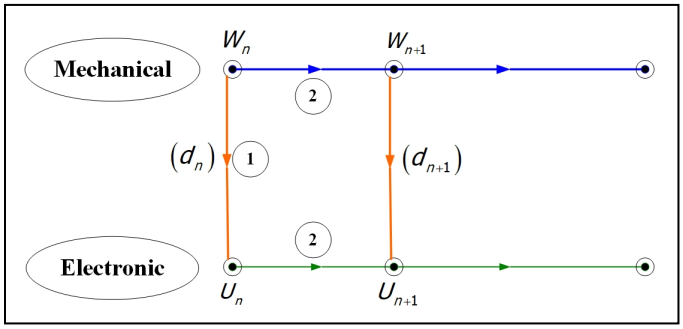

Fig. 5.2: One-way coupled solution procedure.

5.3.1.1 Strain tensor for Silicon layer on SiGe buffer:

We present the biaxial strain tensor together with the corresponding Poisson ratio that is needed to determine the strain component in the third direction. The three axial strain components in terms of the lattice constant a_0 are:

$$\boldsymbol{\varepsilon} = \begin{bmatrix} \varepsilon_{11} & 0 & 0 \\ 0 & \varepsilon_{22} & 0 \\ 0 & 0 & \varepsilon_{33} \end{bmatrix} \tag{5.25}$$

$$\varepsilon_{11} = \varepsilon_{22} = \frac{a_0(Si_{1-x}Ge_x) - a_0(Si)}{a_0(Si)} \tag{5.26}$$

$$\varepsilon_{33} = -\frac{C_{12}}{C_{11}}\varepsilon_{11} \tag{5.27a}$$

$$\begin{aligned} C_{11} &= 1677.2 \text{ Pa} \\ C_{12} &= 649.8 \text{ Pa} \end{aligned} \tag{5.27b}$$

where the lattice constant a_0 of the SiGe buffer is evaluated as function of the lattice constants of bulk Germanium $a_0(\text{Ge})$ and bulk Silicon $a_0(\text{Si})$ as follows:

$$a_0 = (\text{Si}_{1-\alpha}\text{Ge}_\alpha) = a_0(\text{Si}) + 0.200326\,\alpha\,(1-\alpha) + [a_0(\text{Ge}) - a_0(\text{Si})]\,\alpha^2 \tag{5.28}$$

where α is the ratio of Germanium to SiGe buffer. Dependence of the lattice vectors on the spatial coordinates $\boldsymbol{x}$ results requires an update of the primitive lattice vectors of the Brillouin zone. This also affects the *k*-point grid locations. The updated lattice vectors are a function of strain and are given as:

$$\boldsymbol{a}_1 = a_0(1+\varepsilon_{11})\boldsymbol{x} \quad ; \quad \boldsymbol{a}_2 = a_0(1+\varepsilon_{22})\boldsymbol{y} \quad ; \quad \boldsymbol{a}_3 = a_0(1+\varepsilon_{33})\boldsymbol{z} \tag{5.29}$$

5.3.1.2 Strain tensor for bulk Germanium:

Strained bulk Germanium has been shown to have enhanced light emission and electronic conduction properties [36]. Following along Section 5.3.2.1, we strain bulk Germanium biaxially. Utilizing the compliances for bulk Germanium given in (5.30b) the strain in the orthogonal direction ε_{33} is given by (5.27a). The prescribed strains may be incrementally increased as follows:

$$\varepsilon_{11} = \varepsilon_{22} = \{-3, -2, ..., 2, 3\} \ \% \tag{5.30a}$$

where the negative strain values indicate compression of the bulk Germanium and the positive values indicate stretching. The compliance coefficients of Germanium are:

$$\begin{aligned} C_{11} &= 129.2 \ \text{GPa} \\ C_{12} &= 47.9 \ \text{GPa} \end{aligned} \tag{5.30b}$$

Employing (5.29) we are able to find the new lattice vectors used in the evaluation of the effective potential V_{eff} that is employed in solving both the Poisson equation and the SWE.

5.4 Numerical Results

Numerical section investigates five different aspects of the model and the method. Employing triclinic model, we first present a study on the numerical quadrature points that are sufficient for full numerical integration and this aspect relates to numerical efficiency of the method. The second test case employs an all electron potential for Indium atom and total energy of the system is used as a measure of the convergence of the numerical method. Employing bulk Silicon, we investigate the self-consistent solution capability of the method, and then employ bulk Germanium to model the electronic band gap as a function of applied stretching. The last test case investigates doping

where Silicon grown over Germanium substrate to create SiGe buffer results in enhanced electronic conduction properties of the semiconducting nanomaterial.

5.4.1 Poisson problem: Model analytical potential

In the proposed method the nonlinear SWE and its potentials are solved in a self-consistent fashion which requires the solution of the Poisson equation that yields the Hartree and local potentials. To validate the stability and accuracy of the Poisson problem for various order B-splines we employ an analytical potential that is given by

$$V = \sin\left(2\pi x\right)\sin\left(2\pi y\right)\sin\left(2\pi z\right) \tag{5.31}$$

The corresponding forcing function, $f\left(x,y,z\right)$, is given by the Laplacian of the potential.

$$f\left(x,y,z\right) = -12\pi^2 \sin\left(2\pi x\right)\sin\left(2\pi y\right)\sin\left(2\pi z\right) \tag{5.32}$$

The domain under consideration is a unit cube, where periodic boundary condition is applied on corresponding surfaces. Four uniform meshes composed of 4^3, 6^3, 8^3 and 12^3 elements for B-spline order 2, 3 and 4 are considered. In the legend, the numbers in brackets denote the number of degrees of freedom per direction along the three lattice vectors for the corresponding meshes and polynomial orders.

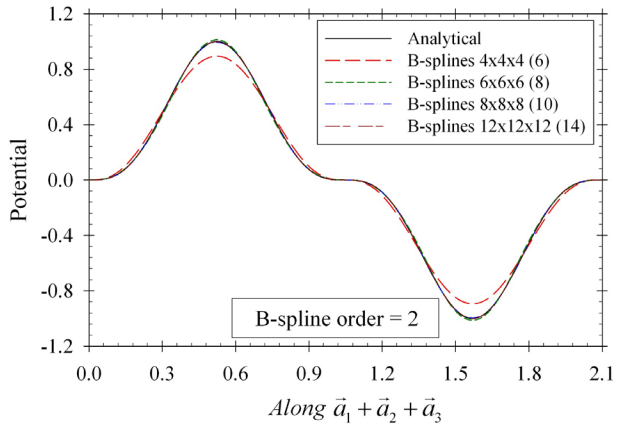

(a)

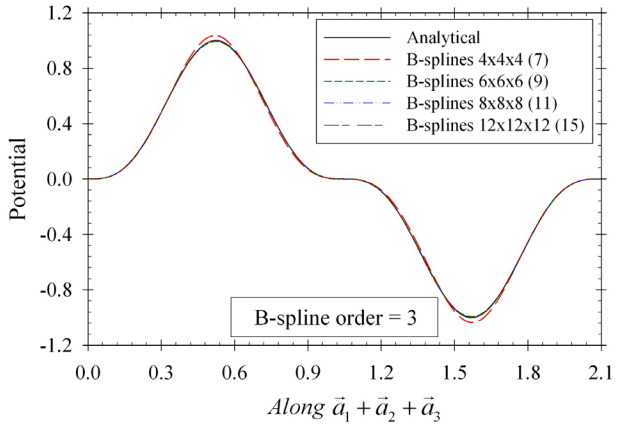

(b)

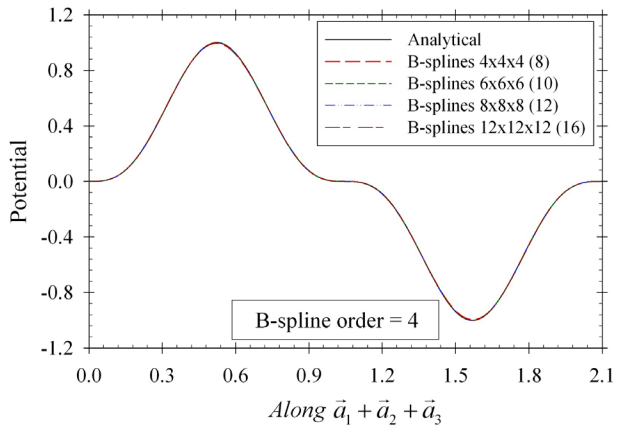

(c)

Fig. 5.3: Plot of the potential along the body diagonal (a) $p = 2$, (b) $p = 3$, (c) $p = 4$

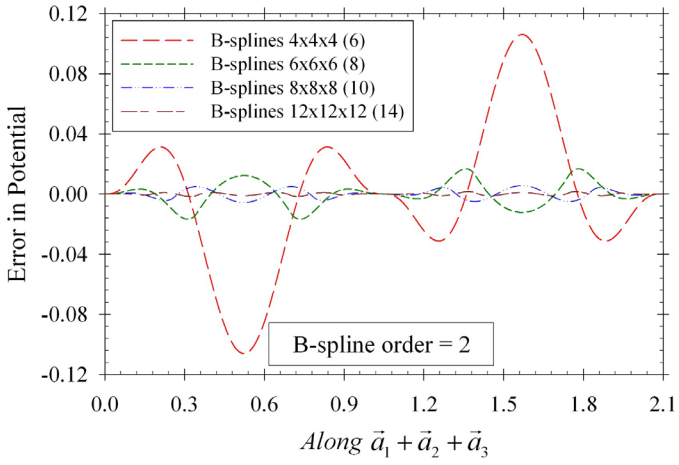

(a)

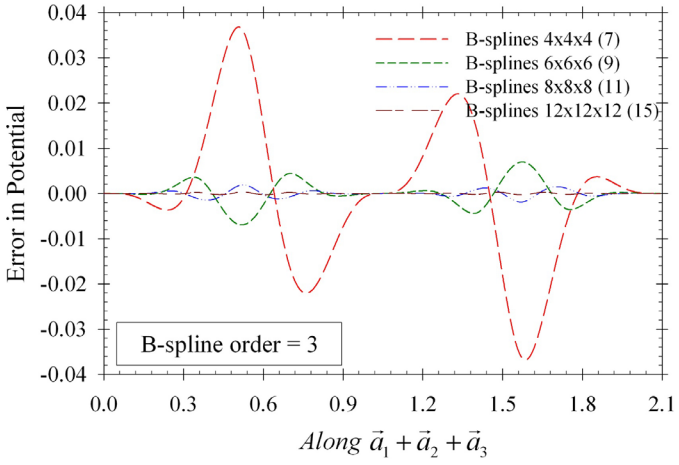

(b)

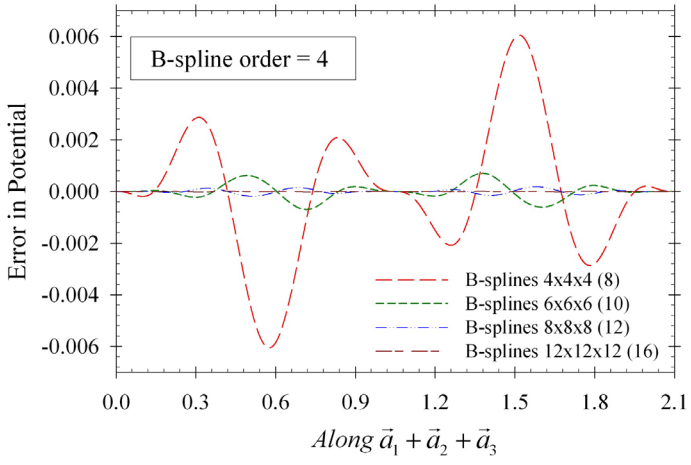

(c)

Fig. 5.4: Error in the potential along the body diagonal (a) $p = 2$, (b) $p = 3$, (c) $p = 4$

Figures 5.3 (a-c) are plots of the potential along body diagonal for $p = 2, 3, 4$. The plots of error in potential along body diagonal are shown in Figures 5.4 (a-c). Even for the crudest mesh, it can be seen that by increasing the NURBS order, the maximum amplitude of error decreases by an order of magnitude. Fig. 5.5 shows the normalized L_2 norm of the error in the computed potential as a function of mesh refinement. Here normalization is done with respect to the L_2 norm of the analytical potential in (5.31), and an optimal convergence rate is attained in each of the cases.

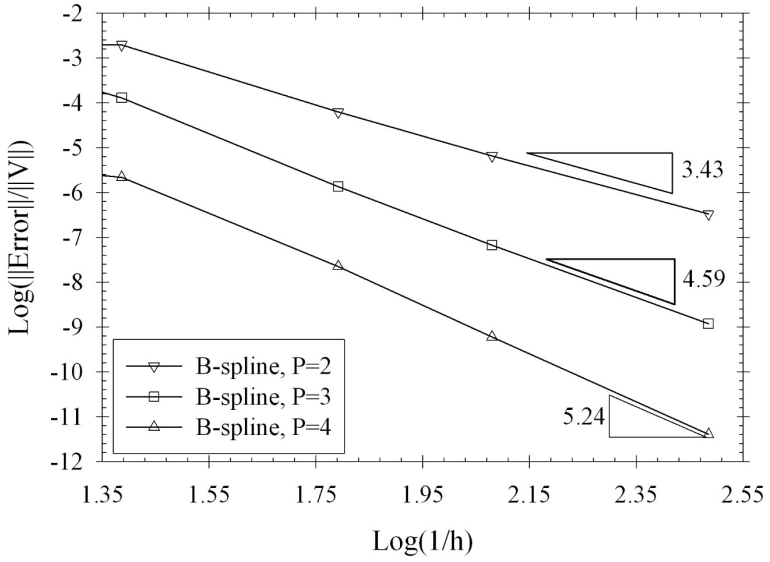

Fig. 5.5: Convergence rates for the Poisson problem with analytical potential in (5.31).

5.4.2 Optimal and Reduced Integration Rules for NURBS: The Triclinic Problem

We employ the triclinic charge density model (for details see section 4.2.1 Masud *et al.* [10]) as a test case to study the optimality, accuracy and computational efficiency of the optimal/reduced integration rules recently developed for isogeometric basis functions [37]. The optimal rule is a quadrature rule that exactly integrates NURBS and B-splines with the least number of quadrature

points. However, the reduced rule is described as the optimal rule for NURBS of order p-1 that is then used to integrate NURBS of order p, and this reduced rule may also be exact in some circumstances. The optimal and reduced integration rules for NURBS are compared to the Gaussian quadrature rule that uses n points to integrate NURBS of order p where $p \le 2n-1$. Using the optimal Gaussian rule (i.e., least number of points) for $p = 2, 3, 4$ and 5 optimal convergence was still not achieved. Optimal convergence in $L_2(\Omega)$ norm was only achieved when a Gauss rule with $n = 5$ was used. Figures 5.6 and 5.7 show a comparison of the convergence in $L_2(\Omega)$ using the 5-point Gauss rule and the optimal rule for NURBS with order $p = 2, 4$ and 5 and reduced rule for order $p = 3$.

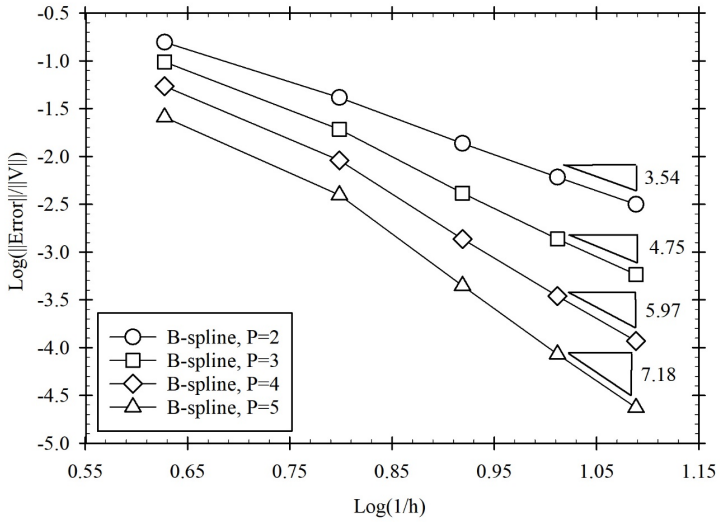

Fig. 5.6: Convergence rates attained with 5-point Gauss quadrature rule.

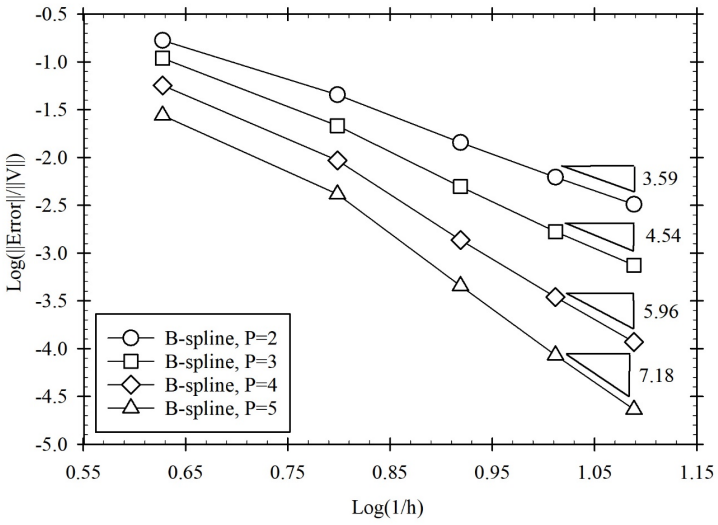

Fig. 5.7: Convergence rates attained using Optimal rule for p = 2,4,5 and using the reduced rule for p = 3.

Comparing the computational cost via number of integration points for the two integration rules that achieve comparable accuracy and convergence rates in Table 5.1, the optimal rule for NURBS can achieve a similar convergence rate with less than 50% the number of integration points than are needed for the 5-point Gaussian rule. Moreover, using the reduced rule for $p = 3$ the number of integration points are reduced by approximately 85% while still retaining the accuracy.

Remark: *Optimal Rule with variable integration points used for NURBS with p=2,4,5 and reduced rule for p=3. The reduced rule is obtained by using the integration points generated for p=2 in evaluating the integrals for NURBS with p=3. This leads to a small decrease in the convergence rate in comparison with the expensive 5-point Gauss rule.*

Table 5.1**:** Comparison of computational cost via the integration point count between two integration methods.

Mesh Size	Total Number of Gaussian Integration Points (P=2,3,4 and 5)	Total Number of Optimal Rule Integration Points (P=2)	Total Number of Reduced Rule Integration Points (P=3)	Total Number of Optimal Rule Integration Points (P=4)	Total Number of Optimal Rule Integration Points (P=5)
4x4x4	8000	729	729	2744	4096
6x6x6	27000	2197	2197	8000	12167
8x8x8	64000	4913	4913	17576	27000
10x10x10	125000	9261	9261	32768	50653
12x12x12	216000	15625	15625	54872	85184

Remark: *When using optimal Gaussian quadrature rule of 2n-1 for NURBS, suboptimal convergence rates are observed. Thus, without a strategic sampling of points, as done in the case of the optimal/reduced rules given in Hughes et.al. [37], an incrementally increasing number of Gaussian integration points is needed to achieve optimal convergence for NURBS of increasing order.*

5.4.3 Self-consistent Study

We now present a set of problems that utilize an iterative self-consistent formulation to solve the Poisson and Kohn-Sham equations to achieve a converged band-gap structure of the underlying semiconductor.

5.4.3.1 Indium atom with all electron potential (1D case)

This case employs all electron potential of Indium atom embedded in the Kohn-Sham equations [24] that are solved in a radial domain defined over interval $[0, \xi]$. Since this is a one-dimensional problem for an isolated atom, we solve the radial Schrödinger equation and Poisson problem in spherical coordinates.

$$\left[-\frac{1}{2}\frac{d^2}{dr^2}+\frac{l(l+1)}{2r^2}+V(r)\right]R_{n,l}(r)=\varepsilon_{n,l}\ R_{n,l}(r) \tag{5.33}$$

$$\lim_{r\to 0}R_{n,l}(r)=\lim_{r\to\infty}R_{n,l}(r)=0 \tag{5.34}$$

where $R_{n,l}(r)$ is the radial wave-function, l stands for orbital angular momentum quantum number, n stands for principal quantum number, $\varepsilon_{n,l}$ stands for eigenvalues.

The all electron potential is given by

$$V(\mathbf{r})=V_n+V_H+V_{XC}=-\frac{49}{r}+V_H+V_{XC} \tag{5.35}$$

$$V_H(\mathbf{r})=\int\frac{\rho_e(\mathbf{r}')}{|\mathbf{r}-\mathbf{r}'|}d\mathbf{r}'=4\pi\int_{r'=0}^{\infty}r'^2\frac{\rho_e(r')}{|r-r'|}dr' \tag{5.36}$$

$$V_{XC}=V_{XC}(\mathbf{r};\rho_e) \tag{5.37}$$

$$\rho_e(r)=\frac{1}{2\pi}\sum_{n,l}(2l+1)f_{n,l}\frac{R_{n,l}^2(r)}{r^2} \tag{5.38}$$

where $\mathbf{r}$ represents position vector in three-dimensional space and r represents radial distance from nucleus of an atom. V_H is the Hartree potential, V_{XC} is the exchange-correlation potential, and $f_{n,l}$ is the occupation number.

Since the electron charge density and Hartree terms are functions of radial co-ordinates only, the corresponding Poisson problem to be solved for obtaining the Hartree term simplifies to

$$\frac{d^2U(r)}{dr^2} = -4\pi r\rho_e \tag{5.39}$$

where $U(r) = rV_H(r)$, and boundary conditions imposed are the zero Dirichlet boundary conditions.

$$U(r)\big|_{r=0} = 0; \quad U(r)\big|_{r\to\infty} = 0 \tag{5.40}$$

We use Vosko-Wilk-Nusair (NWN) functional of density for obtaining correlation terms [38]. A logarithmic mesh is created along the radial direction by varying the control points of the B-spline mesh as follows.

$$r_{\max} = 20; \quad \delta = \frac{10r_{\max}}{\left(10+\left(6-r_{\max}\right)\right)200} \tag{5.41}$$

$$r_p = \frac{r_{\max}}{e^{\delta(numel+p-1)}-1}; \quad B_i = r_p\left(e^{(i-1)\delta}-1\right) \tag{5.42}$$

where *numel* stands for the number of elements along radial direction, B_i stands for the i^{th} control point and p stands for the order of the B-spline.

Once the electron charge density is calculated, the total energy $E_t(\rho)$ can be calculated as follows [23].

$$\begin{aligned} E_t(\rho) &= E_k(\rho) + E_n(\rho) + E_H(\rho) + E_{XC}(\rho) \\ &= \sum_i f_i \varepsilon_i + \int \tilde{V}(\mathbf{r}) \rho(\mathbf{r}) d\mathbf{r} \end{aligned} \tag{5.43}$$

where $E_k(\rho)$ is the kinetic energy, $E_n(\rho)$ is the energy of electrostatic interaction with nuclei, $E_H(\rho)$ is the Hartree energy and $E_{XC}(\rho)$ is the exchange-correlation energy. The integrals extend over all space in three dimensions. These terms in summation are calculated as follows.

$$\begin{aligned} E_k(\rho) &= \sum_i f_i \int \psi_i^*(\mathbf{r}) \left(-\frac{1}{2} \nabla^2 \right) \psi_i(\mathbf{r}) d\mathbf{r} \\ &= \sum_i f_i \varepsilon_i - \int V(\mathbf{r}) \rho(\mathbf{r}) d\mathbf{r} \end{aligned} \tag{5.44}$$

where $\psi_i(\mathbf{r}) = \psi_{n,l,m}(\mathbf{r}) = \frac{1}{r} R_{n,l}(r) Y_{l,m}(\theta, \phi)$ and $Y_{l,m}(\theta, \phi)$ is spherical harmonics.

$$E_n(\rho) = \int V_n(\mathbf{r}) \rho(\mathbf{r}) d\mathbf{r} \tag{5.45}$$

$$E_H(\rho) = \frac{1}{2} \int \frac{\rho(\mathbf{r}) \rho(\mathbf{r}')}{|\mathbf{r} - \mathbf{r}'|} d\mathbf{r} d\mathbf{r}' = \frac{1}{2} \int V_H(\mathbf{r}) \rho(\mathbf{r}) d\mathbf{r} \tag{5.46}$$

$$E_{XC}(\rho) = \int \varepsilon_{XC}[\rho(\mathbf{r})] \rho(\mathbf{r}) d\mathbf{r} \tag{5.47}$$

$$\tilde{V}(\mathbf{r}) = \varepsilon_{XC} - V_{XC} - \frac{1}{2} V_H(\mathbf{r}) \tag{5.48}$$

Table 5.2**:** Total energy for Indium atom for B-Spline order $k = 4$ and mesh resolutions of 200 and 400 elements. Last row NIST provides the reference values. All values are in atomic energy unit (*Ha*).

ξ	$numel = 200$	$numel = 400$
6	-5737.256830	-5737.259150
8	-5737.301165	-5737.302151
10	-5737.307346	-5737.307900
12	-5737.308460	-5737.308833
14	-5737.308716	-5737.308999
20	-5737.308860	-5737.309046
NIST	-5737.309064	-5737.309064

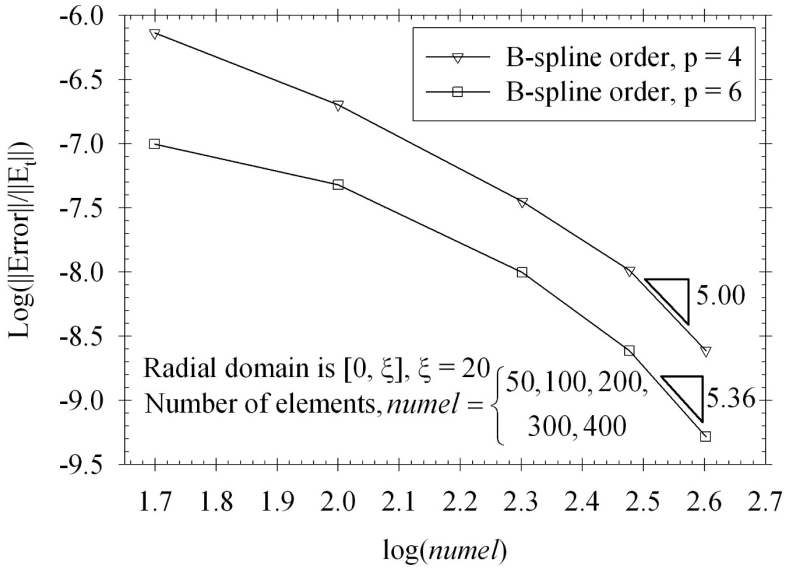

Fig. 5.8: Convergence plot for $E_t(\rho)$ as a function of number of elements.

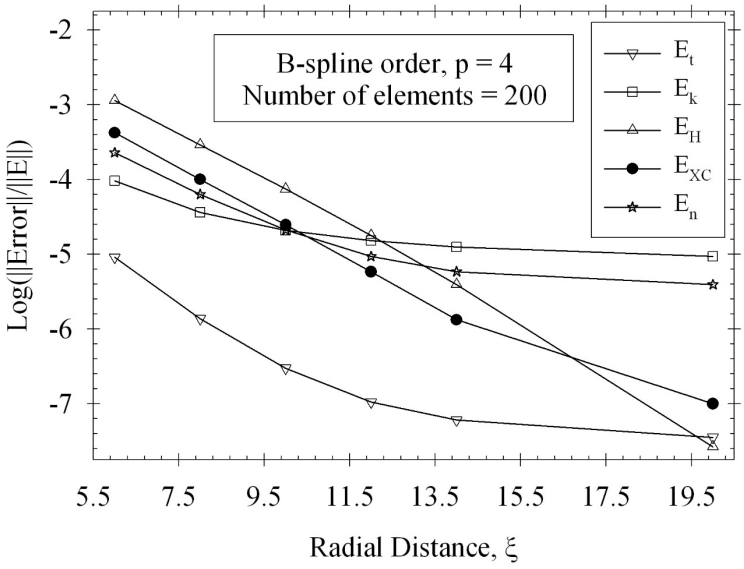

Fig. 5.9: Convergence plot for energies (equations 5.43-5.47) as a function of radial domain length ξ.

Total energy for Indium atom with all-electron density functional theory calculations for fourth order B-splines for two spatial discretization as a function of ξ, where ξ defines the radial domain $[0, \xi]$ is presented in Table 5.2. The calculated values are compared with values obtained from the National Institute of Standards and Technology (NIST) for the Indium atom [7]. As the domain length increases and approaches 20 atomic units, the computed value for total energy, $E_t(\rho)$, approaches reported NIST value.

B-splines of order 4 and order 6 were used with meshes varying from 50 elements to 400 elements and asymptotic convergence is achieved as shown in Fig. 5.8. Fig 5.9 and 5.10 show the convergence for total energy $E_t(\rho)$, energy due to electron-nuclei interaction $E_n(\rho)$, kinetic energy $E_k(\rho)$, Hartree energy $E_H(\rho)$, and exchange correlation energy $E_{XC}(\rho)$, as a function of ξ. Fig. 5.9 gives plots for fourth order B-spline with 200 element mesh, while Fig. 5.10 presents plots for fourth order B-spline with 400 element mesh. We see that errors in these energies

uniformly reduce as $\xi \to 20$. Figures 5.11 and 5.12 are plots for total energy of individual orbitals of Indium atom as a function of ξ for fourth order B-splines with 200 and 400 element meshes, respectively. Again, we find convergence of energy values as $\xi \to 20$. Higher resolution mesh consistently gives better precision in the computed values.

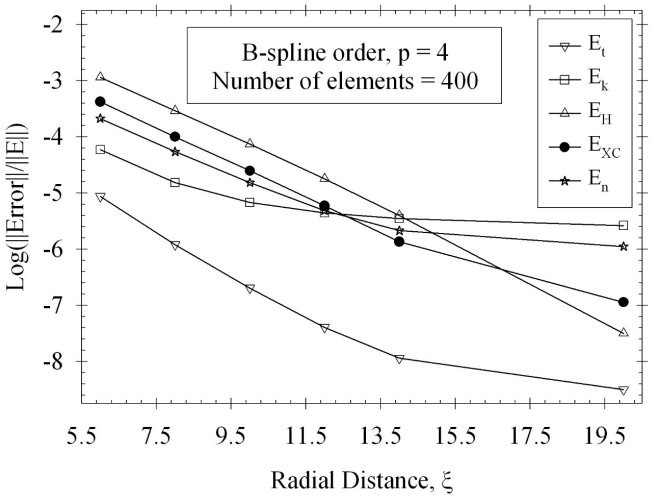

Fig. 5.10: Convergence plot for energies (equations 5.43-5.47) as a function of radial domain length ξ.

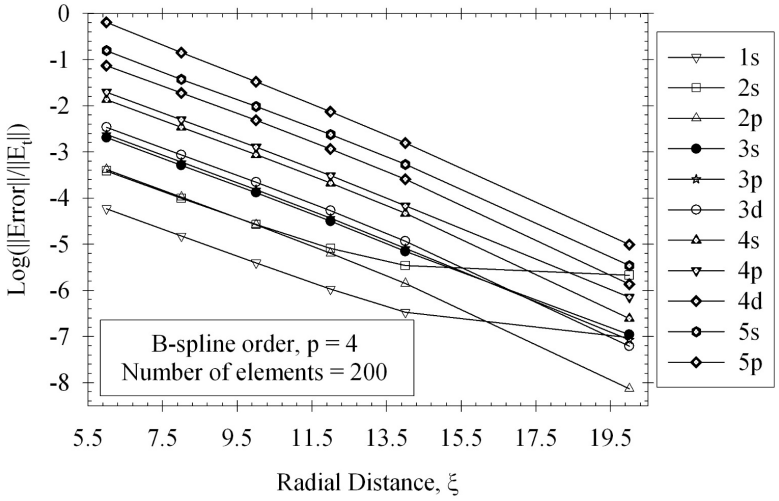

Fig. 5.11: Convergence plot for total energies of each orbital as a function of radial domain length ξ.

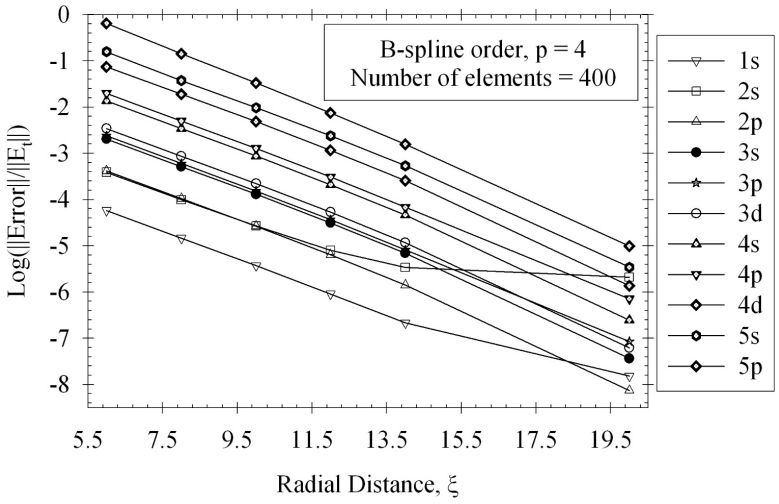

Fig. 5.12: Convergence plot for total energies of each orbital as a function of radial domain length ξ.

5.4.3.2 Bulk Silicon and self-consistent solution procedure

The primitive unit cell (FCC structure [Face centered cubic]) for bulk Silicon is described in [10]. A typical conventional unit cell and a corresponding primitive unit cell is shown in Fig. 5.13. Fig. 5.14 shows the first Brillouin zone (in the reciprocal space) and its irreducible wedge for the corresponding primitive unit cell. The atomic positions are shown with each primitive cell containing two Silicon atoms at positions $(0, 0, 0)$ and $(a/4, a/4, a/4)$.

The high symmetry points of the Brillouin zone are given as follows.

$$\Gamma = (0, 0, 0); \quad L = \frac{2\pi}{a}\left(\frac{1}{2}, \frac{1}{2}, \frac{1}{2}\right); \quad K = \frac{2\pi}{a}\left(\frac{3}{4}, \frac{3}{4}, 0\right);$$

$$X = \frac{2\pi}{a}(1, 0, 0); \quad W = \frac{2\pi}{a}\left(1, \frac{1}{2}, 0\right); \quad U = \frac{2\pi}{a}\left(1, \frac{1}{4}, \frac{1}{4}\right)$$

Since the eigenfunctions are functions of the wavevector $\mathbf{k}$, after the application of Bloch's theorem the electronic charge density needs to be evaluated by performing integration in the Brillouin zone.

$$n_{\mathbf{k}}(\mathbf{x}) = \sum_{i,\varepsilon_{i,k}<\varepsilon_F} f_{i,\mathbf{k}} \left|\phi_{i,\mathbf{k}}(\mathbf{x})\right|^2; \qquad \rho_e(\mathbf{x}) = \frac{1}{\Omega_{BZ}} \int_{\Omega_{BZ}} n_{\mathbf{k}}(\mathbf{x}) d\mathbf{k} = \sum_{\mathbf{k}} \omega_{\mathbf{k}} n_{\mathbf{k}}(\mathbf{x}) \tag{5.49}$$

where Ω_{BZ} is the volume of the first Brillouin zone. Monkhorst-Pack algorithm [39] is used to numerically integrate the electron charge density in the Brillouin zone. For the present study of bulk Silicon, 44 $\mathbf{k}$ points in the irreducible Brillouin zone are used to compute the electron charge density.

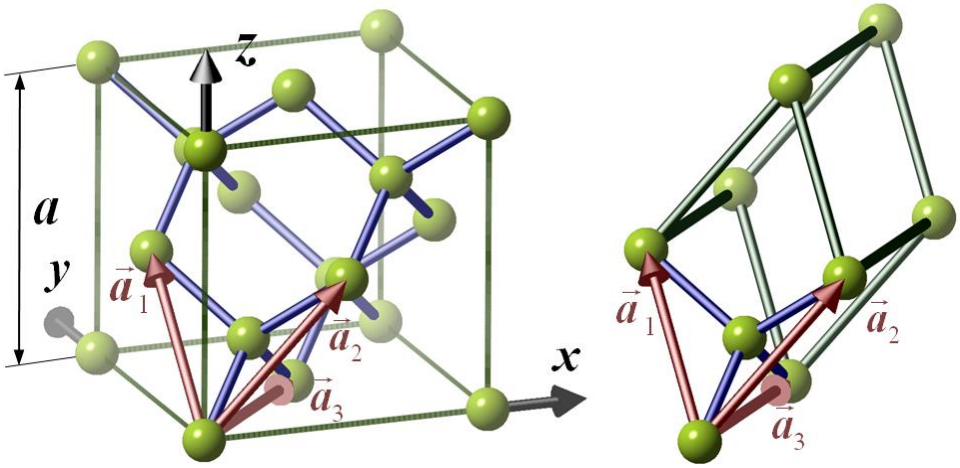

Fig. 5.13: Conventional unit cell and primitive unit cell.

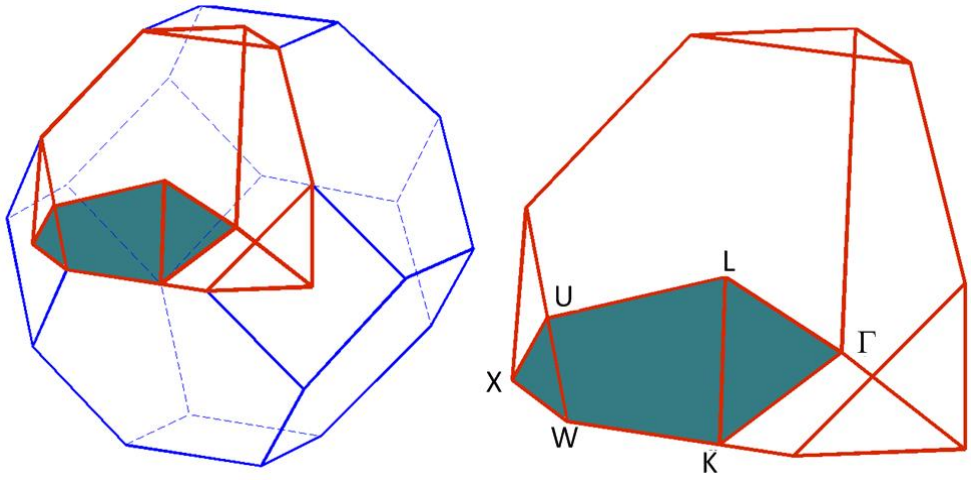

Fig. 5.14: First Brillouin zone and irreducible wedge.

Figures 5.15 and 5.16 show the band diagram plots for second and third order B-spline basis functions along the symmetry points in the Brillouin zone, respectively. The HGH pseudopotentials [40] and Perdew-Wang [41] exchange-correlation potential were used for the calculations presented here. Experimental studies show that Silicon has a band gap of 1.13 eV. The DFT method however underestimates the band gap to below 0.6 eV. This is well known artifact of DFT calculations with LDA (local density approximation) exchange-correlation functional.

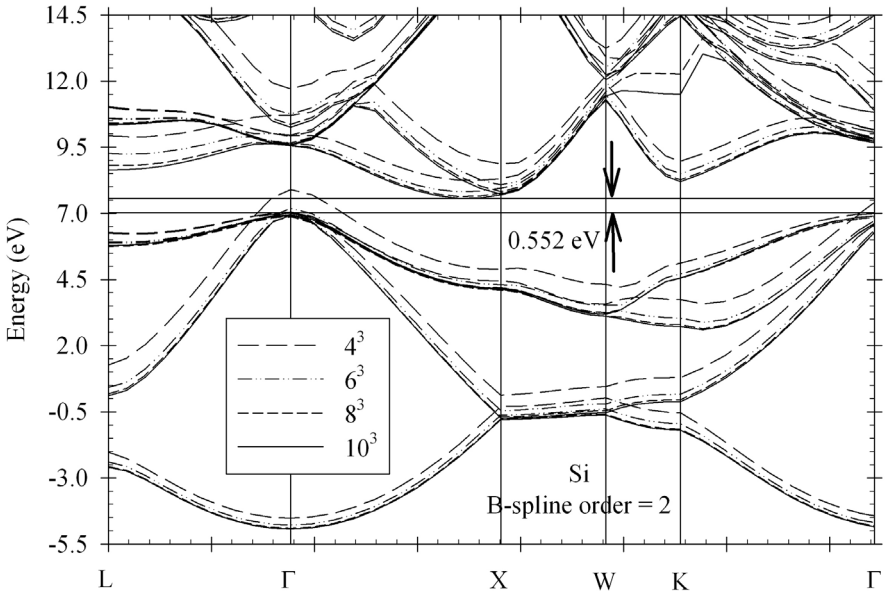

Fig. 5.15: Band diagram for Bulk Silicon for B-spline order $p = 2$.

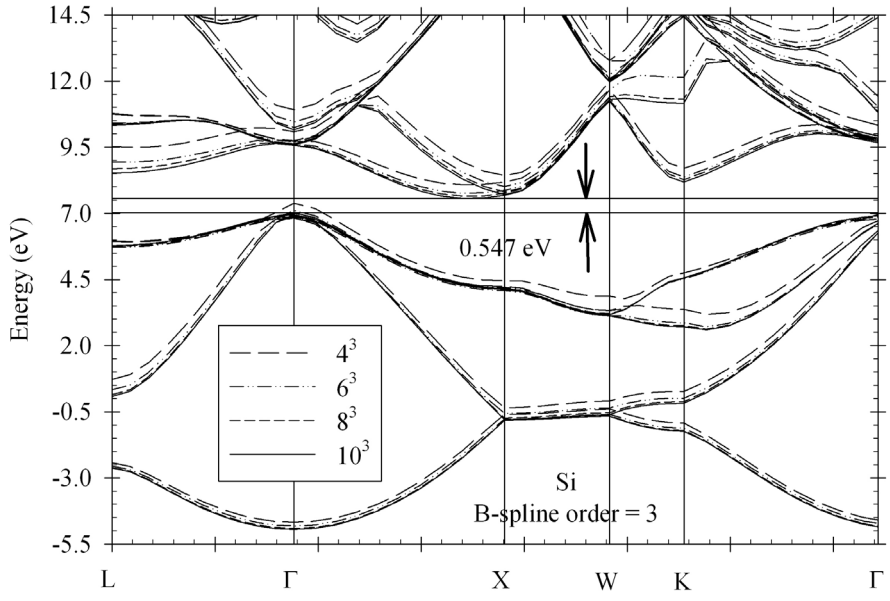

Fig. 5.16: Band diagram for Bulk Silicon for B-spline order $p = 3$.

Remark: *The problem run here is periodic and therefore only the atoms within the primitive unit-cell are modeled which has a lattice vector length of approximately 500-600 picometers including*

8 Si atoms. The self-consistent solution takes approximately 10 wall time minutes for the coarsest mesh (4^3) and 45 wall time minutes for the finest mesh (10^3).

5.4.3.3 Si on SiGe buffer

In this section we study strained Si grown on $Si_{1-\alpha}Ge_{\alpha}$ with different contents α of Germanium between $\alpha = 0.1$ and $\alpha = 1$. The problem is solved using the self-consistent formulation solving the Poisson equation and SWE using the HGH pseudopotentials [40] and Perdew-Wang [41] exchange-correlation potential. Silicon layer deposited on a $Si_{1-\alpha}Ge_{\alpha}$ buffer results in a difference between interatomic forces at the interface. This results in biaxial straining of the deposited layer of Si. The higher the Germanium content the less Si is in the buffer and the more response it will have to the Si overlay. The response to the Si overlay is shown in Fig. 5.17 where the low content of Germanium results in minimal straining and therefore insignificant splitting of the conduction bands at *k*-point X. In the case of little straining, the two energy valleys Δ_2 and Δ_4 have equivalent densities of electrons [42]. Fig. 5.18 shows the response when the buffer is composed only of Ge which leads to increased slipping in the conductive and valence bands at X leading to enhancement in the electronic properties of the material [36]. In this case, there exists a significant shift in the minimum energy of the two energy valleys as shown in Fig. 5.18. This leads to an increase in possibility of the electrons to transfer from the higher energy valley to the lower energy valley. Hence, this yields an increase in the electrons that exhibit higher mobility in the direction of strain [001] compared to those with lower mobility resulting in an increased conductivity in a specific direction due to the electron density imbalance across the energy valleys [42].

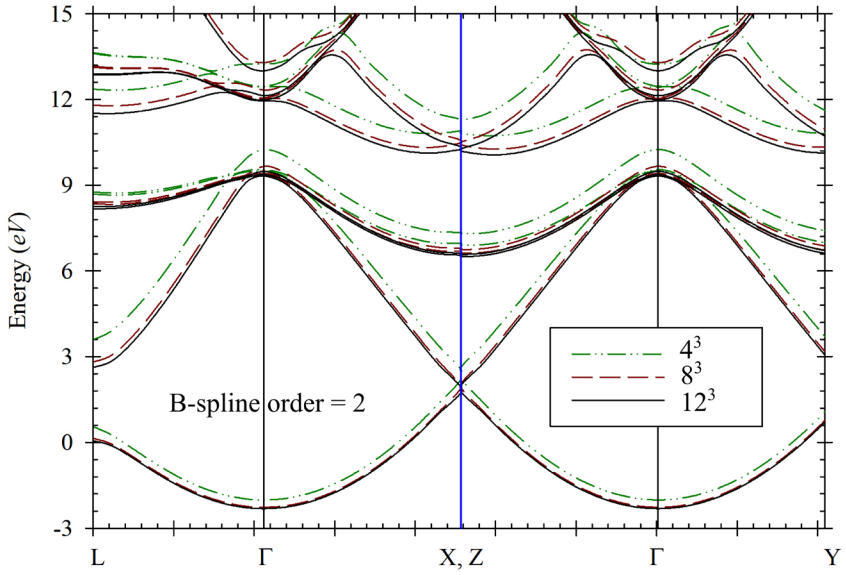

Fig. 5.17: Band diagram for strained Silicon on Silicon Germanium buffer ($Si_{0.9}Ge_{0.1}$).

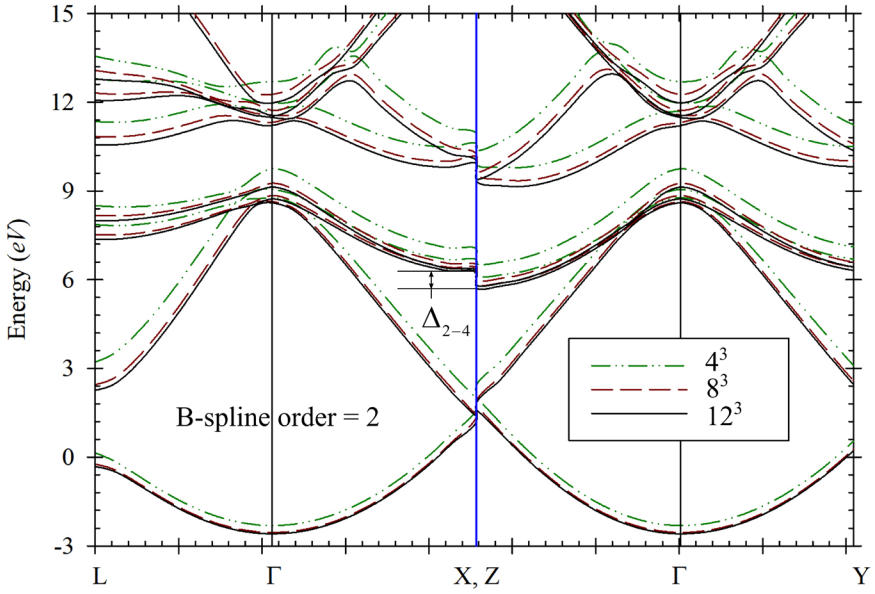

Fig. 5.18: Band diagram for strained Silicon on Silicon Germanium buffer ($Si_{0.0}Ge_{1.0}$).

Table 5.3 presents a comparison between the values of conduction band energy splitting due to the straining. Columns four and six present the potential for various compositions of Si and Ge in SiGe. Columns five and seven show the jump in the band gap at *k*-point X. The proposed finite

element method produces band splitting Δ_{2-4} values that agree very closely with the values in [35]. The table also presents the strain values in the biaxial directions and the orthogonal strain resulting due to the Poisson effects.

Table 5.3**:** Comparison of the conduction band energy splitting Δ_{2-4} using two different SCF solution methods. FE is the proposed finite element solution and the last two column corresponds to values obtained in [35].

α	$\varepsilon_{11}(\%)$	$\varepsilon_{33}(\%)$	FE $\Xi_u(eV)$	FE $\Delta_{2-4}(eV)$	Richard *et al.* [32] $\Xi_u(eV)$	Richard *et al.* [32] $\Delta_{2-4}(eV)$
0.1	0.373	-0.289	11.470	0.076	9.179	0.061
0.2	0.756	-0.586	9.840	0.132	9.216	0.124
0.3	1.147	-0.889	9.261	0.188	9.216	0.188
0.4	1.548	-1.199	9.220	0.246	9.255	0.255

5.4.3.4 Strained bulk Germanium

This section investigates the effects of straining of bulk Germanium which affects its properties as an optoelectronic material. Following along the solution procedure in Section 5.4.3.3 we employ the Poisson problem and SWE with HGH pseudopotentials [40] and Perdew-Wang [41] exchange-correlation potential. Straining is achieved by applying 3% tensile stretch biaxially in the direction [001] using the compliances presented in Section 5.3.2. The band gap structure for unstrained Germanium is shown in Figures 5.19 and that of the strained Germanium is shown in Fig. 5.20. Each problem is run for NURBS of order $p = 2$ using a 3D structured mesh of 4^3, 8^3 and 12^3 for the unit cell. Similar to trends seen in SiGe, Fig. 5.20 shows that the splitting in the valence and

conductive bands alters the conductive properties of the material [36] by reducing the resistivity of the semiconductor.

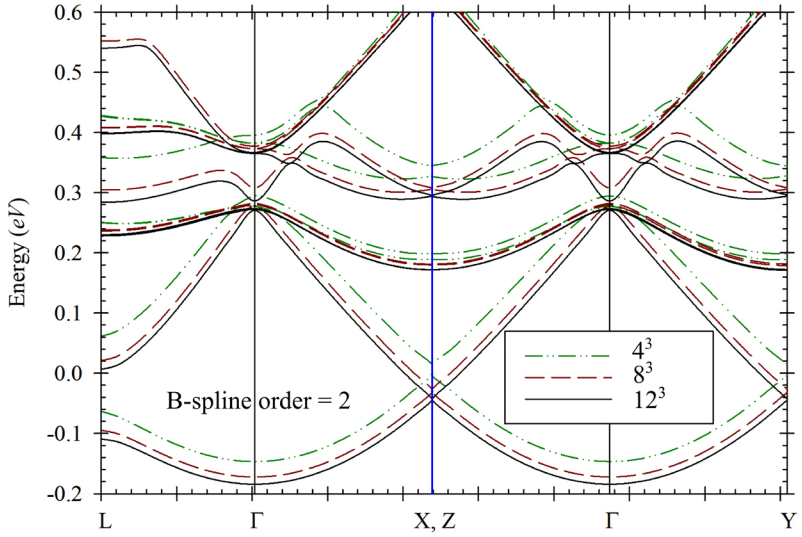

Fig. 5.19: Band diagram for unstrained Bulk Germanium for B-spline order $p = 2$.

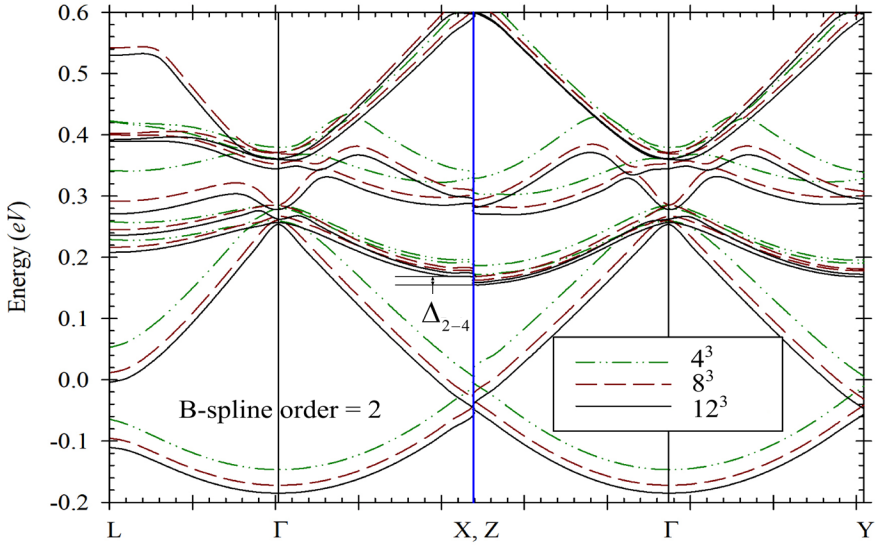

Fig. 5.20: Band diagram for strained Bulk Germanium for B-spline order $p = 2$ with 3% strain.

5.5 References

1. Kohn, W., Sham, L.J., 1965, "Self-consistent equations including exchange and correlation effects," Physical Review, 140(4A), pp. 1133–1138.

2. Viventi, J., Kim, D.H., Vigeland, L., Frechette, E.S., Blanco, J.A., Kim, Y.S., Wulsin, D.F., Rogers, J.A., Litt, B., 2011, "Flexible, foldable, actively multiplexed, high-density electrode array for mapping brain activity in vivo," Nature neuroscience, 14(12), pp.1599.

3. Lu, N., Lu, C., Yang, S., Rogers, J.A., 2012, "Highly Sensitive Skin-Mountable Strain Gauges Based Entirely on Elastomers," Advanced Functional Materials, 22(19), pp. 4044-4050.

4. Sun, Y., Rogers, J.A., 2007, "Inorganic semiconductors for flexible electronics," Advanced Materials, 19(15), pp. 1897–1916.

5. Maiti, A., 2003, "Carbon nanotubes: Bandgap engineering with strain," Nature Materials, 2(7), pp. 440.

6. Pitkethly, M. J., 2004, "Nanomaterials–the driving force," Materials today, 7(12), pp. 20-29.

7. Chelikowsky, J. R., Troullier, N., Saad, Y., 1994, "Finite-difference-pseudopotential method: Electronic structure calculations without a basis," Physical review letters, 72(8), pp. 1240.

8. Belytschko, T., Xiao, S. P., 2003, "Coupling methods for continuum model with molecular model." International Journal for Multiscale Computational Engineering, 1(1).

9. Liu, W. K., Karpov, E. G., Zhang, S., Park, H. S., 2004, "An introduction to computational nanomechanics and materials," Computer Methods in Applied Mechanics and Engineering, 193(17-20), pp. 1529-1578.

10. Masud, A., Kannan, R., 2012, "B-splines and NURBS based finite element methods for Kohn–Sham equations," Computer Methods in Applied Mechanics and Engineering, 241, pp. 112-127.

11. Liu, B., Jiang, H., Johnson, H. T., Huang, Y., 2004, "The influence of mechanical deformation on the electrical properties of single wall carbon nanotubes," Journal of the Mechanics and Physics of Solids, 52(1), pp. 1-26.

12. Thompson, S. E., Sun, G., Choi, Y. S., Nishida, T., 2006, "Uniaxial-process-induced strained-Si: Extending the CMOS roadmap," IEEE Transactions on Electron Devices, 53(5), pp. 1010-1020.

13. Masud, A., Kannan, R., 2009, "A multiscale framework for computational nanomechanics: Application to the modeling of carbon nanotubes," International journal for numerical methods in engineering, 78(7), pp. 863-882.

14. Nogueira, F., Castro, A., Marques, M. A., 2003, A tutorial on density functional theory. In A Primer in Density Functional Theory, Springer, Berlin, Heidelberg, pp. 218-256

15. Martin, R. M., 2004, Electronic structure: basic theory and practical methods. Cambridge University Press.

16. Singh, D. J., Nordström, L., 2006, Planewaves Pseudopotentials and the LAPW Method, Springer. New York.

17. Gavini, V., Bhattacharya, K., Ortiz, M., 2007, "Quasi-continuum orbital-free density-functional theory: A route to multi-million atom non-periodic DFT calculation," Journal of the Mechanics and Physics of Solids, 55(4), pp. 697-718.

18. Gavini, V., Knap, J., Bhattacharya, K., Ortiz, M., 2007, "Non-periodic finite-element formulation of orbital-free density functional theory," Journal of the Mechanics and Physics of Solids, 55(4), pp. 669-696.

19. Suryanarayana, P., Gavini, V., Blesgen, T., Bhattacharya, K., Ortiz, M., 2010, "Non-periodic finite-element formulation of Kohn–Sham density functional theory," Journal of the Mechanics and Physics of Solids, 58(2), pp. 256-280.

20. Hughes, T. J., Cottrell, J. A., Bazilevs, Y., 2005, "Isogeometric analysis: CAD, finite elements, NURBS, exact geometry and mesh refinement." Computer methods in applied mechanics and engineering, 194(39-41), pp. 4135-4195.

21. Pask, J. E., Klein, B. M., Sterne, P. A., Fong, C. Y., 2001, "Finite-element methods in electronic-structure theory," Computer Physics Communications, 135(1), pp. 1-34.

22. Pask, J. E., Sterne, P. A., 2005, "Finite element methods in ab initio electronic structure calculations," Modelling and Simulation in Materials Science and Engineering, 13(3), pp. R71.

23. Pask, J. E., Sterne, P. A., 2005, “Real-space formulation of the electrostatic potential and total energy of solids.” Physical Review B, 71(11), pp. 113101.

24. Chelikowsky, J. R., Troullier, N., Wu, K., Saad, Y., 1994, “Higher-order finite-difference pseudopotential method: An application to diatomic molecules.” Physical Review B, 50(16), pp. 11355.
25. Pickett, W. E., 1989, “Pseudopotential methods in condensed matter applications,” Computer Physics Reports, 9(3), pp. 115-197.

26. Piegl, L., Tiller, W., 2012, The NURBS book, Springer Science & Business Media.

27. Masud, A., 2005, “A 3-D model of cold drawing in engineering thermoplastics.” Mechanics of Advanced Materials and Structures, 12(6), pp. 457-469.

28. Masud, A., 2000, “A multiplicative finite strain finite element framework for the modelling of semicrystalline polymers and polycarbonates,” International Journal for Numerical Methods in Engineering, 47(11), pp. 1887-1908.

29. Masud, A., Truster, T. J., Bergman, L. A., 2011, “A variational multiscale a posteriori error estimation method for mixed form of nearly incompressible elasticity,” Computer Methods in Applied Mechanics and Engineering, 200(47-48), pp. 3453-3481.

30. Masud, A., Calderer, R., 2011, “A variational multiscale method for incompressible turbulent flows: Bubble functions and fine scale fields.” Computer Methods in Applied Mechanics and Engineering, 200(33-36), pp. 2577-2593.

31. Masud, A., Truster, T. J., 2013, “A framework for residual-based stabilization of incompressible finite elasticity: Stabilized formulations and F-bar methods for linear triangles and tetrahedra,” Computer Methods in Applied Mechanics and Engineering, 267, pp. 359-399.

32. Gullett, P. M., Horstemeyer, M. F., Baskes, M. I., Fang, H., 2007, “A deformation gradient tensor and strain tensors for atomistic simulations,” Modelling and Simulation in Materials Science and Engineering, 16(1), pp. 015001.

33. Cormier, J., Rickman, J. M., Delph, T. J., 2001, “Stress calculation in atomistic simulations of perfect and imperfect solids,” Journal of Applied Physics, 89(1), pp. 99-104.

34. Kannan, R., Masud, A., 2009, “Stabilized finite element methods for the Schrödinger wave equation,” Journal of Applied Mechanics, 76(2), pp. 021203.

35. Richard, S., Aniel, F., Fishman, G., Cavassilas, N., 2003, “Energy-band structure in strained silicon: A 20-band k· p and Bir–Pikus Hamiltonian model.” Journal of applied physics, 94(3), pp. 1795-1799.

36. Sakata, K., Magyari-Köpe, B., Gupta, S., Nishi, Y., Blom, A., Deák, P., 2016, “The effects of uniaxial and biaxial strain on the electronic structure of germanium,” Computational Materials Science, 112, pp. 263-268.

37. Hiemstra, R. R., Calabro, F., Schillinger, D., and Hughes, T. J., 2017, “Optimal and Reduced Quadrature Rules for Tensor Product and Hierarchically Refined Splines in Isogeometric Analysis,” Comput. Methods Appl. Mech. Eng., **316**, pp. 966–1004.

38. Chermette, H., 1998, “Density functional theory: a powerful tool for theoretical studies in coordination chemistry.” Coordination chemistry reviews, 178, pp. 699-721.

39. Monkhorst, H. J., Pack, J. D., 1976, “Special points for Brillouin-zone integrations,” Physical review B, 13(12), pp. 5188.

40. Hartwigsen, C., Gœdecker, S., Hutter, J., 1998, “Relativistic separable dual-space Gaussian pseudopotentials from H to Rn,” Physical Review B, 58(7), pp. 3641.

41. Perdew, J. P., Wang, Y., 1992, “Accurate and simple analytic representation of the electron-gas correlation energy,” Physical Review B, 45(23), pp. 13244.

42. Smith, C.S., 1954, “Piezoresistance effect in germanium and silicon,” Physical review, 94(1), pp. 42.

CHAPTER 6

CONCLUSION AND FUTURE WORK DIRECTIONS

6.1 Conclusion

In chapter 2 we presented a variationally consistent derivation of Discontinuity Capturing (DC) finite element methods for application to advection dominated flows, multi-phase flows with jumps in pressure and/or concentration fields, and problems that involve mixing flows of immiscible incompressible fluids. The proposed Variational Multiscale Discontinuity Capturing (VMDC) method finds roots in the Variational Multiscale (VMS) framework that yields a coupled system of coarse and fine-scale variational problems. The structure of the fine-scale variational problem is central to the derivation of VMDC method and facilitates the embedding of weak and/or strong discontinuities in the space of fine-scale functions. This results in sub-grid scale models that are naturally endowed with weak and/or strong discontinuities. Specifically, the fine scales are interpolated by bubble functions that by definition vanish on the element edges, thereby localizing the fine-scale problem to the sum of element interiors. These bubble functions are modified via composition with additional interpolation functions that are endowed with weak discontinuity that helps in accurately modeling weak discontinuities in the unknown fields across the embedded interfaces.

For the case of mixing flow of immiscible fluids, the two-liquid interface is tracked by a signed distance field that acts as a marker for the location of the discontinuity. For this class of problems the fine-scale enrichment function is developed via embedding in it the location of the interface that is facilitated by the signed distance field. The composition of the enrichment

function with the underlying bubble functions results in modified fine-scale interpolations functions that vanish along element boundaries. These functions when employed to model the fine-scale problem result in fine-scale models with embedded discontinuity. Due to the structure of the fine-scale sub-problems we are able to variationally embed the fine-scale models without the need to solve for the fine degrees of freedom explicitly at the global level. This feature is in sharp contrast to global enrichment methods employed in XFEM/GFEM methods that necessitate a modification of the interpolation functions even in the elements that may not be traversed by the discontinuity, thus increasing the size of the discrete problem. VMDC method also bypasses the issues observed in IFEM where the mismatch of functions across adjacent elements results in suboptimal convergence of the method. Numerical integration of the discontinuous functions is carried out via adaptive quadrature technique. VMDC method is applied to advection equation to explore the structure of the stabilization tensor and an analysis with respect to the classical DC operator is presented. Method is tested on three mixed-field problems. First problem is a steady state multiphase flow governed by the Stokes flow equations and involves discontinuous pressure fields that arise due to surface tension effects. The second test case is that of a rising bubble with surface tension effects where the motion is induced by buoyancy. The third test case is a transient nonlinear Rayleigh-Taylor instability problem of immiscible flow of incompressible fluids that is governed by the incompressible Navier-Stokes equations. In all the cases stable response of the unknown fields is observed that highlights the stability and accuracy features of the method and its range of applicability for problems of engineering interest.

In chapters 3 and 4 we have presented a variational DC capturing method coupled with a unified compressible-incompressible flow formulation that allows for modeling two-phase flows, where each phase is modeled separately as compressible or incompressible. The VMDC method

presented accommodates sharp discontinuities in both material properties and state equation coefficients such as the isothermal compressibility coefficient. The resulting flow formulation along with a consistent *div*-stabilization is shown to allow for volume change within the compressible region while still maintaining quasi-incompressibility with near zero divergence of the velocity in the incompressible region. Problems modeling air bubble shrinkage and compression within water cavities are presented along with comparison of the proposed method with other methods showing the advantage of the VMDC method in allowing for the use of coarser time steps while achieving better engineering convergence to the analytical solutions of these problems. Furthermore, the method is extended to model 2D and 3D problems involving incompressible flows of merging and rising bubbles with varying surface tension coefficients. These problems are used to validate the scalability of the method to higher dimensions and its capability to accommodate complex interfaces. An industrially relevant problems is then presented which has significant applications in multiple disciplines. This problem is abundantly used for modeling ocean wave formation, astrophysical hydrodynamics and even metrological flow of clouds, namely the Kelvin-Helmholtz instability. Employing an ideal gas law and with varying surface tension coefficients we study the effects of surface tension on the formation of turbulent flow at the interface between the two phases. Hence, we are able to apply surface tension effects within the unified compressible-incompressible formulation to control the turbulence initiation at the interface.

Finally in chapter 5 we have presented B-splines and NURBS based finite element method for self-consistent solution of the complex-valued generalized eigenvalue problem arising from SWE. Under increasing mechanical strains, the mechano-electronic coupling yields the new equilibrium positions of the atoms as a function of evolving stretching of the underlying primitive

lattice vectors. This results in evolving electronic charge density employed in the Poisson problem that yields evolving effective potential for the SWE. The method is validated on problems with analytical potential to establish the variational convergence properties of the formulation. Newly proposed optimal and reduced integration rules are employed for numerical integration and they result in substantial reduction in computational cost while maintaining optimal convergence in the norms considered. The self consistent solution procedure is applied to strained bulk Germanium and to material system comprised of Si on SiGe buffer with various compositions. The proposed finite element method produces band splitting in the band gap diagrams that agree well with the values reported in the literature, thereby making it a viable method for the modeling of mechano electronic properties of materials used in the burgeoning field of flexible electronics.

6.2 Future Work

A significantly important technical issue in processing of fibrous composites is the appearance and evolution of the gaseous bubbles that form regions of stress concentration as the gelling process is completed. Chemical reactions that accompany curing, together with the ambient temperature at which the composite is manufactured, has a profound impact on the properties of the final product. Specifically, spatial variation of temperature field gives rise to differential curing, and due to variable mechanical material properties of the finished product, cooling down to room temperature gives rise to residual stresses. In addition, chemical reactions give rise to a gaseous phase wherein bubbles grow or collapse depending on the availability of the contaminant, the local pressure and temperature fields. Besides, mean velocity of the resin under hydrodynamic loads together with gradients induced by the concentration field result in migration of the voids, causing merger of multiple bubbles into one larger bubble, or breaking of larger bubbles into

smaller bubbles, and this process is again a function of interplay between the surface tension effects and the hydrodynamic forces induced by bubble convection.

Current engineering practice is to assume the mechanical and thermal coefficients and carry out linear of nonlinear analysis of the produced part. In case of difference in the computed response, the mechanical material properties are invariably statistically distributed for subsequent runs, and a general response is attained.

Keeping in view that even under carefully controlled environments, the process modeling phase of manufacturing is subject to various processing parameter, namely, applied temperature, pressure, humidity, radiation conditions, the resulting material properties has local heterogeneity. In addition, a critical issue is that if one of the products of the chemo-thermal reactions has a gaseous phase, and this is invariably the case, the resulting product has an inherent porosity distribution that should not be neglected because of its effect on the performance of the component under service loads.

Two situations arise: (i) the pores are large and visible which means the molar production of the gaseous phase is much high and the options are to either use different ingredients that can suppress the gaseous phase, or (ii) adjust the processing parameters that can help reduce the size of the pores. In either case, if one looks under the microscope, one can again see the same phenomena of dispersed or interconnected pores. So, the question to ask is if it is possible to develop a method that can be used to optimize the material together with the controlling processing parameters for producing a part with an end objectivity in terms of its performance under service conditions. This section presents another aspect of practical application of the method presented in chapters 2, 3 and 4.

6.2.1 Proposed Time Dependent model for Viscosity

We propose the following time dependent model for viscosity evolution developed in [1] in the following format:

$$\mu = \mu_\infty \exp\left(\frac{\Delta E_\mu}{RT}\right)\left[\frac{\alpha_g}{\alpha_g - \alpha}\right]^{(A+B\alpha)} \tag{6.1}$$

where μ is the viscosity, μ_∞ is the viscosity at saturation temperature, ΔE_μ is the activation energy of flow, R is the universal gas constant and T is the temperature. α is the degree of cure varying from 0 to 1, α_g is the level of cure at the time gelation when the material may no longer be considered as a fluid and *A* and *B* are fitting parameters for the material of choice. Likewise, the degree of cure is assumed to change with time according to a first order reaction such that

$$\alpha = A(1 - e^{-t/\tau}) \tag{6.2}$$

where ΔH_o is the reaction heat and $dH / d\tau$ is the heat flow.

6.2.2 Creating a Temperature Dependent model for Viscosity evolution

To develop time and temperature dependent model, we employ the Kamal-Sourour [2] format of the Arrhenius equations. The curing process has a kinetic process of the form.

$$\frac{d\alpha}{d\tau} = f(T, \alpha) \tag{6.3}$$

The temperature dependent function, $f\left(T, \alpha\right)$ has been used in different contexts in the literature. In our earlier work [2] we employed these ideas to develop evolution of elastic modulus as a function of time and temperature. In this work we employ this framework to extend the viscosity evolution model (6.1) to have temperature dependence as well:

$$f(T,\alpha) = (k_1(T) + k_2(T)\alpha^m)(1-\alpha)^n \tag{6.4}$$

$$k_1(T) = A_1 \exp\left(-\frac{\Delta E_1}{TR}\right) \tag{6.5}$$

$$k_2(\mathrm{T}) = A_2 \exp\left(-\frac{\Delta E_2}{TR}\right) \tag{6.6}$$

where m and n are power constants, R is the gas constant, A_1 and A_2 are frequency like constants, and ΔE_1 and ΔE_2 are the activation energies.

For the case of chemical reactions affecting cure, equation (6.4) can be simplified to depend on a single reaction coefficient by setting $k_2(T)$ to zero. This simplification is justified under the assumption that $k_2(T)$ contributes weakly to the behavior of the overall model. Furthermore, we employ a first order reaction equation that corresponds to the case when there is no time-lag between curing and chemical reactions in the resin. Consequently, the power constant n=1, and this helps introducing temperature dependency to the time dependent curing model given in equation (6.2). It is shown in the following form:

$$\dot{\alpha} = k_1(T)(1-\alpha) \tag{6.7}$$

$$k_1(T) = A_1 \exp\left(-\frac{\Delta E_1}{TR}\right) \tag{6.8}$$

By taking the derivative of equation (6.2) and introducing time dependent curing models into equation (6.7), the following equivalence is shown:

$$\frac{A}{\tau}\exp\left(-\frac{t}{\tau}\right) = k_1(T)\left[1-\left(A - A\exp\left[-\frac{t}{\tau}\right]\right)\right] \tag{6.9}$$

Equation (6.9) has a simple solution when the curing constant A=1 and this corresponds to a maximum degree of cure is 1.0. Solving equation (6.9) yields:

$$k_1(T) = \frac{1}{\tau} \tag{6.10}$$

Equating equations (6.8) and (6.10) provides a solution set for calculating ΔE_1 and A_1.

$$A_1 \exp\left(-\frac{\Delta E_1}{TR}\right) = \frac{1}{\tau} \tag{6.11}$$

$$\Delta E_1 = TR \ln(A_1 \tau) \tag{6.12}$$

Accordingly, for the simplified model, any combination of ΔE_1 and A_1 that satisfies equation (6.12) will have a solution for the curing evolution equation. The presented values obtained for ΔE_1 and A_1, are adopted from [1] and are material dependent, specifically obtained through a fitting to experimental generated cure and viscosity plots.

6.2.3 Evolution of Cure

Within a time dependent loop the degree of cure is updated via a time integration method for the first-order systems.

$$\alpha_{n+1} = \alpha_n + \dot{\alpha}\, \Delta t \tag{6.13}$$

where $\dot{\alpha}$ is the change in the degree of cure with respect to time as calculated in equation (6.7) and Δt is the change in time from α_n to α_{n+1}. By combining equations (6.1) and (6.13) an equation for the viscosity parameter can be developed that has dependency on the degree of cure, which in turn is a function of time and of temperature. Thus, embedding the results from (6.13)

into (6.1) yields an evolution of the viscosity as a function of temperature and degree of cure employing the chemo-rheological kinetic model above. In the following section we show preliminary results for a bracket problem with bubble evolution during an initial curing process.

6.2.4 Preliminary results

In this section we present a case of an angle bracket with embedded fibers represented by wholes in the mesh. This preliminary problem employs the model of chemo-rheological viscosity evolution with thermal dependence. Fig. 6.1 shows the mesh and initial void locations and fibers.

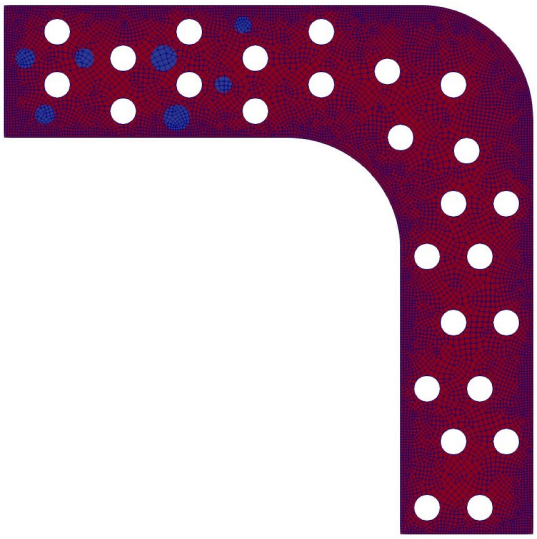

Fig. 6.1. The mesh of the angle bracket problem with mesh and fibers excluded from the mesh along with initial void location.

This problem is modeled to show the pressure jumps, as surface tension is active, with the mesh motion and how surface tension induced jumps are captured sharply. Moreover, the evolution of the bubbles is slowly hindered as the viscosity increases leading to a cured bracket piece. Fig. 6.2 shows the shape and location of the bubbles at different time levels.

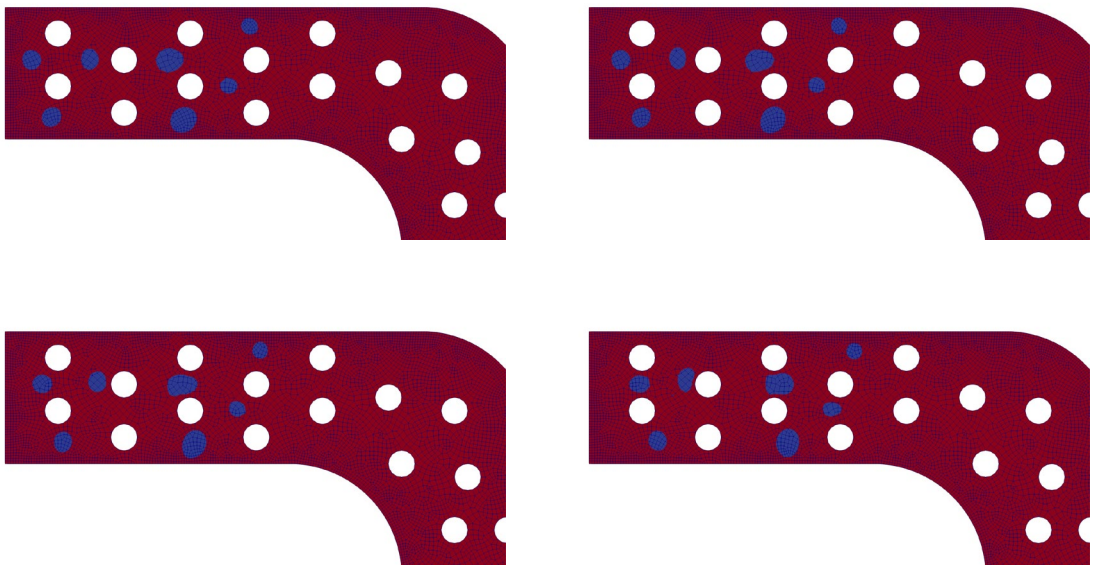

Fig. 6.2. The mesh of the angle bracket problem with mesh and fibers excluded from the mesh along with initial void location.

As the temperature increases the degree of cure and viscosity increase from the initial low viscosity point from which the numerical problem is run. This would model the curing process during the resin infusion process and the vacuum sealed autoclaving of the fibrous bracket. The thermal field evolution is shown in Fig. 6.3 with clear difference in the thermal diffusivity visible in the first time step. Fig. 6.4 shows the pressure profile evolution through the same time steps in Fig. 6.2 with the pressure jumps captured as the interface is evolving and the bubble are changing shape and position. These preliminary results show the potential of the methods developed in this desecration to tackle one possible area of application where predictive models are needed to better understand the processing parameters that would lead to better porosity distributions within composite materials.

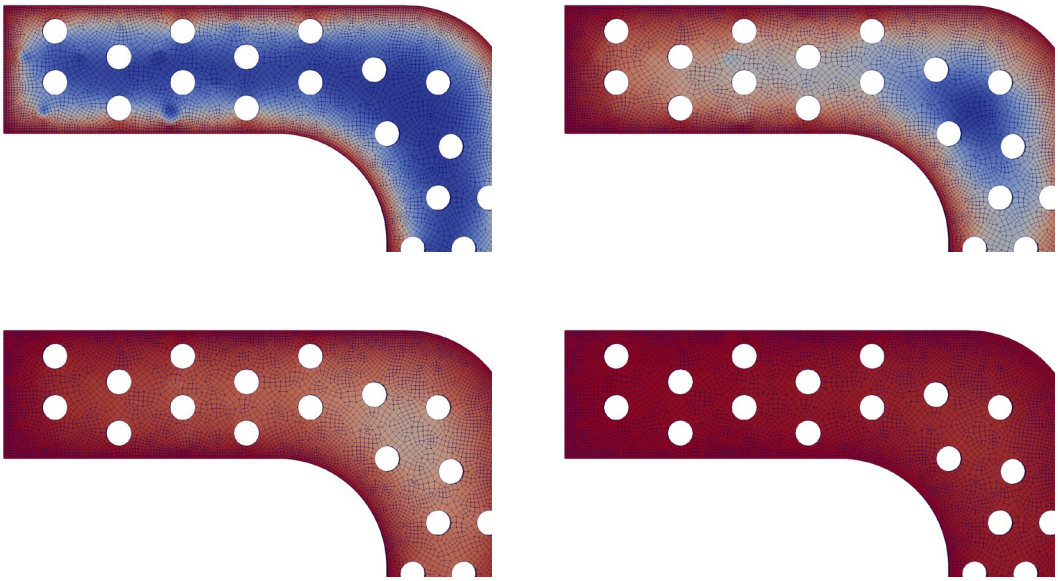

Fig. 6.3. Temperature evolution for different time levels.

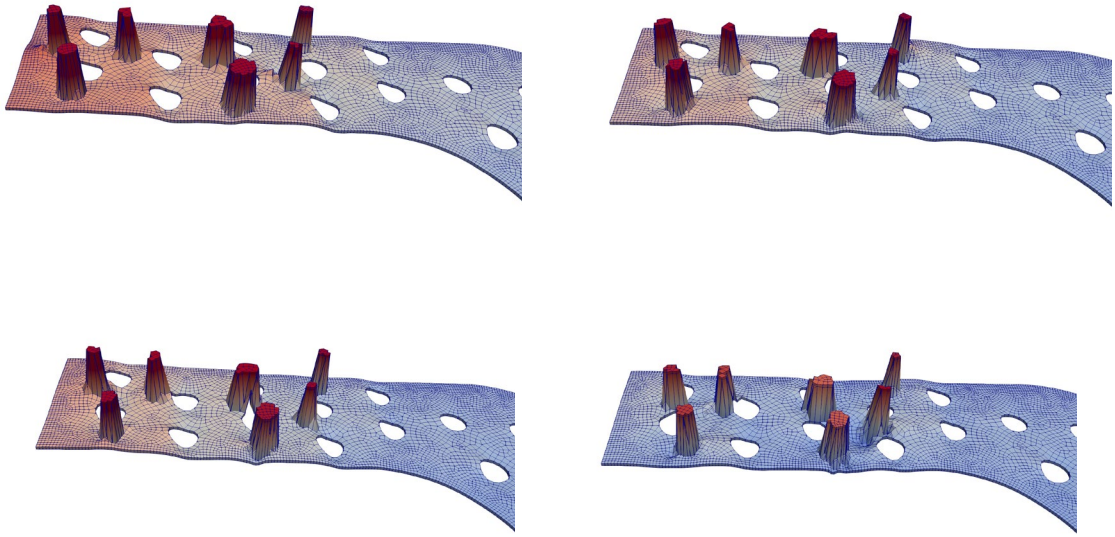

Fig. 6.4. Pressure evolution for different time levels.

6.3 References

1. Garschke, C., Parlevliet, P. P., Weimer, C., & Fox, B. L. (2013). Cure kinetics and viscosity modelling of a high-performance epoxy resin film. Polymer Testing, 32(1), 150-157.

2. Kamal, M. R., & Sourour, S. (1973). Kinetics and thermal characterization of thermoset cure. Polymer Engineering & Science, 13(1), 59-64.

3. Gajendran, H., Hall, R. B., Masud, A., & Rajagopal, K. R. (2018). Chemo-mechanical coupling in curing and material-interphase evolution in multi-constituent materials. Acta Mechanica, 1-22.